



<https://theses.gla.ac.uk/>

Theses Digitisation:

<https://www.gla.ac.uk/myglasgow/research/enlighten/theses/digitisation/>

This is a digitised version of the original print thesis.

Copyright and moral rights for this work are retained by the author

A copy can be downloaded for personal non-commercial research or study,  
without prior permission or charge

This work cannot be reproduced or quoted extensively from without first  
obtaining permission in writing from the author

The content must not be changed in any way or sold commercially in any  
format or medium without the formal permission of the author

When referring to this work, full bibliographic details including the author,  
title, awarding institution and date of the thesis must be given

Enlighten: Theses

<https://theses.gla.ac.uk/>  
[research-enlighten@glasgow.ac.uk](mailto:research-enlighten@glasgow.ac.uk)

**A Topological Study Of  
Multiplicity In Three Jet  
 $q\bar{q}g$  Events With The  
ALEPH Detector At LEP**

Lee Curtis

Department of Physics and Astronomy  
The University of Glasgow  
Glasgow, Scotland

*Thesis submitted for the degree of  
Doctor of Philosophy*

September, 1998

© L. Curtis, 1998

ProQuest Number: 10992322

All rights reserved

INFORMATION TO ALL USERS

The quality of this reproduction is dependent upon the quality of the copy submitted.

In the unlikely event that the author did not send a complete manuscript and there are missing pages, these will be noted. Also, if material had to be removed, a note will indicate the deletion.



ProQuest 10992322

Published by ProQuest LLC (2018). Copyright of the Dissertation is held by the Author.

All rights reserved.

This work is protected against unauthorized copying under Title 17, United States Code  
Microform Edition © ProQuest LLC.

ProQuest LLC.  
789 East Eisenhower Parkway  
P.O. Box 1346  
Ann Arbor, MI 48106 – 1346

GLASGOW  
UNIVERSITY  
LIBRARY

11380 (copy 1)

## Abstract

A study of particle multiplicity in quark and gluon jets is made using events observed by the ALEPH detector at LEP. Events with three separated jets are selected from approximately 4 million hadronic  $Z^0$  decays, recorded in the data-taking period 1990-95.

The energies of the jets are estimated to allow the multiplicity of each event to be located on a two-dimensional Dalitz plane. A given point on this plane corresponds to a distinct jet topology. Multiplicity distributions across the plane are compared to theoretical predictions, which are based on an expression for the multiplicity of a single quark jet.

The gluon jet in each event is not directly identified; instead, the leading order matrix element is used to give the probability that each jet originated from the gluon. This method has the benefit that candidate three-jet events are not biased to include only those which satisfy explicit quark tagging techniques, such as those used to tag heavy flavours.

Colour coherence, which is expected to affect particle production in the regions between quark and gluon jets, is incorporated into theoretical predictions via topological scales. These scales allow the multiplicity of a given jet to be described in terms of both the jet energy and the angular proximity of neighbouring jets. Theoretical predictions are corrected for detector effects and compared directly with ALEPH data.

## Preface

This thesis presents a study of the topological dependence of multiplicity in three-jet  $q\bar{q}g$  events, using data collected by the ALEPH detector at LEP. As part of the ALEPH collaboration, the author was responsible for the upgrade and maintenance of the TPC Laser Calibration System, as well as regular shifts during data taking.

The material presented in this thesis reflects the author's own individual analysis of the ALEPH data. No portion of the work described in this thesis has been submitted in support of an application for another degree or qualification in this, or any other, institute of learning.

## Acknowledgements

This thesis involved, in some way, a very large number of people. I'd like to take this opportunity to thank a selection of them. For the last four years I have been nestled within the Experimental Particle Physics Group at the University of Glasgow. During this time I have had invaluable help from my supervisors, Bert Turnbull and Andy Halley, as well as many other members of the group, including Jim Lynch, Jason Ward and Stan. In particular, I'd like to thank Ian Knowles for his patience and persistence, especially over the final furlongs. Thankfully, I had the companionship of Fiona, Jane, Evelyn and the "boys" to help me through the office hours.

But its not all work. Special thanks are due to Matt (for excursions to the Grand Rue, Genève) and Simon and Steve (for services to the Induni construction corporation). In the occasional moments away from study I was escorted and amused about Glasgow by Farooq and Aidan, who were also foolish enough to share a flat with me. I feel as though I must mention Dave and Briggsy, without whom I wouldn't have accidentally found myself in Glen Coe/Skye/Torridon/the *Cul De Sac* as often as I had. Thanks also to Matthew Gloag & Son Ltd., Perth, for their warmth and guidance over the long Winter evenings.

I would not have remained sane at CERN if not for the amusing interludes supplied by Mike, Doug, Matt, James, Gareth, Ali and Grahame. The fine hostelry provided by the Barneys will never be forgotten, along with the logs, sheep, flue and smelt of Andy Galloni's Hut. Additionally, sizeable gratifications are due to Elizabeth, for housing and helping me through the tricky bits, and my parents, for housing me and my vehicles through the tricky bits.

Finally, I would like to say what a constant pleasure it has been working on this tome over the last few months. However, I would not like to convey a false impression through the introduction of intentional falsehoods. Suffice to say, I would like to give praise heretofore to the one person who, above all, has made all this possible. The poor sod who had to write this thesis.

# Contents

<b>1</b>	<b>Introduction</b>	<b>2</b>
<b>2</b>	<b>Particle Production in <math>e^+e^-</math> Collisions</b>	<b>4</b>
2.1	Introduction . . . . .	4
2.2	Overview Of The Standard Model . . . . .	5
2.3	Quantum Chromodynamics . . . . .	8
2.3.1	Colour And SU(3) . . . . .	8
2.3.2	The Running Coupling . . . . .	10
2.4	Hadronic Jets . . . . .	13
2.5	The Process $e^+e^- \rightarrow q\bar{q}$ . . . . .	14
2.6	The Perturbative Parton Cascade . . . . .	15
2.6.1	$e^+e^- \rightarrow q\bar{q}g$ . . . . .	17
2.6.2	$e^+e^- \rightarrow q\bar{q} + Ng$ . . . . .	18
2.6.3	Coherence effects . . . . .	20
2.7	Hadronization . . . . .	21
2.8	Fragmentation Models . . . . .	21
2.8.1	JETSET . . . . .	22
2.8.2	HERWIG . . . . .	23
<b>3</b>	<b>Overview and Motivation</b>	<b>24</b>
3.1	Introduction . . . . .	24
3.2	QCD And Jets At LEP . . . . .	25
3.2.1	Quark Jets . . . . .	25
3.2.2	Gluon Jets . . . . .	28
3.3	Three-Jet Events . . . . .	30
3.3.1	Interjet Particle Flow . . . . .	31
3.3.2	Topological Scales . . . . .	33
3.3.3	The Dalitz Plane . . . . .	35
3.4	Previous Studies . . . . .	36

3.4.1	Quark-Gluon Differences . . . . .	37
3.4.2	Subjets . . . . .	38
3.4.3	Colour Coherence . . . . .	39
3.5	Motivation For This Analysis . . . . .	40
3.6	Analysis Strategy . . . . .	41
<b>4</b>	<b>The ALEPH Experiment at LEP</b>	<b>42</b>
4.1	LEP . . . . .	42
4.2	ALEPH . . . . .	43
4.3	Overview . . . . .	44
4.4	Magnet . . . . .	45
4.5	Geometry . . . . .	45
4.6	Tracking Detectors . . . . .	45
4.6.1	VDET . . . . .	46
4.6.2	ITC . . . . .	46
4.6.3	TPC . . . . .	47
4.7	Calorimetry . . . . .	49
4.7.1	ECAL . . . . .	49
4.7.2	HCAL . . . . .	50
4.7.3	Muon Chambers . . . . .	51
4.8	Luminosity Measurement . . . . .	51
4.9	Triggering . . . . .	52
4.9.1	Level 1 . . . . .	52
4.9.2	Level 2 . . . . .	53
4.9.3	Level 3 . . . . .	53
4.10	Data Acquisition . . . . .	53
4.11	Event Reconstruction . . . . .	54
4.11.1	Charged Tracks . . . . .	55
4.11.2	Calorimeter Objects . . . . .	55
4.11.3	A Reconstructed Event . . . . .	57
<b>5</b>	<b>Jetfinding</b>	<b>59</b>
5.1	Introduction . . . . .	59
5.2	Clustering Algorithms . . . . .	60
5.2.1	The JADE Algorithm . . . . .	61
5.2.2	The DURHAM Algorithm . . . . .	62
5.2.3	The ‘A’ and ‘C’ Jetfinders . . . . .	63
5.3	Comparison of Jetfinders . . . . .	66

5.3.1	N-Jet Rates . . . . .	67
5.3.2	Jet Widths . . . . .	68
5.3.3	Three-Jet Sample . . . . .	70
5.3.4	TRUTH/RECO levels . . . . .	74
5.4	Summary . . . . .	76
<b>6</b>	<b>Reconstructed Jet Resolutions</b>	<b>80</b>
6.1	Introduction . . . . .	80
6.2	Jet Energy Estimators . . . . .	80
6.3	The ‘Resolution Sample’ . . . . .	83
6.4	Energy Resolution . . . . .	86
6.5	Multiplicity Resolution . . . . .	87
6.6	Resolution With $\theta_Z$ . . . . .	87
6.7	Summary . . . . .	92
<b>7</b>	<b>Event Selection</b>	<b>95</b>
7.1	Hadronic Event Selection . . . . .	95
7.2	3-Jet Selection . . . . .	96
7.3	$q\bar{q}\gamma$ Rejection . . . . .	99
7.4	Angular cuts . . . . .	99
7.5	Summary . . . . .	102
<b>8</b>	<b>Fitting Method</b>	<b>103</b>
8.1	Multiplicity Binning . . . . .	103
8.1.1	The Dalitz Plane . . . . .	103
8.1.2	Discussion Of Estimators . . . . .	104
8.2	Generating Model Planes . . . . .	107
8.2.1	Inclusion Of Topology Dependence . . . . .	108
8.2.2	Which Is The Gluon Jet? . . . . .	108
8.2.3	Energy Options . . . . .	110
8.2.4	Generated Model Planes . . . . .	111
8.3	Correction Procedure . . . . .	113
8.3.1	Introduction . . . . .	113
8.3.2	Monte Carlo Selection . . . . .	113
8.3.3	Migration Matrices . . . . .	114
8.4	Applicability Of Model Predictions . . . . .	117

<b>9</b>	<b>Fits to Charged Multiplicity</b>	<b>120</b>
9.1	Introduction . . . . .	120
9.2	Fits To Jet Multiplicity . . . . .	120
9.2.1	Introduction . . . . .	120
9.2.2	Results . . . . .	122
9.2.3	Conclusions Of Fits To Jet Multiplicity . . . . .	126
9.3	ALEPH Event Multiplicity . . . . .	126
9.3.1	Introduction . . . . .	126
9.3.2	Results With Fitting Option . . . . .	127
9.3.3	The Dependence On Energy Option . . . . .	129
9.3.4	The Dependence On The Jetfinder . . . . .	130
<b>10</b>	<b>Systematic Uncertainties</b>	<b>132</b>
10.1	Introduction . . . . .	132
10.2	Systematic Errors Due To Jetfinding . . . . .	132
10.3	Systematic Errors Due To Selection Cuts . . . . .	134
10.3.1	Fraction of Neutral Energy . . . . .	134
10.3.2	Polar Angle $\theta_Z$ . . . . .	134
10.3.3	Planarity Angle $\theta_P$ . . . . .	135
10.4	Systematic Errors Due To Correction Method . . . . .	136
10.4.1	Jetclass . . . . .	136
10.4.2	Monte Carlo Generator . . . . .	137
10.4.3	Bin-by-bin Correction Factors . . . . .	138
10.5	Systematic Errors Due To Fitting Method . . . . .	138
10.5.1	QCD Scale Factor . . . . .	138
10.5.2	Fitting Option . . . . .	139
10.6	Effect Of Massive Kinematics . . . . .	139
10.7	Combined Systematic Error . . . . .	140
10.8	Final Measurement Of The Gluon Factor . . . . .	142
<b>11</b>	<b>Fits to Subjet Multiplicity</b>	<b>145</b>
11.1	Introduction . . . . .	145
11.2	Binning And Fitting $\langle n_{sub} \rangle$ . . . . .	145
11.3	Results Of Subjet Fits . . . . .	146
11.4	Discussion On $\langle n_{sub} \rangle$ Fits . . . . .	148
11.4.1	Shape Of $f_g$ Distribution . . . . .	148
11.4.2	The “Peak” Region . . . . .	149
11.4.3	The “Tail” Region . . . . .	149

<b>12 Conclusions</b>	<b>151</b>
<b>A The Group <math>SU(3)</math></b>	<b>154</b>
<b>B Example of a MINUIT Minimization</b>	<b>156</b>

# List of Figures

2.1	Nuclear $\beta$ decay, $n \rightarrow p + e^- + \bar{\nu}_e$ . . . . .	7
2.2	The probabilities for the basic QCD processes in terms of the colour factors and strong coupling constant. . . . .	9
2.3	Gluon exchange between a red and blue quark. Diagram (a) shows the leading order diagram, (b) the $\mathcal{O}(\alpha_s^2)$ vacuum polarization correction and (c) a gluon loop. . . . .	11
2.4	Measurements of $\alpha_s$ over a wide range of energy scales [20]. The fit is the running QCD prediction assuming the value of $\alpha_s$ at the $Z^0$ mass as given in the figure. . . . .	12
2.5	A hadronic event separated into four main phases; A. $e^+e^-$ annihilation to a $q\bar{q}$ pair through a photon or $Z^0$ ; B. parton cascade; C. hadronization; D. hadronic decays. The numbers indicate the typical energy transfer in each stage. . . . .	13
2.6	The Born process $e^+e^- \rightarrow f\bar{f}$ . . . . .	14
2.7	(a) Born cross section as a function of centre-of-mass energy $\sqrt{s}$ in $e^+e^-$ colliders: Total fermionic cross section (solid line), hadronic cross section (dashed line) and $\sigma(e^+e^- \rightarrow \mu^+\mu^-)$ (dotted line). (b) Hadronic cross section separated into fractional contributions from each primary quark flavour. . . . .	16
2.8	Muonic cross section with pure photonic exchange (dotted line) and $\gamma+Z^0$ exchange (dashed line). The solid line shows the latter with ISR taken into account. . . . .	16
2.9	Ratio of hadronic and muonic cross sections at various $e^+e^-$ experiments [25]. The fits are the $\mathcal{O}(\alpha_s^3)$ QCD prediction in the $\overline{MS}$ scheme for five flavours with $\Lambda=60$ MeV (lower curve) and $\Lambda=250$ MeV (upper curve). . . . .	17
2.10	Diagrams for the real process $e^+e^- \rightarrow q\bar{q}g$ . . . . .	18
2.11	$\mathcal{O}(\alpha_s)$ 1-loop virtual gluon diagrams contributing to $\sigma(e^+e^- \rightarrow q\bar{q})$ . . . . .	19
2.12	Angular ordering in a cascade: $\theta_1 > \theta_2 > \theta_3 > \dots > \theta_i$ . . . . .	21

2.13	The ‘strings’ attached between the partons in the $q\bar{q}g$ system. The dotted lines depict the strings and the larger pair of arrows indicate their directions of travel. . . . .	23
3.1	An example of the production of a $d\bar{d}$ pair between an initial $u\bar{u}$ in the string model. . . . .	26
3.2	MLLA fit to $\langle n_{ch} \rangle$ measured at several centre-of-mass energies. The dotted line indicates the fit extended into the region where recent measurements have been made by the LEP experiments [47]. Included is the preliminary ALEPH measurement at 183 GeV [48]. .	29
3.3	An example of a three-jet event. (a) The energy and interjet angles of a perfectly reconstructed event. (b) The hardest jet split into four phases; A. Quark produced via $e^+e^-$ annihilation; B. parton cascade; C. hadronization; D. hadronic decays. . . . .	31
3.4	The clustering of final-state particles to form subjets. . . . .	32
3.5	(a) ‘Strings’ attached between the partons in the $q\bar{q}g$ system. The dotted lines depict the strings and the large arrows indicate their directions of travel. (b) The direction of colour flow in the large- $N_c$ limit. . . . .	32
3.6	The Dalitz plane defined by the two hardest jets in a three-jet event.	36
3.7	(a) Energy of jet 3 (softest jet) and (b) angle between this jet and jet 2 binned on the Dalitz plane. . . . .	37
4.1	A schematic diagram of the five major accelerators involved in producing high energy electrons and positrons for ALEPH. . . . .	43
4.2	The ALEPH detector at LEP. . . . .	44
4.3	The ALEPH coordinate system. . . . .	45
4.4	Orientation of the VDET silicon wafers. . . . .	46
4.5	Eight neighbouring ITC drift cells, each $\sim 1$ cm in size. Signals can be induced on the calibration wires to test detector performance. .	47
4.6	(Top) Schematic view of the time projection chamber. (Bottom) Detail of a TPC sector. . . . .	48
4.7	The layout of the electromagnetic calorimeter modules. . . . .	50
4.8	A simplified diagram of the DAQ system of ALEPH. . . . .	54
4.9	The expected error $\sigma_E$ on the measured energy of a jet at an angle $\theta$ to the $z$ -axis with actual energy $E$ . . . . .	56
4.10	A fully reconstructed three-jet event observed in the ALEPH detector.	58

5.1	The ‘seagull’ diagram. . . . .	61
5.2	The minimum interjet angle and jet energy with $y_{\text{cut}}$ in an event clustered with the DURHAM algorithm. . . . .	63
5.3	The area populated with $y_{\text{cut}}$ for events clustered with the DURHAM algorithm. . . . .	64
5.4	Soft gluon emission from a quark $q$ during a cascade. . . . .	64
5.5	Soft, large angle gluon emission from a quark $q$ . . . . .	65
5.6	The angle $\Theta$ between the last pair of particles merged with different algorithms. . . . .	66
5.7	The number of jets remaining after clustering TRUTH level JETSET events at different initial $y_{\text{cut}}, y_0$ . . . . .	68
5.8	The difference in the average number of jets yielded with recombination scheme. $\Delta(E_0, E)$ is the number of jets obtained implementing the E relative to the $E_0$ recombination scheme <i>etc.</i> The relative transverse momentum transfer involved at each $y_{\text{cut}}$ is given by the upper scale in MeV. . . . .	69
5.9	(top) The angle between each track in a jet and the jet direction and (bottom) the maximum angle between a pair of tracks in a jet. The jets are energy-ordered and result from clustering TRUTH level events at $y_0=10^{-2}$ . . . . .	71
5.10	Energy in GeV of each jet in three-jet events obtained from clustering TRUTH level events at $y_0=10^{-2}$ . The jets have been ordered in decreasing energy in each event. . . . .	72
5.11	Charged (top) and neutral (bottom) particle multiplicity of each jet in three-jet events obtained from clustering TRUTH level events at $y_0=10^{-2}$ . The jets have been ordered in decreasing energy in each event. . . . .	73
5.12	The number of subjets, $n_{\text{sub}}$ , obtained with subjet $y_{\text{cut}}$ with the basic and modified DURHAM algorithms. The lower plot shows the difference at each $y_{\text{cut}}$ between DURHAM and DURHAM-‘A’ ( $\Delta_{D-A}$ ) and DURHAM-‘C’ ( $\Delta_{D-C}$ ). . . . .	75
5.13	The number of jets yielded after clustering a Monte Carlo sample at both TRUTH and RECO levels at a chosen $y_{\text{cut}}$ . The DURHAM and JADE algorithms are used with the E recombination scheme, and the relative transverse momentum transfer involved at each $y_{\text{cut}}$ is given by the upper scale in MeV. . . . .	77

5.14	The percentage of N-jet events obtained with $y_{\text{cut}}$ at RECO level with the DURHAM(circle) and JADE(square) algorithms. The dotted curves show the jet rates at TRUTH level, and the relative transverse momentum transfer involved at each $y_{\text{cut}}$ is given by the upper scale in MeV. . . . .	78
6.1	The interjet angles in a three-jet event. . . . .	81
6.2	The jetclass shown as areas on a plot of the number of jets obtained at RECO and TRUTH levels. Events lying in the shaded areas are excluded from this resolution study. . . . .	84
6.3	The number of jets yielded at RECO and TRUTH level after clustering 10 000 Monte Carlo events at $y_o=10^{-2}$ . . . . .	85
6.4	Jet energy resolution with several estimators. The jets are defined using the basic DURHAM algorithm, and the jets in each event have been ordered in decreasing TRUTH level energy. . . . .	88
6.5	Jet energy resolution of the $E_{\text{Lamy}}^M$ estimator, where the jets are defined using different jetfinders. The jets in each event have been ordered in decreasing TRUTH level energy. . . . .	89
6.6	Charged particle multiplicity resolution of jets defined by different jetfinders. The jets in each event have been ordered in decreasing TRUTH level energy. . . . .	90
6.7	The energy resolution of the hardest jet in a three-event, selected with the basic DURHAM jetfinder, with angular cut, $\theta_Z$ . . . . .	92
6.8	Fraction of events that have an energy resolution lying inside a given window, given a cut on the polar angle $\theta_Z$ . The fraction at each cut value is normalized to the total number of events that survive the cut. . . . .	93
6.9	The charged particle resolution of the hardest jet in three-jet events, given various angular cuts. . . . .	94
7.1	‘Class 16’ cut variables. (a) Charged particle multiplicity, (b) Charged particle energy, (c) Total visible energy and (d) Momentum missing in the beam line direction. The arrowed lines mark each cut and those events that pass. . . . .	97
7.2	Number of tracks before (a) and after (b) class 16 cuts. The number of objects rejected during the cuts is shown in (c). In each histogram the $y$ -axis is scaled so that the sum over all bins is 100%. . . . .	97

7.3	Visible charged energy <i>vs</i> charged particle multiplicity. The areas shown highlight some excluded event types: L= leptonic, T= tau, G= two-photon. The arrowed lines mark the class 16 cuts. Events in the rectangular region (H) are considered to be hadronic candidates. . . . .	98
7.4	The largest percentage of jet energy carried by neutral particles in any single jet from a selected three-jet event. The arrow marks the position of the cut. . . . .	100
7.5	The angle between each jet and the $z$ -axis, $\theta_Z$ , where the jets have been ordered in decreasing energy. The arrows mark the position of the cut. . . . .	101
7.6	The planarity angles for events selected from 1994 data, where the jets have been ordered in decreasing energy. The arrows mark the position of the cut. . . . .	101
7.7	Visible energy before and after the angular cuts described in section 7.4. Both samples have been normalized to 100%; the solid line shows the data before the cuts and the points after. . . . .	102
8.1	Dalitz bin numbers. The dashed line marks the populated bins assuming massless kinematics. . . . .	104
8.2	The energy of each jet given by the estimators $E_{Lamy}$ and $E_{Lamy}^M$ . Also shown for comparison is the observed total energy of each jet, $E_{vis}$ . . . . .	105
8.3	The numbers and average charged multiplicity, $\langle n_{ch} \rangle$ , of three-jet events binned on the Dalitz plane. Figures (a)&(b) are binned using the $E_{Lamy}$ jet energy definition and figures (c)&(d) using the $E_{Lamy}^M$ definition. The key at the top of the box diagrams gives the number of entries for several box sizes. . . . .	106
8.4	Predicted multiplicity across the plane with each fitting option, $F_{opt}$ , which are described in section 8.2.1. The predictions are evaluated at the centre of each bin assuming $f_g=1.5$ and $\Lambda=150$ MeV. . . . .	111

8.5	Predicted charged particle multiplicity across the Dalitz plane with different fitting options $F_{\text{opt}}$ . Each of the twelve diagrams represents a different horizontal “slice” across the Dalitz plane, the energy of the second hardest jet being the same for each slice. For example, in the top-left diagram $E_2=45$ GeV, and in the bottom-right diagram $E_2=23$ GeV. The points are separated horizontally for clarity. . . . .	112
8.6	The charged multiplicity across the plane for ALEPH data and reconstructed JETSET Monte Carlo data. The points are separated horizontally for clarity. . . . .	115
8.7	The value of the significance, defined in the text, of ALEPH and MCRECO data across the plane. . . . .	116
8.8	The number of reconstructed events in each bin that have the ‘P’ topology at TRUTH level. One can see that the majority have a similar topology at both levels and hence lie in the same bin, or in the bins immediately surrounding. One event is actually reconstructed in the Mercedes configuration. . . . .	118
8.9	The minimum value of $y_{ij}$ for events lying at the centre of each Dalitz Bin. . . . .	119
9.1	The value of $\chi^2$ , defined in the text, between the mid-jet multiplicity distribution in ALEPH and MCRECO events. Each individual value has been rounded down to the nearest integer: empty squares indicate $\chi^2 < 1$ . . . . .	121
9.2	Charged multiplicity of each TRUTH level jet across the Dalitz plane. Jet 1 is the most energetic and 3 the least energetic. Events have been selected with the basic DURHAM jetfinder. . . . .	122
9.3	The number of Dalitz bins remaining after the cut $E_{1,2} \leq E_{\text{max}}$ . . . . .	123
9.4	Results of fits to individual jet multiplicities in the TRUTH level sample over restricted areas of the Dalitz plane by requiring $E_{1,2} \leq E_{\text{max}}$ . Three options for the scale dependence of the jet multiplicities, $F_{\text{opt}}$ , are used: I= $\circ$ , II= $\square$ , III= $\triangle$ . . . . .	124
9.5	Result of fit to the multiplicity of the hardest jet, selected in MCTRUTH data, across the full Dalitz plane. The naïve QCD model with $F_{\text{opt}}=III$ and $E_{\text{opt}}=3$ is used to predict the multiplicity in each bin. . . . .	125

9.6 The  $\chi^2/dof$  (top) and gluon factor,  $f_g$ , obtained from fits to the total charged multiplicity in ALEPH events with each topological scale,  $F_{opt}$ . The fits are restricted to limited areas of the plane by the cut  $E_{1,2} \leq E_{max}$ . In the lower plot the points are separated horizontally for clarity and the dotted line marks the leading order prediction for the ratio of gluon and quark jet multiplicities. . . . . 128

9.7 Results of fits to the total charged multiplicity in ALEPH events selected with different jetfinders. The fitting option  $F_{opt}=III$  and energy option  $E_{opt}=3$  are used for each fit, which is restricted to areas of the plane with the cut  $E_{1,2} \leq E_{max}$ . The points are separated horizontally for clarity and the dotted line marks the leading order prediction for the ratio of gluon and quark jet multiplicities. . . . . 130

10.1 Comparison of  $f_g$  to several measurements of the gluon-to-quark charged multiplicity ratio. The three lefthand points correspond to the measurements in this analysis. The other points are those quoted in table 10.3: ALEPH<sup>1</sup> [68], ALEPH<sup>2</sup> [85], DELPHI [4], ALEPH<sup>3</sup> [63], and OPAL [3]. Statistical and systematic errors have been added in quadrature as appropriate. . . . . 144

11.1 The value of  $f_g$  obtained from fits to the subjet multiplicity, defined at a resolution  $y_{sub}$ , in three-jet events selected using the basic and modified DURHAM jetfinders. The subjet multiplicity at each  $y_{sub}$  is binned across a Dalitz plane and fit with the same QCD models as used for the charged multiplicity in the previous chapter. Fitting option  $F_{opt}=III$  energy option  $E_{opt}=3$  are used throughout and  $\Lambda$  is fixed at 150 MeV. The dashed line marks the value of  $f_g$  obtained from the  $\langle n_{ch} \rangle$  distribution in section 10.8, and the dotted lines denote the error  $\pm 1\sigma_{stat}$  about each value. . . . . 147

B.1 Selected output from a minimization performed with the MINUIT fitting package. . . . . 157

# List of Tables

2.1	The three generations of quarks ( $u, d, \dots$ ) and leptons ( $e^-, \nu_e, \dots$ ) of the Standard Model. Values show current world estimates or measurements [12]. . . . .	5
2.2	The partonic branchings $a \rightarrow b + c$ ( $a, b, c =$ quark, antiquark or gluon) and their associated Altarelli-Parisi splitting kernels $P_{a \rightarrow bc}$ . In each diagram the lower child branch carries a fraction $z$ of the parent's momentum. . . . .	20
3.1	Measurements of the mean charged particle multiplicity $\langle n_{ch} \rangle$ by several $e^+e^-$ experiments [38]. . . . .	27
3.2	Results of MLLA QCD fit to the $\langle n_{ch} \rangle$ data in table 3.1. The correlation quoted is that between $\kappa$ and $\Lambda$ . . . . .	28
5.1	The E, $E_0$ and p schemes for the combination of tracks $i, j$ with three-momenta $\vec{p}_i, \vec{p}_j$ and energy $E_i, E_j$ respectively. . . . .	60
5.2	The fraction of $N$ -jet events obtained after clustering a 10 K Monte Carlo TRUTH sample with different algorithms at $y_o=10^{-2}$ . . . . .	67
5.3	Average parameters from a three-jet Monte Carlo sample clustered at $y_o=10^{-2}$ . $\langle n_{ch} \rangle$ and $\langle n_0 \rangle$ are the average charged and neutral multiplicity respectively, and energies, $E_{jet}$ , are expressed in GeV. . . . .	72
6.1	Events classified according to the number of jets, $N_{jet}$ , obtained at RECO and TRUTH levels. The final column gives the approximate percentage of events in each class using the basic the DURHAM algorithm. . . . .	83

6.2	Average event and jet properties in three-jet events obtained with the basic DURHAM jetfinder. Jets in each event have been ordered in decreasing TRUTH level energy; the figures in brackets correspond to RECO level events. The table shows the following properties: Visible energy (GeV); Charged, neutral and total multiplicity; Mass ( $\text{GeV}/c^2$ ); Polar angle, $\theta_Z$ ; Angle to the plane defined in equation (6.2), $\theta_P$ ; Interjet angles, $\theta_{\text{interjet}}$ , and angles between the matched TRUTH and RECO jets, $\theta_{\text{match}}$ . All angles are expressed in degrees. . . . .	86
6.3	The fraction of jets included when a cut on the polar angle of the jet, $\theta_Z$ , is imposed. . . . .	91
7.1	Average total multiplicity of events classified by the number of jets obtained after initial clustering. . . . .	99
8.1	The assumed scale dependence of the multiplicity of each primary parton with fitting option $F_{\text{opt}}$ . Note that $S_{ij} = \sin\left(\frac{\theta_{ij}}{2}\right)$ . . . . .	109
10.1	Events classified according to the number of jets, $N_{jet}$ , obtained at RECO and TRUTH levels. . . . .	136
10.2	The combined systematic errors on $f_g$ . . . . .	141
10.3	Measurements of the ratio of $\langle n_{ch} \rangle$ in gluon and quark jets in various three-jet topologies. . . . .	143
11.1	Measurements of the gluon factor for multiplicity distributions obtained with the basic and modified DURHAM schemes. The errors quoted are statistical only. . . . .	150

‘A letter like this’, Milo mumbled despondingly, ‘could ruin any mess officer in the world.’ Milo had come to Yossarian’s tent just to read the letter again, following his carton of provisions across the squadron like a mourner. ‘I have to give you as much as you ask for. Why, the letter doesn’t even say you have to eat all of it yourself.’

‘And it’s a good thing it doesn’t,’ Yossarian told him, ‘because I never eat any of it. I have a liver condition.’

‘Oh, yes, I forgot,’ said Milo, in a voice lowered deferentially. ‘Is it bad?’

‘Just bad enough,’ Yossarian answered cheerfully.

‘I see,’ said Milo. ‘What does that mean?’

‘It means that it couldn’t be better...’

‘I don’t think I understand.’

‘...without being worse. Now do you see?’

‘Yes, now I see. But I still don’t understand.’

‘Well, don’t let it trouble you. Let it trouble me. You see, I don’t really have a liver condition. I’ve just got the symptoms. I have a Garnett-Fleischaker syndrome.’

‘I see,’ said Milo. ‘And what is a Garnett-Fleischaker syndrome?’

‘A liver condition.’

‘I see,’ said Milo, and began massaging his black eyebrows together wearily with an expression of interior pain, as though waiting for some stinging discomfort he was experiencing to go away.

Joseph Heller, “Catch 22”.

# Chapter 1

## Introduction

Data taking at the LEP storage ring in CERN, Geneva has allowed the ALEPH experiment to observe and reconstruct approximately 4 million hadronic  $Z^0$  decays in the period 1989-1995. Together with the three other LEP experiments (OPAL, DELPHI & L3), precision tests of the Standard Model have been made, such as the number of light neutrino species [1]. The top quark is not produced at LEP, having a mass above that of  $Z^0$  peak, but has been observed at Fermilab and completes the third family of quarks and leptons.

A large beneficiary of the LEP facility has been the field of Quantum Chromodynamics (QCD), where the clean environment and high energies are especially favourable. A large number of events produced in the ALEPH detector contain two or more hadronic jets whose origins can lie in the radiation of gluons about a hard (high energy) quark. At high energies, these jets become increasingly well separated and collimated whilst perturbative calculations of their production cross-sections become more reliable. The study of such jets at ALEPH allow a thorough examination of perturbative QCD predictions.

If a gluon radiated from a quark has a sufficiently high transverse momentum it is able to form a separate, distinct jet. The once rare occurrence of this third jet at lower energies is commonplace in the ALEPH environment and detailed studies of these so called *three-jet* events has become possible. The properties of quark and gluon jets have been the subject of much attention over the last few years (see for example [2, 3, 4, 5] and references therein). Analyses often invoke the use of heavy quark tagging to identify quark jets and hence anti-tag gluon jets. To allow an unbiased comparison of jets, symmetric events have been selected where at least two of the jets have the same energy. As a consequence of this and the quark tagging a large number of events are discarded. In principle, however, every hadronic event in which jets can be defined should be suitable for

jet studies. Although in untagged light-flavour events one cannot directly identify which jet originated from the gluon, the probability that each jet is the gluon jet can be estimated from theoretical knowledge of the production cross-sections for different topologies.

Recently it has been suggested [6] that the number or *multiplicity* of gluons produced about a hard parton (quark or gluon) is not simply a function of the energy of the parton. The proximity in angle of other hard partons in the event, referred to as the event *topology*, should be considered. This is because QCD radiation is expected to be *coherent*: emission from two nearby partons is expected to interfere causing a reduction in showered particles. By examining events in a topological way the exact extent of this effect on observed multiplicities can be explored.

The structure of this thesis is as follows; an introduction to the underlying physics is given in chapter 2 including the principles of QCD and the “life” of a three-jet event from conception to detection. To predict the multiplicity of quark and gluon jets in three-jet events, and examine the dependence of multiplicity with topology, energy *scales* are introduced which are functions of the angles between the jets. The scales are discussed in chapter 3 which also outlines the strategy of this analysis.

The apparatus which detects and reconstructs the paths and energies of the hadrons in an event, the ALEPH detector, is described in chapter 4. The process of *jetfinding*, in which individual hadrons are associated into separate jets, is described in chapter 5. Two modifications to the jetfinding procedure have been suggested recently which aim to improve the way hadrons are associated. The relative merits of these and the original jetfinding methods are assessed. Chapter 6 describes the way in which the energy of observed jets is estimated, the “true” energy of the jet being unknown due to the loss and imperfect reconstruction of hadrons in the ALEPH detector.

The selection of a well-reconstructed sample of three-jet events is described in chapter 7, and the method of comparing the multiplicity of these events with theoretical predictions based on the topological energy scales is outlined in chapter 8. The results and systematic uncertainties of the fitting to charged multiplicity distributions are summarised in chapters 9 and 10 respectively. Chapter 11 deals with fits to subjet multiplicity distributions. Final conclusions are made in chapter 12.

# Chapter 2

## Particle Production in $e^+e^-$ Collisions

### 2.1 Introduction

Using the increasing amount of data collected by high energy experiments, the theory of the Standard Model was developed in the 60's & 70's to account for interactions between, and properties of, the menagerie of observed particles. In the intervening years experiments such as those at the LEP collider at CERN have measured parameters of the Standard Model with great accuracy and found no significant inconsistencies with its predictions. As such, the Standard Model is now accepted as the theoretical framework describing particle physics. A brief review of the model is given here in section 2.2.

This analysis is concerned with the area of the Standard Model known as Quantum Chromodynamics (QCD), which represents the theory of strong interactions between quarks and gluons. QCD is introduced in section 2.3 and, with the help of perturbative techniques, see section 2.6, and Monte Carlo models, see section 2.8, is seen to describe the evolution of particles from an initial quark-antiquark pair to the jets observed in electron-positron collider experiments. The properties of these jets are the topic of this thesis.

## 2.2 Overview Of The Standard Model

In this model<sup>1</sup> the Universe is believed to be constructed from a set of fundamental particles which have either half-integral or integral spin: *fermions* (spin  $\frac{1}{2}\hbar, \frac{1}{2}\hbar, \dots$ ) which obey Fermi-Dirac statistics and *bosons* (spin  $0, \hbar, 2\hbar, \dots$ ) which obey Bose-Einstein statistics. Within the Standard Model fermions are classed as either *leptons* or *quarks* with only the latter feeling the effect of the strong interaction. Leptons and quarks are grouped into generations [11], ordered in increasing particle mass, containing a charged lepton, neutral lepton (neutrino) and two quarks, as shown in table 2.1. Cosmological constraints, and the  $Z^0$  line-shape measurement [1] at LEP, suggest that there are three light neutrino generations implying the same number of quark and lepton generations. Each fermion has a corresponding anti-particle of identical mass and spin but opposite charge.

Particle		Mass (GeV)	Charge ( $e$ )
1 <sup>st</sup> Generation			
Up	<b>u</b>	$2 - 8 \times 10^{-3}$	$+\frac{2}{3}$
Down	<b>d</b>	$5 - 15 \times 10^{-3}$	$-\frac{1}{3}$
Electron	<b><math>e^-</math></b>	$5.110 \times 10^{-4}$	$-1$
Electron Neutrino	<b><math>\nu_e</math></b>	$< 1.5 \times 10^{-8}$	$0$
2 <sup>nd</sup> Generation			
Charm	<b>c</b>	$1.0 - 1.6$	$+\frac{2}{3}$
Strange	<b>s</b>	$0.1 - 0.3$	$-\frac{1}{3}$
Muon	<b><math>\mu^-</math></b>	$0.106$	$-1$
Muon Neutrino	<b><math>\nu_\mu</math></b>	$< 1.7 \times 10^{-4}$	$0$
3 <sup>rd</sup> Generation			
Truth	<b>t</b>	$180 \pm 12$	$+\frac{2}{3}$
Beauty	<b>b</b>	$4.1 - 4.5$	$-\frac{1}{3}$
Tau	<b><math>\tau^-</math></b>	$1.777$	$-1$
Tau Neutrino	<b><math>\nu_\tau</math></b>	$< 2.4 \times 10^{-2}$	$0$

Table 2.1: The three generations of quarks ( $u, d, \dots$ ) and leptons ( $e^-, \nu_e, \dots$ ) of the Standard Model. Values show current world estimates or measurements [12].

There are four fundamental interactions between the fermions. *Quantum Elec-*

<sup>1</sup>Only a brief description of the Standard Model is made here; for more insight the reader is directed to [7], [8], [9] and [10].

*rodynamics* (QED) was the first gauge field theory to be developed to describe the interactions between electrically charged particles [13, 14, 15]. Properties of the electromagnetic interaction are determined by the inherent symmetries of the gauge theory, the particle interactions interpreted as being mediated by gauge bosons. QED involves the symmetry group  $U(1)$  [16] under which transformations commute. Such groups are known as *Abelian*. For  $U(1)$  there must be a locally conserved quantity, charge, which the massless  $U(1)$  boson (the photon,  $\gamma$ ) cannot carry. The strength of the interaction, *i.e.*, the strength with which the electron couples to the photon, is given by the coupling constant  $\alpha_{em}$  defined as

$$\alpha_{em} = \frac{e^2}{4\pi} \sim \frac{1}{137} \approx 10^{-2}, \quad (2.1)$$

where  $e$  is the charge associated with the electron and a factor  $\epsilon_0\hbar c$  in the denominator has been set to unity to simplify expressions.

The probability amplitude for an electron to emit a photon is proportional to  $e \propto \sqrt{\alpha_{em}}$ . As  $\alpha_{em} \ll 1$ , perturbative techniques lend themselves well to QED calculations where cross sections have the form  $\sigma = \sum_{n=0}^{\infty} A_n \alpha_{em}^n$  with  $A_n$  finite constants. Calculations to a fixed order  $n$  ( $n=1 \Rightarrow$  leading order (LO),  $n=2 \Rightarrow$  next-to-leading order (NLO) *etc.*) must take account of all Feynman graphs contributing at that order and so the number of such graphs increases rapidly. However, the power of  $\alpha_{em}$  between successive terms means higher order effects are small and theoretical calculations can be more confidently compared with experimental measurements.

The *weak* interaction was first invoked to explain nuclear  $\beta$ -decay, as shown in figure 2.1. The interaction is described within the framework of the Standard Model by  $SU(2)$  gauge theory which requires the existence of three bosons ( $W^\pm, Z^0$ ). Transformations under  $SU(2)$  involve a set of  $2 \times 2$  unitary matrices which do not commute meaning the theory is *non-Abelian*, and to maintain local gauge invariance the bosons carry weak charge and may undergo self-interactions. As the bosons are massive, the  $W^-$  radiated in nuclear  $\beta$ -decay is produced a long way off shell and the neutron has a lifetime of approximately 15 minutes. The effective weak coupling,  $\alpha_W$ , is hence much smaller than that of QED and can be expressed as

$$\alpha_W = \frac{\alpha_{em}}{\{M_W/m_p\}^2} \approx 10^{-6}, \quad (2.2)$$

where  $M_W$  and  $m_p$  are the masses of the weak bosons and the proton respectively.

In the 1950's a great number of short-lived particles were identified which seemed to fall into smaller groups, with each particle in a group having similar mass and properties. Later in the 1970's, proton scattering experiments suggested

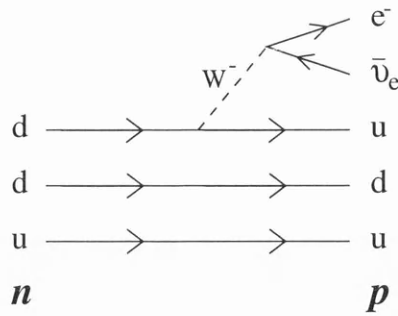


Figure 2.1: Nuclear  $\beta$  decay,  $n \rightarrow p + e^- + \bar{\nu}_e$ . The neutron is made up of three valence quarks ( $d, d, u$ ) whose charge sum is zero. One of the  $d$  quarks decays weakly to a  $u$  quark with the emission of a  $W^-$ , conserving charge. The quark forms a proton with the other two ‘spectator’ valence quarks and the  $W^-$  decays to an electron, again conserving charge, and an anti-electron neutrino to conserve lepton number.

that the proton contained point-like internal components. The constituent quark model was introduced to explain these observations, wherein hadrons are considered to be made up of fundamental quarks, which must be very tightly bound within the hadron to overcome electromagnetic repulsion. The force that keeps them thus bound is known as the *strong force*, with *Quantum Chromodynamics* being the Standard Model gauge theory, with an  $SU(3)$  symmetry describing the interaction [13, 17]. Transformations under  $SU(3)$  involve a set of  $3 \times 3$  matrices which do *not* commute, so that QCD is non-Abelian and the gauge quanta, *gluons*, carry *colour charge* and can undergo self-interactions. The proliferation of hadrons produced in high energy collider experiments originates from the production of these gluons. The strong coupling constant  $\alpha_s$  is defined, in analogy with the QED coupling, using equation (2.1) as

$$\alpha_s = \frac{g^2}{4\pi}, \quad (2.3)$$

where  $g$  is interpreted as the strong coupling strength. The strength of the strong interaction can be estimated by examining the lifetimes of similar electromagnetic and strong decays with comparable  $Q$ -values, for example

$$\frac{\alpha_s}{\alpha_{\text{em}}} \simeq \left\{ \frac{\tau(\Sigma^0 \rightarrow \Lambda + \gamma)}{\tau(\Sigma^{*0} \rightarrow \Lambda + \pi^0)} \right\}^{\frac{1}{2}} \simeq \left\{ \frac{10^{-19}}{10^{-23}} \right\}^{\frac{1}{2}} \approx 100. \quad (2.4)$$

Finally, the *gravitational* force acts between any particles which have mass. The force is believed to be mediated by gravitons although these remain elusive.

The magnitude of the interaction is negligible with respect to the others in the field of accessible particle physics. For example, a pair of electrons experiences electromagnetic and gravitational forces in the ratio of

$$\frac{F_{\text{em}}}{F_{\text{grav}}} = \frac{e^2}{4\pi\epsilon_0 G m_e^2} \simeq 10^{42} .$$

## 2.3 Quantum Chromodynamics

### 2.3.1 Colour And SU(3)

The constituent quark model of hadrons correctly predicts the observed multiplets of mesons (integral spin  $q\bar{q}$  states) and baryons (half-integral spin  $qqq$  states), their parities and spins. A problem was posed, however, with the description of the  $\Delta^{++}$  baryon, which contains three  $u$  quarks with parallel spins in a spin- $\frac{3}{2}$  and with no net orbital angular momentum. This is forbidden by the Pauli exclusion principle as the quarks have identical quantum numbers. It was postulated that quarks possess an additional degree of freedom, *colour*, commonly labelled red( $R$ ), green( $G$ ) and blue( $B$ ). The  $\Delta^{++}$  baryon is then realized as being a  $u^R u^G u^B$  state. The anti-quarks possess the anti-colours  $\bar{R}$ ,  $\bar{G}$  and  $\bar{B}$ . Although the reference to colour is purely pictorial it does offer a way to envisage the hadrons. All known hadrons are “colourless” (they possess no *colour charge*) and this can be achieved by constructing a  $qqq$  state (colours add to give “white”) or a  $q\bar{q}$  state (colours cancel to give “black”). The valence quark structure  $q_1\bar{q}_2$  of a meson can be generalised to

$$\frac{1}{\sqrt{3}}\delta_{ij}q_1^i\bar{q}_2^j . \quad (2.5)$$

For baryons, all quark combinations must be colour singlet and antisymmetric under exchange of colour indices, and the  $q_1q_2q_3$  structure of a baryon can be written as

$$\frac{1}{\sqrt{6}}\epsilon_{ijk}q_1^iq_2^jq_3^k \quad i, j, k = R, G, B , \quad (2.6)$$

where  $\epsilon_{ijk}$  is an antisymmetric permutation tensor. No non-singlet (*i.e.* coloured) combinations such as  $qqqq$ ,  $qq\bar{q}$  *etc.* or free quarks or gluons are allowed or, as yet, are observed.

The gauge theory of Quantum Chromodynamics involves the symmetry group SU(3), the properties of which are summarised in appendix A. The fundamental representation of this group is a triplet, taken to be the quark colour fields  $q^i$  ( $i=R,G,B$ ). The adjoint representation requires eight vector gluons fields  $G_\mu^a$

( $a=1,\dots,8$ ) hence there are eight gluons which mediate the strong interaction. These bosons are massless due to insistence on local gauge invariance. The *generators*  $t^a$  of  $SU(3)$  are an octet of traceless  $3\times 3$  matrices, the commutator algebra of which defines the group properties:

$$[t^a, t^b] = i \sum_c f^{abc} t^c . \tag{2.7}$$

The  $f^{abc}$  are known as the *structure constants* of the group. Not all the  $t^a$  commute with each other so QCD is a non-Abelian theory. For a general  $SU(N)$  theory, invariant quadratic Casimir operators,  $C_A$ ,  $C_F$  and  $T_F$ , can be defined whose eigenvalues are

$$C_A = N, \quad C_F = \frac{N^2 - 1}{2N}, \quad T_F = \frac{1}{2} . \tag{2.8}$$

In QCD these are known as the *colour factors* with expected values  $C_A=3$ ,  $C_F=\frac{4}{3}$  and  $T_F=\frac{1}{2}$ . The colour factors can be associated with the vertices as shown in figure 2.2. The gluon splitting process  $g \rightarrow q\bar{q}$  is attributed a factor  $T_R = n_f T_F$  as the gluon couples equally to all  $n_f$  kinematically accessible quark flavours. The probability for each branching can be approximated as being proportional to the product of the colour factor and the strong coupling,  $C_A$  and  $C_F$  visualized as being the colour charge of a gluon or a quark respectively.

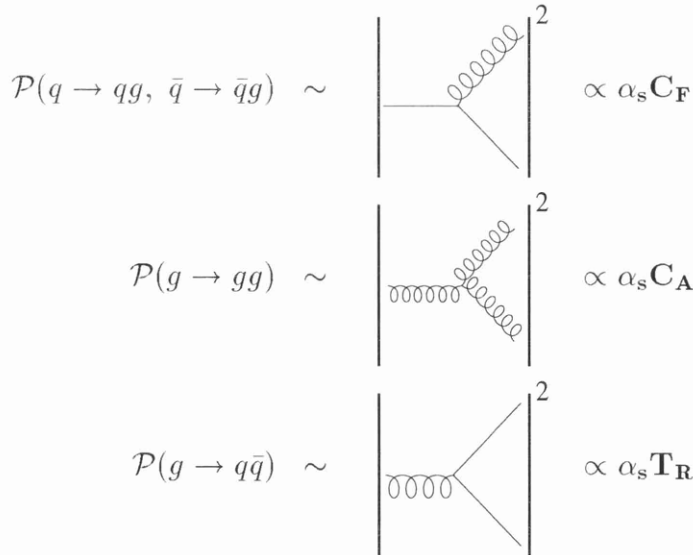


Figure 2.2: The probabilities for the basic QCD processes in terms of the colour factors and strong coupling constant.

### 2.3.2 The Running Coupling

In section 2.2 it was noted that cross sections, when calculated perturbatively, take the form

$$\sigma_{\text{Pert.}} = \sum_{n=0}^{\infty} A_n \alpha_s^n \quad (2.9)$$

where  $\alpha$  is the coupling and  $A_n$  are real finite constants. Equation (2.4) implies that  $\alpha_s \approx 1$  and perturbative calculations for QCD processes will become intractable as higher order terms can contribute significantly to the total cross section. However, the non-Abelian nature of QCD gives rise to a coupling which is *not* constant and in fact becomes small at the energies accessible to current  $e^+e^-$  colliders.

Consider the exchange of a gluon between a red and blue quark as shown in figure 2.3. In the complete calculation of this cross section, Feynman diagrams containing higher order processes have to be included, *eg* the  $q\bar{q}$  vacuum polarisation. In QCD the gauge bosons carry colour charge and so they can couple between each other giving rise to additional gluon loop diagrams at  $\mathcal{O}(\alpha_s^2)$  which are absent in Abelian theories such as QED. Integrations over momentum around loop diagrams introduce *ultraviolet* divergences but meaningful cross sections can be obtained by defining integrals through *dimensional regularization*. The integral is separated into finite and divergent parts according to the chosen scheme, for example the *modified minimal subtraction* ( $\overline{MS}$ ) scheme [18]. In a process known as renormalization of the field theory, divergencies are then removed through a redefinition of the fields and couplings in terms of an arbitrary renormalisation scale  $\mu$ . The coupling is now a “running” coupling,  $\alpha_s = \alpha_s(Q^2)$  where  $Q$  is the typical *scale* or momentum transfer of the process under consideration and can be expressed in terms of the value measured at the renormalisation scale.

In the *leading logarithm approximation* (LLA) the coupling is

$$\alpha_s(Q^2) = \frac{\alpha_s(\mu^2)}{1 + \frac{\alpha_s(\mu^2)}{4\pi} \beta_0 \ln\left(\frac{Q^2}{\mu^2}\right)}, \quad (2.10)$$

where  $\beta_0$  is a function of the colour factors and the number of quark flavours  $n_f$ <sup>2</sup>:

$$\beta_0 = \frac{1}{3}(11C_A - 4T_R) = 11 - \frac{2}{3}n_f. \quad (2.11)$$

This can usefully be re-written by introducing the parameter  $\Lambda$ , where

$$\Lambda^2 = \mu^2 \exp\left[-\frac{4\pi}{\beta_0 \alpha_s(\mu^2)}\right], \quad (2.12)$$

---

<sup>2</sup>Note that  $n_f$  is also a function of  $Q^2$ .

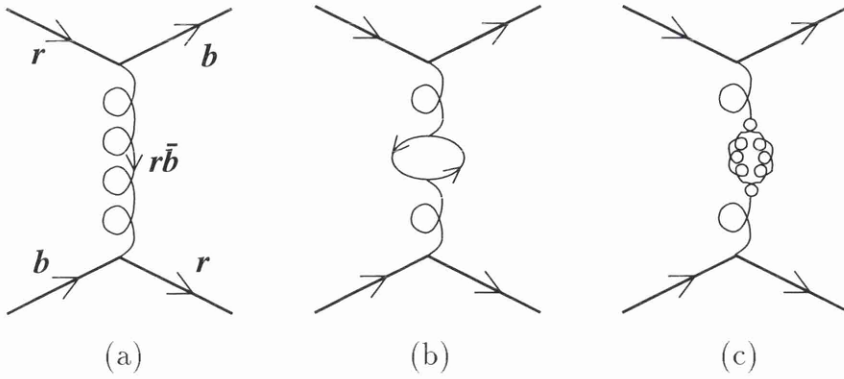


Figure 2.3: Gluon exchange between a red and blue quark. Diagram (a) shows the leading order diagram, (b) the  $\mathcal{O}(\alpha_s^2)$  vacuum polarization correction and (c) a gluon loop.

to give an expression which is independent of  $\mu$ :

$$\alpha_s(Q^2) = \frac{4\pi}{\beta_0 \ln\left(\frac{Q^2}{\Lambda^2}\right)}. \quad (2.13)$$

The coupling has been calculated to higher orders[19]:

$$\begin{aligned} \alpha_s(Q^2) = & \frac{4\pi}{\beta_0 \ln\left(\frac{Q^2}{\Lambda^2}\right)} \times \\ & \left[ 1 - \frac{\beta_1 \ln\left(\ln\left(\frac{Q^2}{\Lambda^2}\right)\right)}{\beta_0^2 \ln\left(\frac{Q^2}{\Lambda^2}\right)} + \frac{\beta_1^2}{\beta_0^4 \ln^2\left(\frac{Q^2}{\Lambda^2}\right)} \times \right. \\ & \left. \left\{ \left\{ \ln\left(\ln\left(\frac{Q^2}{\Lambda^2}\right)\right) - \frac{1}{2} \right\}^2 + \frac{\beta_2 \beta_0}{\beta_1^2} - \frac{5}{4} \right\} \right], \quad (2.14) \end{aligned}$$

where

$$\begin{aligned} \beta_1 &= \frac{34}{3}C_A^2 - \frac{20}{3}C_A T_R - 4C_F T_R, \\ \beta_2 &= \frac{2857}{54}C_A^3 - \frac{1415}{27}C_A^2 T_R + \frac{158}{27}C_A T_R^2 - \\ & \frac{205}{9}C_A C_F T_R + \frac{44}{9}C_F T_R^2 + 2C_F^2 T_R. \quad (2.15) \end{aligned}$$

Equations (2.13) and (2.14) predict that  $\alpha_s$  decreases with  $Q^2$  (provided  $n_f < \frac{33}{2}$ ) and

$$\lim_{Q^2 \rightarrow \infty} \alpha_s(Q^2) = 0. \quad (2.16)$$

This is known as *asymptotic freedom*: when  $Q^2 \gg \Lambda^2$ ,  $\alpha_s$  is sufficiently small to justify the picture of gluons and quarks interacting weakly with each other. Figure 2.4 shows measurements of  $\alpha_s$  over a wide range of scales clearly exhibiting the expected logarithmic decrease. In the region  $Q^2 \approx \Lambda^2$  perturbation theory breaks down and the underlying physics is less easy to evaluate. Quarks become bound together to form colourless hadrons by the strong force which increases as the quarks attempt to separate. This is known as *confinement*, and is thought to explain why only colourless states are seen and not bare quarks. In a sense,  $\Lambda$  marks the boundary between perturbative and non-perturbative QCD. The precise value of  $\Lambda$  is not fixed by theory and must be measured experimentally. A value of the order of the typical hadronic mass is expected, although the value obtained is different by definition for each renormalisation scheme, as are the  $\beta_n$  in equation (2.15) for  $n \geq 2$ . The  $\overline{MS}$  scheme is adopted in this analysis and the scale  $\Lambda = \Lambda_{\overline{MS}}$  is implied throughout.

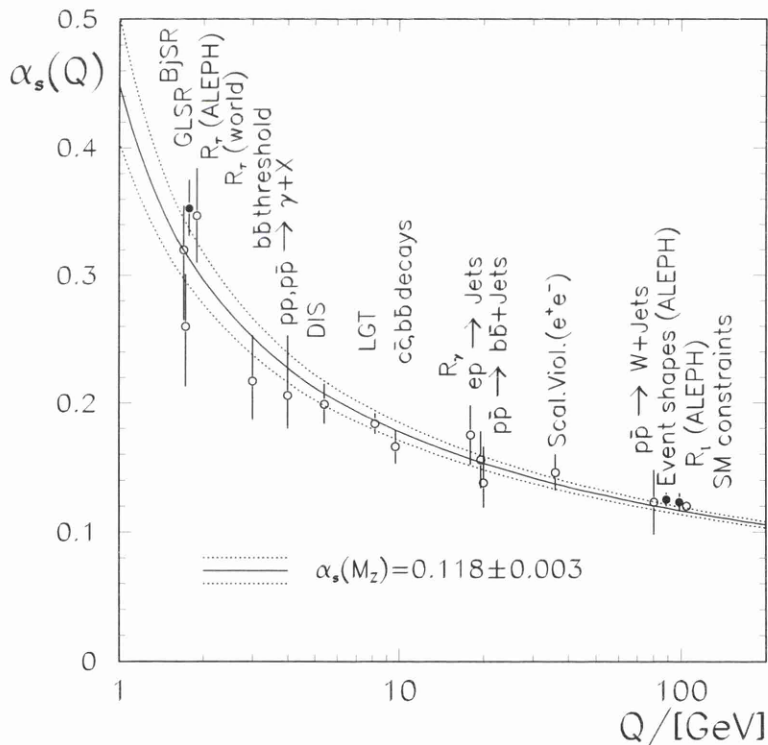


Figure 2.4: Measurements of  $\alpha_s$  over a wide range of energy scales [20]. The fit is the running QCD prediction assuming the value of  $\alpha_s$  at the  $Z^0$  mass as given in the figure.

## 2.4 Hadronic Jets

During the mid-1970's evidence began emerging for jet-like structure in the hadrons produced in  $e^+e^-$  collisions [21]. These jets point back to the interaction point and are increasingly collimated as the centre-of-mass energy increases. At higher energies, the distribution of observed hadrons was found to be inconsistent with that of two back-to-back jets [22]. This anomaly is attributed to the presence of a third jet which originates from a hard gluon radiated from one of the primary quarks. At LEP a significant fraction of hadronic events have three or more distinct jets and the study of these provides an invaluable insight into the mechanisms of QCD.

The complete evolution of a jet from the primary quark–antiquark pair into beams of hadrons can be separated into four phases. Figure 2.5 shows these phases: the typical energy transfer reduces by approximately an order of magnitude in each phase as the jet evolves from left to right.

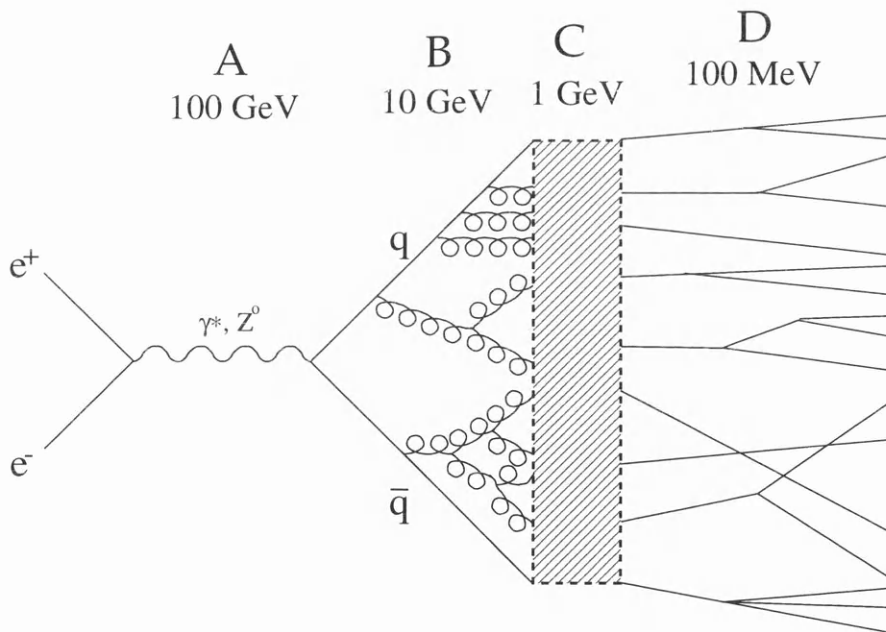


Figure 2.5: A hadronic event separated into four main phases; A.  $e^+e^-$  annihilation to a  $q\bar{q}$  pair through a photon or  $Z^0$ ; B. parton cascade; C. hadronization; D. hadronic decays. The numbers indicate the typical energy transfer in each stage.

The first stage, described in section 2.5, involves the formation of a  $q\bar{q}$  pair through  $e^+e^-$  annihilation. These quarks have appreciable momenta at LEP and fly in opposite directions from the interaction point, radiating gluons in a *cascade*

that, due the low transverse momenta involved, tends to populate a cone around the primary partons. The gluons can also radiate more gluons or produce  $q\bar{q}$  pairs. These processes occurs at a scale of several GeV  $\Rightarrow \alpha_s \ll 1$  and the techniques of perturbative QCD (pQCD) can be employed to describe the multi-parton system. If a sufficiently hard gluon is radiated it will form a separate jet distinct from either quark to produce a three-jet (or  $q\bar{q}g$ ) event. The perturbative cascade is described in section 2.6.

Eventually the typical virtuality scale of the cascade falls to a point where the coupling becomes very strong and the partons arrange themselves into colourless assemblages in the process known as *hadronization*. The hadronization process is discussed in section 2.7, whilst some practical models which attempt to describe the hadronization phase are discussed in sections 2.8.1 and 2.8.2. The final phase involves the decay of unstable particles and resonances. These decays have been studied for many years and this knowledge is built into fragmentation models which try to qualitatively recreate observed hadronic distributions.

## 2.5 The Process $e^+e^- \rightarrow q\bar{q}$

At LEP, events are initiated in  $e^+e^-$  collisions when an electron and positron annihilate to form a quark-antiquark pair through an intermediate photon or  $Z^0$ . Figure 2.6 shows the lowest order (Born level) electroweak process. The total cross section depends on the  $\gamma$  and  $Z^0$  exchange diagrams and the interference between them, although at LEP energies around 91 GeV the reaction proceeds almost exclusively through the  $Z^0$ .

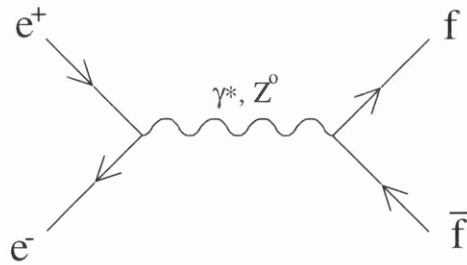


Figure 2.6: The Born process  $e^+e^- \rightarrow f\bar{f}$ .

The predicted cross section and relative proportion of quark flavours as a function of centre-of-mass energy are shown figure 2.7. Figure 2.7(b) highlights the expected production thresholds of the relatively massive  $c$  and  $b$  quarks. At LEP energies mass effects are negligible and the quark flavours  $\{uds:c:b\}$  are

produced in the relative proportion  $\{3:1:1\}$  [23]. This implies that restricting jet studies merely to tagged  $b$  jets excludes approximately 80% of the hadronic events produced at ALEPH.

In the region of the  $Z^0$  mass the weak process dominates, producing a large peak in the cross section. Initial and final state radiative corrections decrease the cross section at the  $Z^0$  peak by  $\sim 30\%$  and shift the peak to the right by  $\sim 100$  MeV. At higher energies the dominant effect is from initial state radiation (ISR) which dramatically increases the Born cross section. Figure 2.8 shows the predicted effect of ISR on the muonic cross section [24].

For scales well below the  $Z^0$  resonance the cross section is approximated by

$$\sigma(e^+e^- \rightarrow f\bar{f}) \propto \frac{\alpha_{\text{em}}^2}{s} N_C^f e_f^2, \quad (2.17)$$

where  $e_f$  is the fermion charge and  $N_C^f$  the colour factor:  $N_C^f \equiv 1$  (leptons) and  $N_C^f \equiv 3$  (quarks). Equation (2.17) implies the ratio

$$\mathcal{R}_{\text{had}} = \frac{\sigma(e^+e^- \rightarrow \text{hadrons})}{\sigma(e^+e^- \rightarrow \mu^+\mu^-)} = N_C \frac{\sum_q e_q^2}{e_{\mu^\pm}^2} = N_C \sum_q e_q^2 \quad (2.18)$$

which can be measured and used to determine the colour degree of freedom,  $N_C$ . The ratio depends (to first order) only on the number of active flavours,  $q$ . Above  $\sim 10$  GeV it is kinematically possible to produce the flavours ( $u, d, s, c, b$ ) giving  $\sum_q e_q^2 = \frac{11}{9}$ .  $\mathcal{R}_{\text{had}}$  has been measured at many centre-of-mass energies and found to be consistent with three quark colours, as shown in figure 2.9.

## 2.6 The Perturbative Parton Cascade

A quark and antiquark, formed through  $e^+e^-$  annihilation, each have equal and opposite momentum of magnitude  $p_{q,\bar{q}} \approx \frac{1}{2}\sqrt{s}$  and hence move in opposite directions. As the quarks separate and decelerate they interact strongly, the bulk of radiation being multiple soft gluon bremsstrahlung. There is a probability of  $\mathcal{O}(\alpha_s)$  that a hard gluon will be emitted at an appreciable angle to a primary quark and may initiate a separate jet. These three-jet, or  $q\bar{q}g$ , events are described in section 2.6.1.  $N$ -jet events are similarly expected with a probability  $\mathcal{O}(\alpha_s^{N-2})$ . Emitted gluons can radiate further gluons or form  $q\bar{q}$  pairs in a partonic cascade which ends when the virtuality scale of the processes involved are of the order of 1 GeV and the coupling becomes sufficiently strong to confine the partons within hadrons.

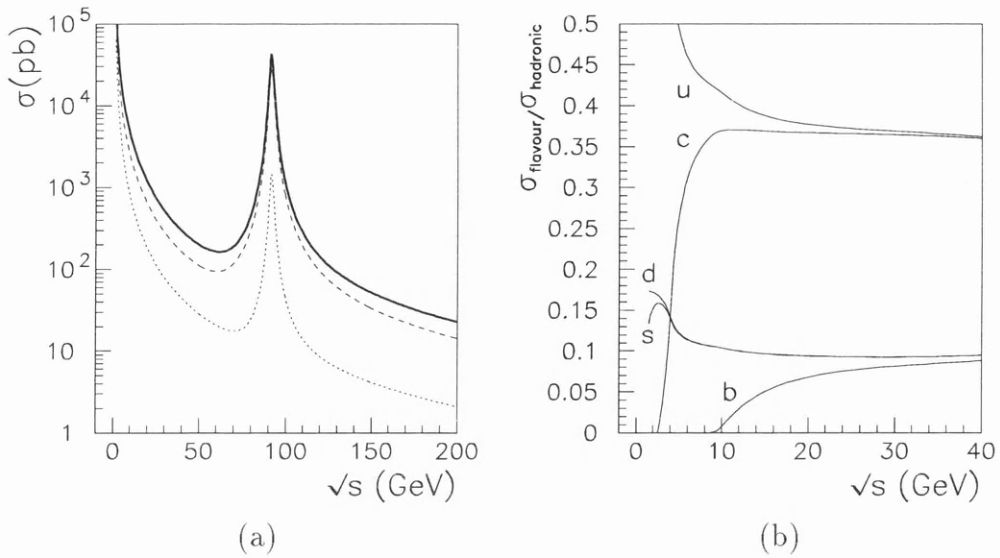


Figure 2.7: (a) Born cross section as a function of centre-of-mass energy  $\sqrt{s}$  in  $e^+e^-$  colliders: Total fermionic cross section (solid line), hadronic cross section (dashed line) and  $\sigma(e^+e^- \rightarrow \mu^+\mu^-)$  (dotted line). (b) Hadronic cross section separated into fractional contributions from each primary quark flavour.

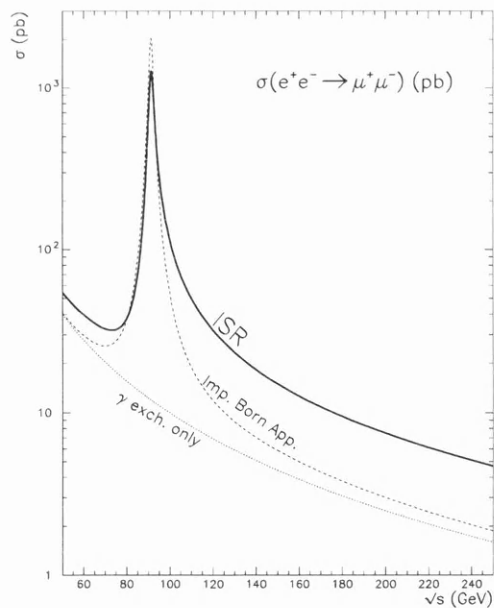


Figure 2.8: Muonic cross section with pure photonic exchange (dotted line) and  $\gamma+Z^0$  exchange (dashed line). The solid line shows the latter with ISR taken into account.

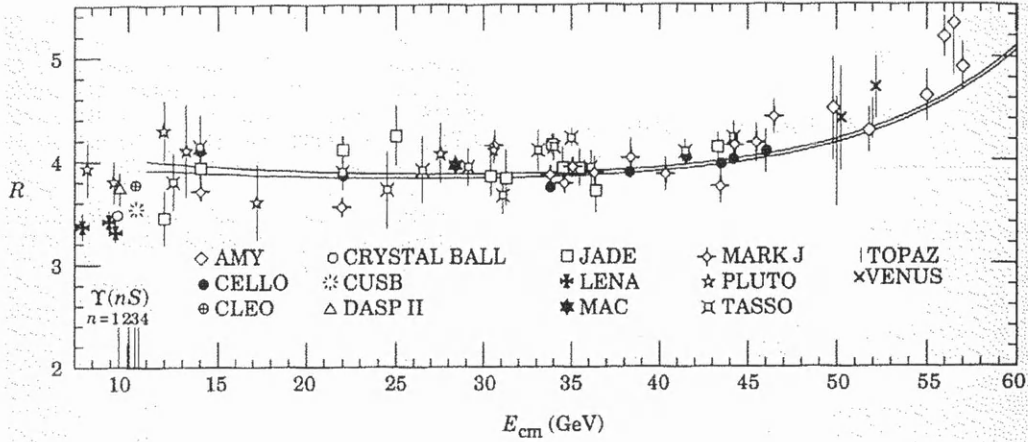


Figure 2.9: Ratio of hadronic and muonic cross sections at various  $e^+e^-$  experiments [25]. The fits are the  $\mathcal{O}(\alpha_s^3)$  QCD prediction in the  $\overline{MS}$  scheme for five flavours with  $\Lambda=60$  MeV (lower curve) and  $\Lambda=250$  MeV (upper curve).

To calculate the complete cross section  $\sigma(e^+e^- \rightarrow q\bar{q} + Ng)$  it is necessary to include all diagrams to  $\mathcal{O}(\alpha_s^N)$  and the interference between them. The complexity of such calculations escalates to such an extent that this exact *matrix element* prediction is only known up to  $N=3$ . The simplest case is described below, where a single hard gluon is radiated to form a three-parton system.

### 2.6.1 $e^+e^- \rightarrow q\bar{q}g$

The  $\mathcal{O}(\alpha_{\text{em}}^2\alpha_s)$  diagrams associated with single real gluon emission are shown in figure 2.10. The differential cross section for this three body final state, assuming massless kinematics, is

$$\frac{1}{\sigma_{q\bar{q}}^{LO}} \frac{d\sigma}{dx_q dx_{\bar{q}}} = \frac{\alpha_s}{2\pi} C_F \frac{x_q^2 + x_{\bar{q}}^2}{(1-x_q)(1-x_{\bar{q}})}, \quad (2.19)$$

where  $\sigma_{q\bar{q}}^{LO}$  is the Born cross section  $\sigma(e^+e^- \rightarrow q\bar{q})$ .  $x_i = 2\frac{E_i}{\sqrt{s}}$  ( $i=1,2,3=q,\bar{q},g$ ) are the scaled energies of the partons, with only two of the  $x_i$  independent as  $\sum_i x_i = 2$ . Equation (2.19) implies that the three jet cross section has *infrared* divergences when  $x_q \rightarrow 1$  and/or  $x_{\bar{q}} \rightarrow 1$ . Infinities occur in either of the scenarios below:

- (i) The gluon is emitted *collinear* to a primary quark (either  $x_q$  or  $x_{\bar{q}} \rightarrow 1$ ) ;
- (ii) The gluon is *soft* ( $x_q$  and  $x_{\bar{q}} \rightarrow 1 \Rightarrow x_g \rightarrow 0$ ).

Therefore collinear and soft divergences arise from gluons emitted at infinitesimal angles and energy respectively. One finds a solution to these infrared singularities when the one-loop corrections to  $\sigma_{q\bar{q}}^{LO}$ , shown in figure 2.11, are taken into account. It is found that interference terms appearing due to these these loop diagrams *exactly cancel* those associated with the  $e^+e^- \rightarrow q\bar{q}g$  diagrams [26] and the inclusive cross section is finite:

$$\sigma(e^+e^- \rightarrow \text{hadrons}) = \sigma_{q\bar{q}}^{LO} \left\{ 1 + \frac{\alpha_s(Q^2)}{\pi} \right\}, \quad (2.20)$$

implying that the ratio  $\mathcal{R}_{\text{had}}$  in equation (2.18) is modified to

$$\mathcal{R}_{\text{had}} = N_C \sum_q e_q^2 \left\{ 1 + \frac{\alpha_s(Q^2)}{\pi} \right\}. \quad (2.21)$$

Considering multiple N-gluon emission the general expression is

$$\mathcal{R}_{\text{had}} = N_C \sum_q e_q^2 \left\{ 1 + \sum_{n=1}^N A_n \left( \frac{\alpha_s(Q^2)}{\pi} \right)^n \right\}, \quad (2.22)$$

where the  $A_n$  for  $n \geq 2$  depend explicitly on the renormalization scale  $\mu$  at  $\mathcal{O}(\alpha_s^{N+1})$  as well as the chosen scheme. If the calculation was known to all orders the result is independent of  $\mu$ . The truncation of perturbative series such as equation (2.22) leads to the scheme dependence of perturbative calculations. In the  $\overline{MS}$  scheme the  $\mathcal{O}(\alpha_s^3)$  calculation [27] gives  $A_2 = 1.411$  and  $A_3 = -12.80$ .



Figure 2.10: Diagrams for the real process  $e^+e^- \rightarrow q\bar{q}g$ .

### 2.6.2 $e^+e^- \rightarrow q\bar{q} + Ng$

The characteristics of a jet are determined by the soft near-collinear bremsstrahlung radiation about the primary quark direction. A careful description of this region of phase space is necessary because, although quasi-collinear gluons carry a small fraction of the jet momentum, they form the bulk of jet multiplicity.

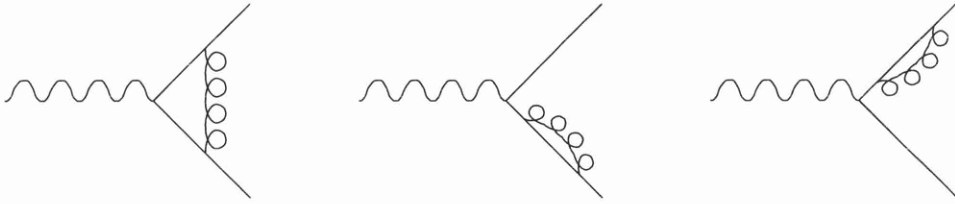


Figure 2.11:  $\mathcal{O}(\alpha_s)$  1-loop virtual gluon diagrams contributing to  $\sigma(e^+e^- \rightarrow q\bar{q})$ .

Attempts have been made, via several levels of approximation, to describe a partonic cascade ensemble in an analytical fashion using Perturbative QCD. As the scale of the interactions is large compared to the QCD scale parameter  $\Lambda$ , this era of jet evolution can be modelled using perturbative expansions in powers of  $\alpha_s$ . As already stated, the exact matrix element expression for an  $N$ -parton final state is beyond current methods of calculation. To facilitate predictions, the cascade phase can be determined using the *parton shower* method. A cascade is divided into a series of parton branchings  $a \rightarrow bc$ , where  $a$  is referred to as the *parent* and  $b, c$  the *children*. Four possible branchings<sup>3</sup> are thus  $q \rightarrow qg$ ,  $\bar{q} \rightarrow \bar{q}g$ ,  $g \rightarrow gg$  and  $g \rightarrow q\bar{q}$ . The probability for each branching is given in terms of the fraction of the parents momentum  $z$  carried by each child using the Altarelli-Parisi splitting kernels [28] given in table 2.2. Branchings stop at some cutoff,  $Q_0^2$ , in a chosen evolution parameter.

In the *leading logarithm* approximation (LLA) the perturbative expansion is simplified by neglecting terms down by powers of  $1/Q^2$  or down by factors of  $\ln Q^2$  or  $\ln z \ln(1-z)$ . Cross sections take the form of equation (2.9) with the coefficients  $A_n$  themselves sums of powers of  $\ln\left(\frac{Q^2}{Q_0^2}\right)$ , so that

$$A_n \sim C_n \left[ \ln\left(\frac{Q^2}{Q_0^2}\right) \right]^n + D_n \left[ \ln\left(\frac{Q^2}{Q_0^2}\right) \right]^{n-1} + \dots$$

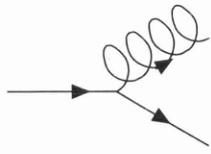
so that the sum should be re-ordered:

$$\begin{aligned} \Rightarrow \sigma &= \sum_n C_n \left[ \alpha_s(Q^2) \ln\left(\frac{Q^2}{Q_0^2}\right) \right]^n \\ &+ \alpha_s(Q^2) \sum_n D_n \left[ \alpha_s(Q^2) \ln\left(\frac{Q^2}{Q_0^2}\right) \right]^n + \dots \end{aligned} \quad (2.23)$$

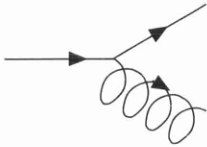
The LLA includes terms in the first line of equation (2.23). The modified leading logarithmic approximation (MLLA) aims to quantitatively improve predictions

<sup>3</sup>There is also the sub-leading branching  $g \rightarrow ggg$  associated with the quartic gluon vertex.

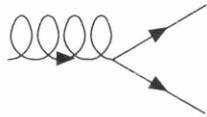
by including single logarithmic terms and accounting for energy-momentum conservation (the ‘recoil effect’). A more detailed description of this and the LLA may be sought in [29].



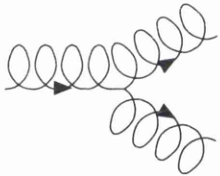
$$P_{q \rightarrow qg}(z) = C_F \frac{1+z^2}{1-z}$$



$$P_{q \rightarrow gq}(z) = C_F \frac{1+(1-z)^2}{z}$$



$$P_{g \rightarrow q\bar{q}}(z) = T_R [z^2 + (1-z)^2]$$



$$P_{g \rightarrow gg}(z) = 2C_A \left[ z(1-z) + \frac{1-z}{z} + \frac{z}{1-z} \right]$$

Table 2.2: The partonic branchings  $a \rightarrow b + c$  ( $a, b, c =$  quark, antiquark or gluon) and their associated Altarelli-Parisi splitting kernels  $P_{a \rightarrow bc}$ . In each diagram the lower child branch carries a fraction  $z$  of the parent’s momentum.

### 2.6.3 Coherence effects

Embodied in perturbative calculations is the effect of colour coherence in soft gluon radiation patterns. Strong angular ordering (AO) [30] within a gluonic cascade proves to be the most striking consequence of colour coherence. Angular ordering means that the probability that a soft gluon will be radiated at an angle larger than that of a gluon produced earlier in a shower vanishes. Gluon bremsstrahlung is effectively ordered by angle, later emissions depending on the history of the cascade, illustrated in figure 2.12. Strong angular ordering results in soft gluon emission being concentrated in the forward quark direction to produce

a collimated jet. A gluon emitted at a given point in a shower is only sensitive to the *net* colour of the subsequent cascade.

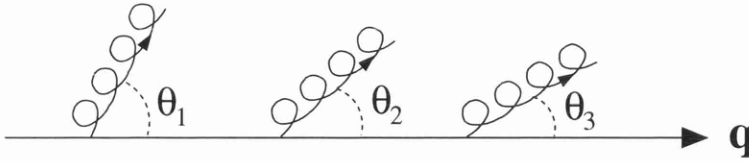


Figure 2.12: Angular ordering in a cascade:  $\theta_1 > \theta_2 > \theta_3 > \dots > \theta_i$ .

Interjet phenomenon occur in events with an underlying skeleton of three or more hard partons. If two of these partons lie close in angle then radiation emitted in the region between them will be sensitive to the colour charge of both the parent *and* the neighbouring parton. This effect alters as the jet orientation changes and so interjet particle flow is a *topology dependent* quantity which can be measured to estimate the effects of colour coherence.

## 2.7 Hadronization

As collimated clusters of hadrons are seen experimentally, it is inferred that at some scale the partons arrange themselves into colourless hadrons. The process is strictly non-perturbative and presently remains incalculable. The hypothesis of Local Parton-Hadron Duality (LPHD)[31] assumes that inclusive hadronic distributions are related to distributions at the parton level simply by constant factors. LPHD is based upon the assumption that momentum transfers are small and happen at a scale  $Q_0$  which is independent of the initial hard scale of the process;  $Q_0 \simeq \Lambda \simeq 200 \text{ MeV}$ . The fact that distributions at hadron and parton levels seem close is encouraging: the study of hadronic spectra can be used to infer the underlying cascade structure of the quarks and gluons.

## 2.8 Fragmentation Models

To assist with studies of hadronic events, several fragmentation or *Monte Carlo* models[32] have been developed which attempt to recreate the complete jet evolution and reproduce observed data distributions. They are generally constructed in four phases, as shown in figure 2.5, with the main differences between models being in their treatment of the cascade and hadronization steps. Angular

ordering in cascades is implicit in so-called WIG'ged (With Interfering Gluons) Monte Carlos which apply coherent parton shower algorithms. The hadronization phase is approximated using models which depend on only a restricted set of free parameters. It should be emphasized that these are purely phenomenological models and the parameters are not fundamental: on the other hand, such models are found to give an adequate description of data and are an invaluable tool in particle physics analyses.

The JETSET and HERWIG models are used throughout this analysis and are described in sections 2.8.1 and 2.8.2 respectively. As the analysis involves inclusive or near-inclusive quantities, it is not necessary to use the Monte Carlo data to unfold parton level distributions from those at the corresponding hadron level; they are utilised with a parameterization of the ALEPH detector to estimate the effect the detector has on final-state hadronic distributions and jet energy resolutions. The ALEPH detector is described in chapter 4. The applicability and performance of Monte Carlo simulations are studied in chapters 6 and 8.

### 2.8.1 JETSET

The JETSET [33] fragmentation model is able to employ either the exact second order matrix element or a parton shower to generate the perturbative cascade. The latter is found to give the best description of data [34]. The non-perturbative phase is modelled by the *Lund String Model* [35] which is motivated by the principle of confinement. Partons are imagined to be tied together by a string or flux tube with an energy per unit length  $\sim 1$  GeV/fm. As the partons separate the potential energy stored in the string increases and the string may break into two pieces terminated by a new quark-antiquark pair. If the invariant mass of the string pieces is large enough further breaks may occur, the final pieces representing the hadrons.

Gluons are perceived as causing “kinks” in the string. In the simple case of the  $q\bar{q}g$  system, strings span the partons as shown in figure 2.13, where the gluon is attached to two strings which are boosted in the directions indicated. As the strings stretch and break hadrons are formed and flow in the regions between gluon and (anti)quark. This is known as the ‘string effect’ [36], and has been verified in many studies (see, for example [5]). Notice that there is no string directly between the quarks: particle flow in this region must originate from “leakage” from the boosted colour strings.

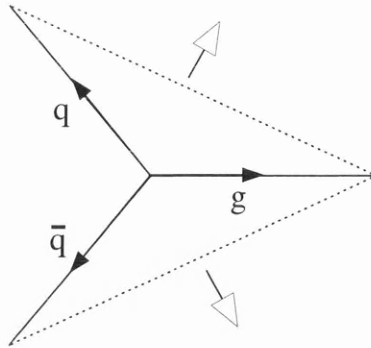


Figure 2.13: The ‘strings’ attached between the partons in the  $q\bar{q}g$  system. The dotted lines depict the strings and the larger pair of arrows indicate their directions of travel.

### 2.8.2 HERWIG

The HERWIG [37] fragmentation model was the first to incorporate intrajet coherence effects through the use of a parton shower with the MLLA. A relatively simple *cluster hadronization* process is applied to produce the final state hadrons. The shower proceeds down to some cut-off scale, whereafter all remaining gluons are forced to split into  $q\bar{q}$  pairs. The (anti)quarks are formed into colourless clusters with a typical mass of a few GeV, and are allowed to decay isotropically in their rest frame into two hadrons of compatible flavours. The decays depend on the available phase space, with the lightest clusters resulting in only a single hadron.

# Chapter 3

## Overview and Motivation

### 3.1 Introduction

In the previous chapter, a qualitative description of jet formation in  $e^+e^-$  collisions was provided by the perturbative shower picture, where many soft gluons are radiated about a hard central parton. This parton may be the quark or antiquark from a  $Z^0$  decay or a high- $P_\perp$  gluon produced earlier in a shower. The yield and distribution of showered gluons in a jet are sensitive to the underlying colour dynamics of an event and hence their study reveals the coherent nature of QCD radiation.

Once a jet has been identified, the source of the particles within it can be estimated by clustering them together into larger groups, effectively playing the cascade tree in reverse until only one group remains which represents the parent parton which initiated the shower. The clusters are known as *subjects* and, by choosing the way clusters are formed, a timeslice can be made through a cascade.

Many perturbative predictions exist for the cascade parton distributions. The principles of LPHD imply that these are closely related to observed hadronic distributions and so the study of jets in modern  $e^+e^-$  detectors allows one to test and measure the fundamental parameters of QCD. Events with three or more jets allow differences between quark- and gluon-initiated jets to be examined. The effect of the coherent nature of QCD radiation can be investigated by studying the particle multiplicity within jets given the relative orientation of nearby jets: the *topology dependence* of the jet multiplicity.

## 3.2 QCD And Jets At LEP

LEP, as with other  $e^+e^-$  colliders, has a “clean” environment for physics given by the pure fermion–anti-fermion initial state. At hadronic colliders, such as  $p\text{--}\bar{p}$  (Fermilab) or  $p\text{--}e$  (DESY) accelerators, jets are typically Lorentz boosted into different inertial frames and additional jets produced from proton remnants make reconstruction more difficult. The cross section for the reaction  $e^+e^- \rightarrow \text{fermions}$  is large in the region around the  $Z^0$  peak (fig. 2.7) and during the five years of LEP I running  $\sim 4$  million hadronic events have been collected by the ALEPH detector alone.

The identification and study of hadronic jets is essential to many high energy physics studies. Techniques for their isolation and reconstruction have been developed, the whole process being known as *Jetfinding* which is described in chapter 5. There have been many  $e^+e^-$  experiments during the last decades, and a vast amount of data has been amassed on the nature of these jets. The isotropic distribution and particle density of hadronic jets has dictated the design of modern detectors. The electromagnetic calorimeter of ALEPH, for example, is hermetic and has a granularity sufficient to identify individual jet constituents. Most hadronic events have a two-jet structure with the majority of final state particles lying in a cone of half-angle  $\approx 30^\circ$  about the primary quark and antiquark directions.

### 3.2.1 Quark Jets

In a two-jet event, an initial  $q\bar{q}$  pair is produced back-to-back and assumed to radiate gluons in independent showers. However, each parton has a colour charge whereas the final jet ensembles are colour neutral. This is accounted for in the Lund String Model [35] by creating a  $q\bar{q}$  between the initial pair such that colour charges cancel and the sum of electric charge for each jet becomes an integer value. Figure 3.1 gives an example of this process where a  $d\bar{d}$  pair is produced upon the breakup of a string stretched between a high-energy  $u\bar{u}$  pair. The quarks make up two colour neutral  $\pi^\pm$  ‘proto-jets’ which then go on to the shower phase.

Only the particles remaining from hadronization and resonance decays are observed in a detector, so that in reconstructed events one experimentally measures the mean number of hadrons  $\langle n_{tot} \rangle$ . Separating these into charged  $\langle n_{ch} \rangle$  and neutral  $\langle n_0 \rangle$  particles we have

$$\langle n_{tot} \rangle = \langle n_{ch} \rangle + \langle n_0 \rangle .$$

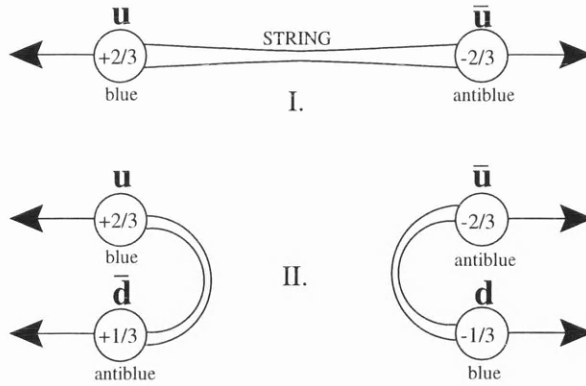


Figure 3.1: An example of the production of a  $d\bar{d}$  pair between an initial  $u\bar{u}$  in the string model.

Some measurements of the charged multiplicity at various centre-of-mass energies are summarised in table 3.1. As hadronic events are predominantly of the 2-jet type, one can ascribe the event multiplicity at a scale  $\sqrt{s}$  to be twice that of an “independent” (anti)quark of energy  $\sqrt{s}/2$ , *i.e.*

$$\langle n_{tot} \rangle^{e^+e^-}(\sqrt{s}) = 2 \langle n_{tot} \rangle^{\text{quark}}\left(\frac{\sqrt{s}}{2}\right), \quad (3.1)$$

and LPHD implies that

$$\langle n_{tot} \rangle^{\text{quark}}(Q) \simeq \mathcal{N}_q(Q), \quad (3.2)$$

where  $\mathcal{N}_q(Q)$  is defined as the soft gluon multiplicity of a jet originating from a quark of energy  $Q$  (and similarly  $\mathcal{N}_g(Q)$  if the jet originated from a gluon).

The MLLA LPHD prediction for the average inclusive particle multiplicity in an  $e^+e^-$  collision at a centre-of-mass energy  $\sqrt{s}$  is [39, 40, 41]

$$\langle n \rangle^{e^+e^-}(\sqrt{s}) \propto [\alpha_s(\sqrt{s})]^b \exp\left\{\frac{a}{\sqrt{\alpha_s(\sqrt{s})}}\right\} \cdot [1 + \mathcal{O}(\sqrt{\alpha_s})], \quad (3.3)$$

where

$$a = \frac{12\sqrt{6}\pi}{33 - 4T_R} \quad \text{and} \quad b = \frac{297 + 44T_R}{1188 - 144T_R},$$

so that in terms of a scale  $Q$  the multiplicity of a free quark is expected to take the form

$$\mathcal{N}_q(Q) = \kappa \cdot [\alpha_s(2Q)]^b \exp\left\{\frac{a}{\sqrt{\alpha_s(2Q)}}\right\}, \quad (3.4)$$

Collaboration	$\sqrt{s}$	$\langle n_{ch} \rangle$
JADE	12.0	$8.4 \pm 0.7$
	30.0	$13.1 \pm 0.7$
	35.0	$13.6 \pm 0.7$
PLUTO	12.3	$8.7 \pm 0.6$
	17.0	$9.4 \pm 0.7$
	22.0	$11.2 \pm 1.0$
	27.6	$12.0 \pm 0.8$
	30.6	$12.3 \pm 0.8$
TASSO	14.0	$9.3 \pm 0.41$
	22.0	$11.3 \pm 0.47$
	34.8	$13.59 \pm 0.46$
	43.6	$15.08 \pm 0.47$
TPC/2 $\gamma$	29.0	$12.8 \pm 0.6$
HRS	29.0	$12.87 \pm 0.30$
TOPAZ	52.0	$15.99 \pm 0.23$
	55.0	$16.85 \pm 0.27$
AMY	57.0	$17.19 \pm 0.49$
ALEPH	91.2	$20.85 \pm 0.24$
DELPHI	91.2	$20.71 \pm 0.77$
L3	91.2	$20.40 \pm 0.43$
OPAL	91.2	$20.79 \pm 0.52$
MARK II	91.2	$20.1 \pm 1.3$

Table 3.1: Measurements of the mean charged particle multiplicity  $\langle n_{ch} \rangle$  by several  $e^+e^-$  experiments [38].

where  $\kappa$  is a normalization depending on the chosen multiplicity.

Equation (3.4) can be fit to the  $e^+e^-$  data in table 3.1 to extract both the normalization  $\kappa$  (which is incalculable in pQCD) and the QCD scale factor  $\Lambda$  which appears in the parameterization of the running coupling. Results of fits using fixed-order expressions for  $\alpha_s$  and  $\kappa$  &  $\Lambda$  left free are given in table 3.2. The MLLA expression is seen to fit well for each order of  $\alpha_s$  with a  $\chi^2/\text{dof} \approx 0.72$ , yielding values of  $\kappa \approx 3.5 \times 10^{-2}$  &  $\Lambda \approx 110$  MeV with  $\kappa$  and  $\Lambda$  fully correlated. The value of  $\Lambda$  measured here is comparable to other measurements based on charged multiplicities [42, 43, 40].

The fit using the NNLO expression for  $\alpha_s$  (eqn. (2.14)) is superimposed on the data in figure 3.2.  $\langle n_{ch} \rangle$  has recently been measured at higher centre-of-mass energies at LEP II and when the fit is extended to  $\sqrt{s}=200$  GeV the new datapoints lie close to the theoretical prediction. Using equation (3.4), and the

extracted values of  $\kappa$  &  $\Lambda$ , one has a reliable method to quantitatively predict the multiplicity of a quark or antiquark at any scale  $Q$ .

The five lightest quark flavours are produced in roughly the same proportion at LEP and the soft gluon radiation pattern should have the same structure at large angles for light ( $u, d, s$ ) and heavy ( $c, b$ ) quarks. However at smaller angles  $\Theta \lesssim \frac{m_q}{E_q}$ , where  $m_q$  is the quark mass and  $E_q$  its energy, radiation is greatly suppressed in a “dead cone” [44]. This effect should be significant for the heavy quarks where one expects a reduction in the net soft gluon multiplicity with respect to light quark jets. To MLLA accuracy the difference in gluon multiplicity  $\delta\mathcal{N}_q = \mathcal{N}_q^{\text{light}} - \mathcal{N}_q^{\text{heavy}}$  between cascades from heavy and light quarks is independent of centre-of-mass energy. Quark mass effects have been verified experimentally for  $b$  quark jets [45, 46] estimating  $\delta\mathcal{N}_q \sim 3.1$ , although subsequent weak decays of heavy  $B$  hadrons results in the mean charged multiplicity  $\langle n_{ch} \rangle^b > \langle n_{ch} \rangle^{\text{light}}$ .

$\mathcal{O}(\alpha_s)$	Eqn.	$\Lambda$ (MeV)	$\kappa \times 10^3$	$\chi^2/\text{dof}$	Correlation (%)
1	2.13	$100 \pm 46$	$43.0 \pm 8.4$	0.72	99.9
2	—	$115 \pm 49$	$30.9 \pm 5.5$	0.73	99.9
3	2.14	$107 \pm 46$	$31.0 \pm 5.6$	0.72	99.9

Table 3.2: Results of MLLA QCD fit to the  $\langle n_{ch} \rangle$  data in table 3.1. The correlation quoted is that between  $\kappa$  and  $\Lambda$ .

### 3.2.2 Gluon Jets

The preparation of two gluon jets in a back-to-back state (*cf* a  $q\bar{q}$  pair) is not possible in an  $e^+e^-$  collider. This configuration may exist via triple-gluon vertices in cascades but their identification is impossible from the resulting hadrons. One may study gluon jets through their leading order production in the three-jet process  $Z^0 \rightarrow q\bar{q}g$  which is described in more detail in the following section. From perturbative calculations, gluon jets are expected to be broader, *i.e.* the final-state particles lie at greater angles than for quark jets [49].

Quantum chromodynamics associates a colour charge to both quarks and gluons, the strength of the basic couplings of the theory at a given scale simply expressed as being proportional to these charges to first order (fig. 2.2). The probability that a gluon will be emitted by a hard parton in a shower is  $\propto C_F$  if the parton is a quark and  $\propto C_A$  if it is a gluon. In the limit of very high energy jets,

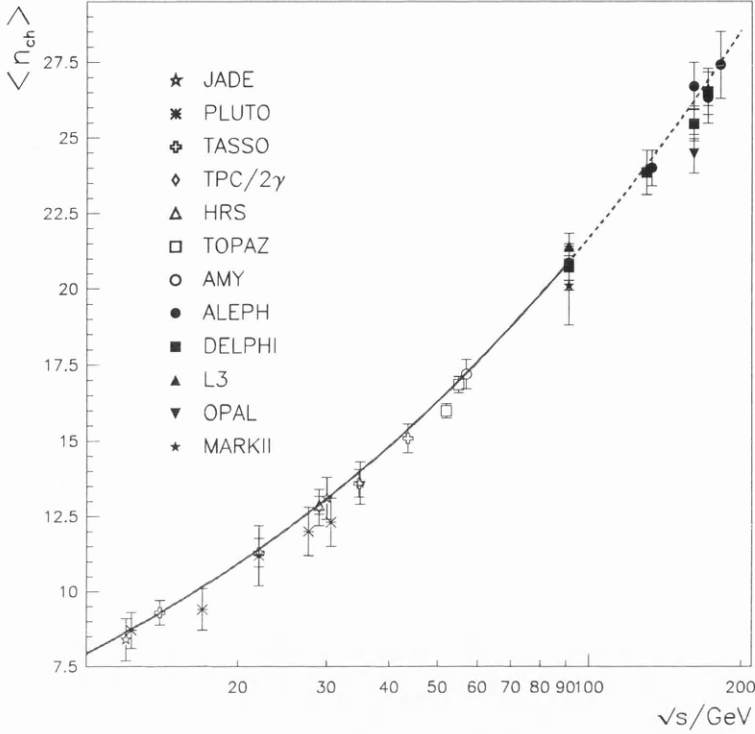


Figure 3.2: MLLA fit to  $\langle n_{ch} \rangle$  measured at several centre-of-mass energies. The dotted line indicates the fit extended into the region where recent measurements have been made by the LEP experiments [47]. Included is the preliminary ALEPH measurement at 183 GeV [48].

one naïvely predicts that the ratio  $\mathcal{R}_{brem}$  of soft radiation from a gluon-initiated jet to that from a quark-initiated jet will be

$$\mathcal{R}_{brem} = \frac{\mathcal{N}_g}{\mathcal{N}_q} = \frac{C_A}{C_F} = 9/4 . \quad (3.5)$$

The presence of the gluon jet therefore increases the average hadron multiplicity in three jet events from that expected if each jet originated from a quark.  $\mathcal{R}_{brem}$  is reduced when higher order effects are taken into account, the  $\mathcal{O}(\alpha_s^2)$  result being [50]

$$\mathcal{R}_{brem} = \frac{C_A}{C_F} \left( 1 - r_1 \gamma_0 - r_2 \gamma_0^2 \right) + \mathcal{O}(\gamma_0^3), \quad (3.6)$$

where

$$r_1 = 2 \left( \frac{11}{24} - \frac{n_f}{12N_C^3} \right) - \frac{3}{4},$$

$$r_2 = \frac{r_1}{6} \left( \frac{25}{8} - \frac{3n_f}{4N_C} - \frac{n_f C_F}{N_C^2} \right)$$

$$\gamma_0 = \sqrt{\frac{2N_C\alpha_s}{\pi}} + \frac{7}{8} - \frac{(67 - 6\pi^2)}{36} - \frac{C_F(4\pi^2 - 15)}{24N_3} + \frac{13n_f C_F}{36N_C^2},$$

Equation (3.6) gives  $\mathcal{R}_{brem}=1.84$  but hadronization effects are expected to further reduce observed particle ratios. For example the ratio of charged particles  $\mathcal{R}_{ch}$  is found to be in the range 1.0–1.6. The exact value not only depends on the chosen multiplicity, but also the Monte Carlo generator used to correct for detector effects in an analysis, and the way in which the jets are defined.

### 3.3 Three-Jet Events

In an  $e^+e^-$  collision, the probability that a high- $P_\perp$  gluon will be radiated from a primary (anti)quark to form a new jet is approximately equal to  $\alpha_s(\sqrt{s})$ . At LEP one therefore expects about one event in ten to have three distinct jets.

An example of an idealized three jet event is given in figure 3.3(a), where massless kinematics have been assumed. The jet energies,  $E_1, E_2, E_3$  are labelled in order of magnitude and the sum of these is exactly equal to  $M_{Z^0}$ . Given any two of these energies, the jet orientation is uniquely defined with momentum conservation forcing the jets to lie in a single *event plane*. Figure 3.3(b) shows the four main phases in jet production. The energy and direction of each jet must be reconstructed from the ensemble of final state hadrons.

Once a jet is defined, smaller sub-groups of particles within it can be made according to some prescription to form *subjets*. The number of these subjets in an event is known as the subjet multiplicity,  $n_{sub}$ . If  $N$  jets have been initially defined in an event then  $n_{sub}$  must lie within the range

$$N \leq n_{sub} \leq \langle n_{tot} \rangle. \quad (3.7)$$

The subjet multiplicity is sensitive to the underlying partonic structure of a jet. When a low number of subjets are resolved,  $n_{sub}$  represents the number of high- $P_\perp$  branchings in the early stages of the parton shower, which are calculable by perturbative techniques. Conversely, when  $n_{sub}$  is found to be of the order of the total multiplicity of the jet, the subjets are likely to only contain particles with a low- $P_\perp$ . Such particles are those that result from hadronization and resonance decays. Therefore, by studying the evolution of  $n_{sub}$  between the limits of eqn.(3.7), one can examine the transition from the calculable perturbative to incalculable non-perturbative regimes. Furthermore, the relative number of

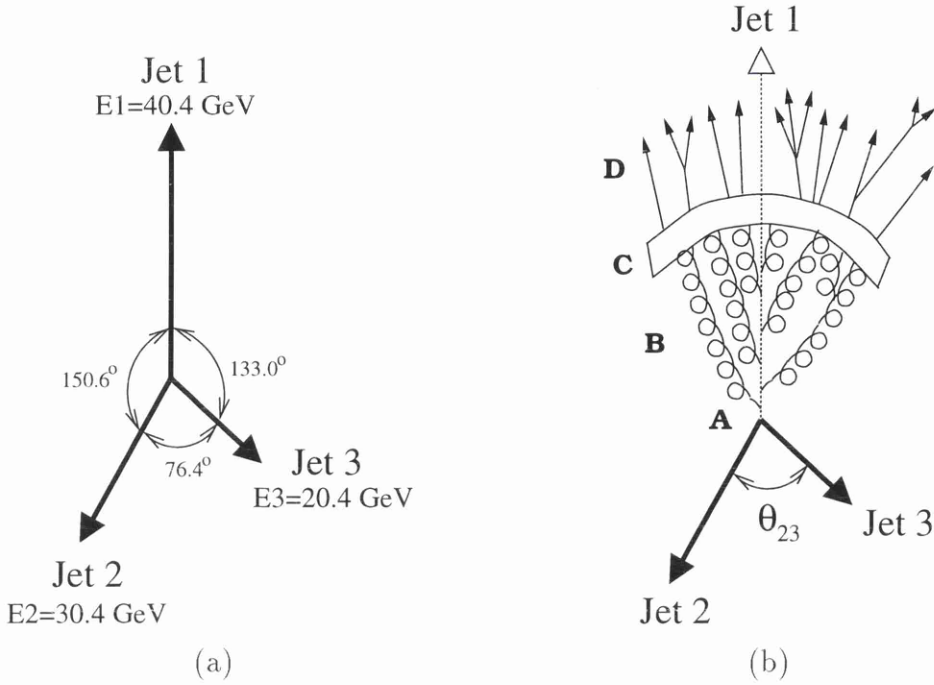


Figure 3.3: An example of a three-jet event. (a) The energy and interjet angles of a perfectly reconstructed event. (b) The hardest jet split into four phases; A. Quark produced via  $e^+e^-$  annihilation; B. parton cascade; C. hadronization; D. hadronic decays.

subjects obtained in quark and gluon jets at different stages of jet formation can be explored.

### 3.3.1 Interjet Particle Flow

It was first noted by the JADE collaboration [51] that, in three-jet events, the particle flow in the region between the two quark jets is significantly lower than in the regions between the quarks and the hard gluon. The phenomenon can be interpreted as a highly colour-charged gluon “dragging” radiation away from the  $q\bar{q}$  interjet region (the  $q\bar{q}$  valley) and so became known as the ‘drag effect’. The effect depends on the relative orientation of the jets and has been verified by many experiments [51, 52, 53] including a comparison of  $q\bar{q}g$  events with kinematically similar  $q\bar{q}\gamma$  events [5] where no colour drag is present.

The drag effect is embodied within the Lund String Model [35] by modelling the initial pair of quarks as being joined by a string whose stored energy increases as the quarks separate. Enough energy can be stored to break the string and

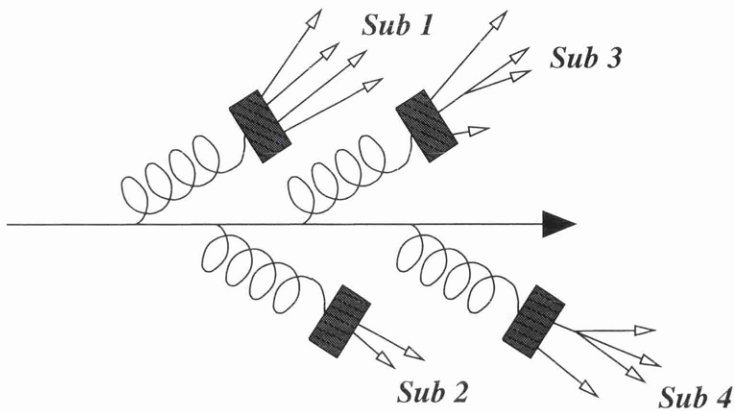


Figure 3.4: The clustering of final-state particles to form subjects. In this case the number of subjects gives information about the hard, high- $P_{\perp}$  branchings in the cascade.

produce a new  $q\bar{q}$  pair or a gluon. Gluons act so as to form “kinks” in the string, producing two new strings which are boosted in different directions (figure 3.5(a)). As hadrons are eventually formed from smaller pieces of these strings they are boosted into the  $q$ - $g$  regions. Models such as JETSET and HERWIG, which are based on string fragmentation, can reproduce the particle drags seen in data [54].

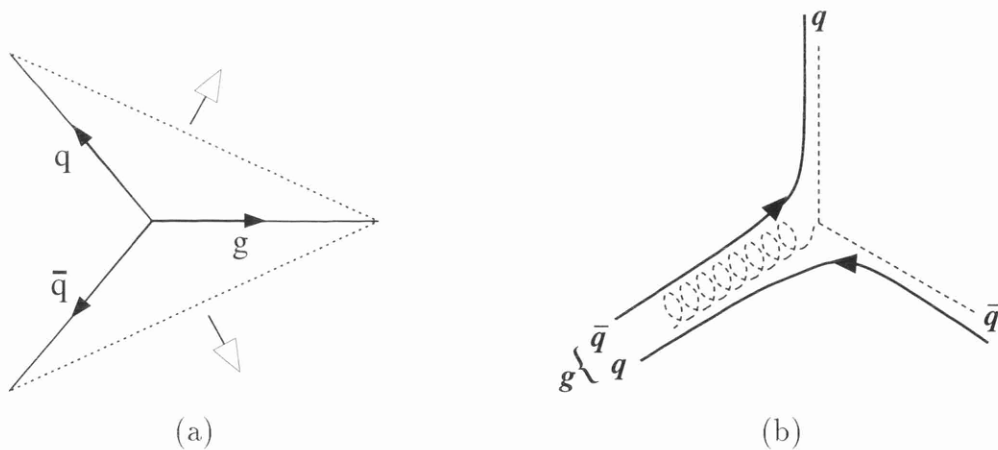


Figure 3.5: (a) ‘Strings’ attached between the partons in the  $q\bar{q}g$  system. The dotted lines depict the strings and the large arrows indicate their directions of travel. (b) The direction of colour flow in the large- $N_c$  limit.

In the pQCD picture, partons in a  $q\bar{q}g$  system form three dipoles which act as ‘colour antennae’ which coherently emit radiation predominantly in the event

plane. Radiation from the antenna spanning the  $q\bar{q}$  pair is suppressed by a factor  $\frac{1}{N_c^2}$  where  $N_c$  is the number of colours. In the ‘large- $N_c$  limit’, terms involving such contributions are neglected in perturbative calculations. The gluon in the three-jet system is replaced by a  $q\bar{q}$  pair with antennae spanning to the primary quark and antiquark. The gluon is therefore given an equal and opposite colour charge to each and the colour flow in the event resembles that in figure 3.5(b). An arbitrarily complex system of dipoles can be reduced in the large- $N_c$  limit to colour connected  $q\bar{q}$  pairs and the global radiation pattern calculated.

The net effect of the antennae causes destructive interference in the  $q\bar{q}$  valley (therefore particle flow in this region is depleted) and constructive interference in the other two regions. In the fully-symmetric configuration, where each interjet angle is  $120^\circ$ , the ratio of particle densities at the centre of the  $q(\bar{q})g$  regions to the  $q\bar{q}$  valley is predicted to be  $\sim 2.46$  [29]. The drag effect is so great that, in this configuration, the particle flow perpendicular to the event plane, which is kinematically unfavourable, is calculated to be greater than that in the  $q\bar{q}$  valley.

### 3.3.2 Topological Scales

In the previous section, the hard gluon in a three-jet event can be replaced in the large- $N_c$  limit with a  $q\bar{q}$  pair which is colour-connected to each of the primary quarks, and which assumes an equal and opposite colour charge to each. It is reasonable to expect that cancellation between two close colour emitters will affect subsequent cascades, as soft-gluon multiplicity is approximately proportional to the effective colour charge of the initiating hard parton.

The global effect in ALEPH events will be a decrease in the hadronic multiplicity as reconstructed jets becomes close to one another in angle. This implies that both event and jet multiplicities will depend on the relative opening angle of the jets and hence on the event *topology*. Therefore, one should consider the proximity of all jets to each other *as well as* the energies when predicting properties of individual jets or events containing several jets.

In the discussion of event topology the following notation is used:

$$\begin{aligned}
 E_i &= \text{energy of jet } i; \\
 \mathcal{N}_i &= \text{final number of soft shower gluons in Jet } i; \\
 \theta_{ij} &= \text{angle between jets } i \text{ and } j; \\
 S_{ij} &= \text{suppression factor on energy of jet } i \text{ due to jet } j.
 \end{aligned}$$

In two-jet events, shower partons have a high angular separation and topological effects can be ignored, so that  $\mathcal{N}_i \simeq \mathcal{N}_i(E_i)$ . However, in three-jet events  $\theta_{23} \leq 120^\circ$

and large interference effects are expected. It is demonstrated by ALEPH [6] that energy alone is insufficient to describe jet properties and an appreciation of the global event topology is required.

The effect of colour coherence is to make each jet-initiating parton act as if its real or “bare” energy is scaled down by a *suppression factor*  $S$  :

$$S_{ij} = S_{ij}(\theta_{ij}) , \quad (3.8)$$

$$\mathcal{N}_i = \mathcal{N}_i(E_i, S_{ij}, S_{ik}) , \quad (3.9)$$

with cyclic values of  $(i, j, k)$ . As perturbative calculations describe cascade evolution in terms of the transverse momentum  $k_{\perp}$ , an intuitive choice for the form of such a suppression would be [55, 56]

$$S_{ij} = \sin\left(\frac{\theta_{ij}}{2}\right) . \quad (3.10)$$

In the  $q\bar{q}g$  event shown in figure 3.5(b), the primary quark and antiquark are each attached by a colour line to the gluon but not each other, so that minimal interference is expected between the two quark jets. The multiplicity of a quark jet is therefore assumed to depend only on the angular proximity of the gluon, and take the form

$$\mathcal{N}_q = \mathcal{N}_q(E_q S_{qg}) , \quad (3.11)$$

and similarly

$$\mathcal{N}_{\bar{q}} = \mathcal{N}_{\bar{q}}(E_{\bar{q}} S_{\bar{q}g}) \quad (3.12)$$

for the antiquark, where the indices  $(q, \bar{q}, g)$  have replaced  $(i, j, k)$ .

The gluon, however, has two colour attachments so there is interference expected in each  $q$ - $g$  region. The corresponding expression for the multiplicity will hence contain a contribution from each colour line, the simplest form being a linear combination of the two components:

$$\mathcal{N}_g = f_g \left[ \frac{1}{2} \mathcal{N}_q(E_g S_{gq}) + \frac{1}{2} \mathcal{N}_{\bar{q}}(E_g S_{g\bar{q}}) \right] , \quad (3.13)$$

where  $f_g$  is a factor, called herein the *gluon factor*, which accounts for the enhancement in gluon jet multiplicity with respect to quark jets due to the higher colour charge of the former.

The scale dependence of  $\mathcal{N}_q$  in equation (3.4) is through  $\alpha_s$ , which to first order has a simple logarithmic dependence, see equation (2.13). It follows that

$$\begin{aligned} \mathcal{N}_q(Q) &\sim \mathcal{N}_q(\ln Q) \\ \implies \mathcal{N}_q(Q_1) + \mathcal{N}_q(Q_2) &= \mathcal{N}_q(\ln Q_1) + \mathcal{N}_q(\ln Q_2) . \end{aligned}$$

Expressing  $Q_1$  and  $Q_2$  in terms of the variables  $\bar{x} = \sqrt{Q_1 Q_2}$  and  $r = \sqrt{Q_1/Q_2}$  to give  $Q_1 = \bar{x}r$  and  $Q_2 = \bar{x}/r$  respectively allows one to write

$$\begin{aligned} \mathcal{N}_q(\ln Q_1) + \mathcal{N}_q(\ln Q_2) &= \mathcal{N}_q(\ln \bar{x} + \ln r) + \mathcal{N}_q(\ln \bar{x} - \ln r) \\ &\approx 2\mathcal{N}_q(\ln \bar{x}) + \text{subleading terms} . \end{aligned} \quad (3.14)$$

Substituting equation (3.14) into equation (3.13) allows the scale dependence of the gluon multiplicity to be given by a single suppression factor:

$$\mathcal{N}_g \simeq f_g \mathcal{N}_q \left( E_g \sqrt{S_{gq} S_{g\bar{q}}} \right) . \quad (3.15)$$

### 3.3.3 The Dalitz Plane

The topology of any three-jet event can be represented on a two dimensional Dalitz plane which allows full multiplicity distributions to be binned and directly compared. To define the axes of the plane, one can choose:

- (i) any pair of jet energies from  $E_1, E_2, E_3$ ;
- (ii) any pair of interjet angles from  $\theta_{12}, \theta_{23}, \theta_{31}$ ;
- (iii) any single energy and angle combination.

Each point in the plane will be unique, provided that  $\sum_i E_i \equiv \sqrt{s}$  and  $\{\theta_{12} + \theta_{23} + \theta_{31}\} \equiv 360^\circ$ . One finds that events are kinematically restricted to an area of a plane which is bounded by three curves. In this analysis the energies of the two hardest jets  $E_1$  &  $E_2$  are chosen to define the plane as the boundaries simplify to straight lines and the populated area becomes triangular which aids the division of the plane into regular bins.

As the jets are numbered in decreasing energy,  $E_1 \geq E_2 \geq E_3$ , the ranges for each jet become

$$\begin{aligned} \frac{\sqrt{s}}{3} &\leq E_1 < \frac{\sqrt{s}}{2} , \\ \frac{\sqrt{s}}{4} &\leq E_2 < \frac{\sqrt{s}}{2} , \\ E_{\min} &\leq E_3 \leq \frac{\sqrt{s}}{3} . \end{aligned} \quad (3.16)$$

$E_{\min}$  depends on the jetfinding method used and is typically  $\sim 10$  GeV.

Figure 3.6 shows the Dalitz plane defined by  $E_1$  &  $E_2$  and the kinematically accessible area. Events lying on the upper and lower boundaries are known as *symmetric* or '*Y*'-shaped events and have two jets with the same energy. Where

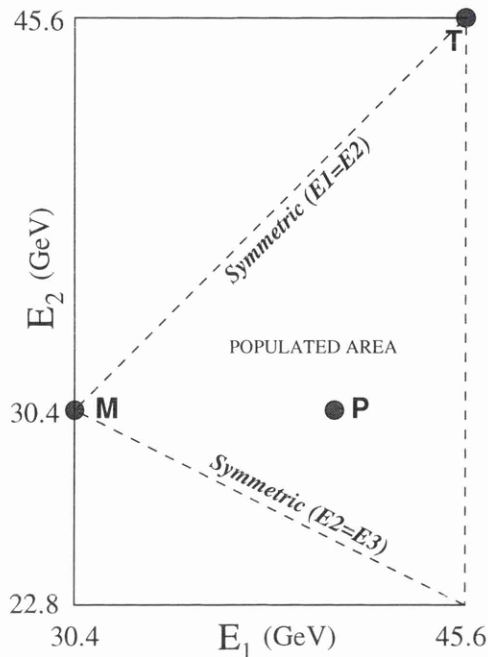


Figure 3.6: The Dalitz plane defined by the two hardest jets in a three-jet event.

the boundaries meet at the lefthand corner all jets have energy  $\frac{\sqrt{s}}{3}=30.4$  GeV and the event is totally symmetric. This unique topology is referred to as the ‘Mercedes’ event<sup>1</sup> where figure 4.10 is an example of such an event. As one moves away from the upper and lower boundaries jet energies are unequal and events become unsymmetric. Three topologies are marked on figure 3.6: the Mercedes point (M), the event shown in figure 3.3 (P) and the ‘2-jet’ point (T) where the energy of the third jet vanishes. Examples of two variables binned on this plane are given in figure 3.7.

### 3.4 Previous Studies

In this section, a brief summary is made of analyses by experiments located at the LEP collider into the properties of QCD jets. Section 3.4.1 lists the properties of quark and gluon jets which are identified by several methods, in particular the ratio  $\mathcal{R}_{ch}$  of the number of charged particles in each type of jet. Some studies of subjects are listed in section 3.4.2 and section 3.4.3 summarises recent analyses which attempt to highlight and account for the effects of colour coherence on jet

<sup>1</sup>So named due to the similarity with the Mercedes car marque.

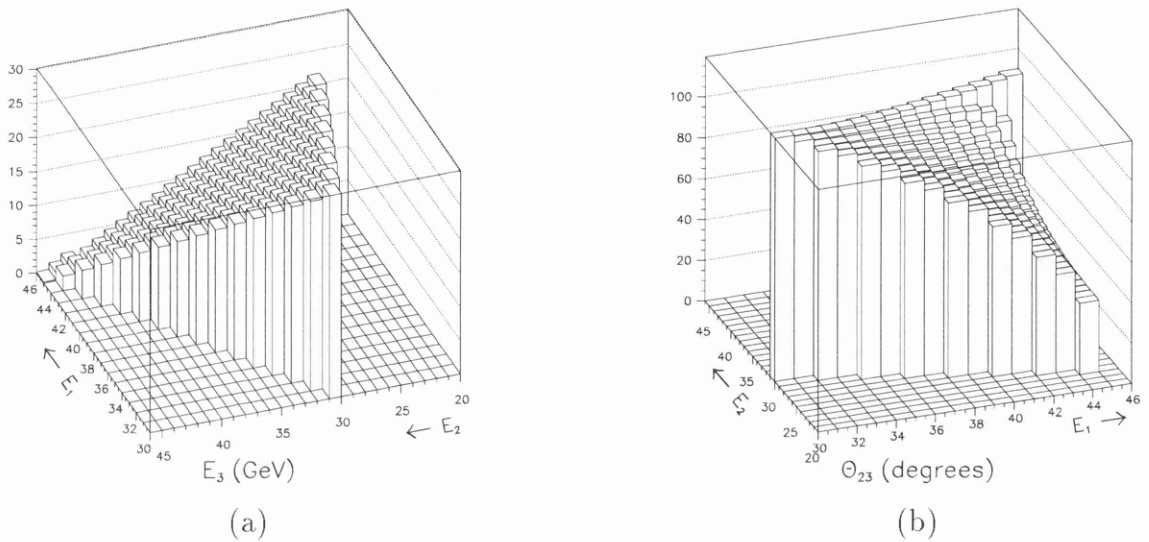


Figure 3.7: (a) Energy of jet 3 (softest jet) and (b) angle between this jet and jet 2 binned on the Dalitz plane. Note the plots are rotated, the Mercedes point being towards the viewer on the first plot and at the leftmost point on the second.

and event multiplicities.

### 3.4.1 Quark-Gluon Differences

Gluon jets were first seen by the experiments at the PETRA ring [22] in the late 1970's and studied by many collaborations in the following decade. The identification of quark-gluon differences was complicated by the need to interpolate results from different energies or environments, but with the inception of the experiments at LEP in the late 1980's more detailed studies were possible.

The OPAL collaboration first studied quark and gluon jets of comparable energy [57], by selecting Y-shaped three-jet events using the JADE algorithm as described in chapter 5. The hardest jet in each event was assumed to be a quark jet and the presence of a high-energy lepton identified the other quark jet as these arise predominantly from decays of charm and beauty hadrons. It was found that gluon jets are broader and have a softer fragmentation function than quark jets but have a similar multiplicity, quoting  $\mathcal{R}_{ch}=1.02\pm 0.04^{+0.06}_-0.00$ <sup>2</sup>.

The study was repeated using the DURHAM algorithm (chapter 5) to define jets and with the lepton tag replaced with a tag that identifies a displaced vertex

<sup>2</sup>In all quoted measurements the first error is statistical and the second systematical.

associated with the appreciable lifetime of the  $b$  quark. The measured values of  $\mathcal{R}_{ch}=1.27\pm 0.04\pm 0.06$  [58] and  $\mathcal{R}_{ch}=1.25\pm 0.02\pm 0.03$  [59] are significantly higher than the previous result, highlighting the fact that multiplicities and their ratios depend on the jet definition. In [60] the ratios of the charged multiplicity in gluon jets to both light ( $uds$ ) and  $b$  quark jets ( $\mathcal{R}_{ch}^{uds}$  and  $\mathcal{R}_{ch}^b$  respectively) were measured to be  $\mathcal{R}_{ch}^{uds}=1.390\pm 0.038\pm 0.032$  and  $\mathcal{R}_{ch}^b=1.089\pm 0.024\pm 0.024$ , finding little difference between gluon and heavy quark jets.

To give an inclusive measurement of gluon jet multiplicity which is less dependent on the jet definition, OPAL studied the rare events where two  $b$  quarks are tagged in the same hemisphere. The gluon jet is defined as every particle in the opposite hemisphere and has an average energy of  $\sim 39$  GeV. They find  $\mathcal{R}_{ch}^{uds}=1.552\pm 0.041\pm 0.060$  [61] and  $\mathcal{R}_{ch}^{uds}=1.471\pm 0.024\pm 0.043$  [3].

Other measurements include  $\mathcal{R}_{ch}=1.241\pm 0.015\pm 0.025$  by DELPHI [4] and ALEPH [62] who also quote [63]:

$$\begin{aligned}\mathcal{R}_{ch}^{nfm} &= 1.194\pm 0.027\pm 0.019 ; \\ \mathcal{R}_{ch}^{uds} &= 1.249\pm 0.084\pm 0.022 ; \\ \mathcal{R}_{ch}^b &= 1.060\pm 0.041\pm 0.020 ; \\ \mathcal{R}_{ch}^c &= 1.183\pm 0.221\pm 0.021 ,\end{aligned}$$

where  $\mathcal{R}_{ch}^{nfm}$  is the ratio to the natural flavour mix of quark jets. The results are consistent with the other measurements, with  $\mathcal{R}_{ch}^b$  the order of unity and  $\mathcal{R}_{ch}^c \sim \mathcal{R}_{ch}^{nfm}$ , although the difficulty in tagging charm jets means the statistical error is large and  $\mathcal{R}_{ch}^c$  is consistent with being unity.

### 3.4.2 Subjets

The subjet multiplicity is an experimentally useful variable as it is easily defined given an initial jet sample and is infra-red and collinear-safe allowing it to be calculated to all orders in pQCD. To define the subjet multiplicity, an event is first clustered at some resolution scale  $y_o^3$ . The jets are then re-clustered at smaller resolutions,  $y_{sub}$ , to give the number of subjets.

OPAL compared the ratio  $\mathcal{R}_{3-2}$  of the number of subjets in two- and three-jet events which at leading order is expected to be [64]

$$\mathcal{R}_{3-2} = \frac{2C_F + C_A}{2C_F} = 17/8 , \quad (3.17)$$

---

<sup>3</sup>See chapter 5 for a complete description of jetfinding and subjets.

although this ratio is greatly reduced in higher-order calculations. It was found that  $\mathcal{R}_{3-2} \approx 1.5$  when  $y_{\text{sub}} \sim y_o$  but falls as  $y_{\text{sub}}$  decreases and non-perturbative effects begin to dominate. As  $y_o$  is decreased, event samples with smaller interjet angles are produced and  $\mathcal{R}_{3-2}$  decreases. This effect is expected in the coherent picture as the gluon jet colour charge will be reduced if it is close to a quark jet. Further weight is given to this picture by Monte Carlo simulations which fail to describe the data if incoherent showers and/or independent fragmentation are used.

ALEPH has investigated subjets in identified gluon jets by obtaining a sample of near-Mercedes three-jet events where two  $b$  quark jets are tagged [65]. The ratio of the subjet multiplicity in the gluon to a natural flavour mix of quark jets was measured over a large range of  $y_{\text{sub}}$  values spanning the whole perturbative and non-perturbative regimes. When  $y_{\text{sub}} \sim y_o$  a ratio of  $1.96 \pm 0.13 \pm 0.07$  was found but this dropped to  $1.29 \pm 0.02 \pm 0.01$  for the smallest  $y_{\text{sub}}$ <sup>4</sup>. This is expected, as the transverse momentum between subjet clusters is small at these values and hadronization effects dominate. The ratio therefore approaches that of the charged jet multiplicity which in this study is quoted as  $\mathcal{R}_{ch} = 1.246 \pm 0.028 \pm 0.014$ .

Using an increased ALEPH data sample, subjet ratios were measured in restricted energy ranges [66]. The peak value of the ratio is seen to be  $\approx 2.5$  for jet energies  $\lesssim 30$  GeV but falls to  $\approx 1.0$  for higher energy jets. An explanation of this effect is that high-energy jets tend to have particles concentrated in two clusters (the jet is practically two jets) and, for both quark and gluon jets, only two subjets are resolved over a large  $y_{\text{sub}}$  range and so their ratio remains  $\mathcal{O}(1)$ . The average ratio over all the energy ranges is of course equal to the value in the earlier study.

### 3.4.3 Colour Coherence

The first investigations of colour coherence focused on the string effect in which particle and energy flow between jets is enhanced if at least one of the jets originated from a gluon. Results from studies in  $q\bar{q}g$  systems [52] and the comparison of interjet flows in  $q\bar{q}g$  to  $q\bar{q}\gamma$  systems [53] all strongly favoured the coherent picture of soft QCD radiation.

The intrajet angular ordering anticipated by pQCD can be examined through the construction of variables sensitive to the correlations between particles in a jet.

---

<sup>4</sup>The primary hard parton is usually not considered to be part of the subjet multiplicity and hence 1 is subtracted from the measured number of subjets. This will only affect regions where the number of resolved subjets is small.

Studies by both OPAL and L3 [67] conclude that only Monte Carlo models which incorporate interference effects, such as JETSET and HERWIG, can reproduce the correlation variable distributions seen in data.

Topological scales were introduced in an ALEPH analysis [66] in an attempt to describe the multiplicity of quark and gluon jets occurring in different jet configurations. It was found that, if jet multiplicities are binned according to a scale which depends on both jet energy and interjet angles, then datapoints lie on a curve for both quark and gluon jets. Gluon jets required two components, as expected in section 3.3.2, and the curve was well described by the perturbative prediction in equation (3.3). However, this was not the case for quark jets and it was pointed out in a later paper [68] that the MLLA prediction contains no information about the way jets are defined and cannot be simply translated to the three-jet system. Nevertheless, Monte Carlo models which embody the MLLA reproduce the observed quark distributions and their use in topological studies is hence justifiable.

The multiplicity of a whole event is less sensitive to jet definition as it becomes unimportant to which jet each particle is attributed. In [68] the multiplicity of each jet is calculated using a topological scale and added to give a prediction for the whole event. A value of  $\mathcal{R}_{ch} \approx 1.5$  was extracted from the fits which is consistent with other analyses in which gluon jets were identified from either a lepton or heavy quark tag.

### 3.5 Motivation For This Analysis

There is now conclusive evidence for coherent nature of QCD cascades, *i.e.* radiation interference (interjet effects) and angular ordering (intrajet effects). The analysis in this thesis aims to develop two recent analyses by the ALEPH collaboration [66, 68] which have shown that jet multiplicities are described not by energy alone but by a scale based on both the observed jet energy and the topology of the event.

Given the successes of these analyses, this work follows a similar method to select a three-jet sample from ALEPH events recorded during the full running of LEP I. With this large sample it becomes possible to impose tight quality cuts to retain only well reconstructed events. Samples are also obtained using modified jetfinding schemes which claim to improve the association of soft, interjet particles to jets, meaning one should see a better agreement between theory and experiment.

### 3.6 Analysis Strategy

The selection of a three-jet sample is made using iterative jetfinding algorithms which are introduced and contrasted in detail in chapter 5. Because of the excellent tracking and calorimetry of the ALEPH detector, individual particles within jets can be resolved and their momenta measured to infer the initial hard parton directions. The accuracy to which one can measure jet directions is closely related to the possible energy resolution of the jets. If jets are badly reconstructed (for example if particles are not measured by the detector) then the position of the event on the Dalitz plane will be incorrect. In an attempt to minimize this jet energy resolution, several methods of defining jet energies are investigated in chapter 6.

The first stage of the analysis, described in chapter 7, is to select candidate hadronic events from ALEPH data and reject events that are leptonic or have significant initial- or final-state radiation. Once a sample has been binned on a Dalitz plane according to a chosen energy definition, the topological dependence of multiplicity distributions is explored by fitting a theoretical prediction across the plane. As this analysis uses no heavy quark tagging, it is not known which jet originated from the hard gluon. Each jet is given a probability that it is the gluon jet, and the predictions weighted by this for all permutations. The fitting procedure is detailed in chapter 8, in which the change in topology of a Monte Carlo event, as it is passed through a simulation of the ALEPH detector, is described. This change causes a movement or ‘migration’ of events around the plane, and the fits to observed data distributions take into account these migrations. The results of such fits to the charged and subjet multiplicity are described in chapters 9 & 11.

# Chapter 4

## The ALEPH Experiment at LEP

### 4.1 LEP

ALEPH is one of four large experiments placed around the Large Electron-Positron (LEP) storage ring at CERN, Geneva [69]. Electrons and positrons are kept circulating in opposite directions around a 27 km circuit by  $\sim 4000$  bending and focusing magnets. Particle beams are injected from the Super Proton Synchrotron (SPS) in four “bunches”, or “trains” of smaller bunches, and accelerated (or ‘ramped’) by radio frequency (RF) cavities. The SPS is just one part of the CERN accelerator chain, shown schematically in figure 4.1, which produces the beams of electrons and positrons which are finally injected into the main LEP ring.

Once accelerated and in stable orbits the beams are made to cross at four points around the ring (PA 2,4,6,8). The beams are typically  $\sim$  few cm long and  $\sim$  few mm in diameter but are focused at collision points to a transverse size of  $\sim 200 \mu\text{m} \times 20 \mu\text{m}$  to provide a concentrated, localized interaction volume. The beams must be constantly accelerated as they lose energy via synchrotron radiation. Collisions occur at  $\sim 10^5$  Hz and these, along with accelerator losses give an exponential decrease in the intensity of the beams and hence a reduction in experimental cross section.

During the first phase of LEP operation (LEP I, 1989–1995) the centre-of-mass energy was that of the  $Z^0$  resonance to allow precision studies of electroweak and strong interactions as well as looking for new physics phenomena. The second phase (LEP II, 1995–2000) involves the installation of many new RF cavities and magnets to allow beams of up to 100 GeV, enabling studies of  $W^+W^-$  pair production and an extension to physics searches. This thesis concerns a study of the data collected with the ALEPH detector during LEP I operation.

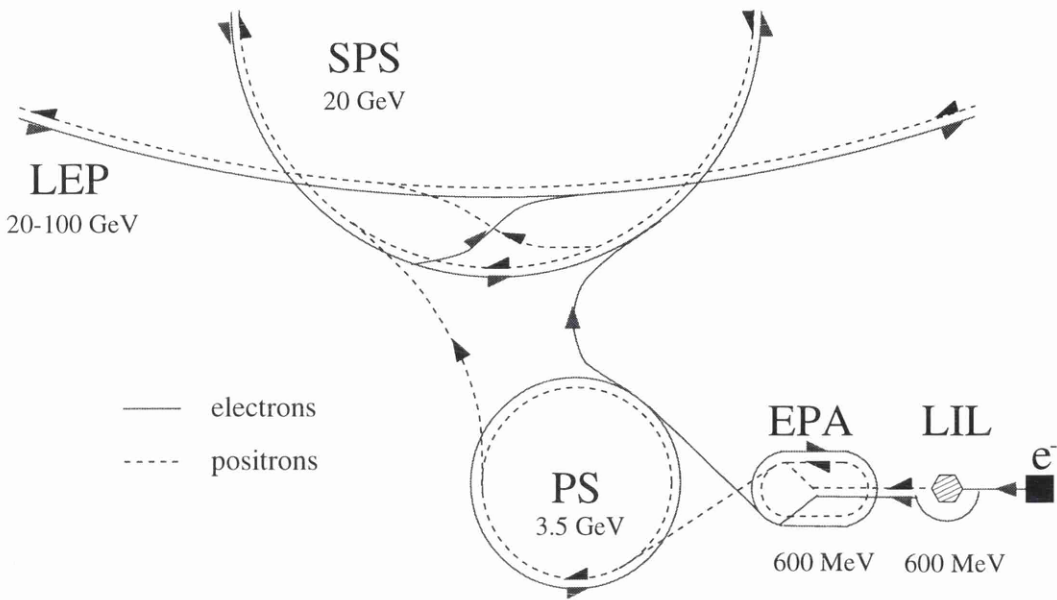


Figure 4.1: A schematic diagram of the five major accelerators involved in producing high energy electrons and positrons for ALEPH. Electrons first pass into the LEP Injection Linac (LIL) and are either stored in the Electron Positron Accumulator (EPA) or fired at a tungsten target to produce positrons. These positrons are accelerated and pass to the EPA. When a sufficient number of particles have been produced they are transferred to the Proton Synchrotron (PS) to be ramped up and then passed to the SPS for further ramping and finally injection into the LEP ring. The figures give the typical beam energy at each stage.

## 4.2 ALEPH

The ALEPH (A detector for LEP Physics) detector is situated 140 m underground at point PA4 on the LEP ring. In the LEP I environment electron and positron beams collide to form a  $Z^0$  boson at rest, which then decays to typically 40 charged and neutral particles which can be sensed and identified within the ALEPH apparatus. The cross section is low compared to hadronic colliders, and ALEPH is designed to efficiently record interesting events and measure the energy and momentum of collision products. Genuine  $e^+e^-$  events are digitized, processed within a computer cluster situated on the surface at Echevex, France and recorded onto disk. The events are then analysed to identify and reconstruct individual particles.

The following sections briefly describe ALEPH hardware, software and operation. A detailed description can be found elsewhere [70], the discussion here is

restricted to areas important to this analysis.

### 4.3 Overview

The apparatus is shown in figure 4.2. The design is basically that of a cylindrical ‘barrel’ with tracking detectors closest to the interaction point (IP) surrounded by calorimeters and muon chambers. Two ‘endcaps’ close the ends of the cylinder and ensure that ALEPH is a self-shielding experiment: all decay products are absorbed within the volume of the apparatus, with the exception of high energy muons and neutrinos, the latter being inferred via the “missing energy” in an event. In all, the apparatus weighs 3000 tons but can be moved (barrel and endcaps independently) out of the beam line for inspection or repair. The endcaps can separate  $\sim 2$  m from the barrel to allow regular maintenance and an alignment of the inner detectors.

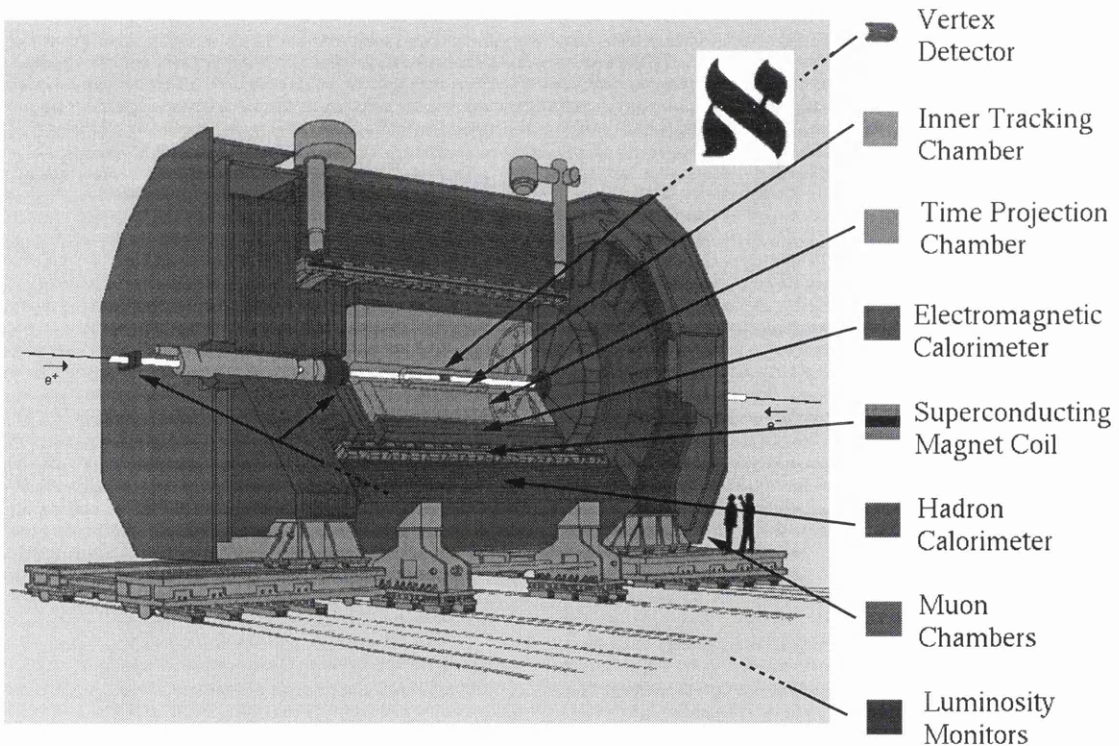


Figure 4.2: The ALEPH detector at LEP.

## 4.4 Magnet

A liquid helium cooled superconducting magnet lies between the two calorimeter shells. The coil operates at 5000 A to produce a 1.5 T field parallel to the  $z$ -axis which incurs curvature of the paths of charged particles as they traverse the magnetic volume. From this curvature, particle charge and momentum can be measured. The iron yoke not only returns the magnetic flux, but also forms an integral part of the outer calorimeter.

## 4.5 Geometry

In a discussion of the subdetectors, it is useful to describe the coordinate system of ALEPH. The  $z$ -axis lies along the beam line down the centre of the barrel, with the  $+z$  direction that of  $e^-$  circulation. This axis is  $\sim 3\frac{1}{2}$  mrad off horizontal as the LEP ring is inclined to allow the tunnels to pass through softer rock strata. The  $x$ -axis points horizontally towards the centre of the ring and the  $y$ -axis points upwards  $\sim 3\frac{1}{2}$  mrad off the vertical. The polar( $\theta$ ) and azimuthal( $\phi$ ) angles (fig. 4.3) are often used, cylindrical coordinates being more appropriate with regards the geometry of ALEPH. The IP is at the centre of the detector and is the origin of all coordinates.

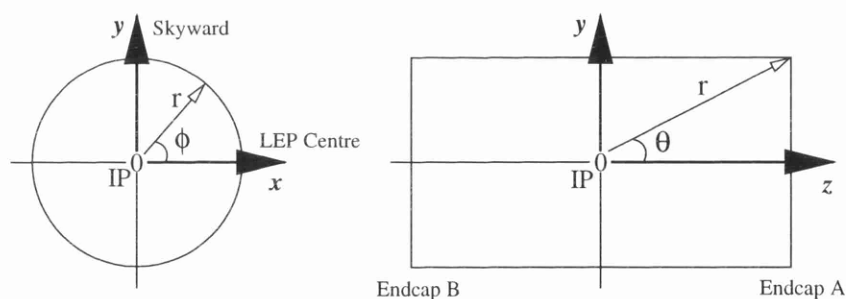


Figure 4.3: The ALEPH coordinate system.

## 4.6 Tracking Detectors

There are three independent tracking detectors, described in the following sections in the order traversed by a decay particle from the IP. Information from these is used to reconstruct decay particles from the helical tracks they produce. From these, the momentum, energy and often the particle type can be obtained.

### 4.6.1 VDET

The Vertex DETector is made up of 96 individual  $51.2\text{ mm} \times 51.2\text{ mm} \times 300\text{ }\mu\text{m}$  silicon wafers formed into two concentric structures (fig. 4.4) at average distances of 65 mm and 113 mm from the beam axis. The length of the VDET<sup>1</sup> is 200 mm and the inner and outer structures cover 76 & 67 % of the solid angle respectively. Signals are read out from  $2 \times 50\text{ }\mu\text{m}$  pitch strips which cover both faces of the wafers, one side having strips parallel to the  $z$ -axis, the other at right angles.

Individual hits are formed from the charge-weighted positions of adjacent strips, and a position accuracy of  $12\text{ }\mu\text{m}$  is achieved on both strip planes to give an accurate three-dimensional position on a particle's path. The VDET is used primarily to identify secondary vertices associated with beauty and charm quark events, but also for extrapolation of tracks identified in outer subdetectors.

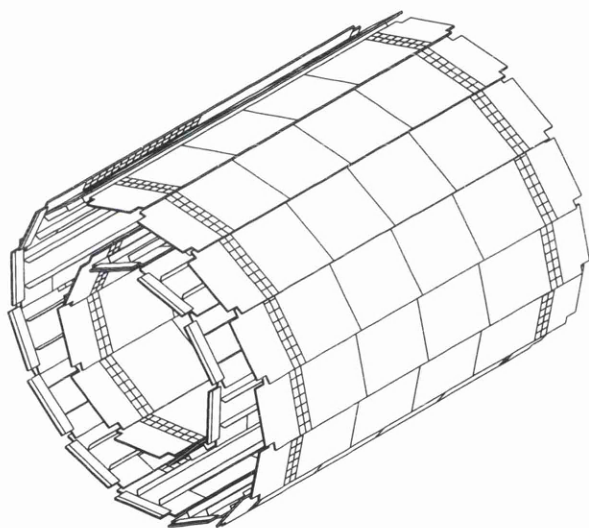


Figure 4.4: Orientation of the VDET silicon wafers.

### 4.6.2 ITC

The Inner Tracking Chamber is a drift device of length 2 m with eight cylindrical layers of wires parallel to the  $z$ -axis. Cylinder radii extend between 160 mm and 260 mm from the beam axis and can give up to eight points on a particle's

---

<sup>1</sup>The dimensions given are for the original VDET which was superseded by a larger but similar version for the inception of LEP II (1995).

path. The  $r\phi$  coordinate is calculated to  $\sim 150\ \mu\text{m}$  by measuring the drift time to adjacent drift cells (fig. 4.5). The ITC is the only tracking device used for the level 1 trigger, the small cell size facilitating a fast readout and discrimination time ( $\sim 2\ \mu\text{s}$ ).

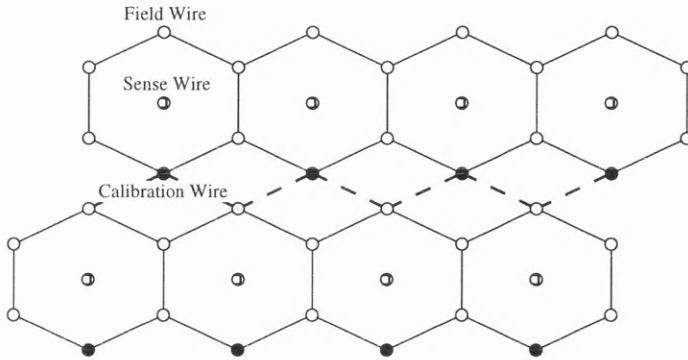


Figure 4.5: Eight neighbouring ITC drift cells, each  $\sim 1\ \text{cm}$  in size. Signals can be induced on the calibration wires to test detector performance.

### 4.6.3 TPC

The Time Projection Chamber is the main tracking subdetector of ALEPH. It forms a large cylinder with inner & outer radii 30 cm & 180 cm whose volume is filled with 91 % argon and 9 % methane. As well as a 1.5 T magnetic field there is a parallel electric field of  $\sim 115\ \text{V/cm}$  inside the TPC which is maintained between a central membrane, which splits the detector into two, and the endplates which are grounded. Strips held at equipotentials along the inner and outer fieldcages ensure the field is uniform.

Charged particles travel in helical paths through the TPC volume and induce ionization of the gas therein. Electrons drift towards an endplate which comprises of 18 multi-wire proportional chambers. Each chamber or ‘sector’ consists of a gating grid, a sense wire plane and, 4 mm behind these, a cathode plane of concentric rows of finely segmented pads. Between the pad rows are longer pads used for the second level trigger. The liberated electrons induce an avalanche and are collected on the sense wires. Figure 4.6 shows a cut-away view of the TPC and detail of an individual sector.

A  $r\phi$  coordinate is found by interpolating the signal induced on the cathode pads, a  $r$  coordinate from the pads’ known radial position, and a  $z$  coordinate

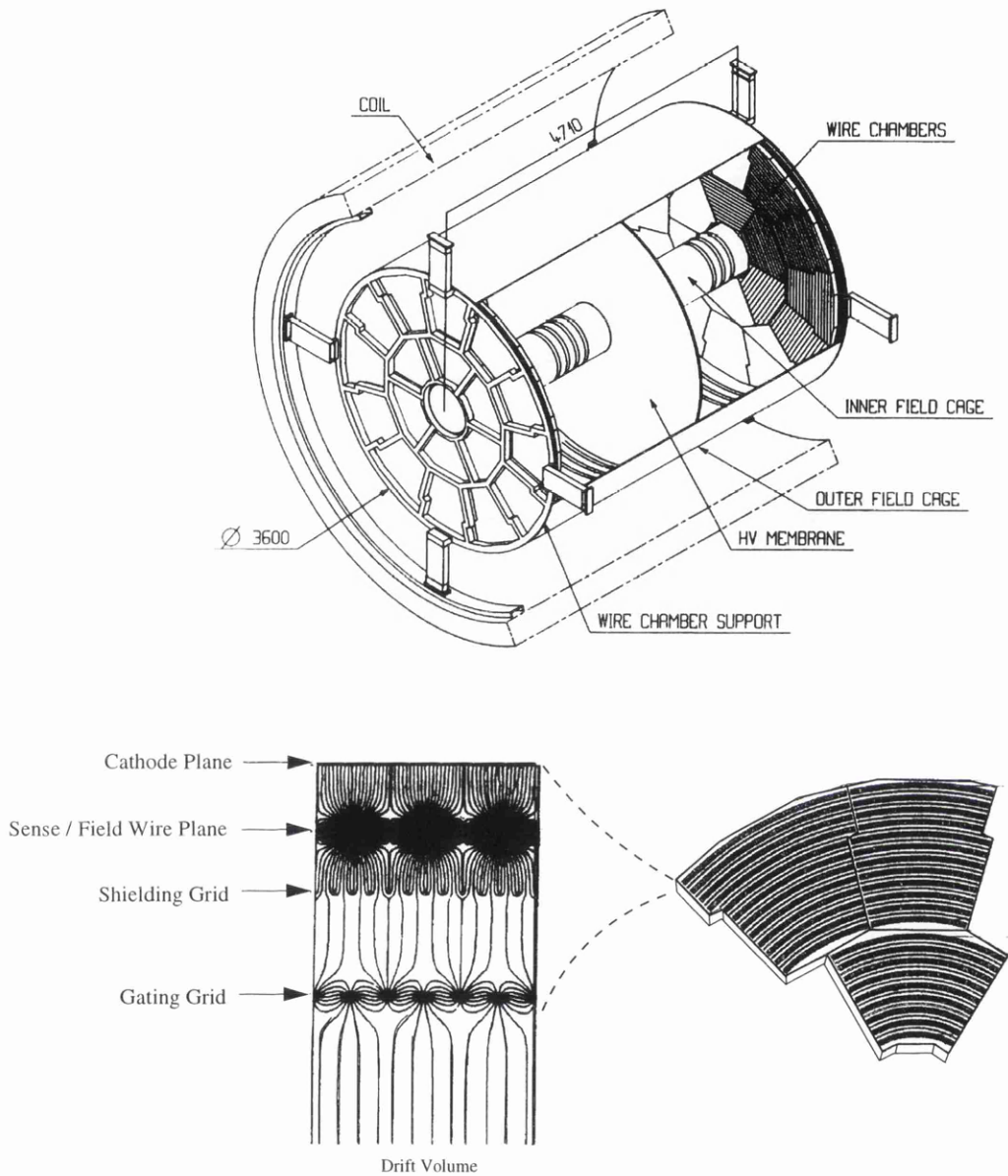


Figure 4.6: (Top) Schematic view of the time projection chamber. (Bottom) Detail of a TPC sector. The left-hand diagram is a simplified cross section showing the gating and sensing planes. The electric field lines are shown for the gating grid in the ‘closed’ (opaque to charged particles) position. The upper plane is divided into radial rows of finely spaced cathode pads and longer triggering pads, shown on the right hand diagram.

from the drift time of the pulse. Furthermore, the pulse height on the sense wires is used to measure an ionization density  $\frac{dE}{dx}$  to provide particle identification.

Positive ions are produced near the sense wires and would cause field distortions if they were not removed by the gating system which is synchronized with beam crossings. Some distortions still remain for the drift field, and di-muon events or laser tracks are used to estimate their magnitude and location. Laser tracks are provided by the laser calibration system for which I was responsible during my periods at CERN. During this time the system underwent considerable modifications to allow the lasers to be run synchronously with ALEPH data taking.

Using hit information from the TPC the error  $\sigma_{P_{\perp}}$  in the transverse momentum  $P_{\perp}$  of a reconstructed track is

$$\frac{\sigma_{P_{\perp}}}{P_{\perp}^2} \simeq 0.0012 ,$$

but if ITC and VDET hits are also assigned then the resolution improves to

$$\frac{\sigma_{P_{\perp}}}{P_{\perp}^2} \simeq 0.0006 .$$

## 4.7 Calorimetry

There are two main calorimeters: the ECAL, which is contained within the solenoid to keep material between itself and the IP to a minimum, and the HCAL which is designed to detect particles that traverse the solenoid as well as forming the return yoke for the magnetic flux.

### 4.7.1 ECAL

The purpose of the Electromagnetic CALorimeter is to identify electrons, positrons and photons over a large solid angle, with a sufficient granularity to resolve individual particles in a jet.

High spatial coverage ( $0 < \phi < 2\pi$ ,  $|\cos \theta| < 0.98$ ) is obtained by separate barrel and endcap structures, each comprised of 12 sections or ‘modules’ (fig. 4.7). Information is lost in the gaps or ‘cracks’ between modules (2% and 6% of barrel and endcap area respectively) but the endcaps are rotated half a module with respect to the barrel so cracks do not match in the region between the two detectors.

Each module comprises 45 layers of lead interleaved with proportional tubes. Particles produce showers of electromagnetic particles which avalanche towards

anode wires in the tubes. A high granularity is obtained by reading the signal induced on  $\sim 30\text{mm}^2$  cathode pads, which are joined to form ‘towers’ that point towards the IP. Towers cover  $\sim 1^\circ$  square of angle and are read out in three depths or ‘storeys’ corresponding to 4, 9 and 9 radiation lengths. The wire signal is used for the level 2 trigger and removal of electronic noise. The energy and direction of a shower in  $(\theta, \phi)$  is found using a charge-weighted mean of signals from individual storeys. Energy resolution  $\sigma_E$  for a particle of energy  $E$  GeV is

$$\frac{\sigma_E}{E} = 0.01 + \frac{0.018}{\sqrt{E}} ,$$

and the angular resolution is

$$\sigma_\phi = \frac{\sigma_\theta}{\sin \theta} = 0.32 + \frac{2.7}{\sqrt{E}} \text{mrad} .$$

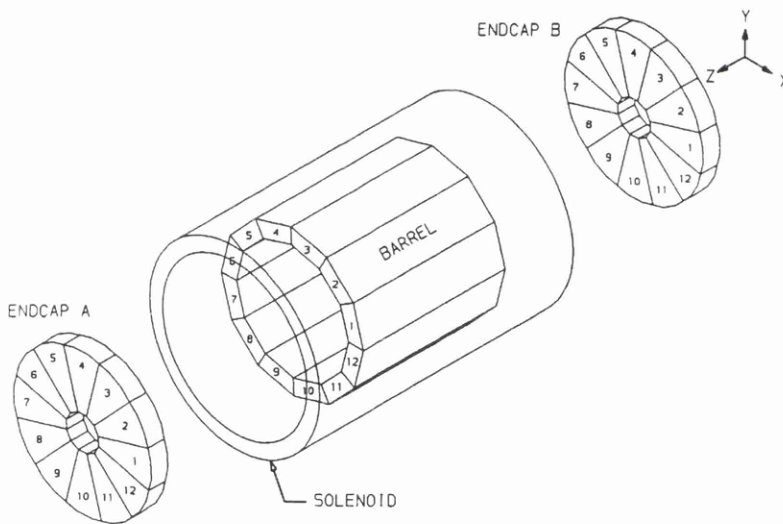


Figure 4.7: The layout of the electromagnetic calorimeter modules.

## 4.7.2 HCAL

The Hadron CALorimeter lies outside the magnet and is similar in construction to the ECAL. The HCAL covers over 93% of the solid angle and is designed to measure the energy and position of hadrons and muons. The HCAL has 23 layers of iron ( $\sim 7$  radiation lengths) interleaved with  $10\text{mm}^2$  streamer tubes. Each

tube has a central anode wire which measures the energy in a plane, and the combined signal from these planes is used for triggering. Running parallel to the wires on the outside of the tubes are aluminium strips used for monitoring the longitudinal profile of a shower which is characteristic for muons and hadrons. Cathode pads are used again to give the position of a shower and are arranged in towers, each covering  $\sim 3.7^\circ$  square in angle. Each tower covers 14 ECAL towers and are rotated by  $2^\circ$  with respect to the latter to cause non-alignment of cracks. The energy resolution (using notation as before) is

$$\frac{\sigma_E}{E} = \frac{0.85}{\sqrt{E}} .$$

### 4.7.3 Muon Chambers

The only charged particles likely to escape from the HCAL are muons. To detect these two double layers of streamer tubes exist outside the HCAL, each with the tubes planes perpendicular to each other, and each tube with cathode strips running parallel and perpendicular to the central anode wire. An angular resolution of  $\sim 10$ – $15$  mrad is obtainable, and for 95 % efficiency the muon/hadron misidentifications are estimated to be

$$\begin{aligned} \mathcal{P}(\pi \text{ identified as } \mu) &= 0.007 \quad \text{and} \\ \mathcal{P}(K \text{ identified as } \mu) &= 0.016 . \end{aligned}$$

## 4.8 Luminosity Measurement

A measure of the total luminosity  $\mathcal{L}$  received by ALEPH is important in the determination of reaction cross sections as the observed reaction rate  $\mathcal{R} = \sigma\mathcal{L}$ . Although this is not fundamental to this analysis the luminosity subdetectors are used to identify background events and low-angle measurements.

The luminosity is determined from the observed rate of elastic  $e^+e^-$  scattering (Bhabha) events whose cross section is well predicted from QED to be proportional to  $1/\Theta^4$  where  $\Theta$  is the scattering angle. This strong angular dependence necessitates the calorimeters to be arranged very close to the beampipe and have good angular resolutions.

The Luminosity CALorimeter lies inside the ECAL endcaps and is very similar in construction and operation to the ECAL. Towers of cathode pads are used to give a energy and position resolution of

$$\sigma_E = 0.014 E + \frac{0.20}{\sqrt{E}} \quad \text{and} \quad \sigma_x = \sigma_y = 1.4 \text{ mm}$$

respectively over the range  $2^\circ < \theta < 9^\circ$ .

The Silicon luminosity CALorimeter lies outside the LCAL on either side of the IP and provides a more precise measurement using layers of silicon pad detectors. SICAL covers  $24 \text{ mrad} < \theta < 58 \text{ mrad}$  and gives energy and angular resolutions of

$$\frac{\sigma_E}{E} = \frac{0.33}{\sqrt{E}} \quad \text{and} \quad \sigma_\phi = 0.2^\circ - 0.3^\circ$$

respectively.

The Bhabha CALorimeter lies at  $\pm 7.7 \text{ m}$  from the IP and measures very small angle Bhabha events to give an online luminosity measurement with a positional accuracy of  $\sim 0.5 \text{ mm}$ .

## 4.9 Triggering

Within ALEPH the  $e^+$  and  $e^-$  bunches cross at a rate of  $45.5 \text{ kHz}$ , although the annihilation rate is only a few per second. A three level triggering system is employed with the ultimate goal of identifying all genuine  $e^+e^-$  interactions whilst discarding background events (beam gas interactions, cosmic rays, scattering from beam pipes and collimators *etc.*) whilst minimising detector “dead time”. Dead time is the term given to the period when the detector is reading out an event, during which it is cannot record any subsequent  $e^+e^-$  collisions.

The trigger is designed to be sensitive to jets or particles produced at the IP from  $Z^0$  decays or Bhabha events, the combined trigger efficiency being close to 100% for both cases.

### 4.9.1 Level 1

The level 1 trigger has the task of making a fast decision to either initiate event digitization (“YES”) or clear and prepare for the next bunch crossing (“NO”). A YES is returned for any of the following scenarios:

- There is a Bhabha hit in the LCAL or SICAL;
- A predefined energy deposition is exceeded in the ECAL or HCAL;
- There is a coincidence between ITC hits and ECAL/HCAL energy deposits.

The level 1 trigger reaches a decision in under  $5 \mu\text{s}$  and the triggering is at the rate of  $< 100 \text{ Hz}$ .

### 4.9.2 Level 2

A level1 YES initiates the readout of the TPC which takes  $\sim 50 \mu\text{s}$  (this is effectively fixed by the physical drift time of electrons from the central membrane region of the TPC to the outer sectors). Information from the long pad rows on the sectors is used to search for charged track patterns in the regions indicated by ITC hits. A YES decision prompts a full readout of the detector whilst a NO causes readout to be aborted and the detector reset, with only five bunch crossings being “missed” due to detector dead time. A YES decision occurs at a rate  $< 10 \text{ Hz}$ .

### 4.9.3 Level 3

The level3 ‘software’ trigger runs within the Data Acquisition system (DAQ) to qualitatively assess information from the whole detector to identify genuine  $e^+e^-$  interactions. A YES causes the event to be finally accepted and written to disk at a reasonable rate of 1–2 Hz.

## 4.10 Data Acquisition

The vast amount of raw data ( $\sim \frac{1}{2}$  TByte per second from over  $7 \times 10^5$  readout channels) supplied by the subdetectors of ALEPH is handled by the data acquisition system. The purpose of the DAQ is to collate data from all the subdetectors in a way that minimizes dead time and reduces the volume of raw data. The trigger system is involved in these requirements. The DAQ emulates the modular structure of ALEPH; the main elements are shown in figure 4.8.

The process starts by the Main Trigger Supervisor (MTS) receiving a timing signal synchronized with the LEP bunch crossing. The signal is passed to the ReadOut Controllers (ROCs) which initialize front-end modules and read them out. The ROCs also reduce data volume by only digitizing channels above predetermined thresholds, and formatting data into BOS [71] structures. Level1&2 trigger information is passed to the ROCs via the MTS and is used to either halt digitization and reset the ROC or digitize the event and assign a trigger number. The trigger number is used by a subdetector Event Builder (EB) to construct a complete sub-event then pass it to the Main Event Builder (MEB) which assembles and synchronizes the entire event. The event is then passed to the *online cluster* in the ALEPH control room where it, given a level3 YES decision, is recorded onto disk ready for the reconstruction process.

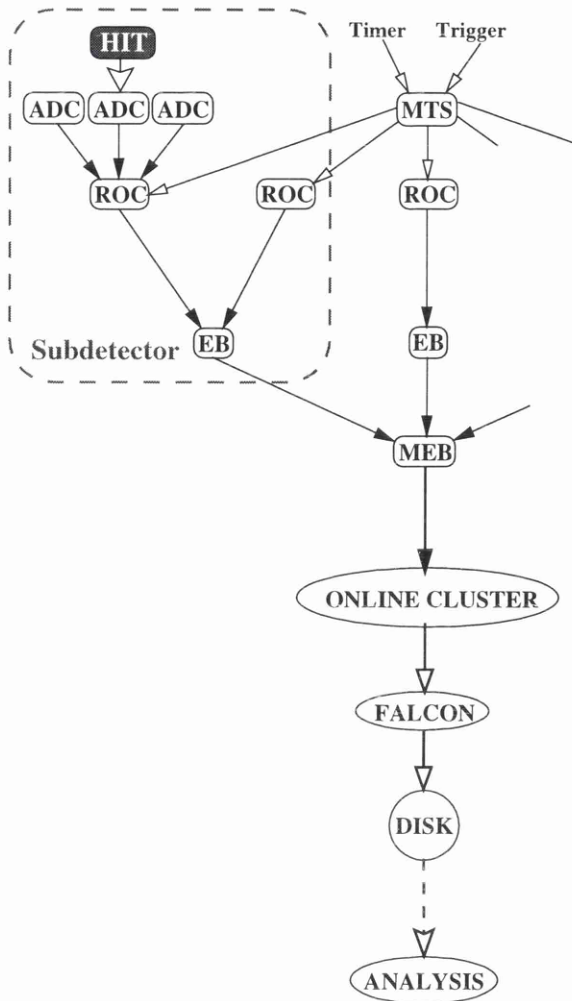


Figure 4.8: A simplified diagram of the DAQ system of ALEPH.

## 4.11 Event Reconstruction

The events recorded onto disk from a physics ‘run’ are passed to a computer cluster known as FALCON (Facility for ALepH COmputing and Networking) which is dedicated to the running of the JULIA reconstruction program. JULIA (Job to Understand Lep Interactions at Aleph) determines the constants of the run, such as the TPC drift velocity, and reconstructs charged tracks from tracking detector hits and neutral particles from calorimeter clusters. The quality of a run is determined by the shift crew where possible detector problems or inefficiencies are quickly identified.

### 4.11.1 Charged Tracks

Charged particles that traverse the TPC have helical paths due to the magnetic field. To find these TPC hits, clusters are used to identify individual  $(r, \theta, \phi)$  coordinates which are grouped into helical ‘chains’. The chains are joined to form track candidates which are extrapolated back to the ITC to search for associated hits. If there are at least 3 hits then a revised helical fit is performed and the track extrapolated back to the VDET where up to 2 additional hits can be attributed. A final fit is made using all available tracking information from the TPC, ITC and VDET, including multiple scattering effects and path ‘kinks’ produced by in-flight decays.

### 4.11.2 Calorimeter Objects

Individual fired storeys in the ECAL and HCAL are clustered together (associated to the same object) if they have at least one corner in common. The total visible energy in an event can be defined as the sum over all fired ECAL and HCAL storeys and muon hits. However, the resolution on a given jet energy measurement is insufficient using calorimetry alone, and an *energy flow algorithm* [72] is used to incorporate information from the tracking subdetectors.

Firstly a cleaning process is performed on all charged tracks and calorimeter clusters to remove noisy channels or objects not originating from the volume surrounding the IP. Thereafter charged and neutral *calorimeter objects* are formed according to the following prescription. Overlapping ECAL and HCAL clusters are combined, then charged tracks are extrapolated into the calorimeters and associated with clusters. Using  $\frac{dE}{dx}$  and shower profile information electrons, muons, photons and  $\pi^0$ 's are identified and removed from the event. The only calorimeter objects remaining should be charged or neutral hadrons. Charged objects are assumed to be pions and given an energy calculated from the track momentum. If the remaining HCAL clusters have energy  $> 500$  MeV they are assigned as neutral hadrons. The resulting set of objects are referred to as *energy flow* or *EFLOW* objects and are used in this off-line analysis to study hadronic jets.

Using calorimetry alone the error on an energy measurement is  $\frac{\sigma_E}{E} = \frac{1.2}{\sqrt{E}}$ , but using the energy flow algorithm the error reduces to  $\frac{0.59}{\sqrt{E}}$ . The energy resolution of a jet of energy  $E$  GeV and angle  $\theta$  to the  $z$ -axis is given by [73]

$$\sigma_{E,\phi} = \frac{3}{5} \left(1 + \sqrt{E}\right) \left(1 + \cos^2\theta\right) . \quad (4.1)$$

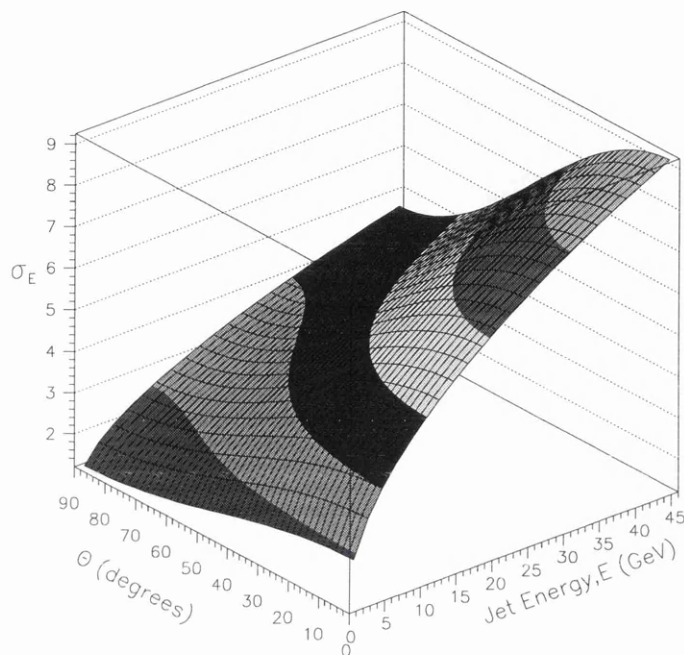


Figure 4.9: The expected error  $\sigma_E$  on the measured energy of a jet at an angle  $\theta$  to the  $z$ -axis with actual energy  $E$ .

### 4.11.3 A Reconstructed Event

Figure 4.10 shows a fully reconstructed hadronic event at ALEPH during run 29755 at 9.15 pm on 15th October 1994. Three jets of particles originating from the decay  $Z^0 \rightarrow q\bar{q}g$  can be identified: the three-fold symmetry is rare and known as the “Mercedes” configuration.

The larger of the plots is an end-on ( $x$ - $y$ ) view of the detector showing the TPC, ECAL, HCAL, solenoid and muon chambers. The view has been distorted to enlarge areas closer to the interaction point, as it has in the upper-right plot which zooms in on the central area of the detector to show the VDET wafers and ITC planes in detail. The small dots denote individual hits in the tracking subdetectors and reconstructed tracks are shown as lines fit through subsets of these hits. ECAL energy deposits are shown as filled rectangles, the three storeys being clearly seen. The histograms on the outer perimeter of the ECAL show the total energy deposition. Individual HCAL pad hits are seen as small squares, and the large block histograms within the HCAL volume again give the total energy deposition. The lower-right plot is a side-on ( $y$ - $z$ ) view showing the detector apparatus in true proportions.

This event is somewhat unusual in that it has a muon identified in two jets (the ‘7 o’clock’ and ‘11 o’clock’ positions) which only happens in about one in forty three jet events. Each muon can be traced through the entire detector, leaving an energy deposit through the calorimeters to finally give hits in the muon chambers.

Made on 13-Feb-1998 11:11:16 by curtis with DALI\_E1.  
 Filename: DC029755\_009646\_980213\_1111.PS

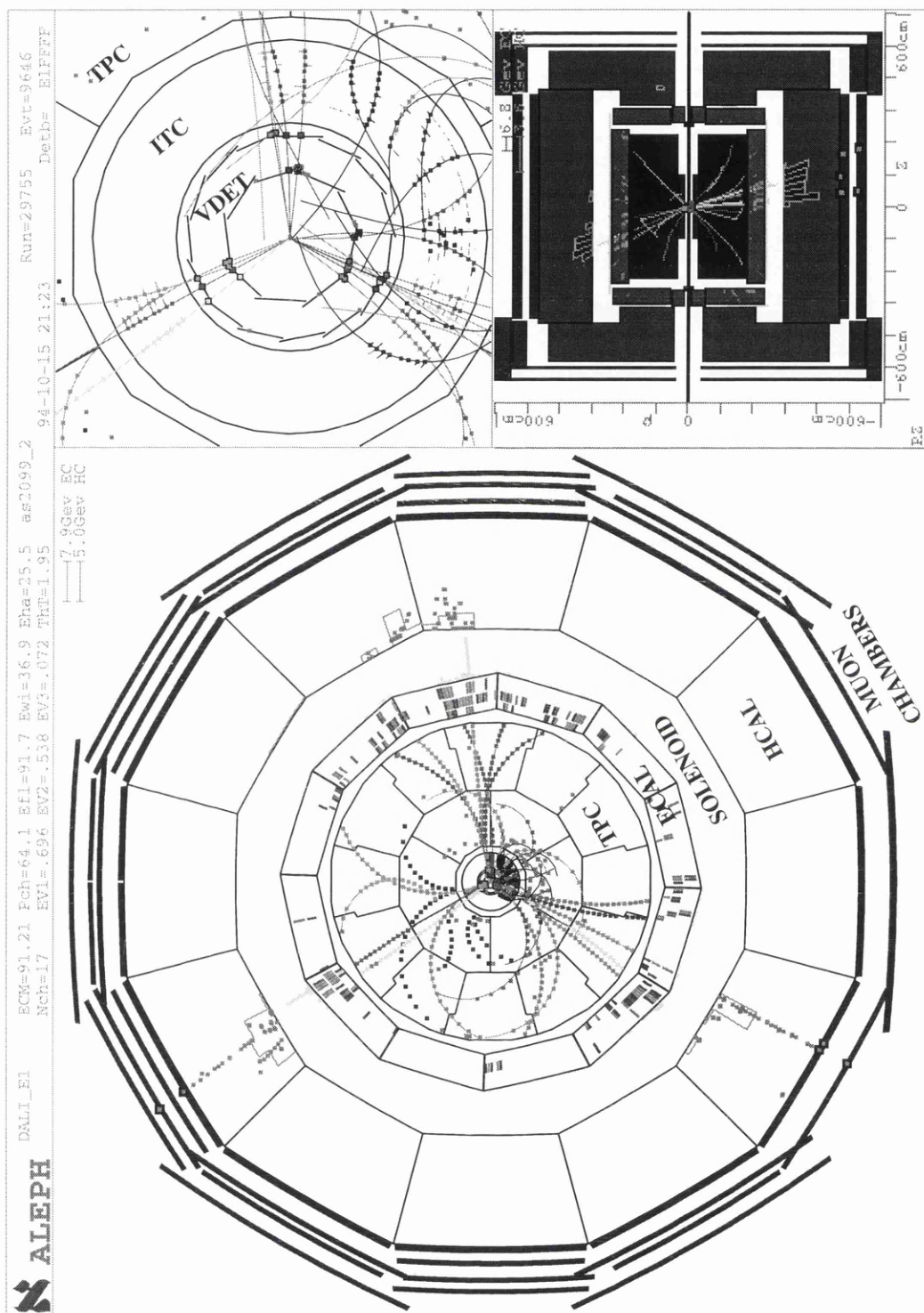


Figure 4.10: A fully reconstructed three-jet event observed in the ALEPH detector.

# Chapter 5

## Jetfinding

### 5.1 Introduction

A typical hadronic  $Z^0$  decay at LEP produces approximately 20 charged particles which are reconstructed in the tracking subdetectors of ALEPH. A similar number of neutral particles are produced and are reconstructed from the energy they deposit in the calorimeters. The process of collecting final-state hadrons together into clusters is known as jetfinding.

The majority of these events consist of two collimated back-to-back jets. However at LEP energies, there is an appreciable probability that a hard, high- $P_{\perp}$  (high transverse momentum) gluon will be radiated from a primary quark to produce a distinct third jet. There is immediately the question of how to associate (*cluster*) hadrons together to infer the energy and momenta of the primary partons in an event. This clustering should be free of infrared divergences and be insensitive to non-perturbative hadronization effects.

Analyses generally employ an iterative clustering algorithm first introduced by the JADE collaboration to study events from PETRA [74]. Later the DURHAM [75] variant became more popular due to its better treatment of soft radiation. Dokshitzer *et al.* recently proposed a modified jetfinding method [76] where particles are associated in a way that intuitively follows from the perturbative cascade mechanism of jet formation. This process of jetfinding, and the different algorithms employed, are discussed in the following sections.

## 5.2 Clustering Algorithms

Most jetfinders use an iterative procedure whereby an initial mass scale or *metric*,  $y_{ij}$ , is defined for every pair of tracks  $(i, j)$  in an event. The pair with minimum  $y_{ij}$  are combined (providing that  $y_{ij}$  does not exceed a predefined cut,  $y_{\text{cut}}$ ) and the tracks  $(i, j)$  replaced with a pseudo-particle whose energy and momentum is defined by a *recombination scheme*. Three such schemes are listed in table 5.1. The E scheme is Lorentz invariant and pseudo-particles are massive whereas the  $E_0$  and p schemes force all pseudo-particles to be massless. The  $E_0$  scheme achieves this by conserving energy but not momentum, the p scheme *vice-versa*.

After each step, new  $y_{ij}$  are calculated for the event and the pairing process repeats until all  $y_{ij}$  are greater than the  $y_{\text{cut}}$ , *i.e.*  $y_{ij} \geq y_{\text{cut}}$  ( $i = 1 \rightarrow n-1, j = i \rightarrow n$ ), where  $n$  is the remaining number of tracks and pseudo-particles. Satisfying this condition, the combined tracks can be defined as final state ‘jets’ and the number of jets in the event,  $n_{\text{jets}} = n$ .

Inclusive quantities such as jet rates and event shapes can be calculated theoretically for a given  $y_{\text{cut}}$ , any infrared singularities manifesting themselves as  $y_{\text{cut}} \rightarrow 0$ . Clearly as  $y_{\text{cut}}$  becomes small less pairs of particles will be combined. Eventually a cut is reached where no jets are resolved at all and

$$\lim_{y_{\text{cut}} \rightarrow 0} n_{\text{jets}} = N ,$$

where  $N$  is the initial number of particles in the event.

Scheme	Pseudo-Particle	
	Energy	Momentum
E	$E_i + E_j$	$\vec{p}_i + \vec{p}_j$
$E_0$	$E_i + E_j$	$\frac{E_i + E_j}{ \vec{p}_i + \vec{p}_j } (\vec{p}_i + \vec{p}_j)$
p	$ \vec{p}_i + \vec{p}_j $	$\vec{p}_i + \vec{p}_j$

Table 5.1: The E,  $E_0$  and p schemes for the combination of tracks  $i, j$  with three-momenta  $\vec{p}_i, \vec{p}_j$  and energy  $E_i, E_j$  respectively.

### 5.2.1 The JADE Algorithm

The method of iterative clustering was introduced and named by the JADE collaboration [74]. The metric  $y_{ij}$  is defined by

$$y_{ij} \cdot E_{\text{vis}}^2 = 2 E_i E_j (1 - \cos \theta_{ij}) , \quad (5.1)$$

where  $E_{\text{vis}}$  is the visible energy of the event,  $E_{i,j}$  are the energies of particles  $i$  and  $j$  respectively and  $\theta_{ij}$  is the angle between them. In the following description it is useful to split  $y_{ij}$  into two components to give  $y_{ij} \cdot E_{\text{vis}}^2 = e_{ij} \times v_{ij}$ , where

$$e_{ij} = E_i E_j , \quad (5.2)$$

$$v_{ij} = 2(1 - \cos \theta_{ij}) . \quad (5.3)$$

The JADE algorithm was motivated by the possibility of measuring  $\alpha_s$  from the three-jet rate which is calculated to NLO [77]. Although the jet rates measured at parton and hadron level are very similar [78], perturbative corrections for the JADE algorithm are large. A major problem is the treatment of soft gluons radiated close to the primary quark direction.

Consider two gluons  $i, j$  in the ‘seagull’ diagram of figure 5.1 which are emitted at low angles to the respective quarks  $A$  and  $B$ . Although the angle between the gluons is large there is a high probability that they will be soft enough to give  $y_{ij} < y_{iB}, y_{jA}$  and be combined together to form a “fake”<sup>1</sup> jet almost at right angles to the quarks. This jet may be clustered with more soft gluons to form a jet of appreciable energy.

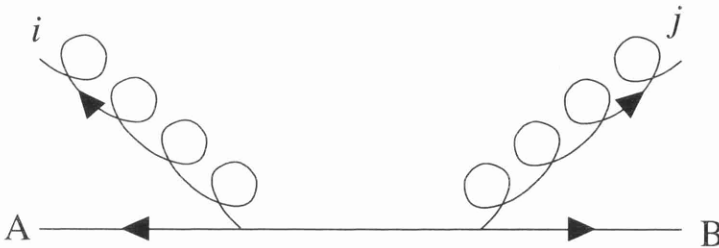


Figure 5.1: The ‘seagull’ diagram.

<sup>1</sup>The jet is defined as being “fake” if it does not originate from a hard bremsstrahlung gluon radiated in a partonic cascade.

### 5.2.2 The DURHAM Algorithm

To overcome the problem of “fake” jet formation the DURHAM algorithm [75, 79] was introduced where

$$e_{ij} = \min \{E_i^2, E_j^2\} . \quad (5.4)$$

$v_{ij}$  is given by equation (5.3) and the product  $e_{ij} \times v_{ij}$  is essentially the transverse momentum squared of the lower energy particle (in the low-angle approximation) with respect to the other. This is immediately seen on writing

$$y_{ij} \cdot E_{\text{vis}}^2 = 2E^2(1 - \cos \theta_{ij}) = \left(2E \sin \frac{\theta_{ij}}{2}\right)^2 \simeq k_{\perp}^2 . \quad (5.5)$$

The DURHAM algorithm has the immediate benefit that the merging scale is related to the transverse momentum,  $k_{\perp}$ , which sets the scale of jet evolution for perturbative calculations. Consequently, more predictions are calculable for event-shape variables, some of which can be treated by resummed QCD calculations [80]. The  $y_{\text{cut}}$  can be imagined as a  $k_{\perp}$ -cut with the simple relation  $k_{\perp}^{\text{max}} = E_{\text{vis}} \sqrt{y_{\text{cut}}}$ .

In the ‘seagull’ diagram one can see that with the new definition of  $e_{ij}$  the gluons will not be clustered together to form a “fake” jet. Additionally, the HERWIG and JETSET Monte Carlo models have been used to estimate hadronization effects and these are found to be significantly larger for the JADE algorithm than the DURHAM algorithm.

The limiting values of jet energies and interjet angles in a three-jet event clustered with the DURHAM algorithm can be expressed in terms of the chosen  $y_{\text{cut}}$ . The closest angle that two jets can approach each other,  $\Theta_{\text{min}}$ , is in the symmetric ‘Y’ configuration where the closest jets each have energy  $\frac{1}{4}E_{\text{vis}}(1+y_{\text{cut}})$ . For a given  $y_{\text{cut}}$ ,

$$\Theta_{\text{min}} = \cos^{-1} \left( \frac{1 - y_{\text{cut}}}{1 + y_{\text{cut}}} \right) , \quad (5.6)$$

$$\begin{aligned} E_{\text{min}} &= \frac{E_{\text{vis}}}{4} \left( \sqrt{y_{\text{cut}}^2 + 8y_{\text{cut}}} - y_{\text{cut}} \right) \\ &\approx E_{\text{vis}} \sqrt{\frac{y_{\text{cut}}}{2}} , \end{aligned} \quad (5.7)$$

where  $E_{\text{min}}$  is the minimum possible jet energy.  $\Theta_{\text{min}}$  and  $E_{\text{min}}$  are plotted as a function of  $y_{\text{cut}}$  in figure 5.2. As the  $y_{\text{cut}}$  restricts the range of jet energies, events selected with a jetfinder cannot populate the entire Dalitz plane depicted in figure 3.6. As the  $y_{\text{cut}}$  is increased, the tendency is for topologies to be more symmetric and, in the limiting case where  $y_{\text{cut}} \rightarrow \frac{1}{3}$ , the population is restricted to

the Mercedes configuration. Figure 5.3 shows the accessible area of the plane with four different initial  $y_{\text{cut}}$ .

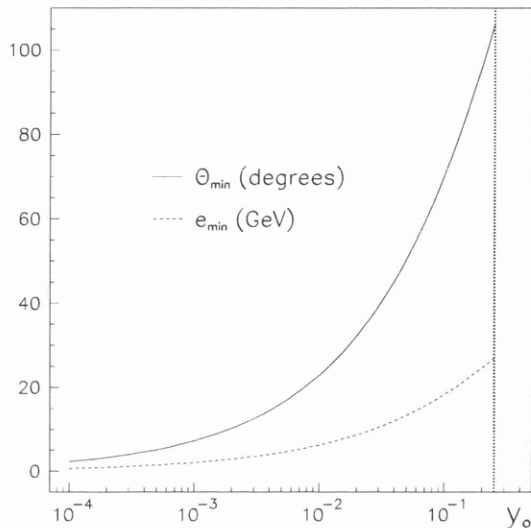


Figure 5.2: The minimum interjet angle and jet energy with  $y_{\text{cut}}$  in an event clustered with the DURHAM algorithm.

### 5.2.3 The ‘A’ and ‘C’ Jetfinders

Despite the success of the DURHAM algorithm in reducing the production of “fake” jets, some problems remain. Two subtle modifications to the basic<sup>2</sup> clustering method have been suggested [76] which attempt to improve particle association to jets by looking at the perturbative cascade picture of jet formation. Although clustering in data is made with final-state hadrons, LPHD assumes that these will bear a close resemblance to the underlying partonic structure of the jets.

The first jetfinder concerns the order of clustering of soft gluons about a hard primary quark (figure 5.4). In the basic DURHAM case, the softest gluon tends to be paired with the closest neighbour in angle and not with the quark in this topology. This can lead to a single genuine jet being resolved as two jets, one of which contains no hard particles. This scenario can be eliminated by pairing particles with minimum angle ( $v_{ij}$ ) first, provided that the cut  $y_{ij}$  is satisfied for

<sup>2</sup>The use of the JADE and DURHAM algorithms in the forms described in section 5.2 will hereafter be referred to as ‘basic’.

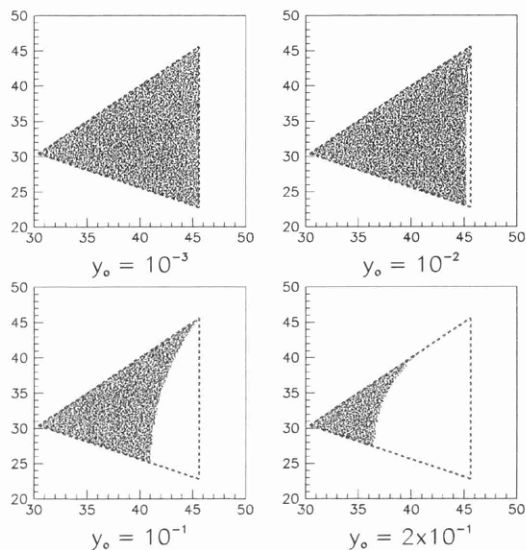


Figure 5.3: The area populated with  $y_{cut}$  for events clustered with the DURHAM algorithm.

the pair. If not, then the next-closest in angle pair is examined and so on. If no pair can satisfy the  $y_{cut}$  then clustering ceases. This method will hereafter be called the ‘A’ jetfinder.

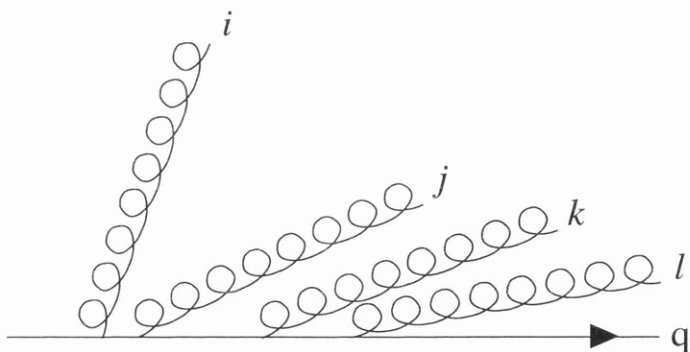


Figure 5.4: Soft gluon emission from a quark  $q$  during a cascade. If gluon  $i$  is the softest parton then the DURHAM algorithm will pair it with the closest neighbour in angle, gluon  $j$ , possibly forming a “fake” jet. In the ‘A’ jetfinder the gluons will be correctly associated with the quark in the order  $l, k, j, i$ .

The *Cambridge* or ‘C’ jetfinder is an attempt to improve the internal resolution of previously defined jets, *i.e.* *subjets*. Consider the situation in figure 5.5 where a

soft gluon  $i$  is radiated from a primary quark  $q$  shortly before gluon  $j$ . According to the coherent picture of cascades, gluon  $i$  will be radiated at a larger angle to the quark than gluon  $j$  and is only sensitive to the net colour charge of  $j + q$ . However if the angle between  $(i, j)$  is smaller than that between  $(j, q)$  then the gluons will be paired with the ‘A’ jetfinder to possibly form a “fake” jet. This jet will give misleading results if the subjet multiplicity of the event is investigated as the underlying colour dynamics of the jets is incorrect. The ‘C’ jetfinder is an attempt to combat this problem. It is identical to ‘A’ up until the point where a pair of particles do not pass the  $y_{\text{cut}}$ . Instead of trying the next-closest pair in angle, the softest of the failing pair is deemed to be a jet and prevented from taking any further part in the clustering process. In this way soft particles are “frozen” and cannot attract any more partners as the clustering continues. Initial studies suggest that hadronization effects for the ‘C’ jetfinder are small *w.r.t.* DURHAM for average jet rates [76], but large for individual jet rates [81].

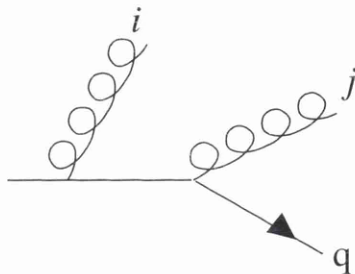


Figure 5.5: Soft, large angle gluon emission from a quark  $q$ .

The change in the order in which particles are clustered with the modified jetfinders is clearly seen in figure 5.6, where the angle between the pair of particles which are last merged is shown at three resolutions. For the basic JADE and DURHAM jetfinders at  $y_{\text{cut}}=0.1$ , the distribution is approximately flat reflecting the fact that particles are clustered predominantly by energy and not angle. The ‘A’ and ‘C’ jetfinders, however, cluster particles closest in angle first and this gives a distribution with a maximum at  $\sim 90^\circ$ . The difference between ‘A’ and ‘C’ starts to become apparent at the lowest  $y_{\text{cut}}$ , the “freezing” of soft jets with ‘C’ forcing the jetfinder to reach to larger angles to find the next possible particle. The E recombination scheme was used in forming the pseudo-particles, but if other schemes are used, the change in the distributions is not visible on the scale of figure 5.6.

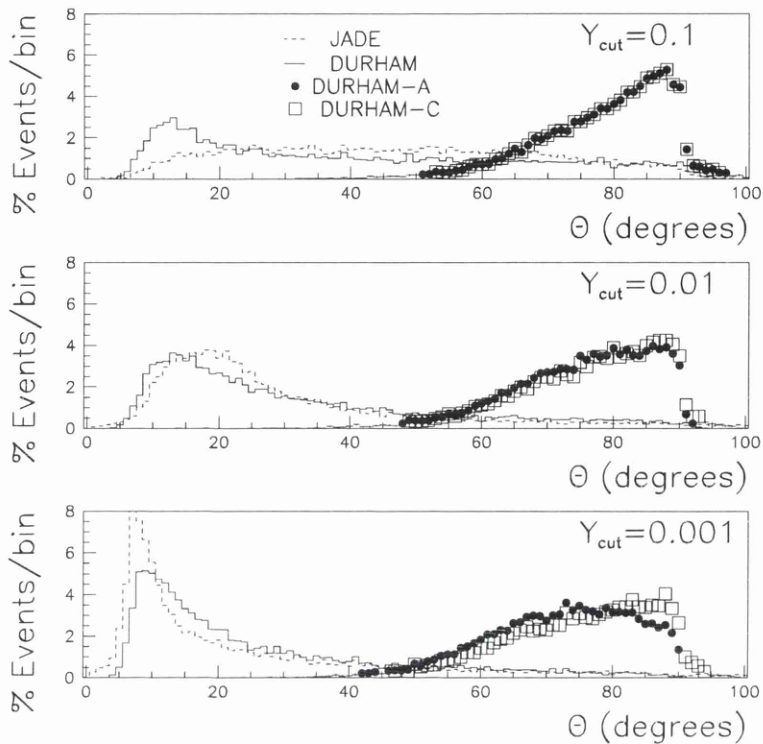


Figure 5.6: The angle  $\Theta$  between the last pair of particles merged with different algorithms.

### 5.3 Comparison of Jetfinders

The findings of any study that involves the formation of jets obviously depends strongly on the jet definition used. For example, an event sample clustered with JADE and DURHAM at a resolution scale  $y_{\text{cut}}$  will not give the same number of three-jet events in each case. In LEP analyses, the DURHAM algorithm is usually chosen because the resolution scale translates to a  $k_{\text{L}}$ -cut between jets and hence the yields and properties of these jets are calculable in pQCD. The modified schemes are relatively untried in LEP analyses and it will be interesting to see the effect these have on measurements such as  $\alpha_s$  in the future.

In this section, the jetfinders discussed in sections 5.2.1–5.2.3 are compared in a study of Monte Carlo data. In particular the ‘A’ and ‘C’ jetfinders are applied in conjunction with the DURHAM algorithm to highlight the main areas where they differ from the basic clustering method. The basic JADE algorithm is included in these comparisons, despite the fact that it no longer used in analyses.

Its inclusion allows one to see how JADE compares to DURHAM in the context of this three-jet analysis.

### 5.3.1 N-Jet Rates

In this study 10 K events produced by the JETSET [33] Monte Carlo generator are clustered at an initial  $y_{\text{cut}}, y_o$ , of  $y_o=10^{-1}$ ,  $10^{-2}$  and  $10^{-3}$ . These events have not been passed through a simulation of the ALEPH detector and so represent “true” events which would be produced in  $e^+e^-$  collisions. Such events are hence known as ‘TRUTH level’ or ‘MC TRUTH’. After detector effects have been included, these Monte Carlo events are analogous to those seen in reconstructed data and are known as ‘RECO level’ or ‘MC RECO’. The JADE and DURHAM algorithms are applied in their basic form, the latter also with ‘A’ and ‘C’ jetfinders, using the E recombination scheme.

The N-jet rate is simply the fraction of events that have N jets remaining when the clustering is complete. The number of jets obtained with each jetfinder at a resolution  $y_o=10^{-2}$  is shown in table 5.2.

Algorithm	Fraction of Jets (%)				
	2	3	4	5	6
JADE	27.16±0.44	52.20±0.50	18.02±0.38	2.51±0.16	0.11±0.03
DURHAM	62.22±0.48	32.64±0.47	4.82±0.21	0.32±0.06	0.00
DURHAM ‘A’	66.03±0.47	29.99±0.46	3.72±0.19	0.26±0.05	0.00
DURHAM ‘C’	66.02±0.47	29.75±0.46	3.95±0.19	0.28±0.05	0.00

Table 5.2: The fraction of N-jet events obtained after clustering a 10 K Monte Carlo TRUTH sample with different algorithms at  $y_o=10^{-2}$ .

JADE yields a higher number of jets on average, as expected by the tendency of this algorithm to form “fake” jets from soft gluons, a feature which is repeated at any chosen  $y_o$ . Figure 5.7 shows the N-jet rates at the three resolutions.

Differences between the basic and modified jetfinders based on the DURHAM algorithm become apparent at  $y_o \lesssim 10^{-2}$ . At  $y_o=10^{-3}$  the modified jetfinders are seen to yield fewer jets due to the suppression of “fake” jet formation.

To assess the effect the choice of recombination scheme has on the jet rates the sample was clustered with the basic algorithms over a large  $y_{\text{cut}}$  range with each scheme in table 5.1. Figure 5.8 shows the difference in the average jet

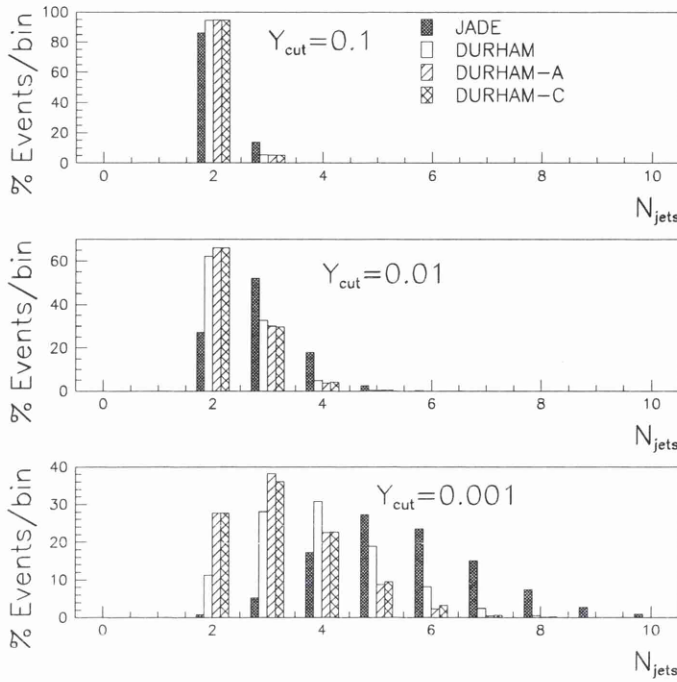


Figure 5.7: The number of jets remaining after clustering TRUTH level JETSET events at different initial  $y_{\text{cut}}$ ,  $y_0$ .

rates with scheme, showing that the rates are approximately equal in the region  $10^{-6} \lesssim y_0 \lesssim 10^{-2}$ . This difference is typically less for DURHAM above  $y_0 \sim 10^{-4}$ . The corresponding  $k_{\perp}$  between jets with this algorithm can be estimated using equation (5.5), and this is shown on the scale on the top of figure 5.8. Below  $y_0 \sim 10^{-5}$ ,  $k_{\perp} \lesssim 200$  MeV, and hadronization effects begin to dominate the showers. The ‘jets’ formed at this scale are thus likely to be separate hadrons.

### 5.3.2 Jet Widths

The angular widths of jets become important when examining reconstructed events, as those that contain jets lying close to the  $z$ -axis (*i.e.* have a low polar angle, see figure 4.3) will have a high probability of losing hadrons down the beampipe. Furthermore some low-angle particles in these jets will be badly reconstructed by virtue of not passing through the inner tracking subdetectors of ALEPH. It is therefore useful to estimate the typical angular jet size, imagining that jets take the form of a cone with an opening-angle  $\Theta_{\text{cone}}$ . Assuming that jet distributions will be similar at both TRUTH and RECO levels, TRUTH level events

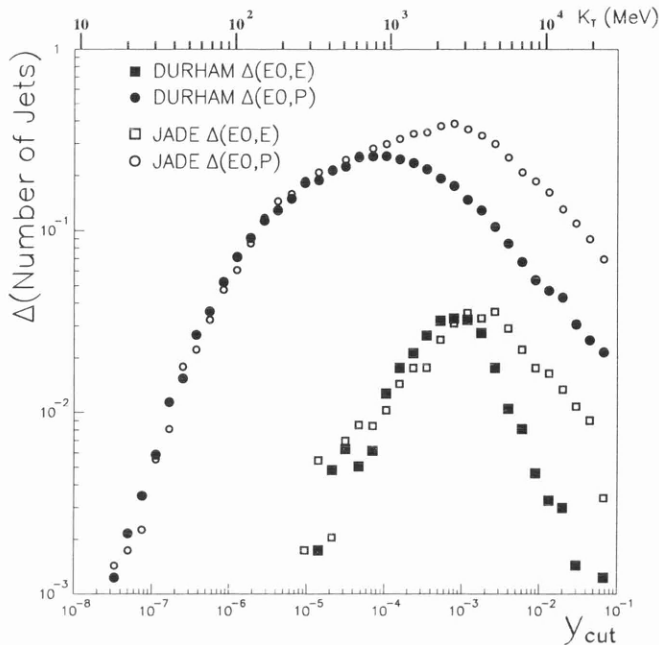


Figure 5.8: The difference in the average number of jets yielded with recombination scheme.  $\Delta(E_0, E)$  is the number of jets obtained implementing the E relative to the  $E_0$  recombination scheme *etc.* The relative transverse momentum transfer involved at each  $y_{cut}$  is given by the upper scale in MeV.

can be clustered with each jetfinder to judge angular widths in reconstructed ALEPH data. This was performed using two simple angular properties in three-jet events:

- (i) The angle of each track in a jet to the direction of the jet which is defined by the pseudo-particle formed at the end of clustering. This in effect measures the particle density across a jet and gives the fraction of particles inside a chosen opening-angle;
- (ii) The maximum angle between a pair of particles in a jet. If this pair are assumed to lie at equal angles to the jet direction then this equals  $\Theta_{cone}$ .

Figure 5.9 shows the parameters described above for each of the three jets which are ordered in energy (jet 1=maximum energy *etc.*). The upper plot indicates that the bulk of particles lie within  $\sim 40^\circ$  of the jet direction. There is little difference between basic and modified DURHAM, but the softest jet given by JADE is clearly broader. Conversely, the two other jets with this algorithm have more particles nearer the centre of the jet.

The lower plot highlights that the softest jet clustered by JADE is likely to be a “fake” jet formed from soft, large-angle particles. The hardest jet given with DURHAM has a similar  $\Theta_{\text{cone}}$  with the basic and modified jetfinders, the latter giving a slightly broader second jet and narrower third jet.

This simple study indicates that angular sizes of jets are of the order of 80-100 $^\circ$ , suggesting that jets found in data within  $\approx 40^\circ$  of the  $z$ -axis are likely to be badly reconstructed. Events containing low-angle jets should therefore be removed from further analysis by a cut on the polar angle of each jet.

### 5.3.3 Three-Jet Sample

As this analysis is concerned with the multiplicity of three-jet events, the Monte Carlo event sample was clustered at  $y_o=10^{-2}$  to select a subsample with  $N_{\text{jet}}=3$ . The energy of each jet is defined as the energy of its associated pseudo-particle. As the E recombination scheme is used on TRUTH level events the energy sum of the pseudo-particles is always equal to the centre-of-mass energy,  $\sqrt{s}=M_{Z^0}$ .

Figure 5.10 shows the energy of each jet with jetfinder. At a  $y_o=10^{-2}$  JADE gives  $\sim 60\%$  more three-jet events than DURHAM, the excess attributable to soft, “fake” jets. Because of this the two higher energy JADE jets tend to be hard and leave the third jet with only a few GeV. The energy of the softest jet yielded with DURHAM is predicted by equation (5.6) to be  $\sim 6.5$  GeV.

The charged and neutral particle multiplicities of the jets, shown in figure 5.11, are seen to be approximately equal between modified and basic DURHAM jetfinders. The JADE jets have a shortfall in multiplicity with respect to DURHAM due to the fact that a significant fraction of clustered events have no underlying hard gluon. The average jet energy and multiplicity of each three-jet sample are summarized in table 5.3.

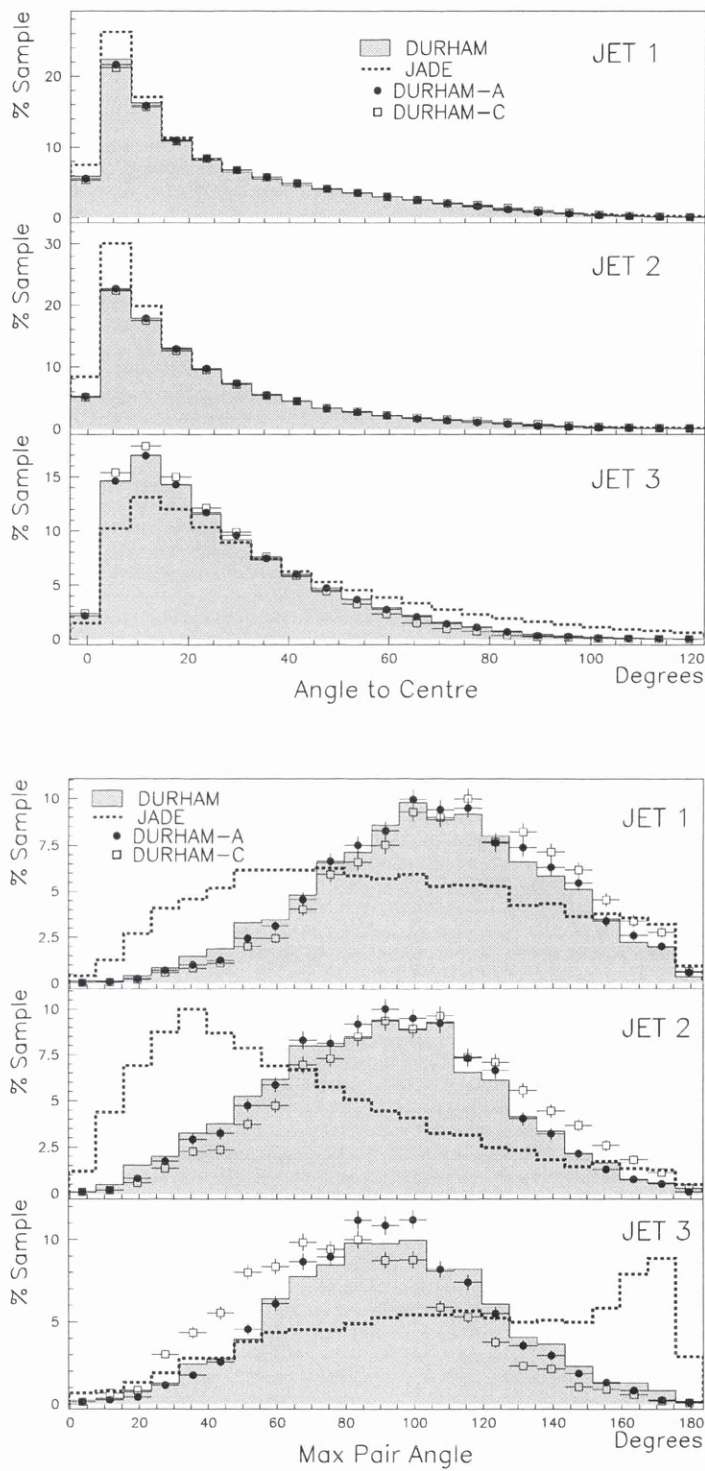


Figure 5.9: (top) The angle between each track in a jet and the jet direction and (bottom) the maximum angle between a pair of tracks in a jet. The jets are energy-ordered and result from clustering TRUTH level events at  $y_o=10^{-2}$ .

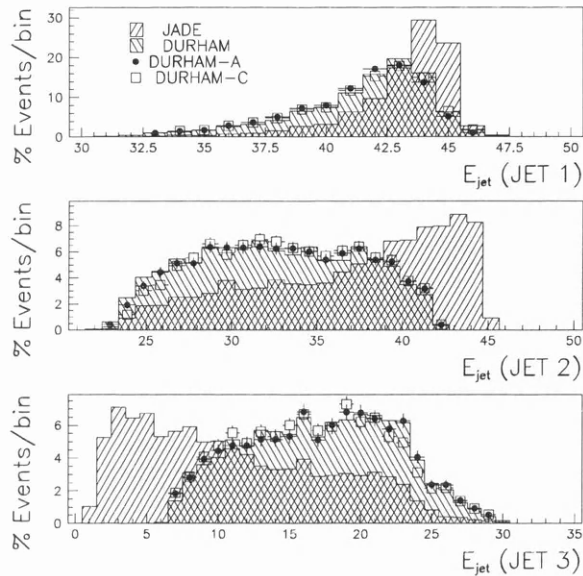


Figure 5.10: Energy in GeV of each jet in three-jet events obtained from clustering TRUTH level events at  $y_o=10^{-2}$ . The jets have been ordered in decreasing energy in each event.

		Jet (energy ordered)		
		1	2	3
$E_{\text{jet}}$	DURHAM	41.46	32.56	17.18
	DURHAM 'A'	41.20	32.79	17.20
	DURHAM 'C'	41.33	33.01	16.85
	JADE	43.12	37.07	11.01
$\langle n_{ch} \rangle$	DURHAM	10.20	9.28	7.67
	DURHAM 'A'	10.38	9.32	7.75
	DURHAM 'C'	10.51	9.50	7.40
	JADE	9.19	7.87	6.18
$\langle n_0 \rangle$	DURHAM	10.06	9.11	7.62
	DURHAM 'A'	10.26	9.22	7.60
	DURHAM 'C'	10.45	9.47	7.14
	JADE	8.97	7.77	6.39

Table 5.3: Average parameters from a three-jet Monte Carlo sample clustered at  $y_o=10^{-2}$ .  $\langle n_{ch} \rangle$  and  $\langle n_0 \rangle$  are the average charged and neutral multiplicity respectively, and energies,  $E_{\text{jet}}$ , are expressed in GeV.

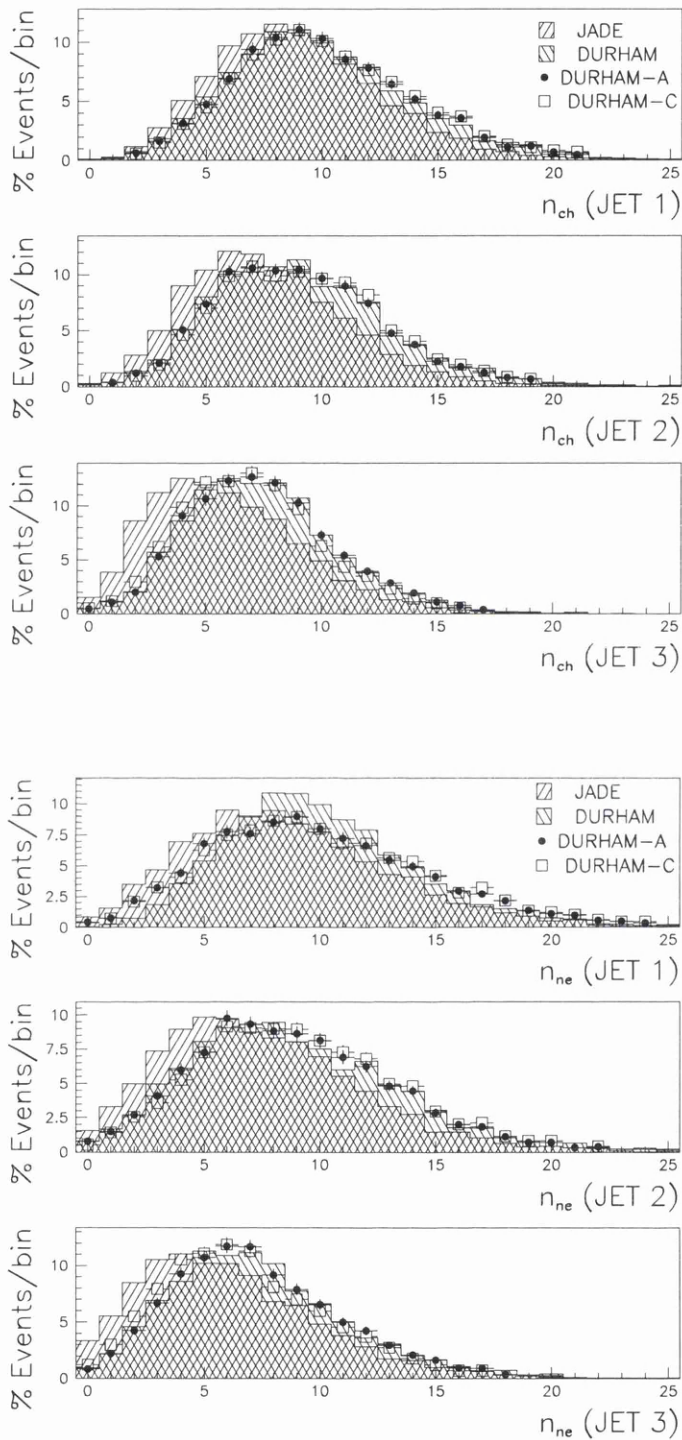


Figure 5.11: Charged (top) and neutral (bottom) particle multiplicity of each jet in three-jet events obtained from clustering TRUTH level events at  $y_0=10^{-2}$ . The jets have been ordered in decreasing energy in each event.

It is seen that, at an initial resolution  $y_o=10^{-2}$ , the number of three-jet events produced is similar for all jetfinders (when the DURHAM algorithm is applied with the E recombination scheme), and that these jets have comparable energy and multiplicity. As the ‘A’ and ‘C’ jetfinders attempt to cluster particles together in an order more representative of the true perturbative structure of a jet, then the differences between them and the basic DURHAM algorithm should become apparent when investigating subjet multiplicity. In effect, the modified jetfinders form a cascade in the reverse direction, soft low-angle radiation being grouped together to form harder subjets until eventually only one subjet remains denoting the original parent parton.

To study subjet multiplicity, the TRUTH sample is clustered with DURHAM in the simple and modified jetfinders at  $y_o=10^{-2}$ . Events with two jets are discarded, while those with four or more jets are re-clustered until three jets remain. This is carried out because it can be argued that in events with a large number of jets, the softest jets do not originate from a hard parton and should be associated with another jet in the event. Each of the three jets are then clustered at successively smaller  $y_{cut}$ ,  $y_{sub}$ , to define the subjet multiplicity.

The upper plot of figure 5.12 shows the subjet multiplicity,  $n_{sub}$ , with basic and modified jetfinders over a large  $y_{sub}$  range corresponding to a transverse momentum between subjets of  $10 \text{ GeV} \lesssim k_{\perp} \lesssim 1 \text{ MeV}$ . The difference between jetfinders is shown in the lower plot. There should be no difference in the limit  $y_{sub} \rightarrow y_o$  as here  $n_{sub}$  tends towards the average event multiplicity; however there is a constant offset at the lowest  $y_{sub}$ . This is because the basic DURHAM jetfinder produces more events with four or more jets at  $y_o=10^{-2}$  than the modified jetfinders, which have a higher average multiplicity than three-jet events. As these are included in the final sample the average multiplicity of the sample is also higher.

Large differences can be seen in the perturbative region  $y_{sub} \gtrsim 10^{-4}$  where the  $k_{\perp}$  between particles is above  $\sim 1 \text{ GeV}$ . It is in this exact region where the modifications are designed to reorder the clustering.

### 5.3.4 TRUTH/RECO levels

It is inevitable that an event reconstructed in the ALEPH detector will have lost, mis-identified or badly-measured particles. As a consequence, the visible energy in the event is unlikely to be equal to the centre-of-mass energy, and the defined jets will not be in the same direction as the hard partons produced in the initial  $e^+e^-$  reaction.

To correct ALEPH data for such detector effects it is necessary to perform

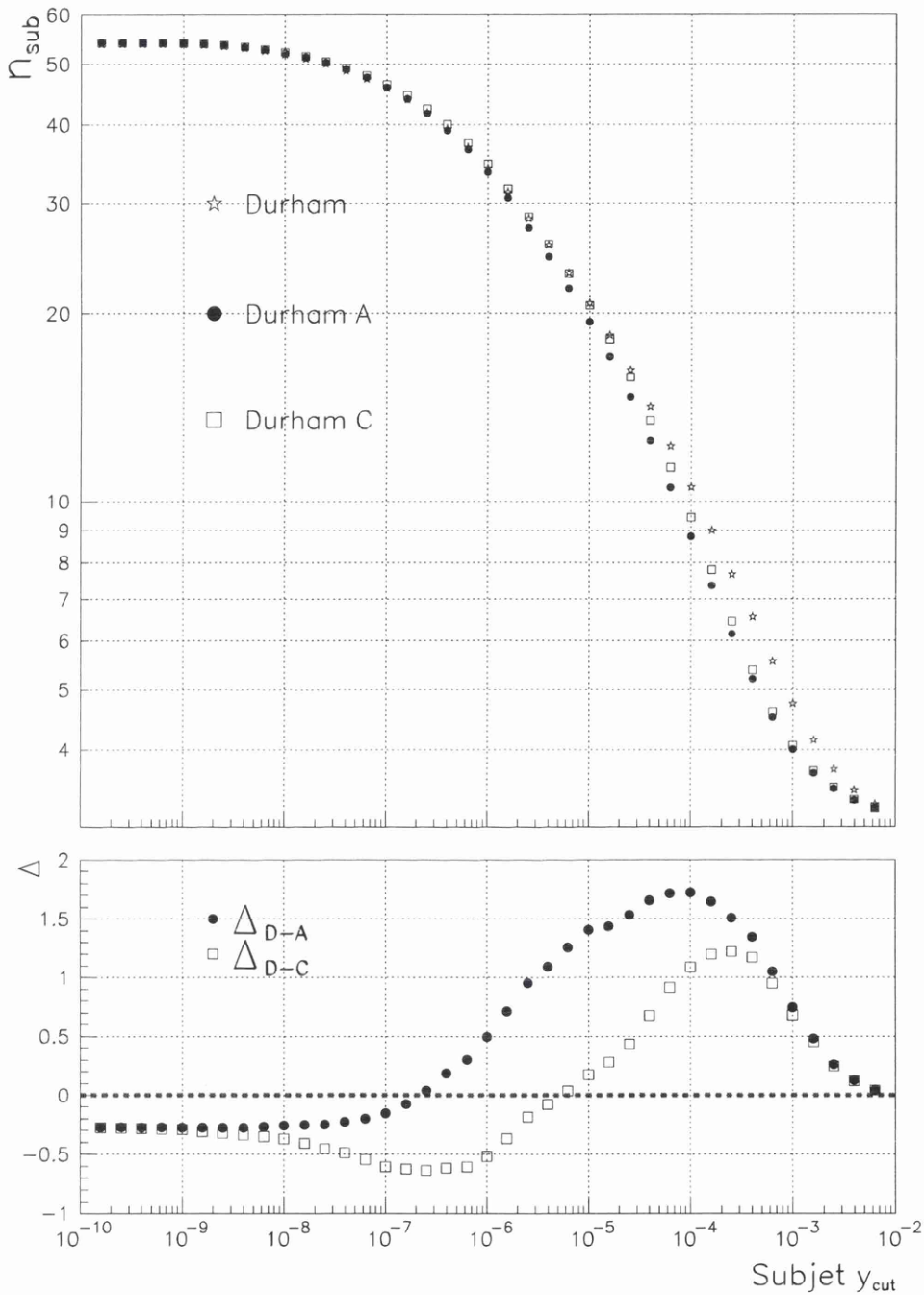


Figure 5.12: The number of subjets,  $n_{sub}$ , obtained with subjet  $y_{cut}$  with the basic and modified DURHAM algorithms. The lower plot shows the difference at each  $y_{cut}$  between DURHAM and DURHAM-‘A’ ( $\Delta_{D-A}$ ) and DURHAM-‘C’ ( $\Delta_{D-C}$ ).

the analysis chain on Monte Carlo generated data and match TRUTH level jets with their closest neighbours at RECO level. If the number of jets at each level is different the method of matching becomes ambiguous. A similar problem is encountered when estimating hadronization effects by comparing jet distributions at parton and hadron levels.

To test the applicability of the JADE and DURHAM algorithms for detector corrections they are employed, in their basic mode, to cluster JETSET Monte Carlo events at both TRUTH and RECO level. A large range of  $y_{\text{cut}}$  is covered and the E scheme used to keep the clustering invariant.

Figure 5.13 shows the average number of jets obtained at each level with  $y_{\text{cut}}$ . As  $y_{\text{cut}} \rightarrow 10^{-8}$  the number of resolved jets becomes large and the limiting value of the average particle multiplicity is approached. Several conclusions can be drawn from this plot:

- (i) The difference between TRUTH and RECO level is more pronounced for JADE and appears at a higher  $y_{\text{cut}}$ , again highlighting the fact that DURHAM is best suited for this analysis.
- (ii) Detector effects such as track loss and smearing have little effect on the number of resolved jets for DURHAM at  $y_{\text{cut}} \geq 5 \times 10^{-5}$ . This is the range commonly used to select three-jets and study their perturbative structure.
- (iii) Little clustering takes place for reconstructed hadrons when  $y_{\text{cut}} \leq 10^{-7}$ . This implies a detector resolution  $\sigma_{P_{\perp}} \approx 10\text{--}20$  MeV.

Figure 5.14 shows the N-jet rates, where  $N = (1, 2, 3, 4, 5, \geq 6)$  in the resolution range  $10^{-4} \leq y_{\text{sub}} \leq 10^{-1}$ . At  $y_{\text{cut}} \sim 10^{-3}$  half of all events have six or more jets when clustered with JADE, but with DURHAM this fraction is reduced to about a tenth. The close agreement with TRUTH level data over the full  $y_{\text{cut}}$  range suggests that detector effects are small when considering low-jet rates at  $y_{\text{cut}} \geq 10^{-4}$ .

## 5.4 Summary

In this section it has been seen that, due to the nature of the JADE algorithm the three jet sample it produces has a poorer energy and multiplicity resolution than a sample obtained with the DURHAM algorithm. For this reason, and the fact that hadronization and detector corrections are expected to be smaller for DURHAM than for JADE, the former algorithm is chosen in this analysis.

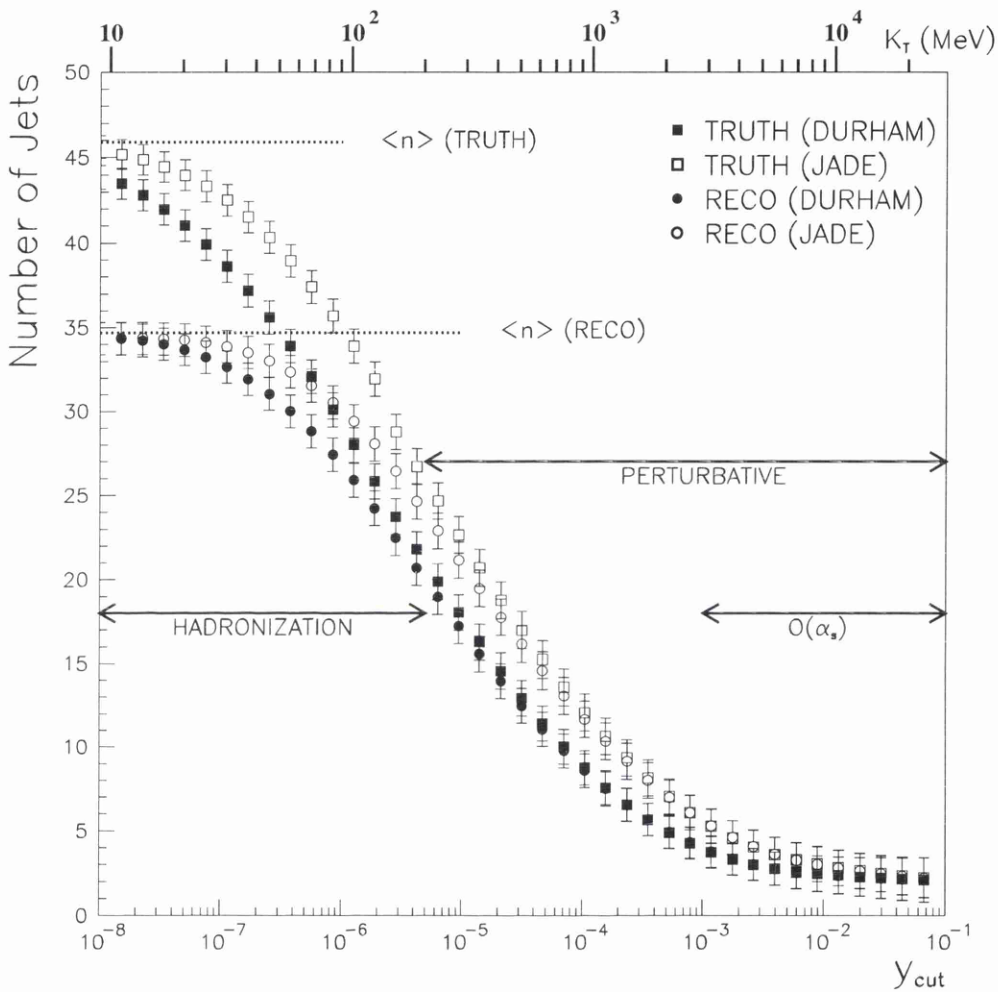


Figure 5.13: The number of jets yielded after clustering a Monte Carlo sample at both TRUTH and RECO levels at a chosen  $y_{\text{cut}}$ . The DURHAM and JADE algorithms are used with the E recombination scheme, and the relative transverse momentum transfer involved at each  $y_{\text{cut}}$  is given by the upper scale in MeV.

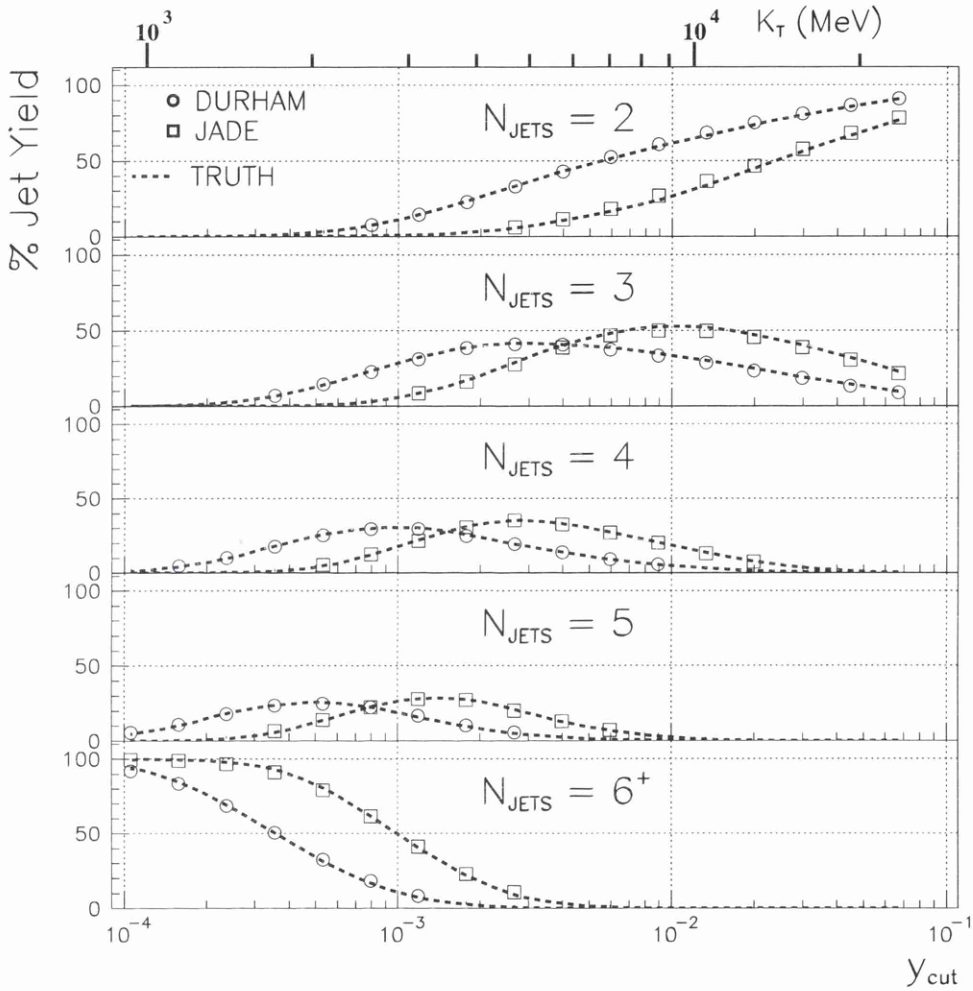


Figure 5.14: The percentage of  $N$ -jet events obtained with  $y_{\text{cut}}$  at RECO level with the DURHAM (circle) and JADE (square) algorithms. The dotted curves show the jet rates at TRUTH level, and the relative transverse momentum transfer involved at each  $y_{\text{cut}}$  is given by the upper scale in MeV.

When the ‘A’ and ‘C’ jetfinders are applied to the basic DURHAM algorithm similar jet energies and multiplicities result. However, the subjet multiplicity is seen to be very jetfinder-dependent and the effect this has on subjet distributions binned across the Dalitz plane will be assessed in the later chapters.

# Chapter 6

## Reconstructed Jet Resolutions

### 6.1 Introduction

The position of a three-jet event in the Dalitz plane is uniquely specified by the energies of the jets. If errors on measured energies are large, then events will be incorrectly binned, making any variations in multiplicity over the plane difficult to observe. It is therefore important that jet energies are defined as accurately as possible. The widths of the Dalitz bins on the plane should be made of the same order as the average errors on jet energy measurements. Binning on the Dalitz plane in this way benefits if the energy sum over the jets is the same for every event. In practice, the loss and smearing of tracks in reconstructed events means that jets rarely have the same energy or multiplicity as the underlying ‘true’ jets. Sophisticated Monte Carlo generators and detector simulations are required to produce events at TRUTH level, which are then passed through an approximation of the ALEPH detector, to give RECO level events which should be comparable to events observed at ALEPH. From Monte Carlo studies, ALEPH data distributions can be then “unfolded” to give the actual distributions prior to passing through the detector.

### 6.2 Jet Energy Estimators

In a reconstructed hadronic event at LEP I, the sum of the energies of all final state hadrons can be anywhere from 20–120 GeV. The average sum is  $\sim 86$  GeV, so that reconstructed jets are softer on average than their ‘true’ counterparts. The hadronic energy of each jet at RECO level, known as the ‘visible’ energy, is denoted in this chapter by  $E_{\text{vis}}$ . The sum of  $E_{\text{vis}}$  over all jets in a three-jet event, as

mentioned above, is not always equal to the centre-of-mass energy,  $\sqrt{s}=91.2$  GeV. A simple definition of jet energy that ensures an equal sum over all jets is obtained by multiplying each visible energy by a factor,  $\lambda$ , where  $\lambda \sum_{i=1}^3 E_{\text{vis}}^i = \sqrt{s}$ , to form a *scaled* energy,  $E_{\text{scale}}$ .  $E_{\text{scale}}$  is defined as  $E_{\text{scale}} = \lambda E_{\text{vis}}^i$  with  $i=(1,2,3)$  so that, trivially,  $\sum_{i=1}^3 E_{\text{scale}}^i = \sqrt{s}$ . This definition has the problem that if a hard particle is lost from one jet, then the energies of the two other jets must increase to compensate. In some cases, a scaled jet energy can become greater than  $\sqrt{s}/2$ , so that the event will be placed outside the limits of the Dalitz plane.

A better approximation should exploit the fact that particles in a jet tend to be highly collimated. Loss of a single particle will not result in a great deviation of the jet direction, and furthermore, multiple losses have a high probability of at least partially cancelling. Interjet angles,  $\theta_j$  ( $j=1,2,3$ ), should therefore give a more robust guide to the underlying parton energies. *Lamy's theorem* can be applied to give an angular estimate,  $E_{\text{Lamy}}^j$ , of the jet energies using the interjet angles:

$$E_{\text{Lamy}}^j = \sqrt{s} \cdot \frac{\sin \theta_j}{\sum_{i=1}^3 \sin \theta_i} \quad j = (1, 2, 3) . \quad (6.1)$$

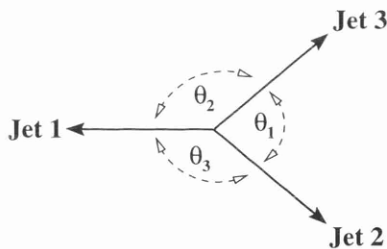


Figure 6.1: The interjet angles in a three-jet event.

The requirement that the energy sum be constant is trivially satisfied. With this definition the jet energies are still correlated. If a single jet becomes deviated at RECO level, then two of the interjet angles in fig. 6.1 will change so that the energy of all the jets will also change. For example, consider a Mercedes event, which has exactly  $120^\circ$  between each (massless) jet of 30.4 GeV. If, after passing through the detector, one of jets is reconstructed at  $5^\circ$  (say) from its true direction, equation (6.1) gives the jet energies as 30.5, 28.8 and 31.9 GeV, despite only one of the jets being incorrectly reconstructed.

It is important to note that equation (6.1) is only valid if the three jets are both *planar* and *massless*. The first condition can be met if the jets are projected

onto a plane defined using the momentum tensor  $T^{\alpha\beta}$ , where

$$T^{\alpha\beta} = \frac{\sum_i p_i^\alpha p_i^\beta}{\sum_i p_i^2}, \quad (6.2)$$

$\alpha, \beta = (x, y, z)$  and  $p_i^\alpha$  is a single momentum component of the  $i$ th particle in the event. The eigenvalues of this tensor, when ordered in size, correspond to three vectors defining the *major*, *semi-major* and *minor* axes of the event. The cross product of the major and semi-major axes defines a normal to the event plane. The angles between jets projected onto this plane are used with equation (6.1) to define a ‘planar’ energy estimate,  $E_{\text{Lamy}}^P$ .

In reality jets are massive, and a better estimate of jet energy should be given by a definition which takes masses into account. As the E recombination scheme is adopted in this analysis, the jets masses are calculated during jetfinding by keeping the clustering invariant (see section 5.2, table 5.1). To incorporate these masses, an iterative Newton-Raphson method is employed as follows. An initial estimate for each jet  $j$  is constructed in terms of the massless estimator, given by equation (6.1), and the jet mass,  $M$ :

$$\left(E_{\text{Lamy}}^M\right)_j = \sqrt{\frac{\lambda}{s} \left(E_{\text{Lamy}}\right)_j^2 + M_j^2}, \quad (6.3)$$

where  $j=(1,2,3)$  and  $\lambda$  is the minimising variable, which is set equal to  $s$  in the first iteration. For each iteration the quantities  $\delta_E$ ,  $G$  and  $\Delta$  are calculated, where

$$\begin{aligned} \delta_E &= \sum_{j=1}^3 \left(E_{\text{Lamy}}^M\right)_j - \sqrt{s}, \\ G &= \frac{1}{s} \sum_{j=1}^3 \frac{\left(E_{\text{Lamy}}\right)_j^2}{\left(E_{\text{Lamy}}^M\right)_j}, \\ \Delta &= 2 \frac{\delta_E}{G}. \end{aligned}$$

After each iteration the variable  $\lambda$  is decremented by an amount  $\Delta$ , each  $E_{\text{Lamy}}^M$  recalculated by equation (6.3), and the process repeated. Iterations cease when either an imposed limit on the number of iterations is reached, or the difference between successive  $E_{\text{Lamy}}^M$  are less than one part in  $10^5$  for each jet.

To prove the stability and applicability of this method, massless Lamy estimates for TRUTH level jets are input along with the masses given by the basic DURHAM jetfinder. After 3–5 iterations the massive estimates become stable and are equal, within the specified tolerance, to the ‘true’ energies of the jets. The Newton-Raphson method is repeated with the ‘planar’ energies,  $E_{\text{Lamy}}^P$ , to give a final jet energy estimator,  $E_{\text{Lamy}}^{PM}$ .

### 6.3 The ‘Resolution Sample’

To compare the energy estimators described in the last section, 100 000 JETSET Monte Carlo events are processed to give a three jet sample at both TRUTH and RECO levels. All RECO events that pass the general hadronic selection<sup>1</sup> are clustered with the jetfinders described in chapter 5. A  $y_{\text{cut}}$  of  $10^{-2}$  is chosen, as this gives an appreciable yield of three-jet events that correspond to topologies which populate the whole Dalitz plane, which is described in section 3.3.3. The DURHAM and JADE jetfinders are used to compare energy and multiplicity resolutions in the three-jet events they select. The DURHAM jetfinder is used in the basic, ‘A’ and ‘C’ forms.

RECO level events that are clustered to two jets are discarded, those with four or more jets re-clustered until only three remain. The same clustering process is then repeated on the TRUTH level event. One is faced with the situation that the number of jets obtained at each level may not be the same, for example a three-jet event at RECO level may only be a two-jet event at TRUTH level or *vice versa*. In this study, events are classified according to a *jetclass*, which depends on the relative number of jets obtained at each level. Table 6.1 gives the possible values of the *jetclass*, which are shown pictorially in figure 6.2.

<i>Jetclass</i>		$N_{jet}(\text{RECO})$	$N_{jet}(\text{TRUTH})$	Events (%)
1	PURE	3	3	26.1
2	IMPURE	4,5,6,...	3	1.5
3	IMPURE	3	4,5,6,...	1.8
4	HIGH	4,5,6,...		3.2
5	2-JET	2	2	58.0
6	R-LOSS	3,4,5,...	2	3.7
7	T-LOSS	2	3,4,5,...	5.8

Table 6.1: Events classified according to the number of jets,  $N_{jet}$ , obtained at RECO and TRUTH levels. The final column gives the approximate percentage of events in each class using the basic the DURHAM algorithm.

<sup>1</sup>These cuts are a set of standard hadronic selection criteria applied in ALEPH jet analyses. They are described in chapter 7.

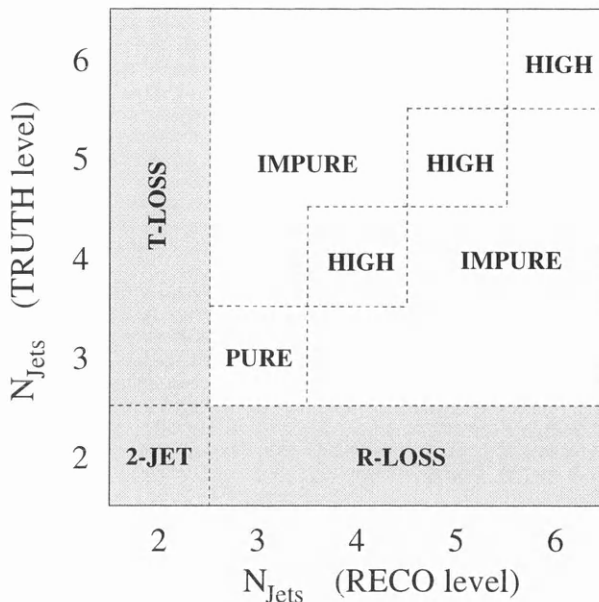


Figure 6.2: The jetclass shown as areas on a plot of the number of jets obtained at RECO and TRUTH levels. Events lying in the shaded areas are excluded from this resolution study.

About a quarter of events are “PURE” three-jet events, *i.e.* there are three jets defined at both Monte Carlo levels. Events with two jets at each level (“2-JET”) are automatically discarded. Approximately one in ten events have three or more jets at one level, but only two at the other. In such cases, forcing the two-jet event into a three-jet configuration tends to result in a very soft third jet being defined, so that the correspondence between levels is poor. For this reason, the “R-LOSS” and “T-LOSS” classifications are excluded from this study.

In events where four or more jets are obtained, the pseudo-particles output from the jetfinder are re-clustered until only three remain. Clustering to three jets is trivial with the basic DURHAM and JADE jetfinders, as the pairing order is uniquely specified for a given event: tracks are combined in a strict order, irrespective of the chosen  $y_{\text{cut}}$ , until the required number of pseudo-particles remain. However, with the ‘A’ and ‘C’ jetfinders, the order in which particles are paired is a function of  $y_{\text{cut}}$ . This is because the ordering variable is the angle and not the value of  $y_{ij}$  between particles. To force ‘A’ and ‘C’ events to have three jets one could lower the  $y_{\text{cut}}$  and repeat the clustering until three jets are obtained. Apart from being time consuming there are some events where it is impossible to arrive at a given number of jets whatever the  $y_{\text{cut}}$ . This peculiarity has been assessed in a recent study [81], which also points out that the number

of jets need not increase monotonically with decreasing  $y_{\text{cut}}$ , so that an event can sometimes be clustered into two completely different three-jet configurations. Because of these problems, during re-clustering the pseudo-particles output from the initial clustering at  $y_0$  are always input into the basic jetfinder to obtain a three-jet configuration. The “IMPURE” and “HIGH” classifications result when events at one or both levels have been re-clustered.

Figure 6.3 shows the number of events in each jetclass for the first 10000 events clustered with each jetfinder. It can be seen that only  $\sim 85\%$  and  $\sim 70\%$  of events have the same number of jets at each level with DURHAM and JADE respectively. This figure is slightly higher ( $\sim 88\%$ ) with the modified algorithms, although there are less events with three jets at each level.

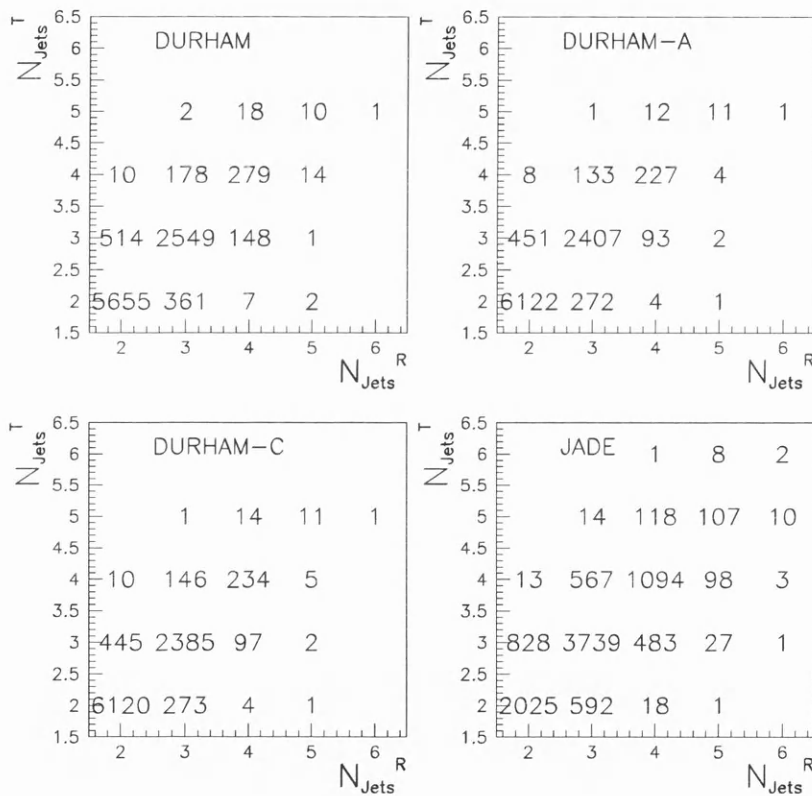


Figure 6.3: The number of jets yielded at RECO and TRUTH level after clustering 10000 Monte Carlo events at  $y_0=10^{-2}$ .

In the next step of the study, jets at TRUTH level are *matched* to jets at RECO level. To do this, the hardest TRUTH jet is first paired with the reconstructed jet that lies closest in angle. The other two jets are then associated by selecting the combination which minimizes the sum of opening angles between the jets at each level. The energy and multiplicity resolutions of jets selected with each

jetfinder can now be compared. Table 6.2 summarises some average properties of the three-jet sample obtained with the basic DURHAM jetfinder.

	Jet 1	Jet 2	Jet 3	Event
$\langle E_{VIS} \rangle$	41.2 (38.2)	32.4 (28.4)	17.7 (15.6)	91.2 (82.3)
$\langle n_{ch} \rangle$	10.6 (8.2)	9.3 (7.1)	7.7 (5.6)	27.6 (20.8)
$\langle n_0 \rangle$	10.6 (7.8)	9.3 (6.7)	7.6 (5.0)	27.5 (19.6)
$\langle n_{tot} \rangle$	20.7 (16.0)	18.5 (13.7)	15.3 (10.6)	55.1 (40.4)
$\langle \text{mass} \rangle$	12.7 (10.4)	9.4 (7.6)	6.8 (5.2)	28.9 (23.3)
$\langle \theta_Z \rangle$	54.4 (57.1)	54.5 (58.1)	58.1 (57.2)	166.9 (172.5)
$\langle \theta_P \rangle$	0.0 (1.8)	0.0 (2.6)	0.0 (5.6)	0.0 (10.0)
	Jet 1 $\rightarrow$ 2	Jet 2 $\rightarrow$ 3	Jet 3 $\rightarrow$ 1	Total
$\langle \theta_{\text{interjet}} \rangle$	131.1 (126.6)	157.8 (153.0)	71.16 (78.5)	360.0 (358.5)
	Jet 1	Jet 2	Jet 3	Total
$\langle \theta_{\text{match}} \rangle$	3.1	3.3	4.8	10.8

Table 6.2: Average event and jet properties in three-jet events obtained with the basic DURHAM jetfinder. Jets in each event have been ordered in decreasing TRUTH level energy; the figures in brackets correspond to RECO level events. The table shows the following properties: Visible energy (GeV); Charged, neutral and total multiplicity; Mass ( $\text{GeV}/c^2$ ); Polar angle,  $\theta_Z$ ; Angle to the plane defined in equation (6.2),  $\theta_P$ ; Interjet angles,  $\theta_{\text{interjet}}$ , and angles between the matched TRUTH and RECO jets,  $\theta_{\text{match}}$ . All angles are expressed in degrees.

## 6.4 Energy Resolution

The jet energy resolution is defined as the energy *estimated* at RECO level,  $E_{\text{RECO}}$ , minus the *actual* energy at TRUTH level,  $E_{\text{TRUTH}}$ .  $E_{\text{RECO}}$  is calculated with each of the estimators described in section 6.2. The energy resolution with each estimator is compared in figure 6.4. For each event, the three jets are ordered according to their ‘true’ energy and the resolutions calculated for each jet separately.  $E_{\text{vis}}$  and  $E_{\text{scale}}$  offer a very poor resolution as expected by the arguments of section 6.2. The estimators based on interjet angles provide a much better resolution, which

are approximately Gaussian with a width of  $\sim 2$  GeV for jet 1,  $\sim 3$  GeV for jet 2 and  $\sim 4$  GeV for jet 3.

The best resolutions are obtained by estimators which incorporate the jet masses, whereas no significant improvement is obtained by projecting the jets onto a single plane. This is because the sum of interjet angles, as indicated in table 6.2, is always close  $360^\circ$ . The limited gain in calculating the plane and projecting the jets onto it is deemed unnecessary for the analysis.

The energy resolution of jets, in events defined by each jetfinder, is compared in figure 6.5, where the estimator  $E_{\text{Lamy}}^M$  has been used. Jets defined with the JADE algorithm give a poorer resolution than jets defined with DURHAM. The difference between the basic and modified schemes is much smaller, as the energy distributions of the jets they define are similar, as shown previously in figure 5.10.

## 6.5 Multiplicity Resolution

Three-jet events selected in RECO level data are expected, on average, to have a shortfall in multiplicity with respect to corresponding TRUTH level events. On average, approximately one in four tracks are lost or excluded during reconstruction. Figure 6.6 shows the charged particle resolution for jets defined with each jetfinder. The resolution is defined as the multiplicity of a jet at RECO level minus that at TRUTH level. As the multiplicity distributions obtained with the basic and modified DURHAM jetfinders are very similar, see figure 5.11, there is little difference between the charged particle resolutions of these jetfinders. Figure 6.6 shows that jets selected with the JADE algorithm have a similar charged particle resolution to those selected with either of the DURHAM variants.

## 6.6 Resolution With $\theta_Z$

In section 5.3.2 it was estimated that most particles within a jet lie in a cone, centred on the jet direction, of half-angle  $\sim 30\text{--}40^\circ$ . One therefore expects that if the angle of a reconstructed jet to the  $z$ -axis,  $\theta_Z$ , is greater than  $40^\circ$ , then a high proportion of the particles in that jet will pass through the ALEPH subdetectors and have a high probability of being accurately reconstructed. The energy and multiplicity resolution of jets should therefore improve as  $\theta_Z$  increases. To test this hypothesis, the hardest jet in three-jet events clustered with the basic DURHAM algorithm are examined. The energy and multiplicity resolution is calculated for

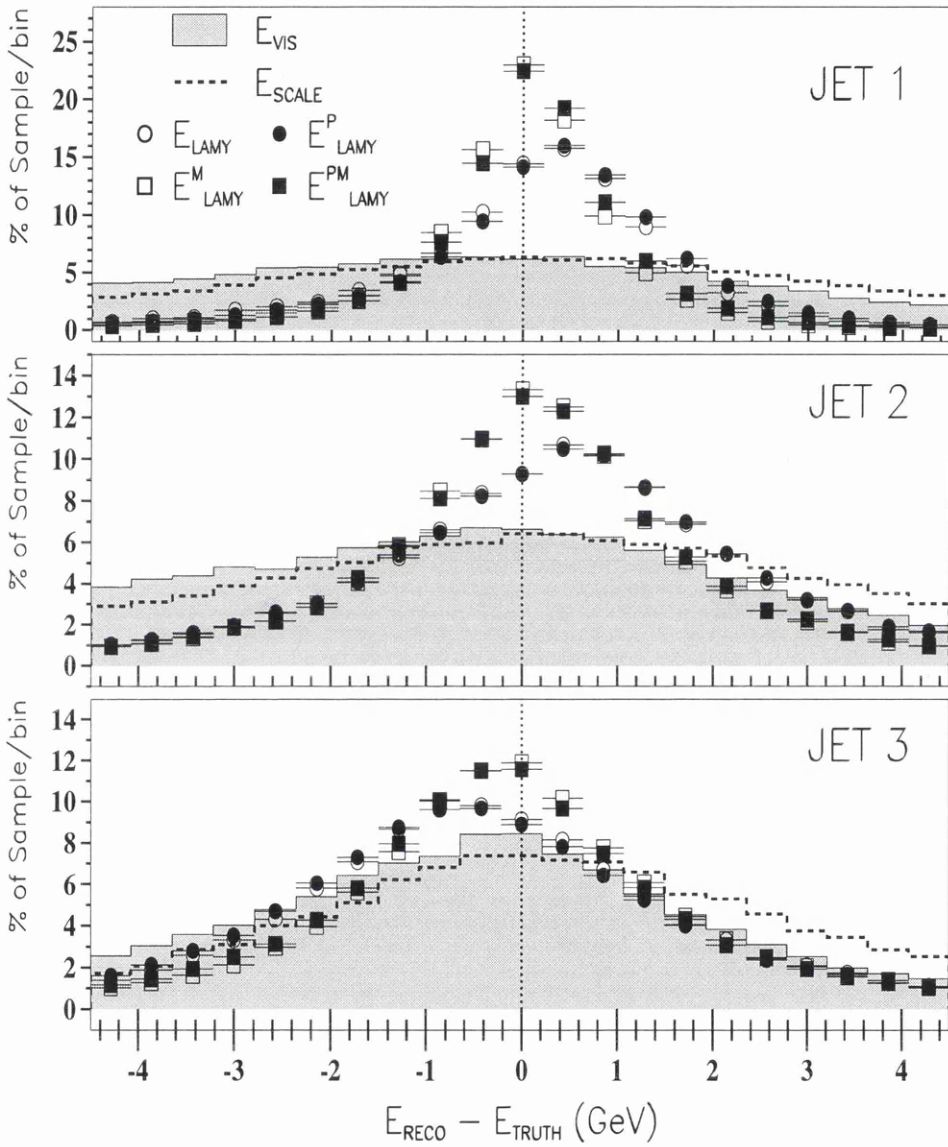


Figure 6.4: Jet energy resolution with several estimators. The jets are defined using the basic DURHAM algorithm, and the jets in each event have been ordered in decreasing TRUTH level energy.

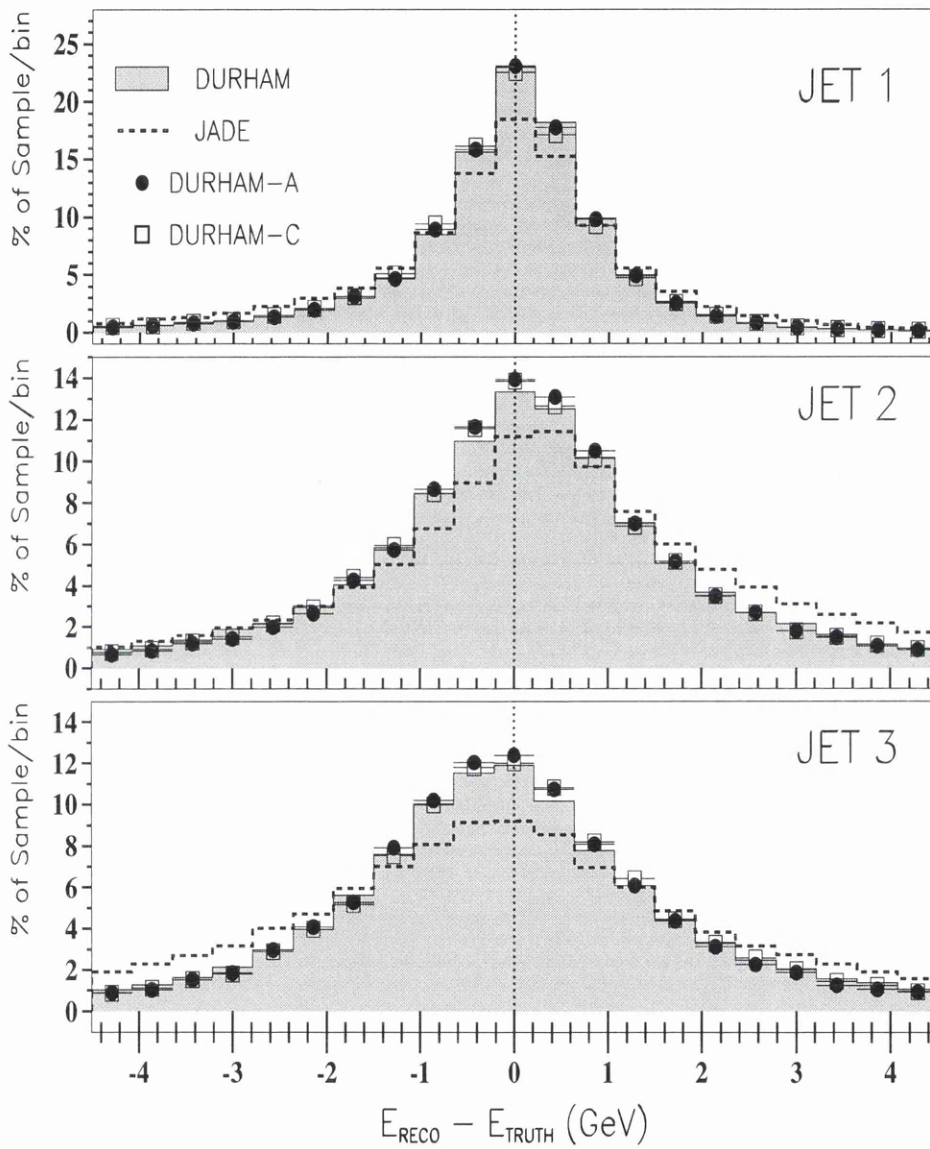


Figure 6.5: Jet energy resolution of the  $E_{\text{Lamy}}^M$  estimator, where the jets are defined using different jetfinders. The jets in each event have been ordered in decreasing TRUTH level energy.

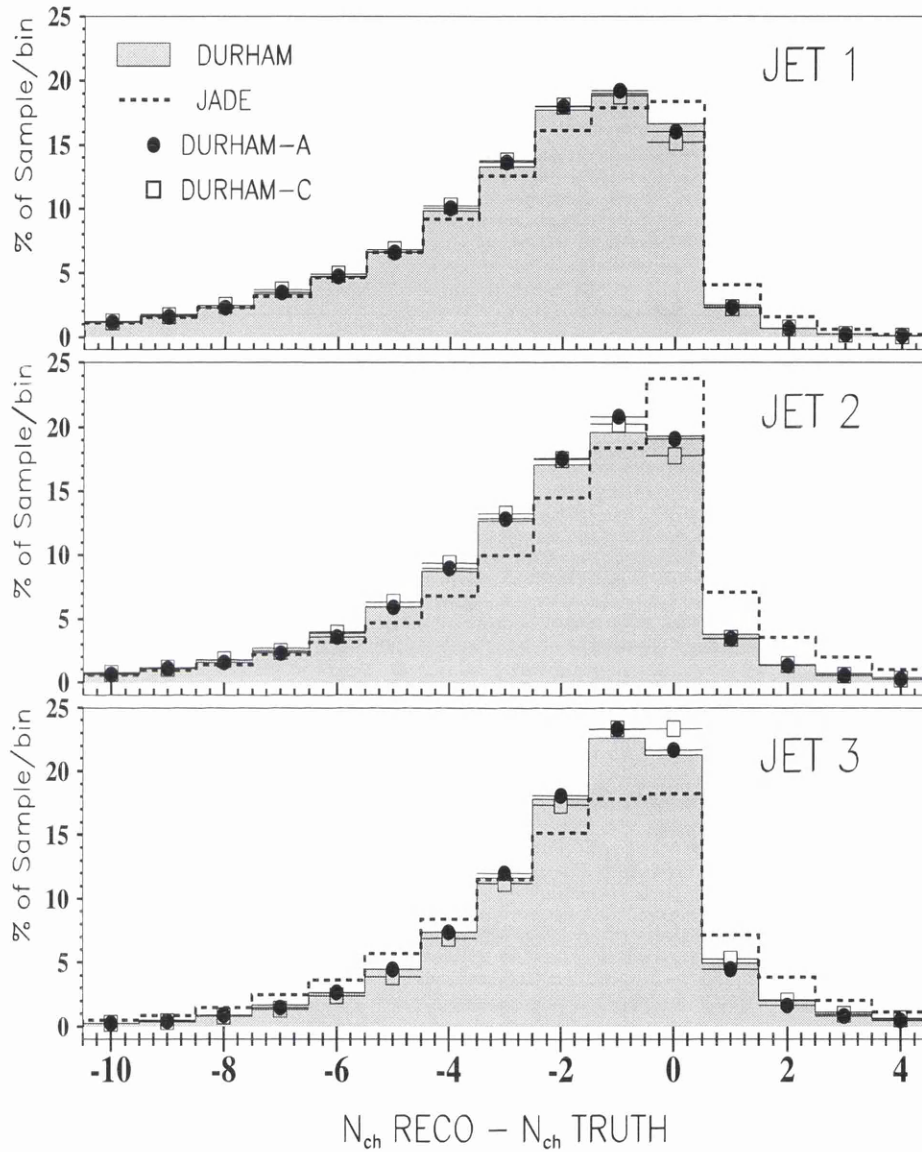


Figure 6.6: Charged particle multiplicity resolution of jets defined by different jetfinders. The jets in each event have been ordered in decreasing TRUTH level energy.

jet subsamples which lie at angles greater than a chosen cut value. Table 6.3 shows the fraction of jets that are included at several  $\theta_Z$  cut values.

$\theta_Z$ Cut	Events included (%)
$0^\circ$	100.0
$10^\circ$	99.8
$20^\circ$	98.4
$30^\circ$	87.8
$40^\circ$	74.4
$50^\circ$	60.0
$60^\circ$	44.8
$70^\circ$	29.7
$80^\circ$	14.8

Table 6.3: The fraction of jets included when a cut on the polar angle of the jet,  $\theta_Z$ , is imposed.

### Energy Resolution

Figure 6.7 shows the jet energy resolution at cut values of 0, 20, 40 and  $60^\circ$ . A significant improvement in resolution is obtained when the  $\theta_Z > 40^\circ$  is imposed. When a stricter cut of  $\theta_Z > 60^\circ$  is used, the additional improvement is relatively small. A way to estimate an optimum cut value is to consider the fraction of jets that have an energy resolution,  $\Delta E = E_{\text{RECO}} - E_{\text{TRUTH}}$ , inside a given range or ‘resolution window’. As the angular cut is increased, the number of jets remaining for analysis falls, but the fraction of the surviving sample that lies within a given resolution window should increase. Figure 6.8 shows this fraction, for each jet in a three-jet event, with  $\theta_Z$  cut for windows of width 1 GeV, 2 GeV, 4 GeV, 6 GeV and 10 GeV.

Clearly the proportion in a window will rise as the window size is increased, but in each window the general trend is an increase in the fraction of events within the window as the  $\theta_Z$  cut is increased. At  $\sim 40^\circ$  (indicated by the vertical dashed lines) there is a marked step in the distributions for each jet in every window. This suggests that most particles in a jet lie within  $\sim 40^\circ$  of the jet direction, an observation that is in agreement with the estimate of jet widths in section 5.3.2.

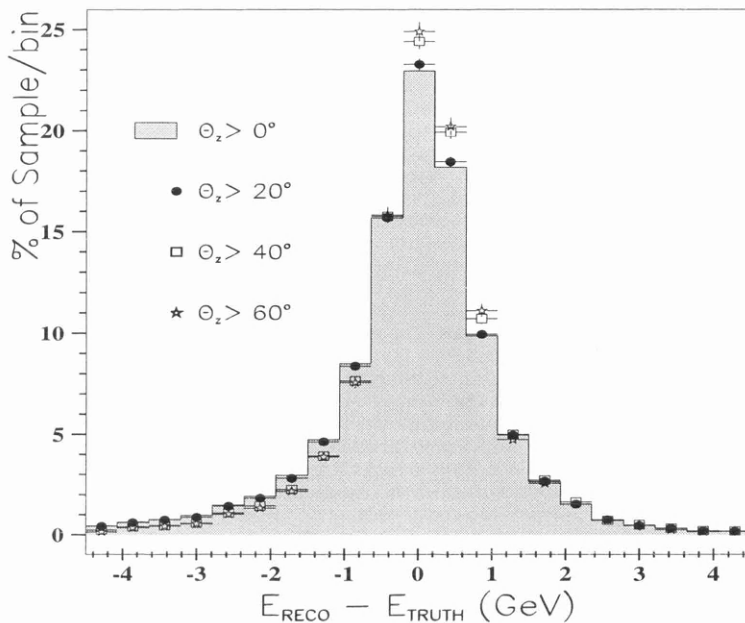


Figure 6.7: The energy resolution of the hardest jet in a three-event, selected with the basic DURHAM jetfinder, with angular cut,  $\theta_Z$ .

### Charged Particle Resolution

The charged particle resolution for subsamples of jets, obtained with a  $\theta_Z$  cut of 0, 20, 40 and  $60^\circ$ , are shown in figure 6.9. As with the energy resolution, shown in figure 6.7, a marked improvement is seen when the cut is set to  $40^\circ$ . As this cut value is increased to  $60^\circ$ , further improvement is obtained as more jets have the same number of particles before and after reconstruction.

## 6.7 Summary

In this section the effect of the ALEPH detector on the energy and multiplicity resolution of jets obtained with different jetfinders has been examined. Several methods of estimating reconstructed jet energies have been investigated, assuming either planar/non-planar and/or massless/massive kinematics. When jet masses are considered, the energy resolution of the jets is improved, especially for the hardest jet in an event. Projecting the jets onto a single plane, however, has a minor effect on the energy resolution.

Jets selected with the DURHAM algorithm have a superior energy resolution

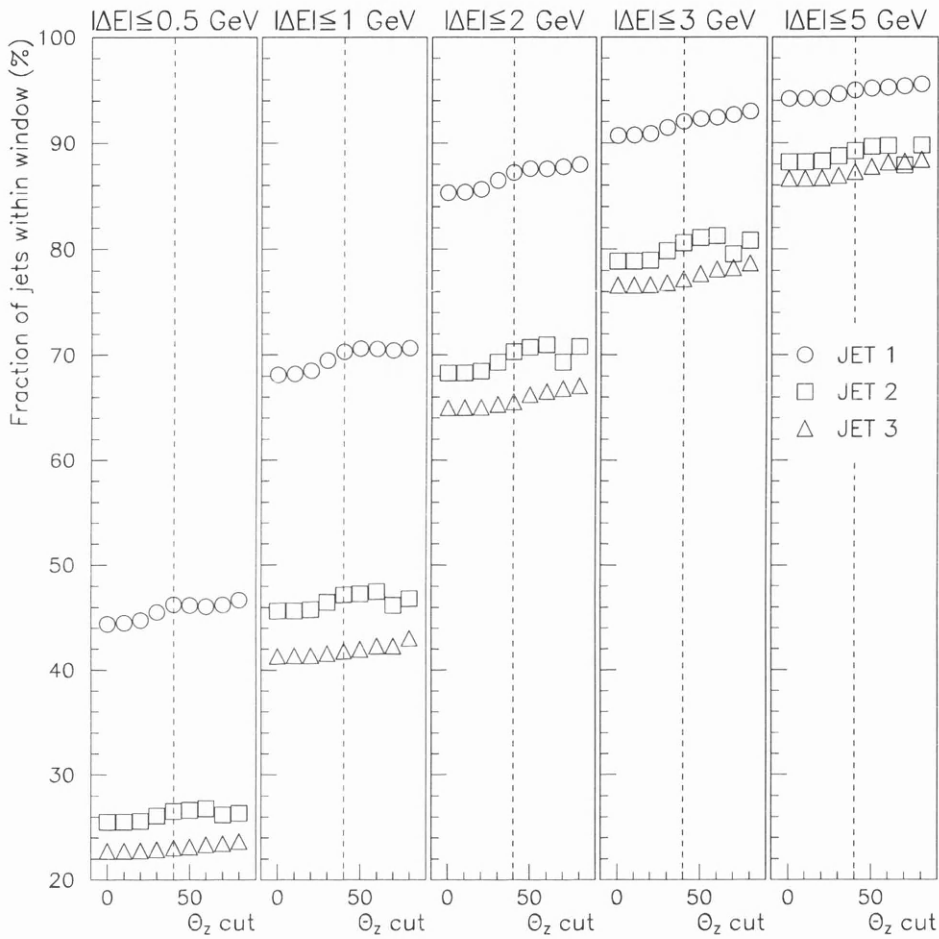


Figure 6.8: Fraction of events that have an energy resolution lying inside a given window, given a cut on the polar angle  $\theta_z$ . The fraction at each cut value is normalized to the total number of events that survive the cut.

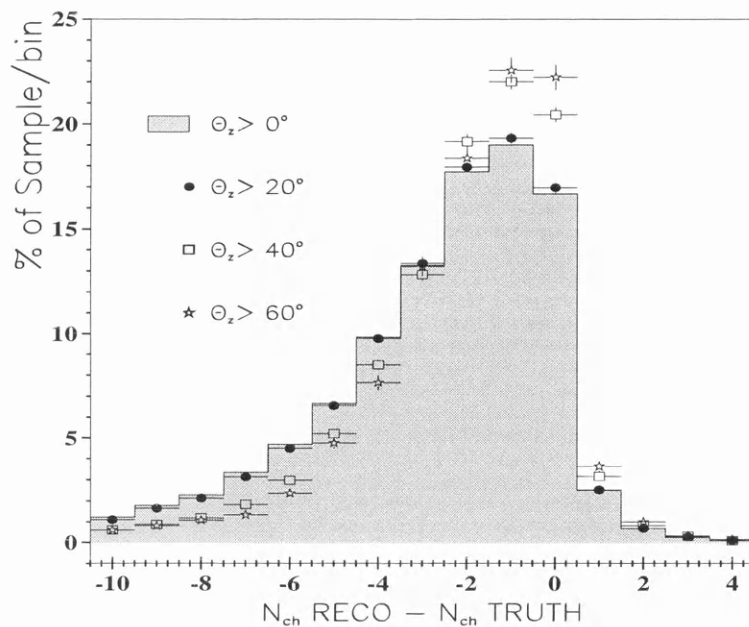


Figure 6.9: The charged particle resolution of the hardest jet in three-jet events, given various angular cuts.

with respect to those selected with JADE, although the multiplicity resolution is more equal between algorithms. The introduction of a cut on the angle a jet subtends to the  $z$ -axis,  $\theta_Z$ , gives an improvement in the energy and multiplicity resolutions when the cut is at or above  $40^\circ$ . Better resolutions are possible at higher angular cuts, but the number of events remaining to be binned on the Dalitz plane falls rapidly with cut. The optimum value appears to be  $\theta_Z > 40^\circ$  for this analysis.

# Chapter 7

## Event Selection

This chapter describes the selection of a three-jet event sample from data collected by the ALEPH detector during the period 1990–95. To ensure only hadronic events are included for analysis, standard cuts are applied as described in section 7.1. Candidate events are obtained with the use of the basic and modified jetfinders based on the DURHAM algorithm and E recombination scheme, see section 7.2. Section 7.3 describes the removal of events of the type  $e^+e^- \rightarrow q\bar{q}\gamma$  to leave a sample with a hard partonic skeleton assumed to originate from the process  $e^+e^- \rightarrow q\bar{q}g$ . To ensure that jet energies and multiplicities are well reconstructed, angular cuts are imposed, as shown in section 7.4.

### 7.1 Hadronic Event Selection

To select suitable event candidates of the type  $e^+e^- \rightarrow \gamma^*/Z^0 \rightarrow q\bar{q} \rightarrow$  hadrons, standard criteria have been developed known collectively as ‘class 16 cuts’ [82]. These are designed to remove leptonic events ( $e^+e^- \rightarrow e^+e^-/\mu^+\mu^-$ ) and hadronic background events which originate from the processes  $e^+e^- \rightarrow \tau^+\tau^-$  (tau),  $e^+e^- \rightarrow \gamma\gamma e^+e^-$  (two-photon) and  $e^+e^- \rightarrow e^+e^- + \gamma \rightarrow q\bar{q} + \gamma$  (ISR). Tau events typically have a low multiplicity and/or missing momentum due to undetected neutrinos from the decay of the  $\tau$  lepton. Two-photon events are identified as having low energy and multiplicity, the bulk of the energy in the reaction being carried by the deflected beam particles which pass into the beampipe regions. The photon emitted in ISR events is typically low-angle and not detected so that these background events have significant missing energy. Non-hadronic events are removed by the class 16 cuts such as cosmic-ray events and beam-gas reactions, as these have particles whose origin is not consistent with coming from the IP.

A quality requirement is first imposed on the energy flow objects which are

assembled from tracking and calorimeter information. These objects are described previously in section 4.11.2. Any objects that fail the requirements are excluded from further analysis. Each charged object must:

- (i) originate within a cylinder of radius 3 cm and length 10 cm centred on the interaction point;
- (ii) have at least four hits in the TPC;
- (iii) subtend more than  $20^\circ$  to the beam line;
- (iv) have a transverse momentum of more than 200 MeV with respect to the beam line;
- (v) have an energy of less than 100 GeV.

Each neutral object must:

- (i) subtend more than  $20^\circ$  to the beam line,
- (ii) have an energy of more than 300 MeV.

After these quality cuts the remaining event is required to have:

- (i) a sum of charged objects  $N_{\text{ch}} > 5$ ;
- (ii) total charged energy  $E_{\text{ch}} > 15 \text{ GeV}$ ;
- (iii) total visible energy  $E_{\text{vis}} > \frac{1}{2}\sqrt{s}$ ;
- (iv) missing momentum in the beam line direction  $< \frac{2}{5}\sqrt{s}$ .

Figures 7.1–7.2 summarise some class 16 variables for the first 100 000 ALEPH events recorded in 1994. The number of tracks<sup>1</sup> before and after the class 16 cuts are plotted in figure. 7.2. Figure 7.3 plots energy against multiplicity for charged particles in each event and identifies some event types that are excluded from the analysis.

## 7.2 3-Jet Selection

If an event passes the class 16 cuts, then all energy flow objects are passed to a jetfinder for clustering. From the study of jetfinders in chapter 5 the DURHAM algorithm was chosen for this analysis with the E recombination scheme. The basic jetfinder and the ‘A’ and ‘C’ modifications to it are employed to give three

---

<sup>1</sup>As all energy flow objects which pass the class 16 cuts are given to a jetfinder as a set of four-momenta, they are also referred to herein as ‘tracks’.

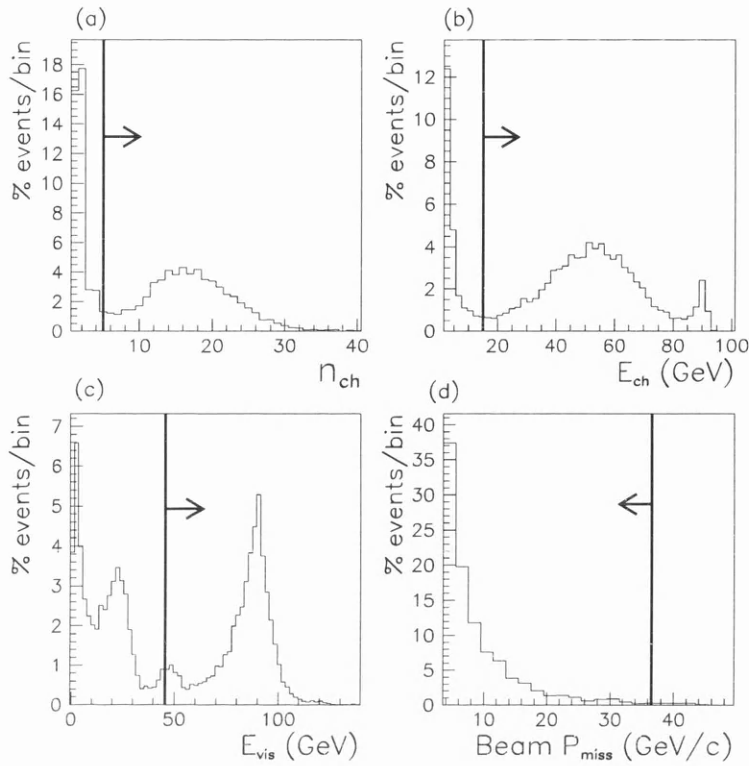


Figure 7.1: ‘Class 16’ cut variables. (a) Charged particle multiplicity, (b) Charged particle energy, (c) Total visible energy and (d) Momentum missing in the beam line direction. The arrowed lines mark each cut and those events that pass.

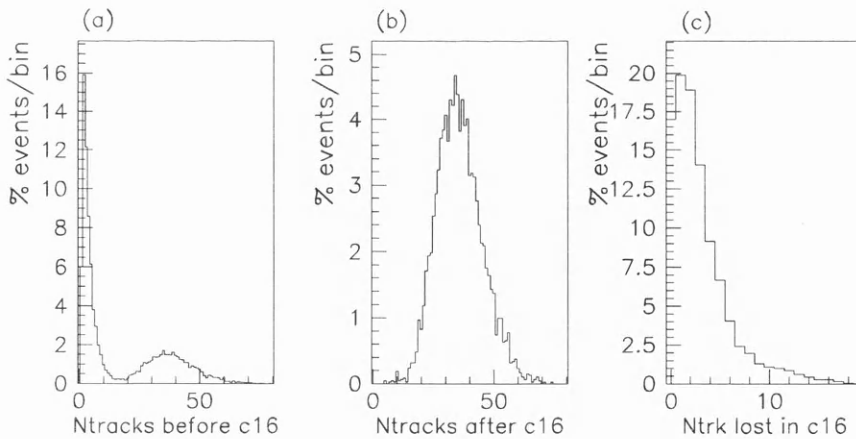


Figure 7.2: Number of tracks before (a) and after (b) class 16 cuts. The number of objects rejected during the cuts is shown in (c). In each histogram the  $y$ -axis is scaled so that the sum over all bins is 100%.

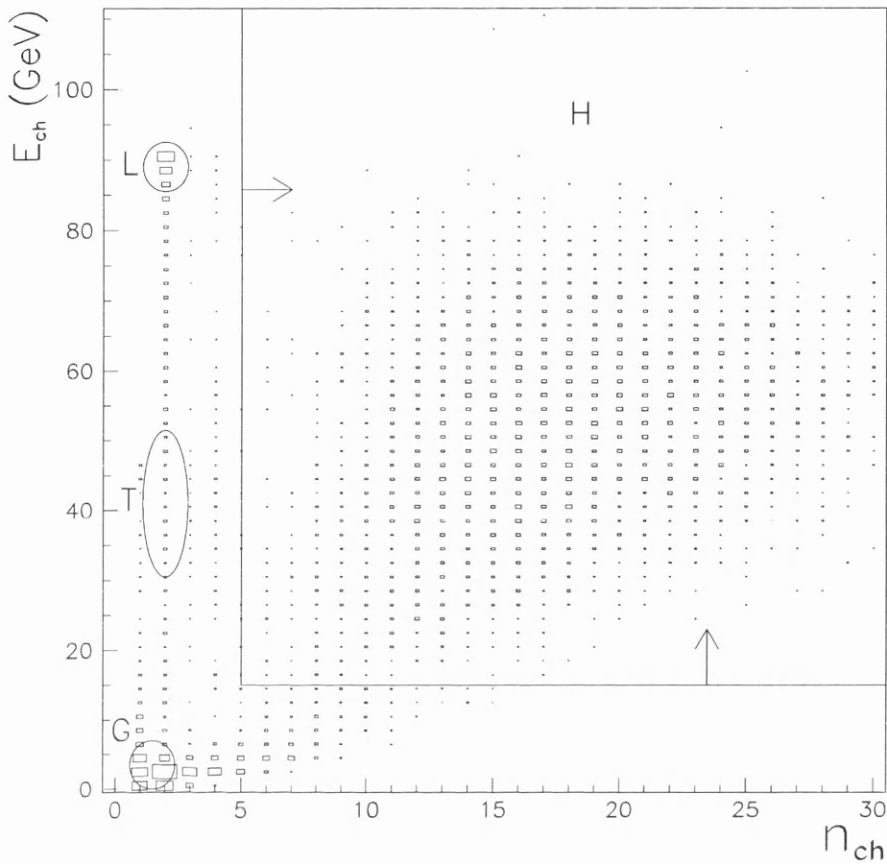


Figure 7.3: Visible charged energy *vs* charged particle multiplicity. The areas shown highlight some excluded event types: L= leptonic, T= tau, G= two-photon. The arrowed lines mark the class16 cuts. Events in the rectangular region (H) are considered to be hadronic candidates.

separate three-jet samples: each is treated in an identical fashion throughout the following selection process.

Events are clustered at a resolution scale defined by the  $y_{cut}$ ,  $y_0$ , chosen to be  $10^{-2}$  which corresponds to a typical minimum transverse momentum,  $k_{\perp}$ , between jets of  $\approx 10$  GeV. Table 7.1 shows the fraction of events obtained with  $N_{jet}$  jets and the average total multiplicity,  $\langle n_{tot} \rangle$ , of each type. It can be seen that  $\langle n_{tot} \rangle$  increases significantly as more jets are resolved because of radiation from hard gluon jets.

If two jets remain after clustering, the event is discarded. Events with more than three jets are re-clustered until only three remain. This is performed with the

$N_{\text{Jet}}$	Fraction (%)	$\langle n_{\text{tot}} \rangle$
2	64.1	32.9
3	30.4	40.5
4+	5.5	46.5
ALL	100.0	36.0

Table 7.1: Average total multiplicity of events classified by the number of jets obtained after initial clustering.

basic DURHAM jetfinder because of the features of the modified schemes discussed in section 6.3.

### 7.3 $q\bar{q}\gamma$ Rejection

Jetfinders cluster tracks together simply by reference to their relative four-momenta, making no distinction between charged and neutral objects. It is therefore possible to cluster events with a hard final-state photon, *i.e.*  $Z^0 \rightarrow q\bar{q}\gamma$ , into a three-jet configuration [83] where one jet contains only a photon.

The relative rates of  $q\bar{q}\gamma$  and  $q\bar{q}g$  events can be approximated as the ratio of the probabilities that a photon and gluon will be radiated from a quark:

$$\frac{\mathcal{P}(q \rightarrow q\gamma)}{\mathcal{P}(q \rightarrow qg)} \sim \frac{\alpha_{\text{em}} \overline{e_q^2}}{\alpha_s C_F} \sim \frac{1}{90} \quad (7.1)$$

where  $\overline{e_q^2}$  is the mean quark charge.

To remove  $q\bar{q}\gamma$  events a cut is made on the fraction of energy in each jet that is carried by neutral objects. An event is discarded if any jet has less than 15% of its energy carried by charged objects. The maximum fraction of neutral energy for a jet in each three-jet event is shown in figure 7.4, with a peak clearly visible at 100% indicating that  $\sim 1.5\%$  of clustered three-jet events are of the  $q\bar{q}\gamma$  type. The cut is chosen at 85% so that photon jets which have had one or more charged particles associated with it are also excluded.

### 7.4 Angular cuts

To reduce the risk of topological effects being hidden by the misplacement of events on the Dalitz plane, angular cuts are implemented to improve the energy

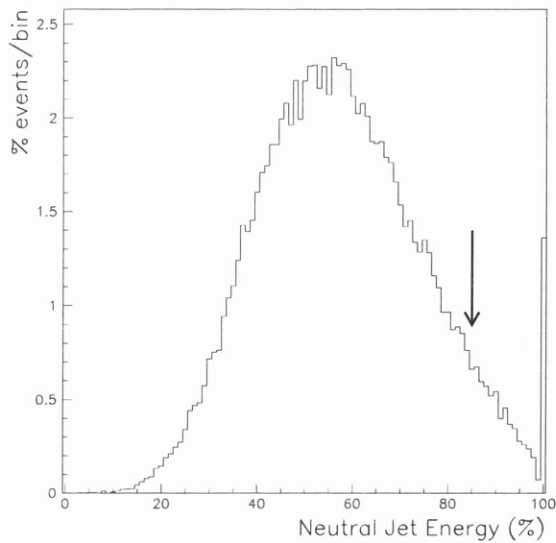


Figure 7.4: The largest percentage of jet energy carried by neutral particles in any single jet from a selected three-jet event. The arrow marks the position of the cut.

and multiplicity resolution of each jet. The polar angle,  $\theta_Z$  is required to be greater than  $40^\circ$  for each jet. It is estimated from Monte Carlo data (section 5.3.2) that the angular size of hadronic jets at LEP is of this order. An improvement in resolution is obtained as this cut is increased (section 6.6), however a cut of  $40^\circ$  represents a good balance between resolution and statistics. Figure 7.5 shows the  $\theta_Z$  distribution prior to the cut for each jet, where the jets have been ordered in decreasing energy in each event.

It was seen in chapter 6 that energy resolution does not improve dramatically when jets are forced to be planar. However events that have a high degree of aplanarity are removed as they are likely to be very badly reconstructed. A cut of  $5^\circ$  is made on the ‘planarity angle’,  $\theta_P$  (fig. 7.6), subtended between each jet and the plane defined in equation (6.2).

The effect of the angular cuts is to increase the average energy (fig. 7.7) and multiplicity in the three-jet sample as fewer tracks are lost from jets in events that survive.

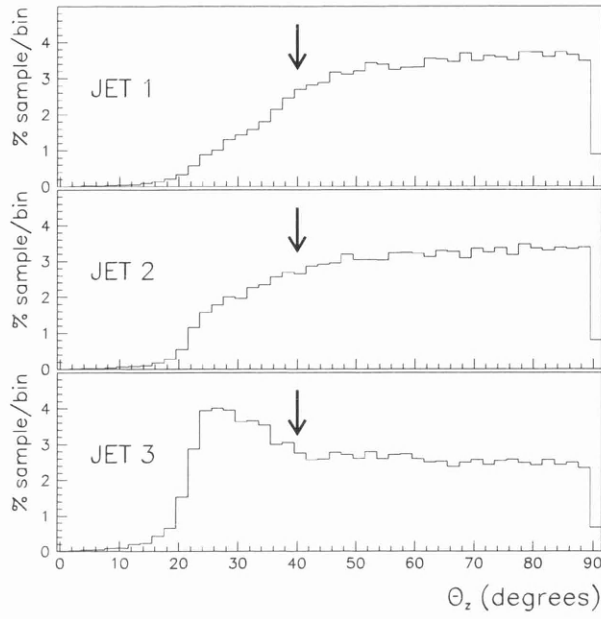


Figure 7.5: The angle between each jet and the  $z$ -axis,  $\theta_z$ , where the jets have been ordered in decreasing energy. The arrows mark the position of the cut.

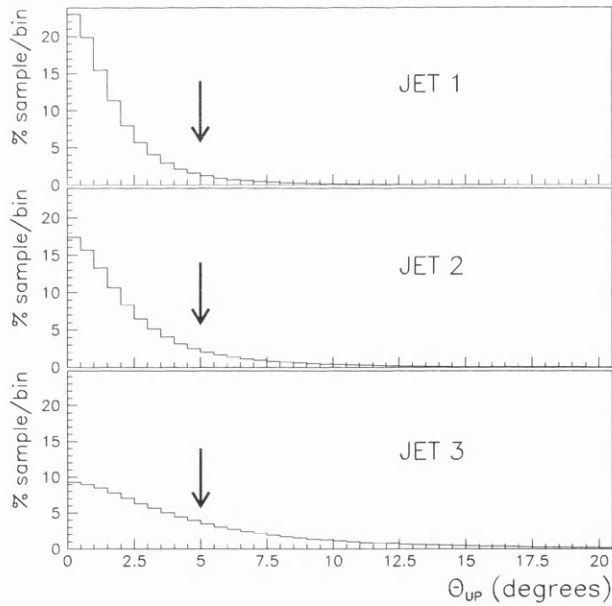


Figure 7.6: The planarity angles for events selected from 1994 data, where the jets have been ordered in decreasing energy. The arrows mark the position of the cut.

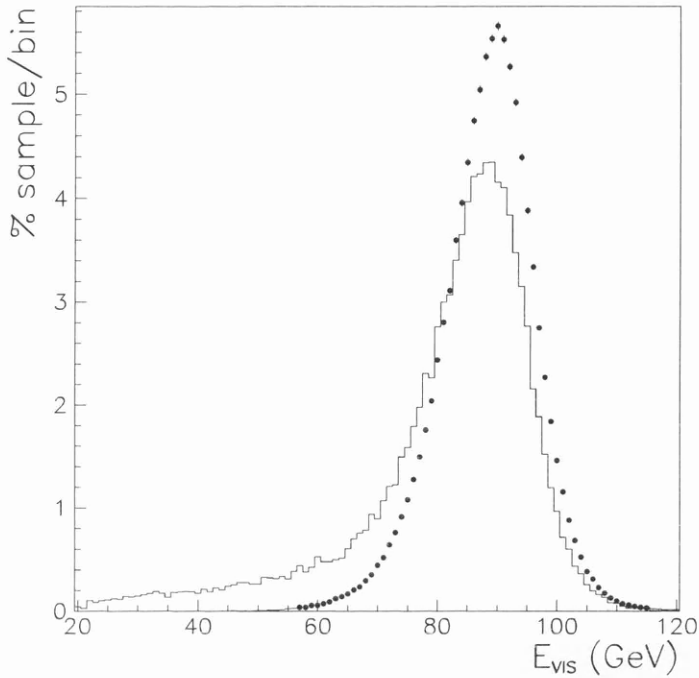


Figure 7.7: Visible energy before and after the angular cuts described in section 7.4. Both samples have been normalized to 100%; the solid line shows the data before the cuts and the points after. The average energy after the cuts is 88.27 GeV.

## 7.5 Summary

This analysis is based on events collected by the ALEPH detector during the running period 1990–95. After the class 16 cuts 3 521 772 candidate hadronic events remain. The basic DURHAM algorithm selects 1 263 146 of these as three-jet events of which 94 474 are rejected as  $q\bar{q}\gamma$  events as outlined in section 7.3. The angular cuts exclude approximately 2/3 of the remaining events: the resulting sample of 364 890 events are binned on a Dalitz plane as described in the following chapter. The corresponding number of selected events is 316 311 and 313 528 when the modified ‘A’ and ‘C’ schemes are used respectively.

For each of the jets in selected events the four-momentum and charged multiplicity are recorded and each jet is re-clustered at several smaller resolutions  $y_{\text{sub}} < y_0$ . The total number of pseudo-particles obtained in each jet is defined as the subjet multiplicity.

# Chapter 8

## Fitting Method

This chapter describes the binning and fitting of the multiplicity of three-jet events on the Dalitz plane. The plane is split into regular bins, in which ALEPH event multiplicities are accumulated as described in section 8.1. Model planes are then generated using different topological scales which attempt to account for the effects of colour coherence, see section 8.2. To compare these models with data, they are transformed with a matrix that represents the effect of the detector on ‘true’ events. This correction procedure is described in section 8.3.

### 8.1 Multiplicity Binning

#### 8.1.1 The Dalitz Plane

The energy resolution of each jet was estimated in chapter 6 to be, after angular cuts, of the order 1 GeV for the hardest jet and 2 GeV for the next hardest. The Dalitz plane is divided up into square bins of side 2 GeV so that it is likely that, to within one standard deviation, an observed event will be placed in the bin that its ‘true’ partner would have occupied.

The divided plane comprises a total of 150 bins, shown in figure 8.1, and labelled with the numbers 1 through 150. If massless kinematics are assumed, then only the bins contained within the dashed lines shown in figure 8.1 are populated. Mercedes events, and the topology depicted in figure 3.3, lie in bins 51 and 56 respectively. The latter is typical of an unsymmetric configuration and is referred to as the ‘P’ topology in this chapter. Events in bin 128 contain the softest jets of the three-jet sample.

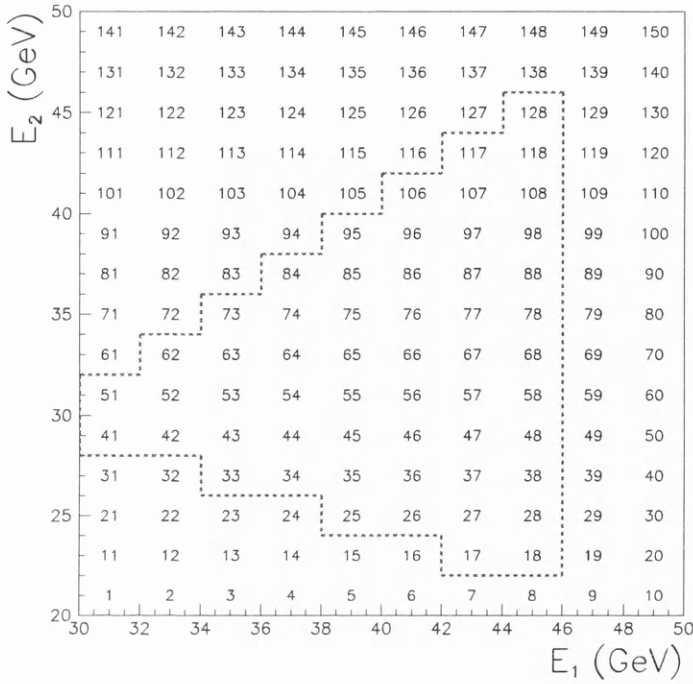


Figure 8.1: Dalitz bin numbers. The dashed line marks the populated bins assuming massless kinematics.

### 8.1.2 Discussion Of Estimators

The accessible area of the Dalitz plane is defined solely by the energy ranges of the two hardest jets. The energy of the third jet follows simply from energy conservation. These energies can be taken to be any one of the estimators described in section 6.2 which are based on Lamy's theorem, as these have the property that the sum over all jet energies is constant.

As discussed in section 6.4, the three-jet event samples are near-planar due to the  $\theta_P$  cut in the final stage of selection. Therefore the 'planar' estimators are not included in the analysis. The jet energy distribution with the 'non-planar' estimators is shown in figure 8.2 for the event sample defined by the basic DURHAM jetfinder. As the distributions for the two estimators are similar for each jet, the difference between massless and massive Dalitz bin populations will be small. However, there is a significant difference between the estimators for the hardest jet above  $\sim 41$  GeV. This is due to the maximum possible energy being limited to  $\sqrt{s}/2=45.6$  GeV with massless kinematics: the massive estimator however can give energies of up to 50 GeV. Some events will therefore lie outside the bordered

region depicted in figure 8.1 when  $E_{Lamy}^M$  values are taken.

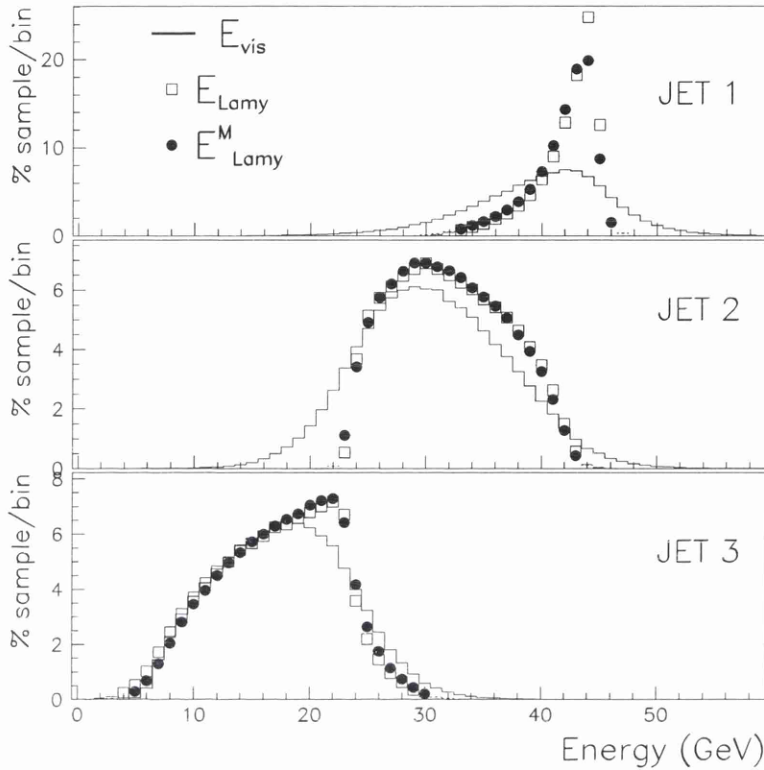
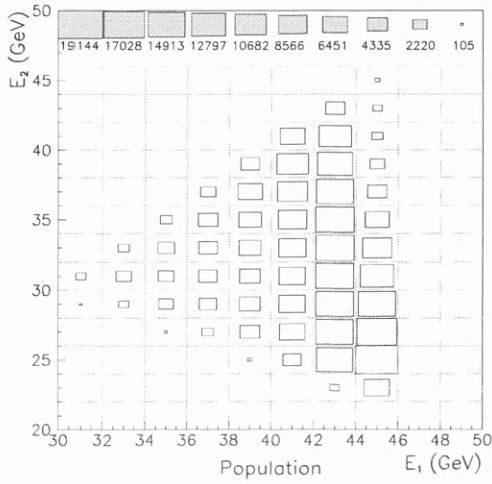


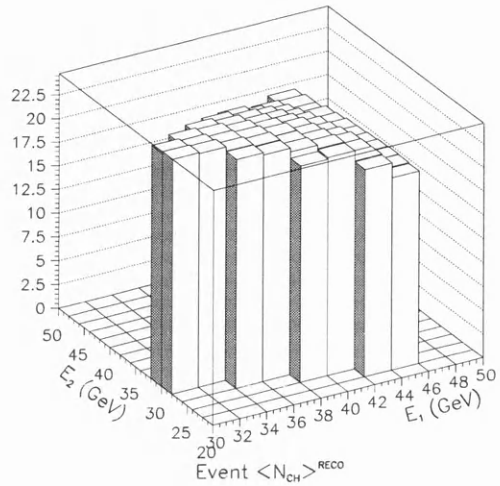
Figure 8.2: The energy of each jet given by the estimators  $E_{Lamy}$  and  $E_{Lamy}^M$ . Also shown for comparison is the observed total energy of each jet,  $E_{vis}$ .

The population and average charged multiplicity of each bin with both definitions are plotted in figure 8.3. Figure (c) shows that few ‘massive’ events actually lie outside the area containing ‘massless’ events. As these bins are sparsely populated the error on the average multiplicity in these bins is large. In figure (d) the smooth multiplicity distribution across the plane is suddenly broken at the boundary  $E_1=45.6$  GeV. Any prediction that can account for this discontinuity in multiplicity must have an intrinsic dependence on the mass of the N-parton jet: as yet no such predictions exist.

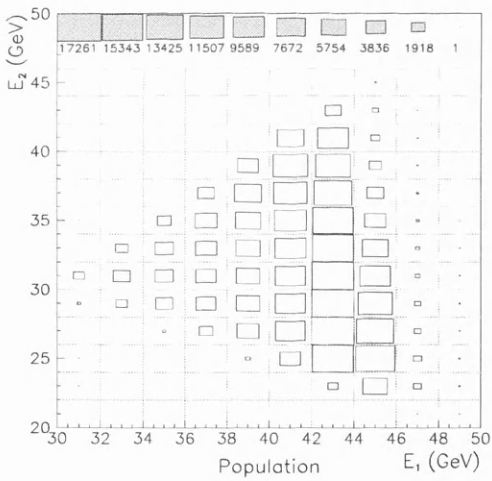
In this analysis the multiplicity as given by equation (3.3), which is independent of the mass of the primary quarks involved, is used to predict the multiplicity of each jet in an event. The prediction for the multiplicity of an entire event is weighted according to the probability that each jet originated from a hard gluon. This probability is given by the leading order massless matrix element which



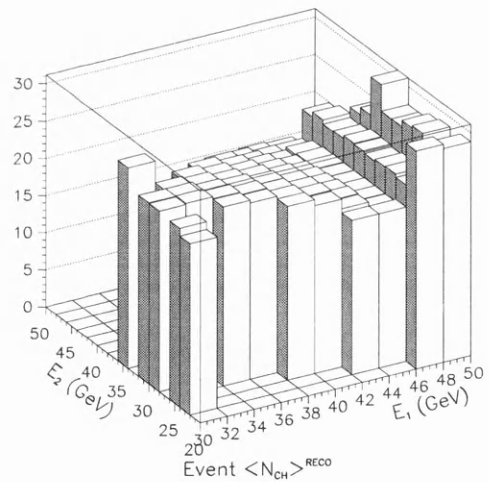
(a)



(b)



(c)



(d)

Figure 8.3: The numbers and average charged multiplicity,  $\langle n_{ch} \rangle$ , of three-jet events binned on the Dalitz plane. Figures (a)&(b) are binned using the  $E_{Lamy}$  jet energy definition and figures (c)&(d) using the  $E_{Lamy}^M$  definition. The key at the top of the box diagrams gives the number of entries for several box sizes.

contains a factor  $(1-x)$ , where  $x$  is the fraction of the beam energy carried by the jet. For  $E_{\text{Lamy}}^M > 45.6 \text{ GeV}$ ,  $(1-x) < 0$  and the probability becomes unphysical. Only events that lie inside the boundary defined by massless kinematics can therefore be used. In practice the difference between massless and massive estimators is of the order  $\pm 0.5 \text{ GeV}$  and the event is likely to be placed in the same bin with each definition. To include all selected events in the analysis, and to be consistent with previous studies, the massless definition is adopted.

## 8.2 Generating Model Planes

The charged and subjet multiplicity can now be topologically fit across the plane by comparing bin-by-bin with the multiplicity predicted with the MLLA. A least squares fit is used, where the function

$$\chi^2 = \sum_b \frac{(M_b - D_b)^2}{\sigma(M_b)^2 + \sigma(D_b)^2}, \quad (8.1)$$

is evaluated over all populated bins  $b$ .  $M_b$  &  $D_b$  are the predicted and actual multiplicities for bin  $b$  and  $\sigma(M), \sigma(D)$  are the errors on these multiplicities.

In section 3.2.1, an expression for  $\mathcal{N}_q(Q)$ , the average multiplicity of a jet originating from a quark or antiquark of energy  $Q$ , was introduced:

$$\mathcal{N}_q(Q) = \kappa \cdot [\alpha_s(2Q)]^b \exp \left\{ \frac{a}{\sqrt{\alpha_s(2Q)}} \right\}. \quad (8.2)$$

The normalization  $\kappa$  was found from a fit to  $e^+e^-$  data to be  $\approx 3.5 \times 10^{-2}$  but, as this value is based on an inclusive definition of quark-jet multiplicity, it need not be the same for quark jets in a three-jet ensemble, where a specific jetfinder is employed. In the fits  $\kappa$  is allowed to be free.

The multiplicity of a gluon jet is expected to be  $f_g$  times larger than that of a quark jet, where  $f_g$  is known as the ‘‘gluon factor’’. Values of  $f_g \approx 1.5$  have been measured, the value obtained depending on the jetfinder and sample multiplicity chosen. The total event multiplicity is expected to be much less sensitive to jet definition. The multiplicity of a three-jet event,  $\mathcal{N}_{\text{ev}}$ , is assumed to have a contribution from each parton,

$$\mathcal{N}_{\text{ev}} = \mathcal{N}_q + \mathcal{N}_{\bar{q}} + \mathcal{N}_g, \quad (8.3)$$

which can be written as

$$\mathcal{N}_{\text{ev}} = \mathcal{N}_q(Q_q) + \mathcal{N}_q(Q_{\bar{q}}) + f_g \cdot \mathcal{N}_q(Q_g), \quad (8.4)$$

where it is assumed that  $\mathcal{N}_q(Q) = \mathcal{N}_{\bar{q}}(Q)$ .

### 8.2.1 Inclusion Of Topology Dependence

One of the effects of colour coherence is expected to be a reduction in particle flow between quark and gluon jets. The primary partons thus act as though they have an effective colour charge which is less than if they were “free”. The corresponding reduction in cascade multiplicity can be accounted for in perturbative calculations by reducing the initial evolution scale in the jet cascade, which is essentially the energy of the primary parton.

Topological scales were introduced in section 3.3.2. It was suggested that to account for interjet coherence, the quark multiplicity should be given in terms of a scale,  $Q_q$ , which is the product of the quark energy and a suppression factor which depends on the quark-gluon angle. The gluon cascade is affected by coherence in both the  $q-g$  and  $\bar{q}-g$  regions so that two suppression factors are necessary to describe the gluon jet multiplicity, see equation (3.13). By assuming that  $\alpha_s$  has a simple logarithmic scale dependence, the gluon multiplicity can be written in terms of a single suppression factor, as given in equation (3.15).

Using equation (3.5) we can write  $\mathcal{N}_g$  in terms of  $\mathcal{N}_q$  and, substituting the expression given in equation (3.4), the multiplicity of any three-jet configuration can be expressed in terms of the parton energies and interjet angles, the QCD scale factor  $\Lambda$ , and an overall normalization,  $\kappa$ . To investigate the validity of using topological scales to describe the multiplicity in three-jet events three “fitting options”,  $F_{\text{opt}}$  ( $F_{\text{opt}}=I, II, III$ ), are introduced. Option I assumes that there is no topology dependence and the suppression factors are all set to unity. Options II and III use the expressions given in equations (3.11) and (3.12) to describe the quark and antiquark multiplicity respectively. The gluon multiplicity is given in option II as the average of two components given in equation (3.13), whereas the two suppressions are combined in option III and the expression in equation (3.15) is used. The parton multiplicities predicted by each fitting option are summarised below in table 8.1.

### 8.2.2 Which Is The Gluon Jet?

There is one important point that has not yet been mentioned in this chapter: exactly *which* jet came from the gluon? To investigate three-jet events in a topological and flavour-independent way, heavy-quark tagging is not employed in the selection procedure. This ensures essentially the same  $u, d, s, c, b$  quark mix in the three-jet sample as the two-jet data shown in figure 3.2, and hence one can compare respective  $\kappa$  and  $\Lambda$  values. However, it is not known if each jet

$F_{\text{opt}}$	Quark	Antiquark	Gluon
I	$\mathcal{N}_q(E_q)$	$\mathcal{N}_q(E_{\bar{q}})$	$\mathcal{N}_q(E_g)$
II	$\mathcal{N}_q(E_q S_{qg})$	$\mathcal{N}_q(E_{\bar{q}} S_{\bar{q}g})$	$\frac{1}{2}\mathcal{N}_q(E_g S_{qg}) + \frac{1}{2}\mathcal{N}_q(E_g S_{\bar{q}g})$
III	$\mathcal{N}_q(E_q S_{qg})$	$\mathcal{N}_q(E_{\bar{q}} S_{\bar{q}g})$	$\mathcal{N}_q(E_g \sqrt{S_{qg} S_{\bar{q}g}})$

Table 8.1: The assumed scale dependence of the multiplicity of each primary parton with fitting option  $F_{\text{opt}}$ . Note that  $S_{ij} = \sin\left(\frac{\theta_{ij}}{2}\right)$ .

originated from a gluon or a quark. The hardest jet is likely to originate from a quark, especially if  $E_1 \geq 40$  GeV. At the Mercedes point, however, all the jets have the same energy and each is equally likely to be the gluon.

To proceed an estimate of the probability that jet  $i$  is the gluon jet out of jets  $(i, j, k)$  is approximated by the leading order massless matrix element (*c.f.* equation (2.19)):

$$\mathcal{P}_{i=g} \propto \frac{(x_j^2 + x_k^2)}{(1 - x_j)(1 - x_k)} \quad i, j, k \text{ cyclic} . \quad (8.5)$$

$x_{i,j,k}$  are the fractions of the beam energy carried by each jet, so that  $\sum_l x_l = 2$ . If the expression for each jet is divided by the sum over all jets one obtains

$$\mathcal{P}_{i=g} = \frac{(1 - x_i)(x_j^2 + x_k^2)}{x_i^3 + x_j^3 + x_k^3} . \quad (8.6)$$

It should be emphasized that equation 8.5 is only a leading order expression and contains no information from higher orders. Additionally, the formula applies to a system of three massless partons, whereas the analysis involves massive jets. However, using the matrix element allows the multiplicity of each jet to be given in terms of a sum, weighted by the probability that each is the gluon jet. For jet  $i$  the sum is

$$\begin{aligned} \frac{1}{\kappa} \mathcal{N}_i(Q_i) &= \mathcal{P}_{i=g} f_g \mathcal{N}_q(Q_i) + \mathcal{P}_{j=g} \mathcal{N}_q(Q_i) + \mathcal{P}_{k=g} \mathcal{N}_q(Q_i) \\ &= \mathcal{P}_{i=g} f_g \mathcal{N}_q(Q_i) + (1 - \mathcal{P}_{i=g}) \mathcal{N}_q(Q_i) \\ &= \mathcal{N}_q(Q_i) \{1 + \mathcal{P}_{i=g} (f_g - 1)\} \end{aligned} \quad (8.7)$$

with fitting option I,

$$\frac{1}{\kappa} \mathcal{N}_i(Q_i) = \mathcal{P}_{i=g} f_g \times [\mathcal{N}_q(Q_i S_{ij}) + \mathcal{N}_q(Q_i S_{ik})] / 2$$

$$\begin{aligned}
& + \mathcal{P}_{j=g} \mathcal{N}_q(Q_i S_{ij}) \\
& + \mathcal{P}_{k=g} \mathcal{N}_q(Q_i S_{ik})
\end{aligned} \tag{8.8}$$

with fitting option II and

$$\begin{aligned}
\frac{1}{\kappa} \mathcal{N}_i(Q_i) & = \mathcal{P}_{i=g} f_g \mathcal{N}_q(Q_i \times \sqrt{S_{ij} S_{ik}}) \\
& + \mathcal{P}_{j=g} \mathcal{N}_q(Q_i S_{ij}) \\
& + \mathcal{P}_{k=g} \mathcal{N}_q(Q_i S_{ik})
\end{aligned} \tag{8.9}$$

with fitting option III. The expressions for jets  $j$  &  $k$  are given by the cyclic permutations of eqns (8.7–8.9). The prediction for the whole event now becomes  $\mathcal{N}_{ev} = \mathcal{N}_i + \mathcal{N}_j + \mathcal{N}_k$ .

### 8.2.3 Energy Options

For each Dalitz bin the value of  $\mathcal{N}_{ev}$  can be evaluated to generate a complete plane. Recalling that the bins are 2 GeV across, one has a choice of where in the bin to evaluate the MLLA expressions. Three possible “energy options” are described below.

(i) Option 1:

In the first approximation the jet energies at the centre of each bin are used. This method is valid only if the distribution of events *across* a bin is flat: inspection of figure 8.3(a,c) shows this not to be the case for ALEPH data. Furthermore bins on the boundary of the populated plane have only a portion of the  $2 \times 2$  GeV area covered.

(ii) Option 2:

A better fit should be obtained if the average energy of jet 1 and jet 2 is taken for each bin, the average energy of jet 3 following automatically. Each bin is subdivided into a grid of  $200 \times 200$  MeV squares and the number of reconstructed events falling in each sub-bin is recorded. The average bin energy is then given by the weighted sum of the energies calculated at the centre of each sub-bin.

(iii) Option 3:

An improvement over option 2 should be achieved if the prediction at the centre of each sub-bin is calculated and summed over each Dalitz bin, with each prediction weighted by the fraction of events falling into each sub-bin.

The weight is obtained from the distribution of Monte Carlo TRUTH level events within each  $2 \times 2$  GeV Dalitz bin. As the multiplicity prediction is a relatively slow function of energy, the difference between this energy option and option 2 should be smaller than that with option 1.

### 8.2.4 Generated Model Planes

An example of a plane generated with each fitting option (I, II and III) is given in figure 8.4, where energy option 1 is chosen. In the model, values of  $\Lambda=150$  MeV and  $f_g=1.5$  have been used, and the value of  $\kappa$  adjusted so that the models give the same predictions at the Mercedes point. Some of the boundary bins are not populated as the median jet energies of these bins result in unphysical predictions.

One can clearly see that the topology *independent* plane given by option I is much flatter than the dependent planes, which by eye are seen to better represent the ALEPH data in figure 8.3(b). Differences between the predictions with fitting options II & III are more clearly seen in figure 8.5 where the plane is separated into horizontal “slices”. Each of the twelve diagrams represent a single slice across the plane, each diagram having the same  $E_2$ . The lefthand points represent more symmetric topologies whilst events become less symmetric as one traverses each diagram. The most populated slice (bins 51–60) contains both the Mercedes and ‘P’ topologies. The topology dependent scales are similar for low jet energies, the prediction of fitting option II being slightly higher than option III as one moves rightwards across the plane.

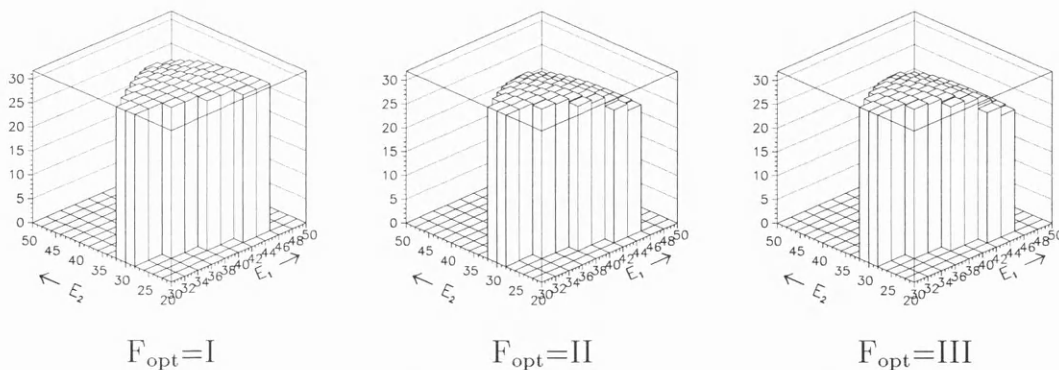


Figure 8.4: Predicted multiplicity across the plane with each fitting option,  $F_{\text{opt}}$ , which are described in section 8.2.1. The predictions are evaluated at the centre of each bin assuming  $f_g=1.5$  and  $\Lambda=150$  MeV.

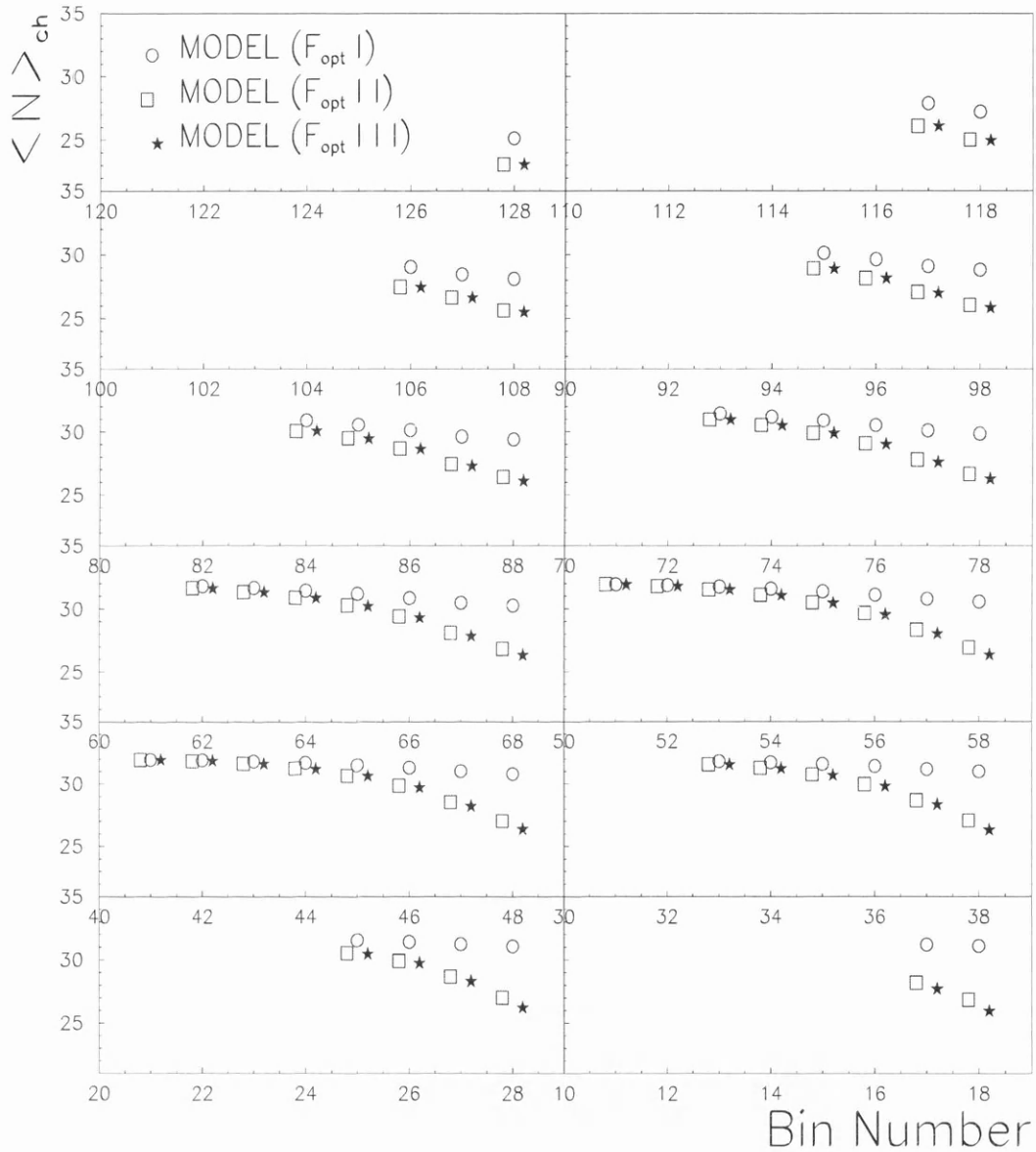


Figure 8.5: Predicted charged particle multiplicity across the Dalitz plane with different fitting options  $F_{opt}$ . Each of the twelve diagrams represents a different horizontal “slice” across the Dalitz plane, the energy of the second hardest jet being the same for each slice. For example, in the top-left diagram  $E_2=45$  GeV, and in the bottom-right diagram  $E_2=23$  GeV. The points are separated horizontally for clarity.

## 8.3 Correction Procedure

### 8.3.1 Introduction

Generated planes such as those in figure 8.4 cannot be directly compared with data. Observed and ‘true’ distributions are considerably different due to the limitations in spatial coverage and resolution of the ALEPH detector. Typically the effects of the detector on observed distributions are corrected by a process known as *unfolding*, which involves the use of Monte Carlo generators in conjunction with detector simulations.

A correction matrix  $C$  of order  $(n \times n)$  is calculated for each variable, where  $n$  is the number of bins for the given distribution. The TRUTH ( $T$ ) and RECO ( $R$ ) level data are related to each other by  $T_i C_{ij} \Leftrightarrow R_j$ . The matrix is then inverted so that an observed data distribution ( $D$ ) can be corrected for detector effects to hopefully give the ‘true’ distribution before the intervention of the detector, *i.e.*  $C_{ij}^{-1} D_j \Leftrightarrow T_j$ . When the order  $n$  becomes large then the inversion of matrix  $C$  may be neither stable nor reliable. As 56 bins of the Dalitz planes are populated a matrix of dimension  $56 \times 56$  would be required to unfold every charged and subjet multiplicity plane.

In this analysis it is not required that theoretical values be obtained directly from the study of ALEPH data. Rather, this study endeavours to account for the change of the charged multiplicity with topology by the introduction of topological scales which are embedded in three fitting options,  $F_{\text{opt}}$ . The multiplicity given by each option is based on the form of the MLLA prediction for two-jet distributions, which is not expected to hold perfectly once a jetfinder is applied to define three or more jets. Instead of correcting the data and comparing to predictions from the three fitting options, a *folding* method is used in this analysis. Each multiplicity prediction across the Dalitz plane,  $M$ , is “smeared” to mimic the intervention of the ALEPH detector, so that  $M_i C_{ij} \Leftrightarrow S_j$  where  $S$  is the smeared distribution. The smeared prediction is then compared directly with the observed distribution.

### 8.3.2 Monte Carlo Selection

The correction procedure involves the study of a JETSET Monte Carlo sample with approximately the same number of events as the ALEPH dataset. It is important that generated events have the same particle distributions after passing through a detector simulation as ALEPH events, as any major discrepancies will affect the correction matrices and hence increase the systematic uncertainty of the fits. As

the simulation of partonic cascades in the JETSET Monte Carlo event generator includes some angular ordering, the multiplicity distribution of reconstructed level events should embody the topological effects expected from colour coherence.

Figure 8.6 shows that the reconstructed charged Monte Carlo multiplicity is close to that in observed data across most of the plane. There is a general decrease in agreement as one move away from symmetric topologies, illustrated in figure 8.7 which plots the significance for each bin, defined as  $(D_b - R_b)/(\sigma D + \sigma R)$ , where  $D(R)_b$  is the data(MCRECO) multiplicity in bin  $b$  and  $\sigma D(R)$  the error on this multiplicity. The conclusion is that for the majority of the plane the JETSET generator is capable of reproducing multiplicity distributions in ALEPH data and is therefore adequate to use in the correction procedure.

Three-jet events are selected in MCRECO data and the same selection procedure applied as for ALEPH data. Any event that passes the selection cuts is ‘matched’ to the event at TRUTH level. The matching of TRUTH and RECO events proceeds exactly as for the resolution study in chapter 6. Section 6.3 explained how events at each level are often clustered to a different numbers of jets and can be placed into separate ‘jetclasses’. Only events with a jetclass less than five are retained.

It was noted in section 8.1.1 that despite the use of angular cuts and energy estimators there is an error on each jet energy measurement of  $\mathcal{O}(1 \text{ GeV})$ . This has the effect of moving events around on the Dalitz plane, possibly moving them into another bin altogether. A thorough correction procedure should take account of these movements or “migrations”.

### 8.3.3 Migration Matrices

In this analysis JETSET Monte Carlo data is used to give a set of correction or ‘migration’ matrices’,  $\mathcal{N}$  and  $\mathcal{F}$ , which together represent the net detector effect on a binned multiplicity distribution. The smeared model prediction,  $S_m$ , for a bin  $m$  is given by

$$S_m = \sum_{\lambda=1}^{150} \mathcal{N}_{\lambda m} \cdot \mathcal{F}_{\lambda m} \cdot M_{\lambda} , \quad (8.10)$$

where  $M_{\lambda}$  is the unsmeared model multiplicity prediction for bin  $\lambda$ . The  $(150 \times 150)$  matrices are defined as:

- $\mathcal{N}_{ab}$  = Fraction of events that are in bin  $a$  at TRUTH level but are reconstructed in bin  $b$ ;

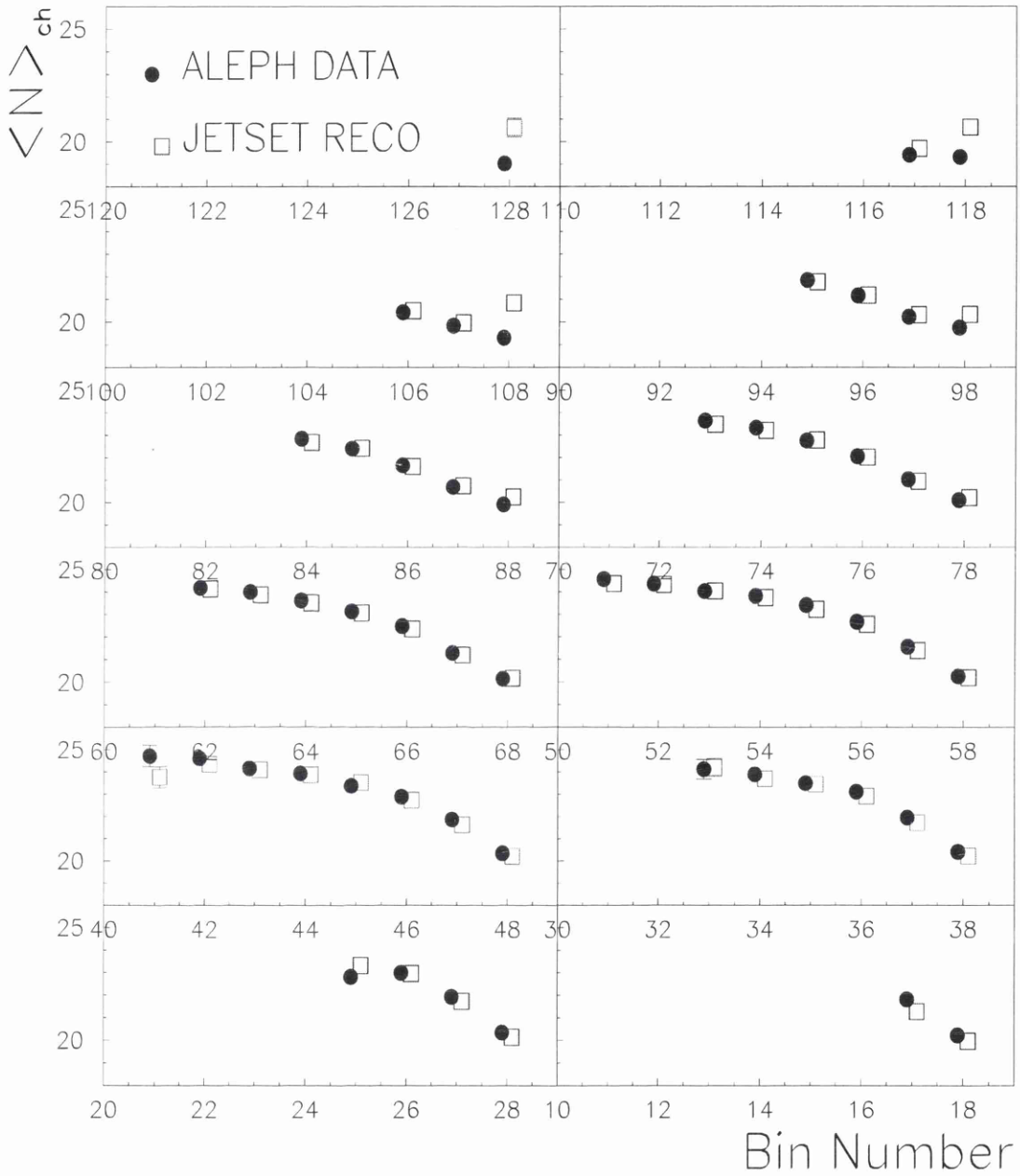


Figure 8.6: The charged multiplicity across the plane for ALEPH data and reconstructed JETSET Monte Carlo data. The points are separated horizontally for clarity.

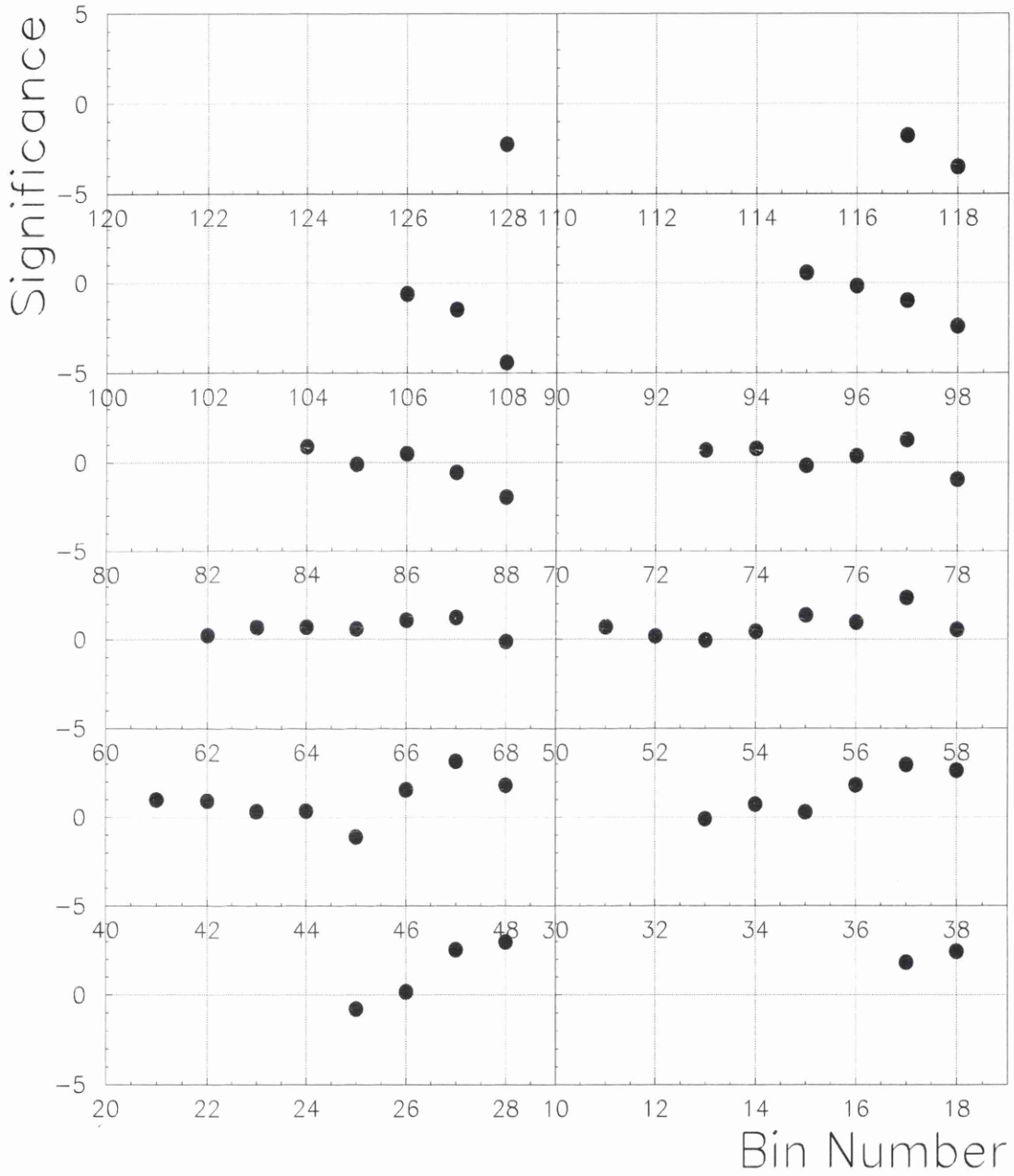


Figure 8.7: The value of the significance, defined in the text, of ALEPH and MCRECO data across the plane.

- $\mathcal{F}_{ab}$  = The mean multiplicity of the RECO level events that migrate from bin  $a$  to  $b$  divided by the mean TRUTH level multiplicity in bin  $a$  ;

As the average charged multiplicity across the plane  $\sim 22$  for MC`TRUTH` events and  $\sim 17$  for MC`RECO` events individual  $\mathcal{F}_{\lambda m}$  elements are typically  $\approx 0.75$ . The least squares function is now defined as

$$\chi^2 = \sum_{b=1}^{150} \frac{(S_b - D_b)^2}{\sigma(S_b)^2 + \sigma(D_b)^2} , \quad (8.11)$$

where  $\sigma S$  is the error on the smeared model prediction  $S_m$ .  $\sigma S$  is estimated to be considerably smaller than  $\sigma D$ , the error on each data bin multiplicity, and hence has little effect on the value of  $\chi^2$  for any multiplicity distribution across the plane. The term is therefore omitted from the denominator in equation (8.11). Multiplicity distributions across the Dalitz plane are then fit using the `MINUIT` fitting package [84].

## 8.4 Applicability Of Model Predictions

The predictions given by the three fitting options are based on naïve QCD models that assume that the multiplicity in a three-jet event can be separated into an individual component from each primary parton. The expected reduction in multiplicity between the gluon and quark jets is accounted for by replacing the ‘true’ energy of each parton with a scale which is a function of the interjet angles. The multiplicity of each parton is assumed to be described by an MLLA expression for jets defined in an inclusive two-jet sample, which need not hold perfectly for multi-jet ensembles.

The deviation of the naïve predictions from observed values is an indication of the dependence of multiplicity on the jet definition. In the selection of three-jet events the `DURHAM` jetfinder, in both the basic and modified forms, pairs tracks together until a test variable,  $y_{ij}$ , between any pair of jets exceeds a predefined cut value,  $y_o$ . For a chosen  $y_o$  the maximum and minimum jet energies are fixed and therefore the range of interjet angles is also restricted. In other words, the multiplicity distribution across the Dalitz plane depends on  $y_o$ , as well as whether the basic or modified `DURHAM` jetfinder is used.

The sensitivity of the fits to both the algorithm and  $y_o$  is assessed later in chapter 9. The worst agreement with data is expected in topologies where the minimum value of  $y_{ij}$  is close to the cut value  $y_o$ . In these configurations, the event can be imagined as being “almost two-jet”, insofar as a small change in

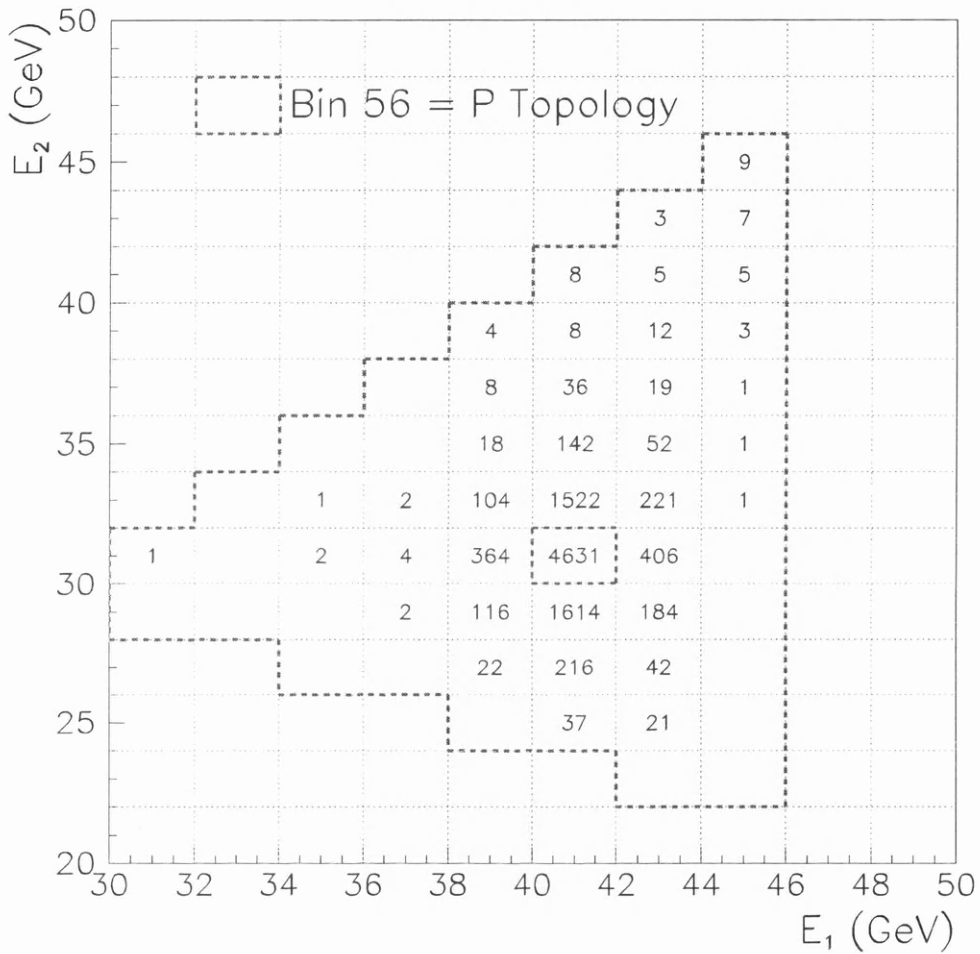


Figure 8.8: The number of reconstructed events in each bin that have the ‘P’ topology at TRUTH level. One can see that the majority have a similar topology at both levels and hence lie in the same bin, or in the bins immediately surrounding. One event is actually reconstructed in the Mercedes configuration.

either the jet energies or interjet angles could result in the pair with the lowest  $y_{ij}$  being clustered together.

Figure 8.9 shows the minimum value of  $y_{ij}$  for each Dalitz bin, where the events are assumed to be concentrated at the centre of each bin. It can be seen that when an event has a jet with energy  $\gtrsim 42$  GeV,  $y_{ij}$  is small and approaches  $y_o$  when two jets become very energetic. In this case it is likely that the softest jet is in fact “fake”, and is comprised from large-angle tracks from the two other hard jets.  $y_{ij}$  is also small in topologies where one jet has  $\gtrsim 42$  GeV and the other two jets have more comparable energies. In these configurations, the softer jets are separated by  $\lesssim 50^\circ$ . As jet tracks typically lie in a cone of half-angle  $\approx 40^\circ$  (see section 5.3.2) it can be imagined that the tracks in the softer jets in fact originate from a single jet which has a broad intrajet particle distribution.

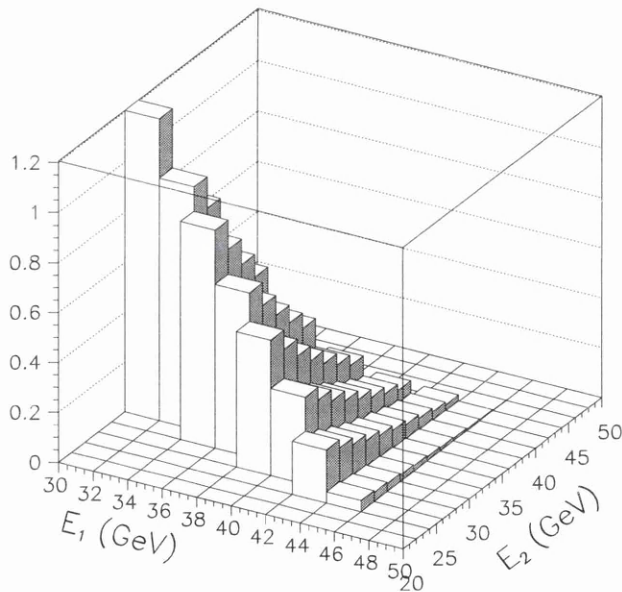


Figure 8.9: The minimum value of  $y_{ij}$  for events lying at the centre of each Dalitz Bin.

One concludes that events that lie in the righthand areas of the Dalitz plane are likely to have a multiplicity which is not well predicted by any of the naïve QCD models described in sections 8.2.1&8.2.2.

# Chapter 9

## Fits to Charged Multiplicity

### 9.1 Introduction

In this chapter the topology dependence of the charged particle multiplicity in three-jet events is examined. The analysis is based on events selected according to the procedure described in chapter 7. Three-jet events are selected with either the basic or modified DURHAM jetfinders, resulting in three separate samples. As motivated by the studies of the jetfinders and resolution in chapters 5&6, an initial  $y_{\text{cut}}$  of  $10^{-2}$  is chosen with the ‘E’ recombination scheme. For each event the energies of the jets are estimated using Lamy’s theorem and ordered in decreasing magnitude. The two largest energies,  $E_1$  &  $E_2$ , are used to define the topology and hence the bin on the Dalitz plane into which the multiplicity is placed.

In section 9.2, it is assessed whether the MLLA-based equations (8.7–8.9) are capable of describing individual jet multiplicities in Monte Carlo TRUTH level data. In section 9.3, the total multiplicity in ALEPH events is subsequently investigated by comparing data to predictions, given by each fitting option  $F_{\text{opt}}$ , which have been smeared for detector and resolution effects. The optimum topological scale is found from these fits and the ratio of the multiplicity in a gluon to a quark jet of the same scale is determined.

### 9.2 Fits To Jet Multiplicity

#### 9.2.1 Introduction

In this section the predictions for individual jet multiplicities, given by equations (8.7–8.9), are compared to data distributions across the Dalitz plane. As these expressions are based on an inclusive definition of jet multiplicity, they

will not necessarily be capable of describing the multiplicity in jets selected by a specific jetfinder. Nevertheless, the extent to which model predictions, calculated with each fitting option  $F_{\text{opt}}$ , disagree with data is assessed in the following study.

The predictions are compared to jet multiplicities in TRUTH level JETSET Monte Carlo events. The motivation for the direct use of MCTRUTH distributions is that, qualitatively, each topological scale can be compared without the need for any bin-by-bin corrections. It was illustrated in figure 8.6 that the total multiplicity in reconstructed JETSET events is comparable to ALEPH data across the Dalitz plane. Similarly, agreement is seen between individual jet multiplicities. Figure 9.1 compares the multiplicity of the mid-energy jet across the Dalitz plane for MCRECO and data events through the variable  $\chi^2$ , defined as

$$\chi^2 = \frac{(D_b - R_b)^2}{\sigma(D_b)^2 + \sigma(R_b)^2}, \quad (9.1)$$

where  $b$  is the bin number,  $D_b$  and  $R_b$  are the data and MCRECO multiplicity in bin  $b$  respectively, and  $\sigma D$  &  $\sigma R$  are the errors on each multiplicity. It is seen that the Monte Carlo model is capable of predicting the observed jet multiplicity over the plane, with the exception of the lower right-hand region.

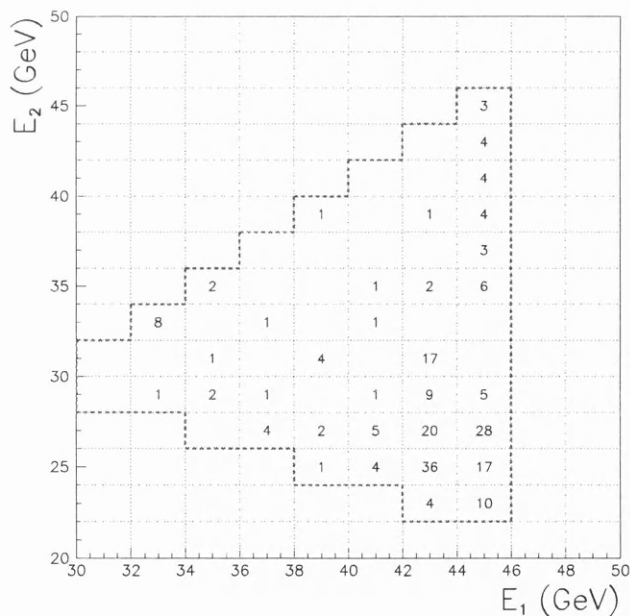


Figure 9.1: The value of  $\chi^2$ , defined in the text, between the mid-jet multiplicity distribution in ALEPH and MCRECO events. Each individual value has been rounded down to the nearest integer: empty squares indicate  $\chi^2 < 1$ .

## 9.2.2 Results

Three-jet events are selected using the basic DURHAM jetfinder. The charged multiplicity of each energy-ordered jet across the Dalitz plane is shown in figure 9.2. In section 8.4 it was discussed that bins on the plane, corresponding to jet energies  $E_1 \gtrsim 42$  GeV, are likely to contain three-jet events that are on the boundary between two- and three-jet configurations. The multiplicity in these bins is therefore likely to be poorly predicted with any fitting option. To ascertain how dependent the fits are to topologies with high-energy jets, limited areas of the plane are selected by imposing a cut,  $E_{\max}$ , on  $E_1$  and  $E_2$ . The cut is applied to both jets simultaneously and is chosen to be 45, 43, 41, 39, 37, 35 or 33 GeV. The number of populated bins remaining at each cut value are shown in figure 9.3.

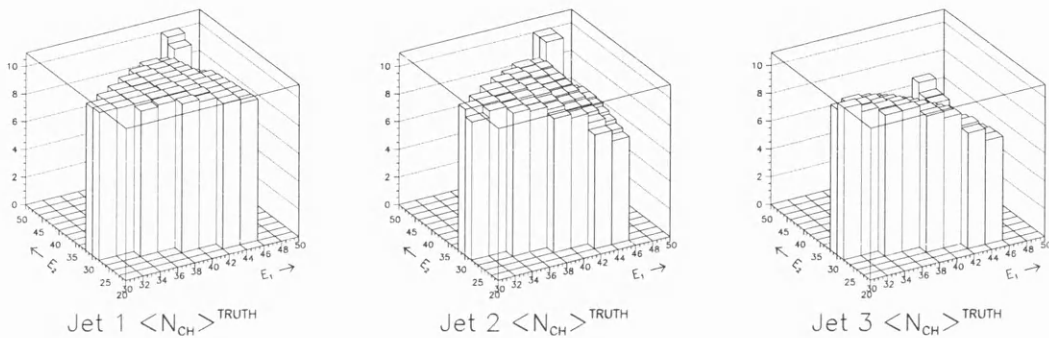


Figure 9.2: Charged multiplicity of each TRUTH level jet across the Dalitz plane. Jet 1 is the most energetic and 3 the least energetic. Events have been selected with the basic DURHAM jetfinder.

The leading order matrix element, see equation (8.5), is used to define the probability that a given jet originated from a quark or gluon. The weighted QCD prediction is calculated for each given topological scale ( $F_{\text{opt}}$ ) and compared to the MCTRUTH distributions by means of a least-squares fit. The construction of the expressions leads to the fitted parameters,  $f_g$ ,  $\Lambda$  and  $\kappa$ , being highly correlated. The fit is often unstable when they all are left free, resulting in unphysical values being obtained. However,  $\Lambda$  is expected to be of the same order as previous measurements of the scale parameter, which lie in the range 100–250 MeV<sup>1</sup>. A value of  $\Lambda=150$  MeV is fixed for the analysis, allowing the gluon factor and multiplicity normalization to be determined. It should be emphasized that the  $\Lambda$  parameter here is not necessarily equal to  $\Lambda$  measured in other analyses; the

<sup>1</sup>For example from fits to  $\langle n_{ch} \rangle$  distributions [42, 43, 40, 85, 64, 68],  $\alpha_s$  measurements [86, 19] or studies of particle spectra [87].

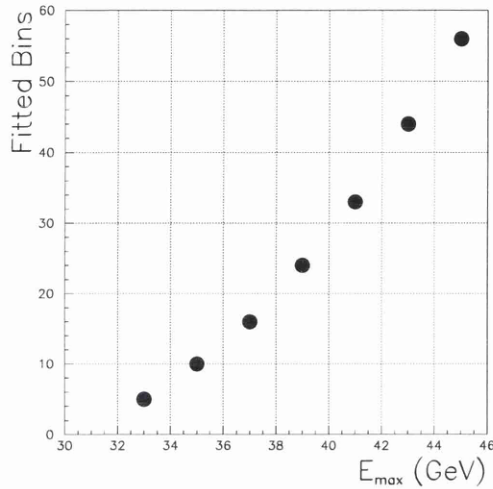


Figure 9.3: The number of Dalitz bins remaining after the cut  $E_{1,2} \leq E_{\max}$ .

$\mathcal{O}(\sqrt{\alpha_s})$  correction to the MLLA expression in (3.3) is not calculated and so, formally, terms sensitive to changes of  $\Lambda$  are missing.

An example of the output from the MINUIT fitting package is given in appendix B, showing typical fit parameters and variable correlations. The  $\chi^2$  and fitted values of  $f_g$  and  $\kappa$  are summarised in figure 9.4 separately for each jet and fitting option. When bins corresponding to jet energies above 40 GeV are included in the fit the  $\chi^2$  is extremely large. As these high-energy bins are heavily populated, the errors on multiplicity values in these bins are small, implying a large contribution to  $\chi^2$  from these bins. These bins, however, correspond to “almost two-jet” events, described in section 8.4, which are expected to be particularly sensitive to jetfinder and initial  $y_{\text{cut}}$ .

Restricting the fit to areas of the plane where jets have energy less than 40 GeV results in both a lower  $\chi^2$  and more stable values of  $f_g$  and  $\kappa$ , the former approaching  $\sim 1.5$  for each jet. This value is in agreement with previous fits to three jet data (see section 10.8) although from these fits one cannot discern whether the topology dependent scales ( $F_{\text{opt}}=\text{II}\&\text{III}$ ) describe the data any better than the independent scale ( $F_{\text{opt}}=\text{I}$ ). The best fit for the multiplicity of the hardest jet, based on the naïve QCD model with  $F_{\text{opt}}=\text{III}$  and  $E_{\text{opt}}=3$ , compared to the MCTRUTH value as a function of position on the Dalitz plane is shown in figure 9.5.

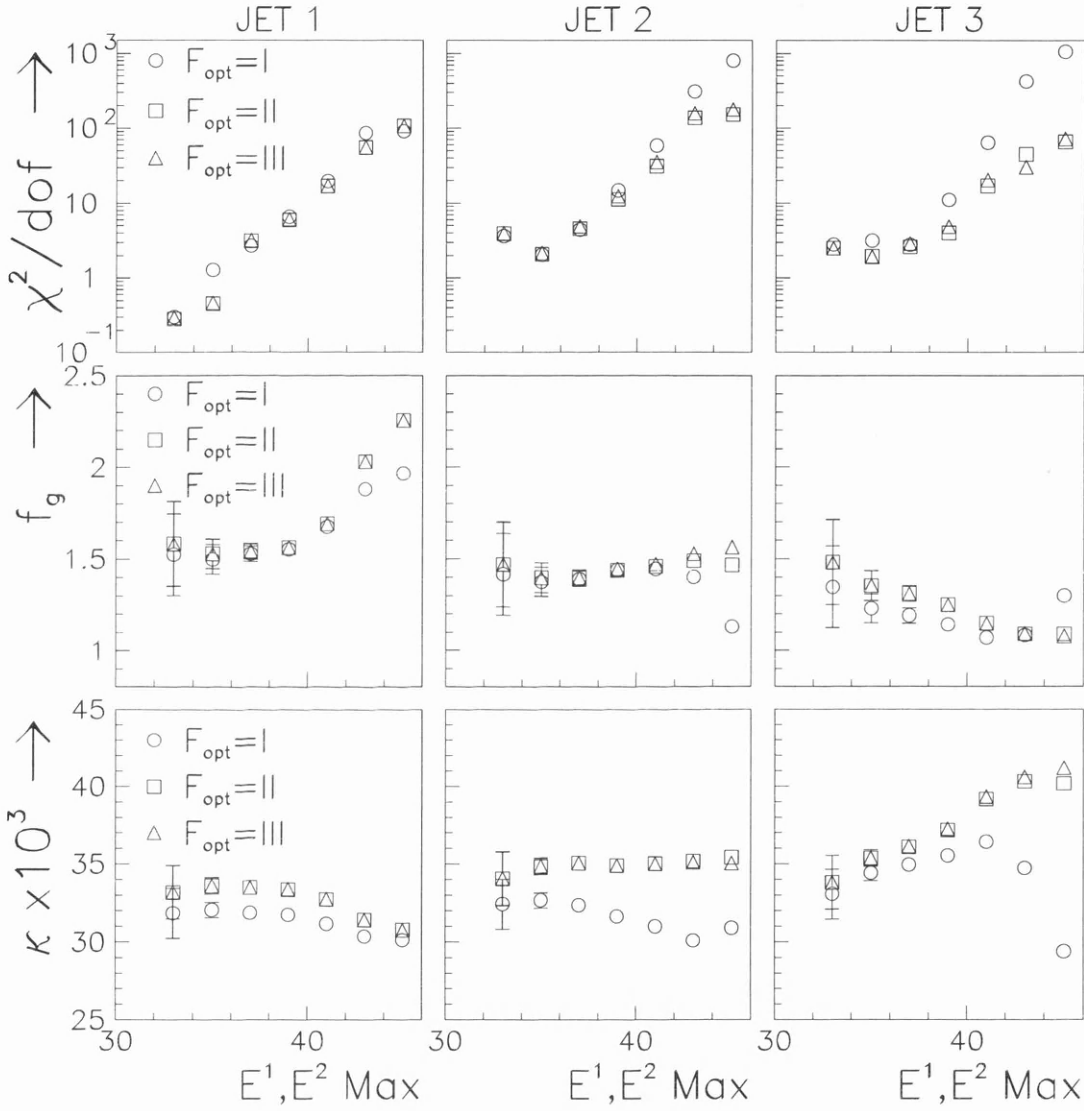


Figure 9.4: Results of fits to individual jet multiplicities in the TRUTH level sample over restricted areas of the Dalitz plane by requiring  $E_{1,2} \leq E_{\text{max}}$ . Three options for the scale dependence of the jet multiplicities,  $F_{\text{opt}}$ , are used: I=○, II=□, III=△.

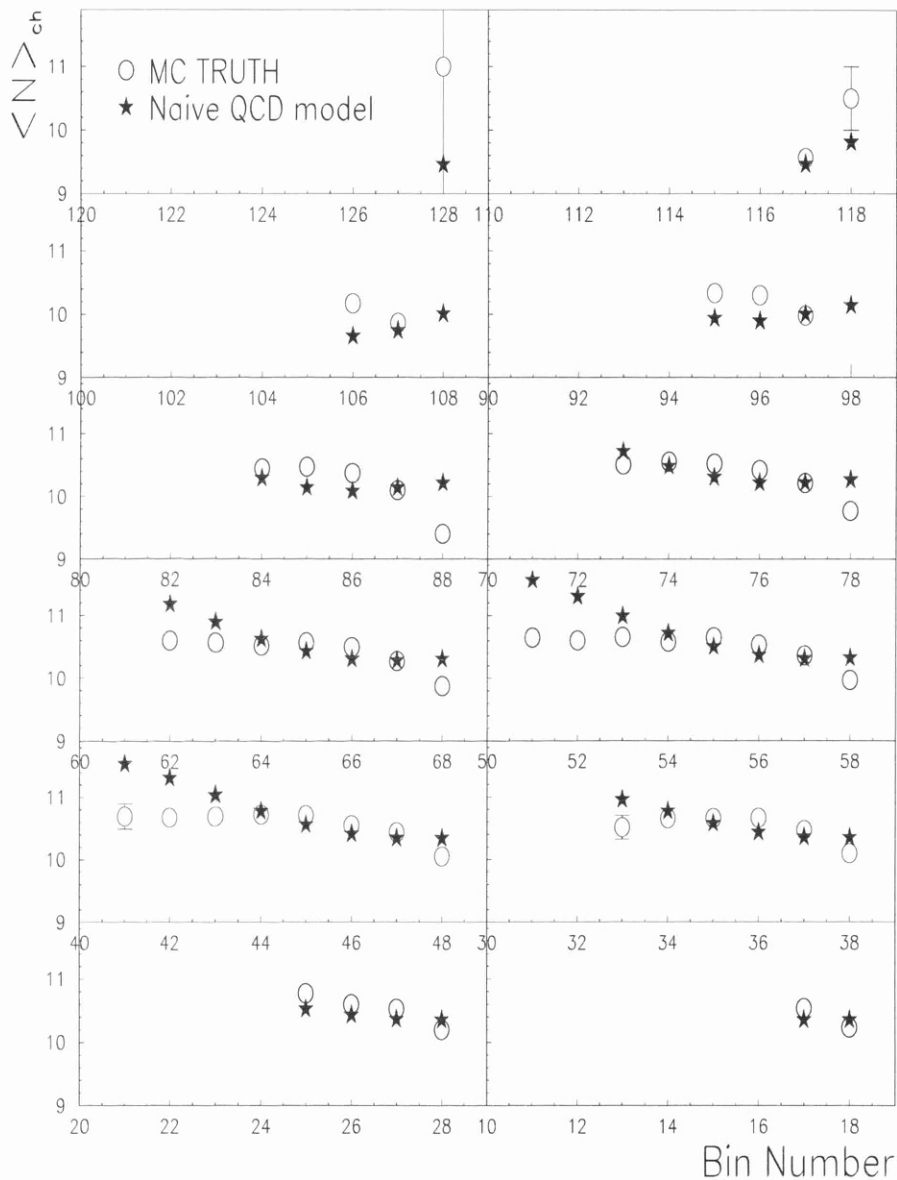


Figure 9.5: Result of fit to the multiplicity of the hardest jet, selected in MCTRUTH data, across the full Dalitz plane. The naïve QCD model with  $F_{opt}=III$  and  $E_{opt}=3$  is used to predict the multiplicity in each bin.

### 9.2.3 Conclusions Of Fits To Jet Multiplicity

The study implies that the naïve QCD model prediction cannot describe individual jet multiplicities over the whole Dalitz plane, especially in the right-hand bins where jets have an energy approaching  $\frac{1}{2}\sqrt{s}$ . The MLLA expression fails to such an extent that the possibility of whether or not there is a topology dependence cannot be determined.

The reason for the failure lies in the fact that the basic MLLA formula is derived for an *inclusive* measurement whereas the jets in this analysis are obtained with the use of a specific jetfinder [68]. During the clustering process, particles lying near the centre of the interjet regions are associated to jets according to a prescription which has no reference in any of the QCD expressions: the predictions, therefore, cannot incorporate any effects that the chosen jetfinder may have on the multiplicity distributions. The direct investigation of topological effects on separate jets is hence impracticable by the method employed in this analysis.

## 9.3 ALEPH Event Multiplicity

### 9.3.1 Introduction

When one considers the total event multiplicity, *i.e.* the *sum* over the jets, the sensitivity to jet definition should be greatly reduced as the association of individual particles to specific jets becomes unimportant. The prediction for the event multiplicity has to take into account the probability that each jet originated from the gluon, and is given as the sum over all permutations of equations (8.7–8.9).

In this section, predictions for the event multiplicity are calculated with a chosen topological and energy option and smeared across the plane according to migration matrices obtained from a study of 4 million JETSET Monte Carlo events. They are then compared directly to the charged multiplicity in ALEPH data events. The dependence of the fit on areas of the plane containing high-energy jets is investigated by repeating the fit over different areas of the plane as described in section 9.2.2.

### 9.3.2 Results With Fitting Option

The results of the fits to the basic DURHAM sample with each fitting option are summarised in figure 9.6. The energy option  $E_{\text{opt}}=3$  is used throughout, that is, the value in each bin of the Dalitz plane, prior to smearing, is the averaged prediction over 100 sub-bins. A cut on the energy of the two hardest jets,  $E_{1,2} \geq E_{\text{max}}$ , is applied to restrict the fits to limited areas of the plane.

For each fit,  $f_g$  and  $\kappa$  are almost fully anti-correlated (see the example given in appendix B), and  $\Lambda$  is fixed to the aforementioned value of 150 MeV. The topology independent scale ( $F_{\text{opt}}=1$ ) is seen to be completely inappropriate to describe the event multiplicity across the plane, with a  $\chi^2/dof$  much greater than one for  $E_{\text{max}} \geq 39$  GeV. Only at the two lowest  $E_{\text{max}}$  cuts is the  $\chi^2$  of the same order of magnitude for every choice of scale, however the errors on  $f_g$  and  $\kappa$  become correspondingly large when the number of available bins is reduced.

The plane is very poorly fit with any choice of scale when highest energy bins are included in the fit. There are a number of possible reasons for this observation. It was noted in section 9.2 that the multiplicity of high-energy quark jets, and correspondingly low-energy gluon jets, are not well predicted by the naïve MLLA expression. If one assumes that this is largely due to the jetfinder dependence of the association of interjet particles to particular jets, then the anomaly should be greatly reduced when the total multiplicity is considered. There will however still be some residual jetfinder dependence which cannot be removed.

For example, consider the case where one of the jets in a “genuine”<sup>2</sup> TRUTH level 2-jet event is reconstructed by the jetfinder as two individual jets. The other reconstructed jet will have (close to) 45.6 GeV, and hence the event will be binned in the rightmost column of the Dalitz plane. Conversely, “genuine” three-jet events could be erroneously reconstructed as two-jet events and not appear in the fit sample. The multiplicity in the righthand bins is therefore not representative of a pure three-jet sample. This systematic uncertainty will decrease as the jets become more separated in phase space.

Without any assumption of topology dependence, the extracted values of  $f_g$  are greater than the leading order prediction given in equation (3.5). At the lowest  $E_{\text{max}}$  cut  $f_g$  becomes larger than 20. The prediction obtained with fitting option III yields the lowest  $\chi^2/dof$  for every value of  $E_{\text{max}}$ , with  $\chi^2/dof \approx 1$  in

---

<sup>2</sup>Here the label “genuine” is used to indicate that no hard gluon is actually emitted in the ‘true’ hadronic event and the  $q\bar{q}$  pair form two independent showers. Similarly, a “genuine” three-jet event has an underlying  $q\bar{q}g$  structure at TRUTH level which may or may not be reconstructed after the event has traversed the detector.

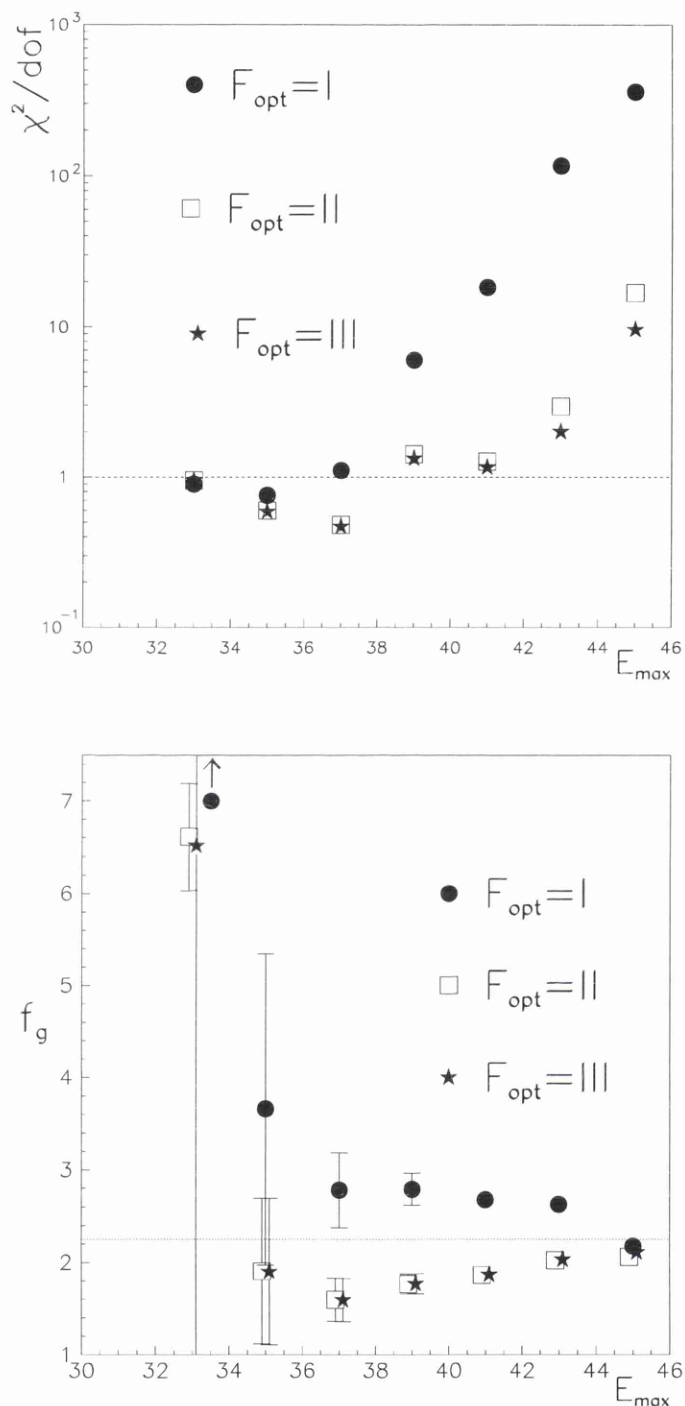


Figure 9.6: The  $\chi^2/dof$  (top) and gluon factor,  $f_g$ , obtained from fits to the total charged multiplicity in ALEPH events with each topological scale,  $F_{\text{opt}}$ . The fits are restricted to limited areas of the plane by the cut  $E_{1,2} \leq E_{\max}$ . In the lower plot the points are separated horizontally for clarity and the dotted line marks the leading order prediction for the ratio of gluon and quark jet multiplicities.

all fits bar when the rightmost column of bins are included. The two options for topology dependent scales become equally capable of describing the data when all jet energies are restricted to be less than 41 GeV. This is because the predictions obtained with these scales are expected to differ significantly only in the highest energy bins of the plane (see fig. 8.5). The parameters extracted from the fits therefore become comparable as  $E_{\max}$  is decreased.

A value of  $f_g \approx 1.6$  is extracted when only the near-Mercedes bins are fit, *i.e.*  $E_{\max} \leq 37$  GeV, but this value increases to  $\approx 2.0$  when bins containing more asymmetric topologies are included. To compare the values between fitting options and jetfinder samples the parameters are taken from fits restricted to  $E_{\max} \leq 41$  GeV. Here the  $\chi^2$  of the topological fits are commensurate with unity, and a sufficient area of the plane is fit so as to keep the relative errors on the fitted parameters small.

The fits to the binned charged multiplicity of the basic DURHAM sample with each  $F_{\text{opt}}$  give the values:

$F_{\text{opt}}=\text{I:}$	$f_g = 2.677 \pm 0.078$	$\kappa = 25.89 \pm 0.40 \times 10^{-3}$	$\chi^2/dof = 18.37$
$F_{\text{opt}}=\text{II:}$	$f_g = 1.862 \pm 0.055$	$\kappa = 34.11 \pm 0.44 \times 10^{-3}$	$\chi^2/dof = 1.27$
$F_{\text{opt}}=\text{III:}$	$f_g = 1.866 \pm 0.055$	$\kappa = 34.11 \pm 0.44 \times 10^{-3}$	$\chi^2/dof = 1.15$

All these fits use  $\Lambda=150$  MeV and energy option  $E_{\text{opt}}=3$ .

### 9.3.3 The Dependence On Energy Option

In the previous fits, a weighted prediction was calculated for each Dalitz bin prior to smearing, that is  $E_{\text{opt}}=3$ . The weights are obtained by recording the population of TRUTH level JETSET events in 100 sub-bins within each  $2 \times 2$  GeV bin. It is therefore assumed that the Monte Carlo produces the correct distribution of events across each bin. To see if the fits are indeed improved by incorporating the sub-bin information, Dalitz planes are binned with the multiplicity given by  $F_{\text{opt}}=\text{III}$  with each energy option, smeared and then fit to the data. The resultant fitted parameters are:

$E_{\text{opt}}=1:$	$f_g = 1.862 \pm 0.053$	$\kappa = 34.09 \pm 0.43 \times 10^{-3}$	$\chi^2/dof = 1.25$
$E_{\text{opt}}=2:$	$f_g = 1.874 \pm 0.054$	$\kappa = 34.02 \pm 0.43 \times 10^{-3}$	$\chi^2/dof = 1.18$
$E_{\text{opt}}=3:$	$f_g = 1.866 \pm 0.055$	$\kappa = 34.11 \pm 0.44 \times 10^{-3}$	$\chi^2/dof = 1.15$

The difference obtained by averaging the prediction across each bin is only slight as the  $\chi^2/dof$  are comparable for each  $E_{\text{opt}}$ . As was previously mentioned, the MLLA-based expressions are relatively slow functions of energy and the difference in extracted values between  $E_{\text{opt}}=1, 2$  and 3 is generally small.

### 9.3.4 The Dependence On The Jetfinder

To investigate the sensitivity of the fitted values to jet definition, the naïve QCD model predictions are fit to the three-jet data samples selected using the basic and modified DURHAM jetfinders. The parameters extracted from the fits at each  $E_{\max}$  cut are summarised in figure 9.7.  $F_{\text{opt}}=\text{III}$  is used throughout to give a direct comparison as it was found to best describe the multiplicity in section 9.3.2.

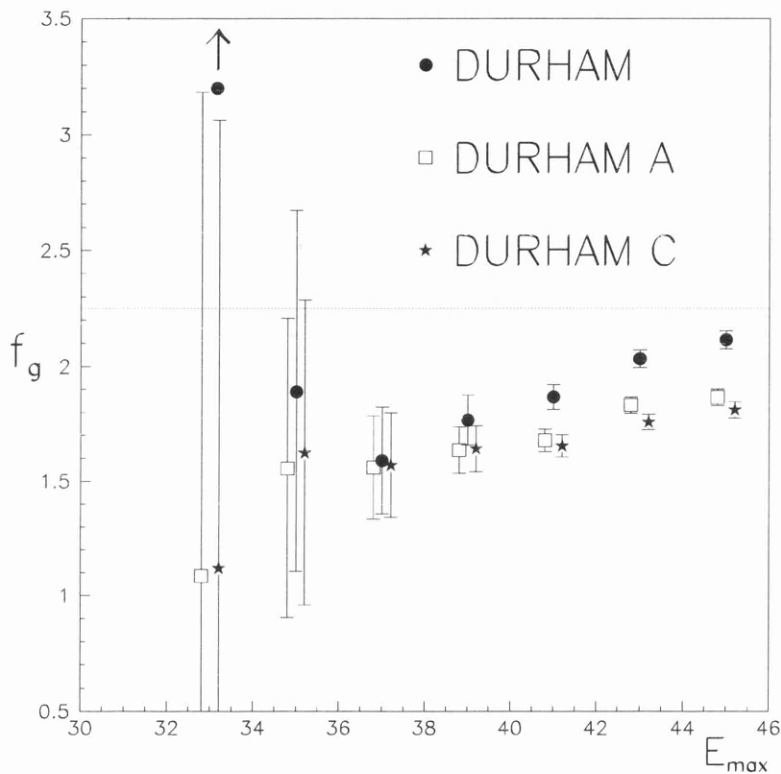


Figure 9.7: Results of fits to the total charged multiplicity in ALEPH events selected with different jetfinders. The fitting option  $F_{\text{opt}}=\text{III}$  and energy option  $E_{\text{opt}}=3$  are used for each fit, which is restricted to areas of the plane with the cut  $E_{1,2} \leq E_{\max}$ . The points are separated horizontally for clarity and the dotted line marks the leading order prediction for the ratio of gluon and quark jet multiplicities.

It is seen that  $f_g$  is lower in magnitude and a little more stable to the choice of  $E_{\max}$  with the ‘A’ and ‘C’ samples than for the basic sample. The stability of the gluon factor might suggest that the modified schemes select a higher proportion of events that have a true three-parton skeleton so that there is less contamination from “genuine” two-jet events. The QCD formulae contained in the three fitting

options do not however describe the ‘A’ and ‘C’ planes as well as the basic plane, reflected in larger  $\chi^2/dof$  values with each choice of  $E_{\max}$ .

The fitted values are similar for both ‘A’ and ‘C’ modified schemes due to the angular ordering which is common to both jetfinders. At a cut of  $E_{\max} \leq 41$  GeV the fits for each jetfinder are:

DURHAM:	$f_g = 1.866 \pm 0.055$	$\kappa = 34.11 \pm 0.44 \times 10^{-3}$	$\chi^2/dof = 1.15$
DURHAM-‘A’:	$f_g = 1.677 \pm 0.050$	$\kappa = 35.67 \pm 0.43 \times 10^{-3}$	$\chi^2/dof = 1.70$
DURHAM-‘C’:	$f_g = 1.653 \pm 0.050$	$\kappa = 35.88 \pm 0.43 \times 10^{-3}$	$\chi^2/dof = 2.04$

All these fits use  $\Lambda = 150$  MeV, fitting option  $F_{\text{opt}} = \text{III}$  and energy option  $E_{\text{opt}} = 3$ .

# Chapter 10

## Systematic Uncertainties

The values of the gluon factor obtained from the fits are quoted in the previous chapter with a statistical error only. Here we consider the systematic error on these measurements due to various biases introduced during the analysis chain. They are discussed and evaluated in the following sections, with final systematic errors quoted in section 10.7.

### 10.1 Introduction

In the following studies the value and error of the resulting gluon factor,  $f^{syst} \pm \sigma_f^{syst}$ , are used to construct the difference,  $\Delta f_g$ , and significance,  $S_f$ , of the measurements with respect to the values of  $f_g \pm \sigma f_g$  quoted in section 9.3.4.  $\Delta f_g$  and  $S_f$  are defined in the systematic studies as:

$$\begin{aligned}\Delta f_g &= f^{syst} - f_g, \\ S_f &= \frac{|\Delta f_g|}{\sqrt{(\sigma_f^{syst})^2 + (\sigma f_g)^2}}.\end{aligned}$$

The value of  $\chi^2$  is given for each least-squares fit to illustrate how well the distributions are described by the QCD model prediction. Unless otherwise stated all the fits are performed using fitting option  $F_{opt}=III$  and energy option  $E_{opt}=3$ , with the Dalitz plane restricted to bins where  $E_{1,2} \leq 41$  GeV.

### 10.2 Systematic Errors Due To Jetfinding

It has been stressed that measurements in quark-gluon jet studies are strongly dependent on the adopted jet definition. The DURHAM jetfinder uses an initial

$y_{\text{cut}}$ , called  $y_o$ , that forces all jets in an event to have a minimum transverse momenta with respect to each other and hence be clearly separated. The value of  $y_o=10^{-2}$ , corresponding to a  $k_{\perp}$  of  $\approx 10$  GeV, was chosen to give a large range of jet energies and hence event topologies. Although this value is common to several other analyses [85, 68, 4, 62, 63] the choice still remains somewhat arbitrary; for example OPAL employ the larger value  $y_o=2\times 10^{-2}$  [58, 59, 60]. A smaller  $y_o$  means that more “genuine” two-jet events are interpreted as having three or more jets. As one changes the three-jet sample then the jet energy and multiplicity distributions, which influence the fitted values of  $f_g$  and  $\kappa$ , also change.

The association of interjet particles to specific jets will have a complex effect on the fits across the Dalitz plane. Firstly, the jet multiplicities are correlated as the loss of a particle from one jet has to result in a gain in another. Secondly the angles between the jets will change, changing not only the energies obtained via Lamy’s theorem but also the suppression factors. The analysis is repeated at a larger and smaller initial  $y_{\text{cut}}$ ,  $y_o=2\times 10^{-2}$  and  $y_o=5\times 10^{-3}$ , to estimate the systematic uncertainties on the measured gluon factors from each jetfinder sample. The resultant fits to each jetfinder multiplicity distribution with  $y_o$  yield the values:

	DURHAM			DURHAM ‘A’			DURHAM ‘C’		
	$\Delta f_g$	$S_f$	$\chi^2$	$\Delta f_g$	$S_f$	$\chi^2$	$\Delta f_g$	$S_f$	$\chi^2$
$y_o = 2 \times 10^{-2}$	+0.062	0.73	1.44	+0.117	1.50	1.69	+0.097	1.25	1.87
$y_o = 1 \times 10^{-2}$	$f_g=1.866\pm .055$		1.15	$f_g=1.677\pm .050$		1.70	$f_g=1.653\pm .050$		2.04
$y_o = 5 \times 10^{-3}$	+0.037	0.39	1.64	-0.012	0.14	2.64	+0.002	0.03	2.62

Using the higher value of  $y_o=2\times 10^{-2}$  results in a significant increase in the measured value of  $f_g$  for each jetfinder sample.  $S_f>1$  for the ‘A’ and ‘C’ multiplicity samples suggesting that they are more sensitive to the initial  $y_{\text{cut}}$  which is equivalent to a  $k_{\perp}$  cut of  $\approx 13$  GeV. However,  $f_g$  is almost unchanged for these jetfinding schemes when  $y_o=5\times 10^{-3}$  ( $k_{\perp}\approx 6$  GeV) is used. It would be interesting to see how the values compared at the larger value of  $y_o=10^{-1}$  employed in recent ALEPH three-jet studies [65, 66, 2]: however, the number of candidate events becomes small and the populated area is reduced (see figures 5.3&5.7) so that the topological fitting technique employed in this analysis becomes impractical. The choice of recombination scheme has a negligible effect on the value of  $f_g$  in this analysis compared to the choice of  $y_o$ .

## 10.3 Systematic Errors Due To Selection Cuts

### 10.3.1 Fraction of Neutral Energy

Once three-jet event candidates are selected by a jetfinder, they are subjected to quality cuts which could introduce biases in the remaining sample. The cut on the fraction of energy in each jet that is carried by neutral objects will affect the charged multiplicity in the sample— increasing the cut, so as to accept jets with a larger neutral to charged energy ratio, results in a decrease in  $\langle n_{ch} \rangle$ . The analysis is repeated with the cut on neutral energy changed from 85% to 70% & 100%, the latter implying no limit on the energy fraction. The average charged multiplicity in three-jet ALEPH events, selected with the basic DURHAM jetfinder, at each neutral energy cut are; 22.08 (cut=70%); 21.50 (cut=85%); and 21.13 (cut=100%).

The results from the fits are:

	DURHAM			DURHAM 'A'			DURHAM 'C'		
	$\Delta f_g$	$S_f$	$\chi^2$	$\Delta f_g$	$S_f$	$\chi^2$	$\Delta f_g$	$S_f$	$\chi^2$
cut=100%	+0.062	0.62	1.37	+0.026	0.29	1.91	+0.027	0.31	1.94
cut=85%	$f_g=1.866 \pm .055$		1.15	$f_g=1.677 \pm .050$		1.70	$f_g=1.653 \pm .050$		2.04
cut=70%	-0.022	0.22	1.55	-0.034	0.38	1.82	-0.028	0.30	1.88

For each jetfinder sample, the measured value of  $f_g$  decreases when a stricter cut on the fraction of neutral energy is applied, whilst  $f_g$  increases when the cut is relaxed. As the cut is relaxed the fraction of  $q\bar{q}\gamma$  events in the binned samples is increased. The average multiplicity of the softest jet, most likely consisting of the hard  $\gamma$  and some other clustered tracks, will have a lower average multiplicity than a gluon jet of the same energy. The net effect on the fitted parameters is complex, although  $f_g$  is relatively stable to the cut.

### 10.3.2 Polar Angle $\theta_Z$

The polar and planarity cuts are designed to select only those events that are well reconstructed. The distribution of events across the plane is affected by these cuts, those with a low interjet angle tending to be suppressed as either cut is increased. The cut  $\theta_Z$  was introduced to ensure that each jet in an event

subtends an angle larger than  $40^\circ$  to the  $z$ -axis– this was motivated by the studies in section 5.3.2 which found that the typical jet opening angle is  $\approx 40^\circ$ .

Although the fraction of jet tracks lost in a reconstructed event will decrease as the  $\theta_Z$  cut is increased, the population binned on the Dalitz plane falls and the fits becomes statistically limited. A study of the effect of the  $\theta_Z$  cut was carried out in section 6.6, showing that  $\sim 75\%$  of events pass a cut  $\theta_Z > 40^\circ$ . Figure 6.7 showed that the improvement in energy resolution of the hardest jet, which is a function of the number of lost or badly reconstructed tracks in an event, is minimal if a stricter cut of  $60^\circ$  is applied.  $\theta_Z$  is therefore varied by  $\pm 10^\circ$  in this study to cover a practical range of possible cut values.

The following table summarises the systematic effect of the  $\theta_Z$  selection cut on the quoted value of the gluon factor:

	DURHAM			DURHAM 'A'			DURHAM 'C'		
	$\Delta f_g$	$S_f$	$\chi^2$	$\Delta f_g$	$S_f$	$\chi^2$	$\Delta f_g$	$S_f$	$\chi^2$
$\theta_Z < 50^\circ$	+0.010	0.11	1.08	-0.034	0.42	1.50	-0.021	0.26	1.61
$\theta_Z < 40^\circ$	$f_g = 1.866 \pm .055$		1.15	$f_g = 1.677 \pm .050$		1.70	$f_g = 1.653 \pm .050$		2.04
$\theta_Z < 30^\circ$	+0.004	0.06	1.36	+0.036	0.55	1.45	+0.040	0.61	1.90

The polar angle cut has little effect on the value of  $f_g$  measured using the events selected with the basic algorithm. The modified jetfinders are more sensitive, each change in  $\theta_Z$  changing  $f_g$  by  $\sim 2\%$ . It is shown in figure 7.5 that a significant number of the softest jets in an event have a polar angle of around  $30^\circ$ , implying that most events fail the  $\theta_Z$  cut due to the softest jet lying at small angles. This does not imply that soft (and hence “gluon”) jets have a higher probability of being emitted close the beampipe than the harder “quark” jets– rather, any low-angle jet is likely to lose particles, and therefore energy, during reconstruction.

### 10.3.3 Planarity Angle $\theta_P$

The value of the cut on  $\theta_P$  was chosen to ensure that all the jets in a three-jet event lie close to a single plane. Figure 7.6 shows the cut relative to the  $\theta_P$  distribution of each jet. To estimate the dependence of  $f_g$  on  $\theta_P$ , the cut was changed to  $10^\circ$  and  $2^\circ$  and the analysis repeated. The lower cut forces events to be very planar whilst almost all jets pass the higher cut value. The measurements of  $f_g$  are given below.

	DURHAM			DURHAM 'A'			DURHAM 'C'		
	$\Delta f_g$	$S_f$	$\chi^2$	$\Delta f_g$	$S_f$	$\chi^2$	$\Delta f_g$	$S_f$	$\chi^2$
$\theta_{UP} < 10^0$	+0.160	2.19	1.42	+0.079	1.20	3.35	+0.070	1.07	4.13
$\theta_{UP} < 5^0$	$f_g=1.866 \pm .055$		1.15	$f_g=1.677 \pm .050$		1.70	$f_g=1.653 \pm .050$		2.04
$\theta_{UP} < 2^0$	-0.132	1.21	0.86	-0.044	0.43	1.16	-0.047	0.46	1.20

An increase in the cut value leads to a higher measured value of  $f_g$  and *vice-versa*. The binned multiplicity across the Dalitz plane of the basic DURHAM jetfinder sample is the most sensitive to  $\theta_P$ –  $f_g$  changes by  $\approx \pm 8\%$  as the cut is varied about the nominal value of  $5^0$ .

## 10.4 Systematic Errors Due To Correction Method

The fits to ALEPH data rely on the smearing of QCD predictions across the Dalitz plane with correction matrices obtained from JETSET Monte Carlo events which are compared at TRUTH and RECO levels. The correction method is explained in detail in section 8.3.

### 10.4.1 Jetclass

Monte Carlo events are associated with a *jetclass* (see section 6.3) depending on the relative number of jets in the event that remain after clustering with  $y_o=10^{-2}$  at both levels. The jetclasses that contribute to the correction matrices are given in table 10.1. The nominal correction or migration matrices include “IMPURE” events, which have a different number of jets at each level, and “HIGH” events, which have  $N$  jets at both levels where  $N \geq 4$ .

	<i>Jetclass</i>	$N_{jet}(\text{RECO})$	$N_{jet}(\text{TRUTH})$
1	PURE	3	3
2	IMPURE	4,5,6,...	3
3	IMPURE	3	4,5,6,...
4	HIGH	4,5,6,...	

Table 10.1: Events classified according to the number of jets,  $N_{jet}$ , obtained at RECO and TRUTH levels.

Table 6.1 showed that the majority of retained Monte Carlo events have  $\text{jetclass}=1$ . The sample of events used to correct the data in the nominal case contains approximately 80% events with  $\text{jetclass}=1$ , 10% events with  $\text{jetclass}=2\&3$  and 10% events with  $\text{jetclass}=4$ . To investigate the effect of including “IMPURE” and “HIGH” events, the fits are repeated using migration matrices re-calculated using only “PURE” events, or with “HIGH” events excluded, to obtain the following values:

	DURHAM			DURHAM ‘A’			DURHAM ‘C’		
	$\Delta f_g$	$S_f$	$\chi^2$	$\Delta f_g$	$S_f$	$\chi^2$	$\Delta f_g$	$S_f$	$\chi^2$
<b>Jetclass 1</b>	-0.026	0.34	1.14	+0.081	1.13	1.15	+0.075	1.06	1.41
<b>Jetclass 1-3</b>	-0.016	0.21	1.19	+0.003	0.04	1.53	+0.007	0.10	1.84
<b>Jetclass 1-4</b>	$f_g=1.866\pm .055$		1.15	$f_g=1.677\pm .050$		1.70	$f_g=1.653\pm .050$		2.04

When only “PURE” Monte Carlo events are used  $f_g$  falls only slightly for fits to the basic DURHAM sample, but rises significantly for the ‘A’ and ‘C’ samples. If events with  $\text{jetclass}=4$  are omitted from the correction procedure then the extracted values of  $f_g$  remain relatively unchanged irrespective of the jetfinder used.

### 10.4.2 Monte Carlo Generator

The dependence on the Monte Carlo used to smear the theoretical predictions can be judged by re-calculating the correction matrices using events generated by HERWIG. As the HERWIG event sample contains only  $\sim 150\,000$  events, the error on each individual correction matrix element, discussed in section 8.3.3, can no longer be neglected. As a rough estimate the error on the smeared prediction in each bin is assumed to be three times the data error in the corresponding bin. The fitted values with this approximation are tabulated below. Although the smearing error is somewhat crudely fixed the measured values of  $f_g$  are stable if this error is doubled or halved. The DURHAM ‘A’ three-jet sample is seen to be most sensitive to the choice of Monte Carlo generator.

	DURHAM			DURHAM 'A'			DURHAM 'C'		
	$\Delta f_g$	$S_f$	$\chi^2$	$\Delta f_g$	$S_f$	$\chi^2$	$\Delta f_g$	$S_f$	$\chi^2$
HERWIG	-0.032	0.18	3.68	+0.098	0.57	3.37	+0.025	0.15	3.32
JETSET	$f_g=1.866 \pm .055$		1.15	$f_g=1.677 \pm .050$		1.70	$f_g=1.653 \pm .050$		2.04

### 10.4.3 Bin-by-bin Correction Factors

As a final test of the applicability of the folding method employed in this analysis, the fits are repeated using a bin-by-bin factor to correct the un-smearred Dalitz planes. The factor is simply the charged multiplicity in each Dalitz bin at RECO level divided by that at TRUTH level.

The fitted values are:

	DURHAM			DURHAM 'A'			DURHAM 'C'		
	$\Delta f_g$	$S_f$	$\chi^2$	$\Delta f_g$	$S_f$	$\chi^2$	$\Delta f_g$	$S_f$	$\chi^2$
bin-by-bin	-0.027	0.35	1.46	-0.024	0.35	1.79	-0.014	0.20	2.30
smearred	$f_g=1.866 \pm .055$		1.15	$f_g=1.677 \pm .050$		1.70	$f_g=1.653 \pm .050$		2.04

The use of the bin-by-bin correction factors results in a slightly lower measured value of  $f_g$  for each jetfinder event sample. By taking into account migrations across the plane a better fit is achieved, reflected in the larger  $\chi^2$  obtained with the simple bin-by-bin method.

## 10.5 Systematic Errors Due To Fitting Method

### 10.5.1 QCD Scale Factor

Due to the construction of the MLLA-based expressions, the MINUIT package fails to reach a minimum when the normalization, QCD scale factor and gluon factor are all left free. To remedy this problem the scale factor,  $\Lambda$ , was fixed to 150 MeV in all the fits (see section 9.2.2). This value lies in the range  $\approx 100$ –250 MeV of previous experimentally determined values– the impact of this assumption is investigated by repeating the fits with  $\Lambda$  fixed at 100, 200 and 250 MeV.

	DURHAM			DURHAM 'A'			DURHAM 'C'		
	$\Delta f_g$	$S_f$	$\chi^2$	$\Delta f_g$	$S_f$	$\chi^2$	$\Delta f_g$	$S_f$	$\chi^2$
$\Lambda=100$ MeV	+0.060	0.75	1.18	+0.051	0.71	1.85	+0.049	0.68	2.23
$\Lambda=150$ MeV	$f_g=1.866 \pm .055$		1.15	$f_g=1.677 \pm .050$		1.70	$f_g=1.653 \pm .050$		2.04
$\Lambda=200$ MeV	-0.044	0.58	1.14	-0.035	0.50	1.60	-0.035	0.51	1.91
$\Lambda=250$ MeV	-0.078	1.04	1.15	-0.063	0.87	1.53	-0.062	0.91	1.81

The results indicate that the systematic effect is essentially equal amongst the three event samples. The measured gluon factor increases as the QCD scale factor is decreased and *vice-versa*. A variation in  $f_g$  of  $\approx 4\%$  is seen when  $\Lambda$  is varied across the range 100–250 MeV.

### 10.5.2 Fitting Option

The results to the charged multiplicity, summarized in section 9.3.4, are quoted for fits with option  $F_{\text{opt}}=\text{III}$ . This option incorporates a single gluon scale which stems from the assumption that  $\alpha_s$  has a simple logarithmic scale dependence. The effect this assumption has on  $f_g$  is assessed by repeating the fits with  $F_{\text{opt}}=\text{II}$  which has a two-component expression for the gluon scale. The fitting options are described in section 8.2.1.

	DURHAM			DURHAM 'A'			DURHAM 'C'		
	$\Delta f_g$	$S_f$	$\chi^2$	$\Delta f_g$	$S_f$	$\chi^2$	$\Delta f_g$	$S_f$	$\chi^2$
$F_{\text{opt}}=\text{II}$	-0.004	0.05	1.27	-0.005	0.07	2.06	-0.006	0.09	2.49
$F_{\text{opt}}=\text{III}$	$f_g=1.866 \pm .055$		1.15	$f_g=1.677 \pm .050$		1.70	$f_g=1.653 \pm .050$		2.04

One concludes that the difference in fitted values is negligible. Nevertheless, the combined gluon scale incorporated within the naïve QCD prediction is seen to describe the data better than the two-component scale.

## 10.6 Effect Of Massive Kinematics

The jet energies in each three-jet event were estimated using Lamy's theorem with the assumption that the jets were massless. It was discussed in section 6.2

that the jet masses can be incorporated to give a “massive” energy definition for the jets. These energies can take values up to  $\sim 50$  GeV, but only events lying within the area depicted in figure 3.6 can be fit with the QCD expressions. The actual number of events excluded is generally small, as shown in figure 8.3(c), but the multiplicity distribution across the Dalitz plane will be different depending on whether the “massless” or “massive” definition is used, simply because the difference between jet energies obtained with each definition is typically  $\approx 1$  GeV.

The fits are repeated using the “massive” estimator to define each event’s position on the plane to give the values tabulated below. The effect is an increase in  $f_g$  for the fits, the greatest change being for the modified jetfinder samples. The  $\chi^2$  are large indicating the problems associated with fitting the “massive” binned sample. During the least-squares fit, a QCD prediction can only be calculated for Dalitz bins lying inside the boundary marked on figure 8.1. However, the correction matrices take into account migrations to and from *every* bin on the plane—the contribution from those events that lie outside the fit region at TRUTH level, but are reconstructed inside, is therefore lost. A consequence is that the smeared QCD prediction becomes unreliable, especially in bins lying on the upper or righthand boundaries.

		DURHAM			DURHAM ‘A’			DURHAM ‘C’		
		$\Delta f_g$	$S_f$	$\chi^2$	$\Delta f_g$	$S_f$	$\chi^2$	$\Delta f_g$	$S_f$	$\chi^2$
$E_{Lamy}^M$		+0.152	1.85	3.79	+0.292	3.81	2.70	+0.217	2.89	2.40
$E_{Lamy}$		$f_g=1.866 \pm .055$		1.15	$f_g=1.677 \pm .050$		1.70	$f_g=1.653 \pm .050$		2.04

These values are not included in the overall systematic uncertainty. Rather, to be consistent with recent topological studies [85, 68], the gluon factor is quoted in this analysis as being that obtained given the assumption of massless kinematics.

## 10.7 Combined Systematic Error

To estimate the total systematic error, the maximum increase and decrease in  $f_g$  for each systematic variable described in sections 10.2–10.5 are added. This in effect give the ‘maximum’ systematic error in the sense that each component is assumed to be independent—in practice they are expected to cancel to some degree. The components are summarized below in table 10.2.

A large contribution to the error on  $f_g$  measured from each jetfinder sample

Systematic error	$\Delta f_g$		
	DURHAM	DURHAM 'A'	DURHAM 'C'
<b>Jetfinding</b>			
$y_o$	+0.062 -0.000	+0.117 -0.012	+0.097 -0.000
<b>Selection</b>			
Neutral Energy Fraction	+0.062 -0.022	+0.026 -0.034	+0.027 -0.028
Polar Angle $\theta_Z$	+0.010 -0.000	+0.036 -0.034	+0.040 -0.021
Planarity Angle $\theta_P$	+0.160 -0.132	+0.079 -0.044	+0.070 -0.047
<b>Correction</b>			
Jetclass	+0.000 -0.026	+0.081 -0.000	+0.075 -0.000
Monte Carlo	+0.000 -0.031	+0.098 -0.000	+0.025 -0.000
Bin-by-bin	+0.000 -0.027	+0.000 -0.024	+0.000 -0.014
<b>Fitting</b>			
QCD Scale Factor $\Lambda$	+0.060 -0.078	+0.051 -0.063	+0.049 -0.062
Fitting Option	+0.000 -0.004	+0.000 -0.005	+0.000 -0.006

Table 10.2: The combined systematic errors on  $f_g$ .

comes from the choice of the initial  $y_{\text{cut}}$ ,  $y_o$ , and the planarity angle,  $\theta_P$ . The cut on the neutral energy fraction, described in section 7.3, and the polar angle cut, described in section 7.4, have a much smaller bearing on the fitted values. Fits to the multiplicity distribution obtained using the basic DURHAM jetfinder prove relatively insensitive to the correction method. However the modified jetfinders, especially the 'A' scheme, have a larger systematic error associated with the smearing process. Although it proved necessary to fix the QCD scale parameter  $\Lambda$  in the fits, the change in  $f_g$  as  $\Lambda$  is varied over a range of possible values is not greater than that of the other systematic uncertainties.

## 10.8 Final Measurement Of The Gluon Factor

The positive and negative errors are added for each systematic variable in table 10.2 to give the following values of  $f_g$ :

$$\begin{array}{llllll}
 \text{DURHAM} & f_g & = & 1.866 & \pm & 0.055(\text{stat}) \quad +0.354(\text{syst}) \\
 \text{DURHAM-‘A’} & f_g & = & 1.677 & \pm & 0.050(\text{stat}) \quad +0.488(\text{syst}) \\
 & & & & & -0.216(\text{syst}) \\
 \text{DURHAM-‘C’} & f_g & = & 1.653 & \pm & 0.050(\text{stat}) \quad +0.383(\text{syst}) \\
 & & & & & -0.178(\text{syst})
 \end{array}$$

The systematic errors can be averaged and combined in quadrature with the statistical error to give a single uncertainty on each gluon factor:

$$\begin{array}{llllll}
 \text{DURHAM} & f_g & = & 1.866 & \pm & 0.341 \\
 \text{DURHAM-‘A’} & f_g & = & 1.677 & \pm & 0.356 \\
 \text{DURHAM-‘C’} & f_g & = & 1.653 & \pm & 0.285
 \end{array}$$

These values are compared with previous measurements of the gluon factor, summarised in table 10.3, in figure 10.1. It is important to note that the values of  $f_g$  quoted in this thesis are not directly comparable to quark-gluon multiplicity ratios obtained in previous measurements. These typically involve different selection methods to obtain jet samples, and do not necessarily distinguish between jets with different mixes of flavours and scales.

Experiment	Ratio	Comment	Ref.
ALEPH	$1.48 \pm 0.08^1$	Weighted topological fit to $\langle n_{ch} \rangle$ in an untagged three-jet sample	[68]
ALEPH	$1.32 \pm 0.22^2$	Topological fit to unfolded jet multiplicities	[85]
DELPHI	$1.276 \pm 0.055 \pm 0.022$	<i>b</i> -tagged Mercedes events	[4]
ALEPH	$1.194 \pm 0.027 \pm 0.019$ $1.249 \pm 0.085 \pm 0.022$ $1.060 \pm 0.041 \pm 0.020$ $1.183 \pm 0.221 \pm 0.021$	Ratio in symmetric events for: a natural flavour mix <i>uds</i> quark jets <i>b</i> quark jets <i>c</i> quark jets	[63]
OPAL	$1.471 \pm 0.024 \pm 0.043$	Ratio calculated in rare events where two tagged quark jets lie in the same hemisphere	[3]

Table 10.3: Measurements of the ratio of  $\langle n_{ch} \rangle$  in gluon and quark jets in various three-jet topologies.

---

<sup>1</sup>Statistical error only.

<sup>2</sup>Estimated error.

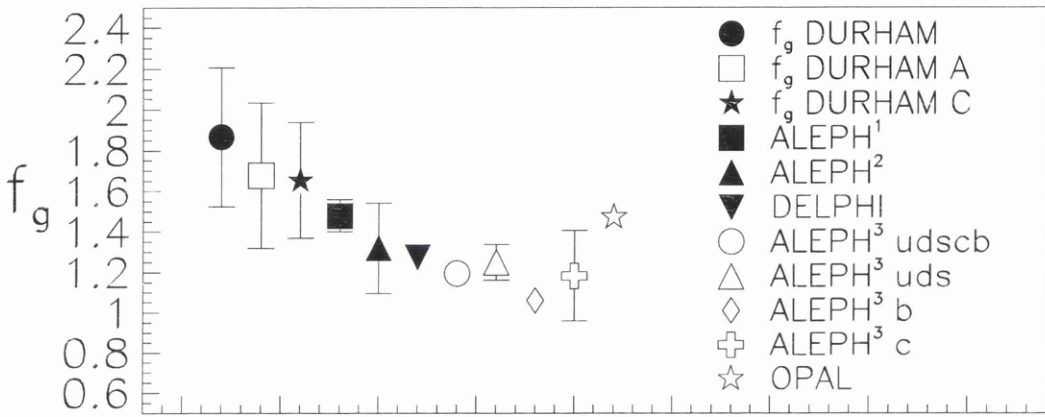


Figure 10.1: Comparison of  $f_g$  to several measurements of the gluon-to-quark charged multiplicity ratio. The three lefthand points correspond to the measurements in this analysis. The other points are those quoted in table 10.3: ALEPH<sup>1</sup> [68], ALEPH<sup>2</sup> [85], DELPHI [4], ALEPH<sup>3</sup> [63], and OPAL [3]. Statistical and systematic errors have been added in quadrature as appropriate.

# Chapter 11

## Fits to Subjet Multiplicity

### 11.1 Introduction

This chapter summarises the results of a study of the topology dependence of the subjet multiplicity in three-jet events. The definition and significance of subjets is discussed in section 3.3; previous subjet studies are summarised in section 3.4.2. The modified versions of the DURHAM jetfinder, the ‘A’ and ‘C’ or Cambridge schemes, are expected to be more sensitive to the subjet multiplicity by virtue of the way in which they cluster particles into jets, see section 5.2.3. It was shown in section 5.3.3 that as each jet in a three-jet event is probed at a resolution scale,  $y_{\text{sub}}$ , the average number of subjets obtained is not equal between jetfinders. The difference was found to be most pronounced in the region  $5 \times 10^{-5} \lesssim y_{\text{sub}} \lesssim 10^{-3}$ .

### 11.2 Binning And Fitting $\langle n_{\text{sub}} \rangle$

To examine the subjet multiplicity, the energy flow objects in each event are separated according to which jet they are associated. Chapter 5 explains the way that the basic and modified jetfinders associate objects together, and gives the typical distribution of charged and neutral objects in three-jet events. All the objects in a single jet are then re-clustered at a subjet  $y_{\text{cut}}$ ,  $y_{\text{sub}}$ , which is smaller than the initial  $y_{\text{cut}}=y_0$ , into separate subjets. The  $y_{\text{sub}}$  essentially sets the minimum permissible transverse momentum  $k_{\perp}$  between any pair of subjets. The number of subjets remaining after the clustering process is recorded and the clustering repeated for the two remaining jets. The subjet multiplicity,  $n_{\text{sub}}$ , of the event is defined as the sum of the subjets obtained in each of the three jets.

As the orientation of the jets in a three-jet event uniquely defines the position

of the event on the Dalitz plane, the subjet multiplicity at *any*  $y_{\text{sub}}$  for a chosen event will be placed in the same Dalitz bin. The three-jet samples obtained using the basic, ‘A’ and ‘C’ DURHAM jetfinders are examined at nineteen values of  $y_{\text{sub}}$ . These are chosen in the interval  $10^{-6} \leq y_{\text{sub}} \leq 10^{-2}$  to cover the a range of inter-subjet  $k_{\perp}$  from hadronic resononace phenomena ( $y_{\text{sub}} \sim 10^{-6}$ ,  $k_{\perp} \sim 100$  MeV) through to hard intra-jet emission ( $y_{\text{sub}} \sim 10^{-2}$ ,  $k_{\perp} \sim 10$  GeV).

The value of  $n_{\text{sub}}$  at each  $y_{\text{sub}}$  is binned on a separate Dalitz plane so that for each jetfinder sample there are a total of 19 subjet multiplicity distributions. Each of these is then fit using the same naïve QCD model as was used to fit the charged multiplicity in chapter 9. It is therefore assumed that the subjet multiplicity varies with energy according to the MLLA formula (3.3). It is also assumed that the formation of subjets in the interjet regions is suppressed due to colour coherence in a similar manner to the charged multiplicity. The validity of these assumptions is discussed later in section 11.4.

The ‘gluon factor’,  $f_g$ , is now interpreted as the ratio of the number of subjets with a chosen  $k_{\perp}$ -separation in gluon and quark jets. As the average subjet multiplicity in reconstructed events,  $\langle n_{\text{sub}} \rangle$ , can take any value between 3 and  $\langle n_{\text{had}} \rangle$  the normalization  $\kappa$  is left free in each fit to compensate for the relative magnitude of  $n_{\text{sub}}$  across each Dalitz plane at each value of  $y_{\text{sub}}$ .

### 11.3 Results Of Subjet Fits

The values of  $f_g$  obtained at each  $y_{\text{sub}}$  for each jetfinder sample are summarised in figure 11.1. When all three fit parameters  $\Lambda$ ,  $\kappa$  and  $f_g$  are left free the fits exhibit the same instability as found when fitting the  $\langle n_{\text{ch}} \rangle$  distribution. To allow the gluon factor to be compared to that measured in the previous chapter, the QCD scale factor is fixed to 150 MeV as described in section 9.2.2. As fitting option  $F_{\text{opt}}=\text{III}$  and energy option  $E_{\text{opt}}=3$  were found to give the best fits to the charged multiplicity they are used throughout for the subjet fits.

One can see from figure 11.1 that the measured values of  $f_g$  can be split into three distinct parts:

- The first region,  $y_{\text{sub}} \lesssim 10^{-5}$ :

The gluon enhancement factor is approximately constant as a function of  $y_{\text{sub}}$ , with  $f_g \sim 1.7$  for the basic jetfinder and  $\sim 1.5$  for the ‘A’ and ‘C’ jetfinders. At resolution scales below  $10^{-5}$  the subjets represent either individual or low- $k_{\perp}$  groups of hadrons. Although this region is not presently

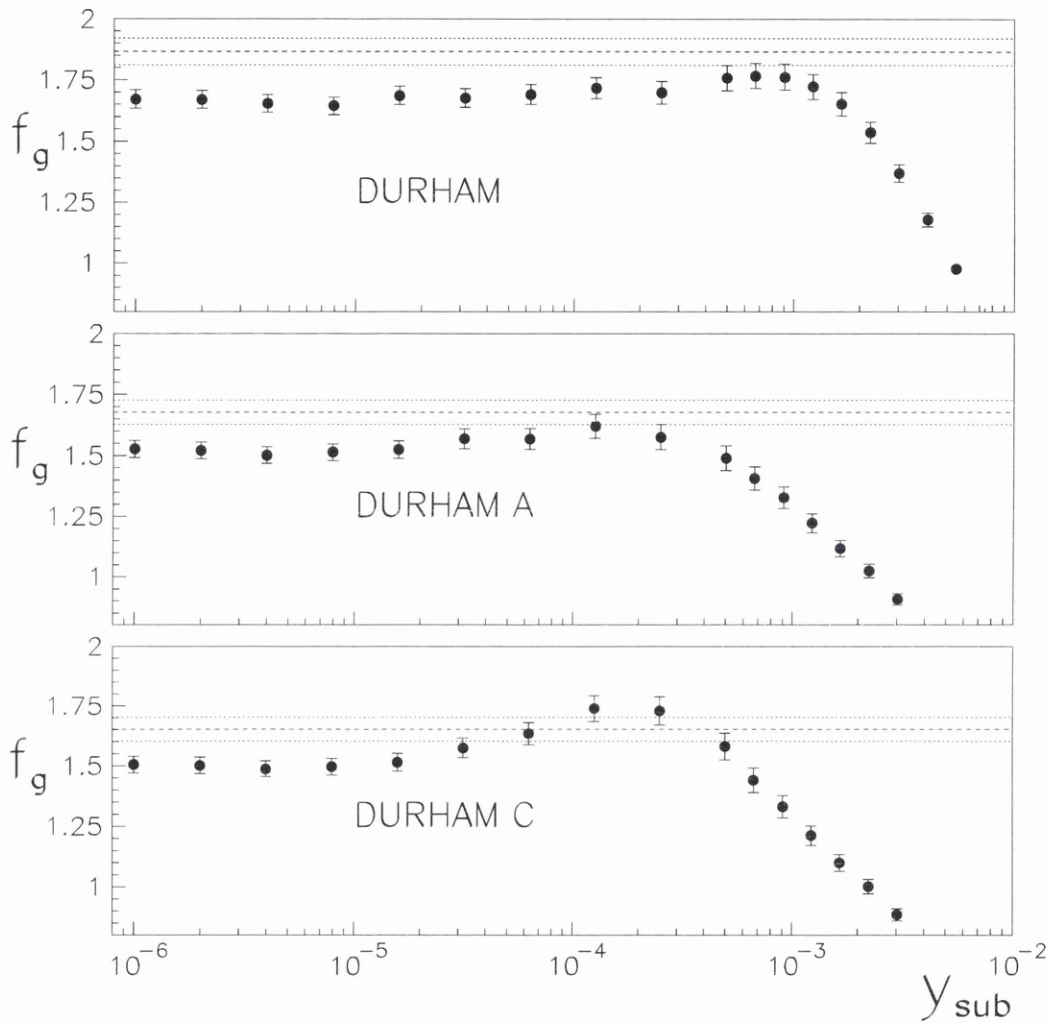


Figure 11.1: The value of  $f_g$  obtained from fits to the subjet multiplicity, defined at a resolution  $y_{\text{sub}}$ , in three-jet events selected using the basic and modified DURHAM jetfinders. The subjet multiplicity at each  $y_{\text{sub}}$  is binned across a Dalitz plane and fit with the same QCD models as used for the charged multiplicity in the previous chapter. Fitting option  $F_{\text{opt}}=\text{III}$  energy option  $E_{\text{opt}}=3$  are used throughout and  $\Lambda$  is fixed at 150 MeV. The dashed line marks the value of  $f_g$  obtained from the  $\langle n_{ch} \rangle$  distribution in section 10.8, and the dotted lines denote the error  $\pm 1\sigma_{\text{stat}}$  about each value.

well understood in QCD it is assumed in the LPHD hypothesis that the hadronization phases of quark and gluon jets are similar. This manifests itself in a flat distribution at the lowest  $y_{\text{sub}}$ .

- The second region,  $10^{-5} \lesssim y_{\text{sub}} \lesssim 5 \times 10^{-4}$ :

Here  $f_g$  rises to a maximum whose position and magnitude is different for each jetfinder. With the basic DURHAM algorithm the peak occurs at  $y_{\text{sub}} \approx 10^{-4}$  ( $k_{\perp} \approx 2.5$  GeV) where  $f_g$  reaches  $1.767 \pm 0.052$ . The peak is slightly more pronounced with the sample obtained with the ‘A’ jetfinder,  $f_g$  reaching a maximum of  $1.620 \pm 0.049$  at  $y_{\text{sub}} \approx 8 \times 10^{-4}$  ( $k_{\perp} \approx 1.0$  GeV). The peak is most prominent with the Cambridge three-jet sample,  $f_g$  rising to  $1.739 \pm 0.054$  at  $y_{\text{sub}} \approx 2 \times 10^{-4}$  ( $k_{\perp} \approx 1.3$  GeV).

- The third region,  $y_{\text{sub}} \gtrsim 5 \times 10^{-4}$ :

Here  $f_g$  falls almost linearly with  $\log y_{\text{sub}}$  to values below unity. At these high resolution scales the distribution of the number of subjets is almost flat across the Dalitz plane with  $\langle n_{\text{sub}} \rangle \sim 3$ . The  $\chi^2$  of the fits becomes very large in the limit  $y_{\text{sub}} \rightarrow y_o$ : as each jet has a subjet multiplicity approaching one all trace of topology dependence disappears and the fits, which are sensitive to topology, break down in this  $y_{\text{sub}}$  regime.

## 11.4 Discussion On $\langle n_{\text{sub}} \rangle$ Fits

### 11.4.1 Shape Of $f_g$ Distribution

The ratio of subjet multiplicities in gluon and quark jets depends on the resolution scale chosen to define the multiplicity. The  $f_g$  distribution is flat at low  $y_{\text{sub}}$  and reaches a maximum value at  $\approx 5 \times 10^{-4}$  before falling away to values less than unity. A similar structure has been observed previously in ALEPH data [65, 66, 2], where  $b$ -tagged quark and gluon jets are selected with the basic DURHAM algorithm at  $y_o = 10^{-1}$ . In these studies the subjet multiplicity is defined as not including the primary parton in each jet, so that the subjet multiplicity of the event is reduced by three. This definition cannot be adopted in this analysis because at high values of  $y_{\text{sub}}$  the multiplicity, when binned on the Dalitz plane, is close to zero and the QCD model fails to fit the data. At small  $y_{\text{sub}}$  the increasing value of  $\langle n_{\text{sub}} \rangle$  means that the effect of the subtraction is reduced.

In this analysis the average subjet multiplicity is assumed to have a similar distribution with scale for both gluon and quark jets, that of the former enhanced

by a factor  $f_g$ . In analyses which employ tagging, the average subjet multiplicity in quark and gluon jets have been compared directly and have been shown to have different energy dependences [66, 2, 4]. Furthermore the value of  $n_{sub}(\text{gluon jets})/n_{sub}(\text{quark jets})$  obtained in these studies can be described in the range  $y_{sub} \gtrsim 10^{-3}$  by a leading order parton-level prediction which is a function of both the initial and subjet  $y_{cut}$  [88].

A direct comparison of the tagged analyses to the study in this thesis is not possible as topological effects were not considered in previous studies. Due to the lower  $y_o$  and naïve method adopted in this analysis the LO prediction [88] is not expected to predict the gluon factor distributions shown in figure 11.1. Nevertheless, the results here still exhibit a similar structure to that in the tagged analyses, and the distribution is qualitatively reproduced in JETSET data.

### 11.4.2 The “Peak” Region

$f_g$  rises to a maximum of  $\sim 1.70$  in the approximate  $k_{\perp}$ -range 1–3 GeV. This implies that the greatest enhancement in radiation from gluons with respect to quarks occurs for bremsstrahlung gluons of energy  $\mathcal{O}(1 \text{ GeV})$ . The absolute maximum value of  $f_g$  is dependent on the jet definition– the basic DURHAM and Cambridge jetfinders yield a value of  $f_g$  of the same order as the NLO prediction [50] for the ratio of the total number of cascade gluons produced in a gluon jet to a quark jet. The subjet multiplicity as defined with the Cambridge jetfinder proves to be most sensitive to the subjet resolution– the increase in  $f_g$  from the value at  $y_{sub}=10^{-5}$  to the maximum value is  $\sim 16\%$ . This figure is approximately 7% & 4% for the basic and ‘A’ DURHAM schemes respectively.

A possible explanation for the enhanced peak is that the Cambridge jetfinder forms subjets in a way that better represents the partonic cascade than the basic or ‘A’ jetfinders. This, in effect, suggests that the number of “Cambridge subjets” found in a jet at each resolution scale has a greater probability of being equal to the number of bremsstrahlung gluons radiated from the primary parton at the equivalent  $k_{\perp}$ . As the Cambridge jetfinder clusters tracks primarily in decreasing angle, the observation of a significant peak in the gluon factor adds weight to the hypothesis that radiation is strongly angular ordered in parton showers.

### 11.4.3 The “Tail” Region

At the lowest  $y_{sub}$ ,  $f_g$  attains an almost constant value as hadronization effects start to dominate. At very low resolutions it is expected that  $f_g$  should become

comparable with the value obtained from fits to the hadronic multiplicity, which is equivalent to the subjet multiplicity in the limit  $y_{\text{sub}} \rightarrow 10^{-\infty}$ . To verify this fact the same fitting process applied to the  $\langle n_{ch} \rangle$  distribution across the plane is repeated with both the neutral and hadronic multiplicities ( $\langle n_0 \rangle$  and  $\langle n_{had} \rangle$  respectively) obtained with each jetfinder. The measured values of  $f_g$ , summarised below in table 11.1, are commensurate for each chosen multiplicity.

Jetfinder	Multiplicity Distribution		
	$\langle n_{ch} \rangle$	$\langle n_0 \rangle$	$\langle n_{had} \rangle$
DURHAM	$1.866 \pm 0.055$	$1.845 \pm 0.062$	$1.855 \pm 0.045$
DURHAM‘A’	$1.677 \pm 0.050$	$1.699 \pm 0.056$	$1.688 \pm 0.041$
DURHAM‘C’	$1.653 \pm 0.050$	$1.688 \pm 0.057$	$1.671 \pm 0.041$

Table 11.1: Measurements of the gluon factor for multiplicity distributions obtained with the basic and modified DURHAM schemes. The errors quoted are statistical only.

The gluon factor measured at  $y_{\text{sub}} = 10^{-6}$  is seen to be approximately 10% less than that extracted from the hadronic multiplicity. Figures 5.12 and 5.13 show that the subjet and hadronic multiplicity become comparable only at  $y_{\text{sub}} \sim < 10^{-8}$ . One concludes that in the region  $10^{-8} \lesssim y_{\text{sub}} < 10^{-6}$  the distribution of  $f_g$  in figure 11.1 must rise to the values given in table 11.1, and at even smaller resolutions become constant as each individual particle in the event becomes defined as a subjet.

# Chapter 12

## Conclusions

This thesis presents studies of the charged and subjet multiplicity in three-jet events with the use of topological scales motivated by the colour dynamics of the  $q\bar{q}g$  system. It is found that the total multiplicity in three-jet events cannot be described simply as a function of the jet energies alone. QCD models are constructed wherein the multiplicity of a jet is given in terms of a topological scale which is a function of both the energy of the jet and the interjet angles. Quark jets are assumed to behave as if their ‘real’ energy  $E_q$  is scaled by a factor  $\sin \frac{\theta_{qg}}{2}$  where  $\theta_{qg}$  is the angle to the gluon jet. The gluon scale depends on the angle to each neighbouring quark as it is colour-connected simultaneously to both. The models allow the multiplicity in  $q\bar{q}g$  events to be described in terms of a MLLA formula for the inclusive multiplicity in two jet events originating from  $e^+e^-$  collisions.

Candidate  $q\bar{q}g$  events are selected from ALEPH data collected from 1990–94. The particles in each event are clustered together using the DURHAM algorithm, in the ‘basic’ form and with the modified ‘A’ and ‘C’ (or Cambridge) schemes, to compare their relative merits. The modified schemes differ from the basic DURHAM jetfinder in that they cluster particles in an angular order which attempts to imitate the angular ordering of bremsstrahlung gluons in partonic cascades.

An initial  $y_{\text{cut}}, y_o=10^{-2}$  is adopted in this analysis. Events with three or more jets are retained for analysis and re-clustered to three jets if necessary. If each jet in an event passes a series of angular and energy cuts the charged multiplicity,  $n_{ch}$ , is recorded along with the subjet multiplicity,  $n_{sub}$ , which is defined at a number of resolution scales  $y_{\text{sub}} < y_o$ . These multiplicities are then binned on a Dalitz plane, the position on the plane determined by the energies of the jets



will be interesting to compare the findings contained herein with future subject studies which involve the direct comparison between tagged quark and gluon jets. The findings of this work imply that such studies must take the jet topology into account and cannot relate jet properties simply in terms of the observed or calculated energies of the jets.

# Appendix A

## The Group $SU(3)$

The group  $SU(3)$  is a subset of  $U(3)$  formed from a set of unitary  $3 \times 3$  transformation matrices  $U$  where  $\det U = 1$ . It is possible to write any  $U$  in terms of the  $(3 \times 3 - 1)$  *generators* of  $SU(3)$  Lie algebra,  $t^a$ . The  $t^a$  are an octet of linearly independent traceless hermitian  $3 \times 3$  matrices, conventionally chosen as  $t^a = \lambda^a / 2$  where  $\lambda^a$  are known as the Gell-Mann matrices:

$$\begin{aligned} \lambda^1 &= \begin{pmatrix} 0 & 1 & 0 \\ 1 & 0 & 0 \\ 0 & 0 & 0 \end{pmatrix}, \\ \lambda^2 &= \begin{pmatrix} 0 & -i & 0 \\ i & 0 & 0 \\ 0 & 0 & 0 \end{pmatrix}, \lambda^3 = \begin{pmatrix} 1 & 0 & 0 \\ 0 & -1 & 0 \\ 0 & 0 & 0 \end{pmatrix}, \lambda^4 = \begin{pmatrix} 0 & 0 & 1 \\ 0 & 0 & 0 \\ 1 & 0 & 0 \end{pmatrix}, \\ \lambda^5 &= \begin{pmatrix} 0 & 0 & -i \\ 0 & 0 & 0 \\ i & 0 & 0 \end{pmatrix}, \lambda^6 = \begin{pmatrix} 0 & 0 & 0 \\ 0 & 0 & 1 \\ 0 & 1 & 0 \end{pmatrix}, \lambda^7 = \begin{pmatrix} 0 & 0 & 0 \\ 0 & 0 & -i \\ 0 & i & 0 \end{pmatrix}, \\ \lambda^8 &= \frac{1}{\sqrt{3}} \begin{pmatrix} 1 & 0 & 0 \\ 0 & 1 & 0 \\ 0 & 0 & -2 \end{pmatrix}. \end{aligned}$$

The commutator of any pair of  $t^a$  is a linear combination of all the generators,

$$[t^a, t^b] = i \sum_c f^{abc} t^c ,$$

where  $f_{abc}$  are antisymmetric under interchange of any pair of indices. The only non-zero  $f_{abc}$  are (permutations of)

$$\begin{aligned} f_{123} &= 1 , \\ f_{147} = f_{246} = f_{257} = f_{345} &= \frac{1}{2} , \\ f_{156} = f_{367} &= -\frac{1}{2} , \\ f_{458} = f_{678} &= \frac{\sqrt{3}}{2} . \end{aligned}$$

For a general group SU(N) the invariants  $C_A$ ,  $C_F$  and  $T_F$  are defined in terms of  $t^a$  and  $f^{abc}$  by

$$\begin{aligned} \delta_{ab} C_A &= \sum_{cc'} f^{acc'} f^{bcc'} , \\ \delta_{ik} C_F &= \left( \sum_a t^a t^a \right)_{ik} , \\ \delta_{ab} T_F &= Tr t^a t^b . \end{aligned}$$

One arrives at the simple expressions

$$C_A = N, \quad C_F = \frac{N^2 - 1}{2N}, \quad T_F = \frac{1}{2} ,$$

and for SU(3)  $N = 3$  giving  $C_A = 3$ ,  $C_F = \frac{4}{3}$  and  $T_F = \frac{1}{2}$ . The relationship

$$D^c C_F = D^a T_F$$

holds for an SU(3) symmetry group where  $D^c$  and  $D^a$  are the dimensions of the fundamental and adjoint representations of the group respectively.

# Appendix B

## Example of a MINUIT Minimization

An example of a fit to ALEPH data with the MINUIT fitting package [84] is given in figure B.1 on the following page. The distribution chosen was the charged multiplicity in three-jet events selected according to the procedure outlined in chapter 7 with the basic DURHAM jetfinder, which is described in chapter 5. Only bins on the plane that satisfy  $E_{1,2} \leq 41$  GeV are included in the fit, where  $E_1$  and  $E_2$  are the energy of the hardest and next-to-hardest jets respectively.

The output is from a least-squares minimization, comparing data to a theoretical prediction, which has been smeared to account for detector and selection effects. A full description of the fitting and smearing process can be found in chapter 8. Fitting option III, see section 8.2.1, and energy option 3, see section 8.2.3, have been selected and the QCD scale factor fixed to  $\Lambda=150$  MeV.

The first part of the output in figure B.1 shows the parameters extracted from the fit:  $f_g=1.866\pm 0.055$  and  $\kappa=34.11\pm 0.44\times 10^{-3}$ , which are 99.7% anti-correlated. In the diagram the relationship between  $f_g$  and  $\Lambda$  is shown. The contour is constructed from several least-squares fits, where  $\kappa$  has been fixed to the previous fit value and  $\Lambda$  left free. The contour, formed as the two free parameters are varied by  $\pm 1\sigma$  about their fit values, traces a very flat ellipse, signifying that  $f_g$  and  $\Lambda$  are almost fully correlated.

```

EXT PARAMETER
NO.  NAME      VALUE      ERROR
  1   Fg       1.8657    0.54915E-01
  2   Lambda   0.15000   fixed
  3   factor   0.34112E-01 0.43739E-03

```

```

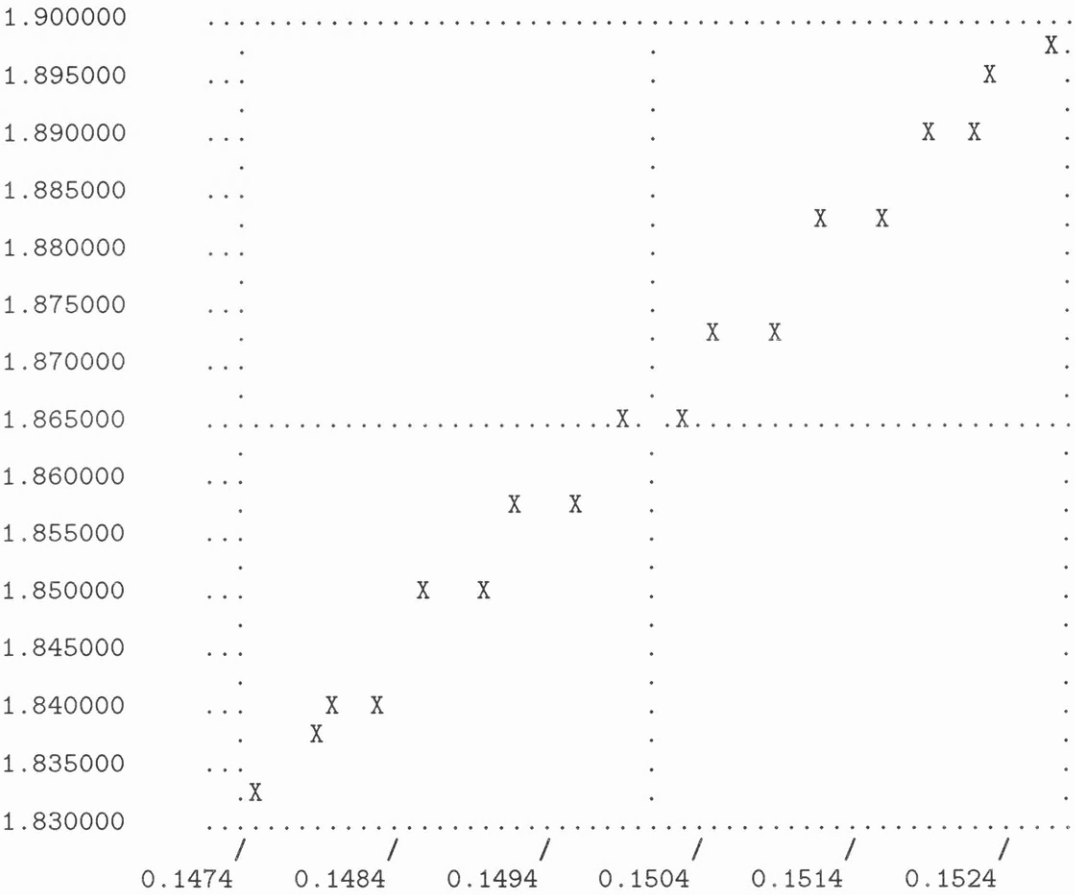
PARAMETER CORRELATION COEFFICIENTS
NO.  GLOBAL  1    3
  1  0.99730 1.000 -0.997
  3  0.99730 -0.997 1.000

```

```

START MNCONTOUR CALCULATION OF 20 POINTS ON CONTOUR.
Y-AXIS: PARAMETER 1 Fg

```



```

ONE COLUMN=0.1000000E-03
X-AXIS: PARAMETER 2 Lambda

```

Figure B.1: Selected output from a minimization performed with the MINUIT fitting package.

# Bibliography

- [1] J. Alcarez *et al.*, *Combination of Preliminary LEP and SLD Electroweak Measurements and Constraints on the Standard Model*, LEPEWWG/02 (1996).
- [2] ALEPH Collaboration *R. Barate et al.*, CERN PPE/98-016, *Submitted to Eur. Phys. J. C*.
- [3] OPAL Collaboration, K. Ackerstaff *et al.*, *Eur. Phys. J.* **C1** (1998) 479.
- [4] DELPHI Collaboration, *P. Abreu et al.*, *Z. Phys.* **C70** (1996) 179.
- [5] M. Acciarri *et al.*, *Phys. Lett.* **B345** (1995) 74.
- [6] ALEPH NOTES 94-171 & 95-008, *Contributions from Philippe Ghez, Oliver Buchmüller and Ann Moutoussi*.
- [7] J.D. Bjorken and S.D. Drell, *Relativistic Quantum Mechanics*, (1964).
- [8] F. Halzen and A. Martin, *Quarks and Leptons*, Wiley (1984).
- [9] F. Close, *An Introduction to Quarks and Partons* (1979).
- [10] I.J.R. Aitchison and A.J.G. Hey, *Gauge Theories in Particle Physics*, Adam Hilger, (1989).
- [11] H. Harari, *Phys. Rep.* **42C** (1978) 235.
- [12] R.M. Barnett *et al.*, *Review of Particle Properties*, *Phys. Rev.* **D54** (1996).
- [13] S.L. Glashow and M. Gell-Mann, *Gauge Theories of Vector Particles*, *Annals Phys.* **15** (1961) 437.
- [14] S. Weinberg, *A Model of Leptons*, *Phys. Rev. Lett.* **19** (1967) 1264.
- [15] A. Salam, *Elementary Particle Theory*, ed. H. Svartholm, Almquist, Stockholm, Proc. 8th Nobel Symposium (1968).
- [16] R.P. Feynman, *Space-Time Approach to Nonrelativistic Quantum Electrodynamics*, *Rev. Mod. Phys.* **B20** (1948) 367.

- [17] F.J. Ynduráin, *Quantum Chromodynamics: An Introduction to the Theory of Quarks and Gluons*, Springer, 1983.
- [18] W.A. Bardeen *et al.*, Phys. Rev. **D18** (1978) 3998.
- [19] Particle Data Group, *Review of Particle Physics*, Phys. Rev. **D56** (1996) 77.
- [20] The ALEPH Collaboration, *Studies of Quantum Chromodynamics with the ALEPH Detector*, Phys. Rep. **194** (1998) 1.
- [21] R.F. Schwitters *et al.*, Phys. Rev. Lett. **35** (1975) 1609.
- [22] R. Brandelik *et al.*, Phys. Lett. **B86** (1979) 243.  
D.P. Barber *et al.*, Phys. Rev. Lett. **43** (1979) 830.  
Ch. Berger *et al.*, Phys. Lett. **B86** (1979) 418.  
W. Bartel *et al.*, Phys. Lett. **B91** (1980) 142.
- [23] I.G. Knowles and G.D. Lafferty, J. Phys. **G23** (1997) 731.
- [24] F. Boudjema and B. Mele, *Z<sup>0</sup> Physics at LEP I*, eds. G. Altarelli, R. Kleiss and C. Verzegnazzi, CERN-PPE/01 Vol.1 (1996).
- [25] Particle Data Group, *Review of Particle Properties*, Phys. Rev. **D50** (1994) 1334.
- [26] F. Bloch and A. Nordsieck, Phys. Rev. **52** (1937) 54.  
T. Kinoshita, J. Math. Phys. **3** (1962) 650.  
T.D. Lee and M. Nauenberg, Phys. Rev. **133** (1964) 1549.
- [27] M. Dine and J. Sapirstein, Phys. Rev. Lett. **43** (1979) 668.
- [28] G. Altarelli and G. Parisi, Nucl. Phys **B126** (1977) 298.  
Yu.L. Dokshitzer, Sov. Phys. JETP **46** (1977) 641.
- [29] Yu.L. Dokshitzer, V.A. Khoze A.H. Mueller and S.I. Troyan, *Basics of Perturbative QCD*, Editions Frontieres (1991).
- [30] A.H. Mueller, Phys. Lett. **B104** (1981) 161.  
B.I. Ermolaev and V.S. Fadin, JETP Lett. **33** (1981) 285.
- [31] Ya.I. Azimov, Yu.L. Dokshitzer, V.A. Khoze and S.I. Troyan, Z. Phys. **C27** (1985) 65.
- [32] B. Bambach *et al.*, *Z<sup>0</sup> Physics at LEPI*, eds. G. Altarelli, R. Kleiss and C. Verzegnazzi, CERN-PPE/08 Vol.3 (1989) 43.
- [33] T. Sjöstrand, Comp. Phys. Comm. **39** (1986) 347.  
M. Bengtsson and T. Sjöstrand, Comp. Phys. Comm. **43** (1987) 367.  
T. Sjöstrand, Comp. Phys. Comm. **82** (1994) 74.  
T. Sjöstrand, PYTHIA 5.7 and JETSET 7.4, CERN-TH/7112 (1993).

- [34] M. Acciarri *et al.*, *Z. Phys.* **C55** (1992) 39.
- [35] B. Andersson, G. Gustafson, G. Ingelman and T. Sjöstrand, *Phys. Rep.* **97** (1983) 31.
- [36] B. Andersson, G. Gustafson and T. Sjöstrand, *Phys. Lett.* **B94** (1980) 211.
- [37] G. Marchesini and B.R. Webber, *Nucl. Phys* **B238** (1984) 1.  
G. Marchesini and B.R. Webber, *Nucl. Phys* **B310** (1988) 461.  
G. Marchesini, B.R. Webber, G. Abbiendi, I.G. Knowles, M.H. Seymour and L. Stanco, *Comp. Phys. Comm.* **67** (1992) 465.  
HERWIG Version 5.9, HEP-PH/9607393.
- [38] JADE Collaboration, W. Bartel *et al.*, *Z. Phys.* **C20** (1983) 187.  
PLUTO Collaboration, C. Berger *et al.*, *Phys. Lett.* **B95** (1980) 313.  
TASSO Collaboration, W. Braunschweig *et al.*, *Z. Phys.* **C45** (1989) 193.  
TPC/2 $\gamma$  Collaboration, H. Aihara *et al.*, *Phys. Lett.* **B134** (1987) 299.  
HRS Collaboration, M. Derrick *et al.*, *Phys. Rev.* **D34** (1986) 3304.  
TOPAZ Collaboration, M. Yamauchi *et al.*, *Proc. XXIVth International Conference on High Energy Physics, Munich* (1988) 852.  
AMY Collaboration, H.W. Zheng *et al.*, *Phys. Rev.* **D42** (1990) 737.  
ALEPH Collaboration, D. Decamp *et al.*, *Phys. Lett.* **B273** (1991) 181.  
DELPHI Collaboration, P. Abreu *et al.*, *Z. Phys.* **C50** (1991) 185.  
OPAL Collaboration, P.D. Acton *et al.*, *Z. Phys.* **C53** (1992) 539.  
L3 Collaboration, B. Adeva *et al.*, CERN-PPE/92.  
MARK II Collaboration, G.S. Abrams *et al.*, *Phys. Rev. Lett.* **64** (1990) 1334.
- [39] A.H. Mueller, *Nucl. Phys.* **B213** (1983) 85.
- [40] B.R. Webber, *Phys. Lett.* **B143** (1984) 501.
- [41]  $Z^0$  Physics at LEP I, Z. Kunszt, P. Nason, G. Marchesini and B. Webber, CERN-PPE/08 Vol.1 (1989) 434.
- [42] DELPHI Collaboration, P. Abreu *et al.*, *Z. Phys.* **C50** (1991) 185.
- [43] OPAL Collaboration, P.D. Acton *et al.*, *Z. Phys.* **C53** (1992) 539.
- [44] Yu.L. Dokshitzer, V.A. Khoze and S.I. Troyan, *J. Phys* **G17** (1991) 1602.  
B.A. Schumm *et al.*, *Phys. Rev. Lett.* **69** (1992) 3025.
- [45] R. Akers *et al.*, *Z. Phys.* **C61** (1994) 209.
- [46] J. Chrin, *Proc. XXVIIth International Conference on High Energy Physics, Glasgow, 20–27 July 1994, Vol II* 893.

- [47] OPAL Collaboration, K. Ackerstaff *et al.*, *Z. Phys.* **C75** (1997) 193.  
DELPHI Collaboration, P. Abreu *et al.*, *Phys. Lett.* **B372** (1996) 172.  
DELPHI Collaboration, P. Abreu *et al.*, *Phys. Lett.* **B416** (1998) 233.  
L3 Collaboration, M. Acciarri *et al.*, *Phys. Lett.* **B404** (1997) 390.
- [48] ALEPH Collaboration, G. Cowan, Y. Gao and R. Jones, *QCD studies with  $e^+e^-$  annihilation data from 130 to 172 GeV and Preliminary ALEPH results at 183 GeV*, *Contributions to EPS-HEP Conference*, Jerusalem 19–26 August (1997).
- [49] E.D. Mazala and B.R. Webber, *Phys. Lett.* **B149** (1984) 501.
- [50] J.B. Gaffney and A.H. Mueller, *Nucl. Phys.* **B250** (1985) 109.  
I.M. Dremin and V.A. Nechitailo, *Mod. Phys. Lett* **A9** (1994) 1471.
- [51] JADE Collaboration, W. Bartel *et al.*, *Phys. Lett.* **B101** (1981) 129.
- [52] ALEPH Collaboration, *Contribution to the International Europhysics Conference on High Energy Physics*, Brussels, Belgium 27 July–2 August (1995).  
OPAL Collaboration, M.Z. Akrawy *et al.*, *Phys. Lett.* **B261** (1991) 334.
- [53] M. Acciarri *et al.*, *Phys. Lett.* **B345** (1995) 74.  
OPAL Collaboration, R. Akers *et al.*, *Z. Phys.* **C68** (1995) 531.
- [54] ALEPH Collaboration, *Contribution to the International Europhysics Conference on High Energy Physics*, Brussels, Belgium 27 July–2 August 1995.
- [55] ALEPH NOTE 94-171, *Contribution from Ian Knowles*.
- [56] Ian Knowles, *Private Communication*.
- [57] OPAL Collaboration, G. Alexander *et al.*, *Phys. Lett.* **B265** (1991) 462.
- [58] P.D. Acton *et al.*, *Z. Phys.* **C58** (1993) 387.
- [59] OPAL Collaboration, *Z. Phys.* **C68** (1995) 179.
- [60] OPAL Collaboration, *Z. Phys.* **C69** (1996) 543.
- [61] OPAL Collaboration, G. Alexander *et al.*, *Phys. Lett.* **B388** (1996) 659.
- [62] ALEPH Collaboration *D. Buskulic et al.*, *Phys. Lett.* **B384** (1996) 353.
- [63] ALEPH Collaboration, *Contribution to International Conference on High Energy Physics*, Warsaw, July 1996.
- [64] R. Akers *et al.*, *Z. Phys.* **C63** (1994) 363.
- [65] ALEPH Collaboration, *D. Buskulic et al.*, *Phys. Lett.* **B346** (1995) 389.
- [66] F. Stephan, internal report ALEPH **96-115**.

- [67] M. Acciarri *et al*, Phys. Lett. **B353** (1995) 145.  
OPAL Collaboration, P.D. Acton *et al.*, Z. Phys. **C58** (1993) 207.
- [68] ALEPH Collaboration R. Barate *et al.*, Z. Phys. **C76** (1997) 191.
- [69] S. Myers, *The LEP Collider from Design to Approval and Commissioning*, CERN-PPE/08 (1991).
- [70] *The ALEPH Handbook*, D. Decamp *et al.*, ed. W. Blum.  
Nucl. Inst. Meth. **A294** (1990) 121.  
*ALEPH in Numbers*, eds. D. Schlatter, G. Redlinger and P. Perrodo, March 1993.
- [71] V. Blobel, DESY **R1-88-01** (1988).
- [72] The ALEPH Collaboration, Nucl. Inst. Meth. **A360** (1995) 481.
- [73] Günther Dissertori, Dissertation (1997).
- [74] W. Bartel *et al.*, Z. Phys. **C33** (1986) 23.  
S. Bethke *et al.*, Phys. Lett. **B213** (1988) 235.
- [75] S. Bethke, Z. Kunszt, D.E. Soper and W.J. Stirling, Nucl. Phys. **B370** (1992) 310.
- [76] Yu.L. Dokshitzer, G.D. Leder, S. Moretti and B.R. Webber, JHEP08 (1997) 1.
- [77] G. Kramer and B. Lampe, Z. Phys. **C34** (1987) 497.
- [78]  $Z^0$  Physics at LEP I, eds. G. Altarelli, R. Kleiss and C. Verzegnazzi, CERN-PPE/08 Vol.1 (1989) 203.
- [79] N. Brown and W.J. Stirling, Z. Phys. **C53** (1992) 629.
- [80] S. Catani *et al.*, Phys. Lett. **B269** (1991) 432.
- [81] S. Bentvelsen and Irmtraud Meyer, *Submitted to Eur. Phys. J. C*.
- [82] The ALEPH Collaboration, D. Decamp *et al.*, Phys. Lett. **B284** (1992) 151.
- [83] ALEPH Collaboration, D. Buskulic *et al.*, Z. Phys. **C69** (1996) 365.
- [84] F. James, *MINUIT Reference Manual*, CERN Program Library Long Writeup **D506** (1994) 1.
- [85] Oliver Buchmüller, ALEPH/96-109 (1996).
- [86] J.M. Campbell, E.W.N. Glover and C.J. Maxwell, hep-ph/9803254.



- [87] A.J. Buras, Proc. 1981 International Symp. on Lepton and photon interaction at high energies, Bonn.  
Yu.L. Dokshitzer, V.A. Khoze and S.I. Troyan, J. Phys **G17** (1991) 1481.  
S. Lupia and W. Ochs, Phys. Lett. **B365** (1996) 339.  
V.A. Khoze, S. Lupia and W. Ochs, Phys. Lett. **B394** (1997) 179.  
S. Lupia and W. Ochs, Phys. Lett. **B418** (1998) 214.  
Yu.L. Dokshitzer, Phys. Lett. **B305** (1993) 295.
- [88] M. Seymour, CERN-TH/**95-255** (1995).